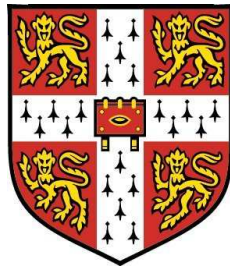


Source modelling of extreme and intermediate mass ratio inspirals



Eliu Antonio Huerta Escudero

Institute of Astronomy

University of Cambridge

A thesis submitted for the degree of

Doctor of Philosophy

June 2011

Declaration

This dissertation is submitted in partial fulfilment of the requirements for the degree of Doctor of Philosophy. No part of it has been submitted for any other qualification, and it is the result of my work under the guidance of my supervisor Dr Jonathan Reavley Gair. It includes nothing that is the outcome of collaborative work except where specifically indicated in the text. The following chapters are based on articles that have been, or are being, peer-reviewed and published:

- Chapter 2
Huerta, EA and Gair, JR. Influence of conservative corrections on parameter estimation for extreme-mass-ratio inspirals. *Phys. Rev. D*, 79:084021, 2009.
- Chapter 3
Huerta, EA and Gair, JR. The importance of including small body spin effects in the modelling of extreme and intermediate mass-ratio inspirals. Submitted to *Phys. Rev. D*.
- Chapter 5
Huerta, EA and Gair, JR. Intermediate-mass-ratio inspirals in the Einstein Telescope. I. Signal-to-noise ratio calculations. *Phys. Rev. D*, 83:044020, 2011.
- Chapter 6
Huerta, EA and Gair, JR. Intermediate-mass-ratio inspirals in the Einstein Telescope. II. Parameter estimation errors. *Phys. Rev. D*, 83:044021, 2011.

The length of this dissertation including footnotes and bibliography is less than 60000 words.

Eliu A Huerta
June 2011

Acknowledgements

I would like to thank my supervisor, Jonathan R Gair, for his guidance over the last four years. Working with him has been a very productive and enlightening experience.

I am also grateful to my mentor, Sir David Wallace, for being a continuous source of encouragement ever since I started Part III at Churchill College.

I would like to thank Sian Owen, Rebecca Sawalmeh, Judith Moss and Margaret Harding for their kind support and advice in all bureaucratic related matters. I am particularly indebted to Rebecca for always being so helpful in various matters I had to deal with at Churchill, ranging from travel grants to visa extensions, over the last five years.

My wife, Yolanda Gago-Sanz, truly deserves special words of praise. She has always had the appropriate words to persuade me to work consistently during my PhD. Undoubtedly, the completion of this thesis could not have been possible without her support. Talking to her has always helped me see things from a different (always more positive) perspective, especially when work was not going as good as expected. I am deeply thankful to her for being an (apparently, and in practical terms) infinite source of comfort and love. I am also grateful to her parents and Ismael for being so kind, generous and loving with me, and for making me feel part of their family.

Still on this side of the pond, I want to thank a few friends that made my stay in Cambridge a joyous time, and helped me see the good in Britain: Brian Ward and his family, Michael Martin and his family, Luke and Pele Griffith, Sam and Dona Burkin, Lin and Caroline, Ron Bailey, Denise and Tony Cutts, John Broad, Frank and Nina Cowell. But in particular to Brian and Michael, who proved to be true friends in times of distress.

My parents have also played a fundamental role on the emotional side of things. I am grateful for their comforting and refreshing words, invaluable advice and continuous encouragement, in particular during my first year

in Cambridge. I thank my mother for teaching me with her example the value of being truthful and honest in all aspects of my life. I will always be grateful to my dad for giving me the book “The meaning of relativity” nearly two decades ago, and the countless hours that he spent with me reading great books and doing maths when I was a kid.

I would also like to honour the memory of a few friends and relatives who sadly passed away during my stay in the UK: my paternal grandmother, Brandon Carter, Bill Watts, Elvis Nwachukwu and Alan Broad.

Finally, I must thank the Consejo Nacional de Ciencia y Tecnología (CONACyT), whose generous fellowship paid for my studies. I also thank Churchill College, the Institute of Astronomy, Cambridge, and Stanford University for travel grants that enabled me to present my work at various conferences.

Abstract

Source modelling of extreme and intermediate mass ratio inspirals

Eliu Antonio Huerta

Gravitational wave (GW) astronomy is a powerful tool to study the astrophysical properties of compact objects (COs), i.e., black holes (BHs), neutron stars (NSs) and white dwarfs (WDs), which are the most extreme bodies known, and which are hard to probe via other means.

In the first part of this thesis I have investigated the precision with which future low-frequency space-based GW detectors will be able to measure the fundamental properties —mass and spin— of supermassive black holes (SMBHs) that exist in the centres of galaxies. This study has two different aspects. The first one consists of developing an accurate waveform template to study the inspiral of stellar mass COs into SMBHs. This study suggests that space-based detectors, such as LISA, will be able to perform a very accurate census of the mass and spin distributions of SMBHs. Furthermore, by augmenting the waveform template with corrections that take into account the interaction of the inspiralling body with the curvature of the background spacetime, I have found that for LISA the systematic errors that arise from omitting these conservative self-force corrections are generally smaller than the parameter errors that arise from instrumental noise. However, parameter estimation results also suggest that the second-order radiative piece of the self-force may be as important as the first-order conservative part. Hence, conservative self-force corrections can probably be ignored in search templates, but it may be necessary to follow-up with more accurate templates to get more precise parameter estimates.

The second investigation involves the modelling of the inspiral of stellar mass and intermediate mass black holes (IMBHs) into SMBHs. I have

studied whether the inclusion of small body spin effects is of any relevance for this type of event. I have found that these corrections are important for mergers that involve bodies with masses $\gtrsim 10^3 M_\odot$ that inspiral into central objects with masses $\sim 10^6 M_\odot$. By including spin-orbit and spin-spin couplings in waveform templates, GW observations may allow an accurate determination not only of the properties of the central SMBH, but also of an IMBH that spirals into it.

The second part of this thesis deals with IMBHs in the context of ground-based detector networks. The inspiral of stellar mass COs into IMBHs—events which may take place in core-collapsed globular clusters—will generate GWs that could be detected with ground-based detectors. I have modeled these sources using the best information currently available from the extreme and comparable-mass-ratio regimes. The waveform models I have developed include the inspiral, merger and ringdown phases in a consistent way. In order to cross-check the accuracy of my predictions, I have built two alternative models. One of them is valid for intermediate mass black holes of arbitrary spin, whereas the second model is valid for non-spinning sources. I have used these models, in the context of the proposed Einstein Telescope, to compute signal-to-noise ratios and parameter estimation errors for a sample of binary systems, assuming a variety of ground-based detector networks. The two models make predictions that are consistent to better than ten percent. Using these models, I have explored the dependence of parameter estimation errors on the network configuration, and the improvement that may be achieved if this instrument achieves good low frequency sensitivity.

Contents

Contents	vi
List of Figures	ix
1 Introduction	1
1.1 Gravitational Waves — A brief account	1
1.2 Extreme-mass-ratio inspirals	12
1.3 Intermediate-mass-ratio inspirals in the context of space-based detectors	16
1.4 LISA descoper studies	17
1.5 IMRIs in the context of ground-based interferometers	18
2 Influence of conservative corrections on signal detection and parameter estimation for extreme-mass-ratio inspirals	23
2.1 Overview	23
2.2 Kludge waveform	24
2.3 A comparison with the SF formalism for non-spinning BHs	34
2.3.1 Assessing SF calculations using the kludge model	35
2.4 Noise induced parameter errors	39
2.4.1 Waveform prescription	39
2.4.2 Implementation of LISA’s response function	41
2.4.3 Signal analysis	43
2.4.4 Noise model	45
2.5 Parameter estimation error results	47
2.6 Model-induced parameter errors	53
2.7 Conclusions	62

3	The importance of including small body spin effects in the modelling of extreme and intermediate mass-ratio inspirals	65
3.1	Overview	65
3.2	Kludge waveform with small body spin effects	66
3.3	Parameter estimation error results	75
3.3.1	Determination of SNR detection thresholds	75
3.3.2	Parameter estimation results	77
3.4	Model-induced parameter errors	84
3.5	Conclusions	92
4	Extreme-mass-ratio inspirals in the context of LISA descope studies	94
4.1	Overview	94
4.2	LISA descope studies	94
4.3	Parameter estimation results	96
4.4	Conclusions	100
5	Source modelling of intermediate-mass-ratio inspirals	101
5.1	Overview	101
5.2	Assumptions	102
5.2.1	Einstein Telescope Design	102
5.2.2	Sample IMRI systems	104
5.3	IMRI waveform modelling - Inspiral phase	104
5.4	Transition and plunge phases for an initially spinning IMBH	107
5.5	Ringdown waveform	112
5.6	Plunge and merger waveform from the effective one-body approach	115
5.7	Dynamics of the waveform models	124
5.7.1	Implementation of the response function	125
5.7.2	Noise model	126
5.7.3	Sample waveforms	126
5.8	SNRs for spinning and non-spinning binaries	128
5.9	Conclusions	138
6	Parameter estimation using intermediate-mass-ratio inspirals	140
6.1	Overview	140
6.2	Assumptions	140
6.3	Signal analysis	141
6.4	Parameter estimation error results	142

6.4.1	Dependence of parameter estimation errors on system parameters	142
6.4.2	Dependence of parameter estimation errors on network configuration	147
6.5	Conclusions	156
7 Conclusions		159
Appendix A		165
.1	Dependence of parameter estimation errors on network configuration . .	165
References		169

List of Figures

1.1	Total effective noise density for LISA	13
2.1	Gravitational waveform cycles completed over the last year of inspiral before plunge by a sample of EMRIs using conservative–self force (SF) corrections at second post–Newtonian (PN) order	33
2.2	Time taken by the conservative SF corrections up to 2PN order to contribute one cycle to the phasing of a binary system as a function of the central SMBH spin parameter	33
2.3	Time taken by the 2PN conservative SF corrections to contribute one cycle to the phasing of a binary system as a function of the central SMBH spin parameter	34
2.4	Total LISA noise curve for stellar mass BH inspirals into SMBHs during the last year before plunge	46
2.5	Monte Carlo distributions of noise–induced errors for a canonical system.	50
2.6	Noise–induced errors for intrinsic parameters of a canonical system as function of time before plunge	51
2.7	Noise–induced errors for extrinsic parameters of a canonical system as function of time before plunge	52
2.8	Monte Carlo distribution of the ratio of the model error to the noise–induced error of the intrinsic parameters of a canonical EMRI	59
2.9	Model and noise–induced errors for the intrinsic parameters of a canonical EMRI as a function of time before plunge	60
2.10	Model and noise–induced errors for the extrinsic parameters of a canonical EMRI system as function of time before plunge	61
3.1	Signal-to-noise-ratio distributions for a sample of spinning massive black hole binary mergers.	76

3.2	Signal-to-noise-ratio distributions for a sample of slowly rotating massive black hole binary mergers.	77
3.3	Distribution of parameter measurement error estimates for a spinning IMRI system.	82
4.1	Noise curves for LISA descope concepts	96
5.1	Sensitivity curve for the Einstein Telescope.	103
5.2	Complete gravitational waveforms for two different binary systems with spinning intermediate-mass BHs.	127
5.3	Complete gravitational waveforms for two non-spinning binary systems using two independent waveform models.	127
5.4	Signal-to-noise ratio for binary systems with component masses $10M_{\odot} + 100M_{\odot}$	129
5.5	Signal-to-noise ratio for binary systems with component masses $1.4M_{\odot} + 100M_{\odot}$	129
5.6	Signal-to-noise ratio for binary systems with component masses $10M_{\odot} + 500M_{\odot}$	130
5.7	Signal-to-noise ratio for binary systems with component masses $1.4M_{\odot} + 500M_{\odot}$	130
5.8	Signal-to-noise distributions as a function of the IMBH spin for a sample of binary systems	132
5.9	Signal-to-noise distribution at a frequency cut-off of 1Hz for a system with component masses $10M_{\odot} + 100M_{\odot}$	135
6.1	Parameter error distributions for a spinning IMRI system with component masses $10M_{\odot} + 100M_{\odot}$	145
6.2	Fractional measurement errors in the component masses and IMBH spin parameters of binaries with slowly rotating IMBHs.	146
6.3	Expected measurement errors in the component masses and IMBH spin parameter as a function of the network configuration for slowly rotating binary systems with masses $10M_{\odot} + 100M_{\odot}$	148

Chapter 1

Introduction

1.1 Gravitational Waves — A brief account

The greatest achievement of the Newtonian gravitational theory occurred in the XIX century with the prediction, by Leverrier and Adams, and discovery, by Johann Galle, of the planet Neptune. It is appropriate then that the subsequent observation of planetary motions and anomalies in celestial mechanics eventually brought this theory to a critical stage that triggered the development of a new framework to explain these observations. The most famous of these anomalies is the shift of Mercury’s perihelion by 43 arc-second per century. Numerous attempts at explaining this phenomenon within Newtonian gravity by invoking perturbations from other planets were ultimately unsuccessful.

In an effort to save the Newtonian theory, the existence of the hypothetical planet Vulcan, nearer to the Sun than Mercury, was proposed. It was speculated that the perturbative effect of Vulcan on Mercury would account for the shift. However, repeated searches for such a perturber by several astronomers at the end of the XIX century were in vain. Astronomers then went to the extent of proposing modifications to the theory of gravity. Inspired by Maxwell’s theory of electromagnetism and the work of François-Félix Tisserand on the radiation reaction of a particle moving in an electromagnetic field, Henri Poincaré proposed, in 1908, a revolutionary idea to explain the shift in Mercury’s perihelion: in the same manner that an accelerating charge emits radiation and modifies its own motion, a massive object near the Sun should likewise lose energy and emit an unknown type of radiation. Poincaré referred to this unknown radiation as “waves of acceleration”, or what one would now call “gravitational waves (GWs)”, a term he used as early as 1905 [79].

Using the relativistic theories of Lorentz and Max Abraham — early attempts at

unifying gravitational and electrostatic forces, Poincaré tried to extend the Special Theory of Relativity to the gravitational case and estimated the shift in the perihelion of Mercury to be of $\sim 7''$ and $\sim 5.6''$ per century, respectively. Having obtained these results, Poincaré argued that his new Dynamics had succeeded in predicting the motion of Mercury's perihelion, in good accord with the observations, but that his predictions were considerable smaller than the observed effect at the time, $38''$. Yet, Poincaré insisted that these results could not be used either in favour or against his new Dynamics.

Max Abraham was a Jewish theoretical physicist, a contemporary of Einstein's, who believed that all physical phenomena could be explained in terms of interactions between the electromagnetic field and the ether. Influenced by Einstein's early work on the general theory of gravity, he developed his own theory in 1912. Using his theory, he showed that GWs would not play an important role in a relativistic theory of gravity. Two years later he showed that dipole GWs did not exist. Abraham then became the first skeptic of the existence of GWs. Not only that, he also developed a rivalry with Einstein that would last until his untimely death at the age of 37. His work was severely criticized by Einstein, and eventually forgotten.

In the meantime Einstein continued his work on the extension of his special theory of relativity [49] to the gravitational case. In 1915 Einstein published his field equations, which provided a unified description of gravitational interactions in the framework of spacetime [50]. Einstein's classical field theory asserts that matter does not move through a passive spacetime continuum, instead it distorts spacetime causing the deflection of material particles and of light from their classical paths, i.e., space tells matter how to move. Additionally, *matter reacts back on space, telling it how to curve* [99]. This geometrodynamical interpretation is at the heart of Einstein's field equations.

Einstein quickly realized that finding analytic solutions to his equations would be a very difficult endeavor, so he developed approximation schemes to perform useful calculations. One such calculation, which had motivated Einstein to develop his general theory of gravitation in the first place, was to predict the perihelion advance of the planet Mercury. Previous attempts had failed not only to provide the right explanation for this celestial anomaly, but had also failed to predict the observed value of the shift. Einstein was ready to put his theory to the test, but with a minor inconvenience: he had to find an exact solution for the gravitational field of the Sun. As he did not know such a solution, he re-expressed all of his quantities as series expansions in terms of the speed of Mercury divided by the speed of light v/c , and some other factors that included the strength of the gravitational field of the Sun. This scheme was the foundation for the

post-Newtonian (PN) formalism that he, Infeld and Hoffmann developed to obtain the first PN order solution for the motion [53]. In his calculations he did not include terms of higher order than $(v/c)^2$. Although he had no way to know that neglecting these terms would not have a significant impact on the calculation, what he did know was that the term v/c was already small, and hence the impact of higher order terms should be further suppressed by small multiplicative factors in the expansion. This approach allowed him to obtain results that were in excellent agreement with the observations. Not only that, he also showed that the advance in the perihelion was a conservative effect, and not a radiative one, as François-Félix Tisserand and Poincaré had assumed.

As time went by, exact solutions for the gravitational field of a single body were obtained, e.g., Karl Schwarzschild’s solution [31] —which was not initially taken as the solution of a black hole, but of a star or another material body; Einstein made use of such new solutions. For instance, for his course on GR given in Zurich in 1919, he used a perturbative method to study the orbital motion of Mercury based on the Schwarzschild solution [94]. He modelled the gravitational field of the system as due to the mass of the Sun plus a small perturbation due to the mass of Mercury.

From November 1915 to February 1916, Einstein tried to find out whether his field theory predicted the existence of GWs. Correspondence with Schwarzschild in early 1916 shows that Einstein knew that his theory ruled out the existence of dipole GWs as a result of the “one-sidedness” of the trace of the energy-momentum tensor —no negative masses in the Universe. In his letter to Schwarzschild he also commented on his discovery that GWs did not exist.

Einstein would quickly changed his opinion on this matter, however. In 1916, he published a paper entitled *Approximate Integration of the Field Equations of Gravitation* [51], in which he developed the linearized approximation scheme for the first time, and showed that GWs naturally arise within his theory. Fruitful correspondence with de Sitter helped Einstein solve his linearized tensorial equations using an approach similar to that of retarded potentials in electrodynamics. The GW equation derived by Einstein resembled the electromagnetic case, and naturally led him to the conclusion that GWs travel at the speed of light, and consist of oscillations in the gravitational field.

In that paper Einstein also computed the amount of energy carried away by GWs from a material source. To do this calculation he defined a pseudo-tensor —a quantity that looks like a tensor but is not invariant to all coordinate transformations— to describe the amount of energy in a gravitational field. Einstein did not build this object consistently and, as a result, he derived a radiation formula that allowed the

radiation of GWs from monopole sources. This result was in clear contradiction with his early discoveries shared with Karl Schwarzschild in 1916. Unfortunately, he simply ignored these previous considerations.

A year later the Finnish physicist Gunnar Nördstrom —the first physicist who developed, in collaboration with Einstein, a self-consistent relativistic theory of gravity in 1914, but whose final mathematical form is due to Einstein— found an inconsistency with Einstein’s 1916 paper. He was trying to compute the mass of a body in Einstein’s theory. Using a particular coordinate system, the so-called unimodular coordinates, in which the square root of the determinant of the metric tensor is set to one, $\sqrt{-g} = 1$, he found that the energy stored in the field around the source was zero. However, Einstein’s pseudo-tensor rendered a non-zero result. He then realized that Einstein had used a coordinate system in which the metric tensor satisfied the condition $\frac{\partial g_{\mu\nu}}{\partial x_\nu} = 0$. Using this coordinate system, he now found a non-zero result, but which still disagreed by a factor of two. Einstein took to heart Nördstrom’s observations, and submitted a paper in January 1918 in which he corrected his radiation formula and replaced it by the famous quadrupole formula. This equation then showed that the emission of GWs would be generated, at the lowest multipole order, by changes in the quadrupole moment of the source.

At that time, Arthur Eddington published two papers on GWs which addressed two important issues: (i) in the first paper [47], he made a thorough analysis on the emission and propagation of GWs, and examined how spacetime curvature itself propagates through spacetime. He also derived the quadrupole formula correctly for the first time, as Einstein’s original equation had an extra factor of two [52]; and (ii) he studied the interaction of the wave and its own source, and concluded that GWs are so weak that the chances of detecting them would be very slim [48].

Eddington’s approach to study the propagation of GWs was entirely different to Einstein’s. He even considered that Einstein’s choice of harmonic coordinates, which helped him recast his linearized equations as electrodynamics field equations, had played a significant role in his concluding that GWs propagate at the speed of light. Being a skeptic, Eddington took a geometric approach, and focused on the spacetime curvature of the waves. He then found three types of waves, just as Einstein [52] and Weyl did [134], namely, longitudinal-longitudinal (LL), longitudinal-transverse (LT) and transverse-transverse (TT). However, his analysis showed that only the TT waves satisfied the condition that the speed of propagation was independent from the coordinate condition, and indeed coincided with the speed of light. He then went on to show that the two other type of waves were spurious as the Riemann tensor vanishes

entirely for those waves. Eddington’s analysis then confirmed Einstein’s result on his 1918 paper with regard to the fact that LL and LT “waves” do not represent a solution to the linearized equations, as these waves are simply flat space. Still today, GWs are referred to as TT waves, as they are usually represented using the transverse–traceless gauge.

In 1936 Einstein and Nathan Rosen submitted a paper to *Physical Review* entitled “Do Gravitational Waves exist?”. Their answer to this question was a conclusive no. They arrived at this conclusion indirectly, though. They were originally trying to find an exact solution for plane GWs. To that effect they built a metric tensor, the Einstein–Rosen metric, which had to include singularities to model GW sources. Using this metric, they realized that no regular periodic wavelike solutions were allowed using the linearized equations.

When the editor of the journal, John T. Tate, received the paper, he sent it to an expert on the topic, Howard Percy Robertson. He found a mistake in their analysis, and showed that, by making a coordinate transformation, it was possible to move the coordinate singularity of the Einstein–Rosen metric to the central axis of the spacetime, and then identify it with the source of GWs. In such a scenario, it was then clear that Einstein and Rosen were effectively dealing with cylindrical GWs.

When Einstein received the anonymous referee’s report, he was infuriated to know that their paper had been seen by specialists before it was printed. He may have reacted in this way because such practice was not common among German journals. In any case, he withdrew the paper and never submitted another one for publication to the *Physical Review*. The paper was eventually submitted and published in the *Journal of the Franklin Institute* in early 1937, but with a different title, “On Gravitational Waves”, and with completely different conclusions.

Robertson had failed to convince Einstein and Rosen that their conclusions were wrong by paper, but when he returned to Princeton in August 1936, he used a less confrontational approach. Because Rosen was in Russia at the time, Robertson went over the various calculations with another one of Einstein’s assistants, Infeld, and showed him that there was an error in the proof. Infeld communicated this to Einstein, who already had detected another mistake in his calculations. As a result, Einstein sent a letter to the editor of the *Journal of the Franklin Institute* in November 1936, in which he made all the necessary changes to the paper [54]. Interestingly enough, the Austrian physicist Guido Beck had already discovered a solution for cylindrical GWs in 1925, but this was not known until one of his students, Peter Havas, entered the field in the 1950’s.

When Rosen was informed by Einstein about what had happened following the submission of their article to *Physical Review*, he was disappointed to hear that, in correcting the errors in the paper, the conclusion had changed from “do plane GWs exist?” to: “cylindrical waves exist”. In response, Rosen published a paper in 1937 in which his conclusion was that plane GW do not exist as a result of singularities in the metric. His argument was eventually disproved by Hermann Bondi, Felix Pirani and Ivor Robinson, who showed that Rosen’s singularities were not physical singularities, and thus GWs do exist in the framework of general relativity [20].

Research in general relativity as a whole was also making steady progress. In 1939, Robert Oppenheimer and Hartland Snyder published a paper in *Physical Review* entitled “On Continued Gravitational Contraction” [103], in which they showed that a massive star that exhausts its thermonuclear fuel would collapse until its radius approaches the so-called Schwarzschild radius — twice the mass of star times the gravitational constant G , divided by the square of the speed of light. It turned out that this radius coincided with the region of the Schwarzschild solution where components of the metric tensor became infinite. These studies were not taken seriously for a simple reason. When Schwarzschild first presented his exact solution, he solved Einstein’s field equations for two different problems, namely, the gravitational field for a mass point, and for a spherical body of finite extension. In the first solution, he found a “pathological solution”, re-discovered by Oppenheimer and Snyder in 1939. However, people at the time, including Einstein himself, thought that astrophysical objects would not be so small in radius that the gravitational radius would lie outside them. So, they considered that the second solution, in which the gravitational radius lies inside the star and has no pathological behaviour at all, represented stationary, spherical astrophysical bodies. In consequence, these studies did not attract much attention for about two decades.

From 1925 through to 1955, research in general relativity was overshadowed by extensive research carried out in a more experimentally driven field, that of quantum mechanics. The fact that general relativity was not an experimentally oriented field is evident from the fact that the vast majority of active researchers in the field during this period were mathematicians. The two basic problems that relativists tried to address were back-reaction and detectability of GWs. These two problems fueled decades of controversy, particularly on the existence of GWs and radiation damping in binary systems. On this latter topic, Lev Landau and Evgeny Lifshitz made the most remarkable contributions in this period by showing, in 1941, that a binary star system radiates energy in accord with Einstein’s quadrupole formula.

In 1955, Rosen again argued that GWs do not carry energy. His argument was quickly overturned in 1957 when Bondi and others proposed thought experiments to show exactly the opposite. A few years later, 1962, Bondi and his group showed that binary systems that emit GWs lose mass during the process [21]. Several groups would challenge this picture, and a few basic concepts that had already been settled in the past, e.g., the very existence of GWs. This chaotic scenario was bluntly captured in a letter that Feynman wrote to his wife while he was at the second GR conference at Warsaw in 1962. In the letter, he states that researches in the field were occupied either trying to show that previous results were wrong, or doing nothing useful, or engaged in something “promising”. He even went to the extent of describing the situation as “a lot of worms trying to get out a bottle by crawling all over each other”. At the end of the meeting, he gathered that the subject was progressing very slowly, not because it was difficult *per se*, but because good people were occupied elsewhere (*sic*) [79].

This situation soon changed for the better. General relativity entered into its golden age in the 1960s as a result of two major events, namely, the discovery of Roy Kerr of an exact solution for the gravitational field of a spinning mass [82], and the discovery of quasars [93]. Astronomers thought that a possible explanation for the enormous energy output of these objects would involve strong gravitational fields from superdense objects [89], similar to the astrophysically collapsed stars of Oppenheimer and Snyder. Inspired by the quasar problem, astrophysicists spent the next ten years studying properties of the Kerr and Schwarzschild solutions. It soon became apparent that the gravitational radius of the Kerr and Schwarzschild solutions were simply coordinate singularities that defined a boundary for communication. An observer inside this boundary, or “event horizon”, could not communicate with an observer outside by any means, including light signals. This feature motivated John A. Wheeler to call these objects black holes (BHs) at a conference in New York in 1967. Penrose then introduced the cosmic censorship hypothesis, which conjectures that all singularities are enclosed within a horizon [107]. Another leading figure in the field, Brandon Carter, showed that, under certain assumptions, the Kerr metric is the unique BH solution with axisymmetry of the general relativity equations [30]. If cosmic censorship is valid, then this implies that the Kerr metric is the unique end state of gravitational collapse to a BH.

Intense work during the 1960s from the Bondi–Pirani group in London, and the Wheeler group in Princeton, reshaped the mathematical theory of GWs into a physical theory that had addressed many of the theoretical issues that had caused so much controversy in the previous decades. Their efforts were accompanied by independent studies, like those of Chandrasekhar and Esposito in 1970, who showed that it was

possible to recover the quadrupole formula for a binary system modelled not as a two point particle system, but as physically realistic extended bodies [32]. GWs were no longer a mere analogy to electromagnetic phenomena, they had attained the status of a solid theory with strong physical foundations.

Parallel to this theoretical development, Joseph Weber started his own experimental program in the 1960s. By 1962, Weber had already built a detector and presented some results at the Warsaw conference. His detector, a resonant bar, had been carefully designed to detect sources in the frequency band near 1661 Hz. This bandwidth had been selected after much work done in collaboration with John Wheeler at Princeton. Freeman Dyson initially suggested Weber to search for asymmetric supernova collapse as promising sources of GWs, expecting that the gravitational radiation from these events would sweep through the bandwidth of the bar. In 1963, Dyson advised Weber to search for another source of GWs, namely, binary systems formed by a pair of neutron stars (NSs) —objects whose very existence was uncertain at the time. The discovery of pulsars by Jocelyn Bell and Anthony Hewish [68], would promote these systems from speculative sources to promising candidates for these sources.

In the spirit of Dyson’s guess that NS binaries would be promising sources of GWs, Phillip C. Peters and Jon Mathews [108] published a paper in which they used the quadrupole formula to calculate the pattern of radiation from particles in Keplerian orbits, and the dynamical evolution of the binary system under radiation–reaction. Their studies were along the philosophy proposed by Feynman, in the sense of being driven by intuition, to calculate various things to check whether the theory was self–consistent. This was certainly the way forward, even though people had not reached agreement on the validity of the quadrupole formula, or whether the energy radiated had any physical meaning.

In 1968, Joseph Weber reported the simultaneous detection of pulses in two bars spaced 1000 km apart, one in Maryland, and the other at the Argonne National Accelerator Laboratory near Chicago, that were above expected Gaussian noise. Amazed by the “discovery”, various groups built their own detectors with sensitivities similar or better than Weber’s, but no detection was reported between 1970 and 1975. This problem, along with the fact that Weber’s data implied an event rate 1000 times higher than what had originally been estimated, led other GW experimentalists to eventually reject his results.

Nonetheless, Weber’s problem with theoretical predictions made it clear that experimentalists would need theoretical guidance in future endeavors to detect GWs for at least two reasons: i) the design of a GW detector should be driven by theoretical calcula-

tions that spell out the science that can be accomplished, and ii) once the detector was on-line, the development of accurate waveform templates would play a decisive role in detecting signals from the detector output by means of intelligent signal-filtering methods. This realization brought forth another boost in theoretical activity in the 1970s.

Another great milestone for GWs was the detection of the pulsar PSR B1913+16 by Hulse and Taylor in July 1974 [76]. The observation of this pulsar provided evidence, though indirect, for the existence of GWs. This discovery was the result of a systematic survey for new pulsars using the 305 m radio-telescope at the Arecibo Observatory in Puerto Rico. The signal of the system consisted of radio-frequency pulses with a spacing between pulses of 59 ms. However, it showed changes in the period by up to $\sim 80 \mu\text{s}$ per orbital period. This feature was particularly remarkable, as the largest secular changes in period known at that time, for pulsars, were of order $10 \mu\text{s}$ per year. Hence, this was an indication that GR effects may play a significant role in the dynamics of the system. Unlike Newtonian theory, which states that the orbital decay for an isolated binary system of compact stars is expected to be immeasurably small, Hulse and Taylor got a small but extremely well measured figure. Their observations clearly indicated that the orbital period of the pulsar was steadily decreasing at a rate of $-2.40(9) \times 10^{-12} \text{s s}^{-1}$. Using GR, they estimated the decay rate for the orbit of PSR B1913+16 to be: $-2.403(2) \times 10^{-12} \text{s s}^{-1}$ [81]. In 1978, Taylor and collaborators made the announcement that the orbital decay of PSR B1913+16 was in excellent agreement with the quadrupole formula. This observational evidence constituted a solid confirmation for the validity of GR outside the solar system, and impelled the scientific community to intensify the quest for a direct detection of GWs.

But to accomplish this task, it was first necessary to lay down the foundations to compute GWs. Emboldened by Peters and Mathews's approach, Kip Thorne and his student Sandor Kovás started a research program that shed light on the range of applicability of the quadrupole formula [129], and developed new techniques to calculate the GW emission from fast-motion systems, i.e., the relativistic *bremssstrahlung* problem [84], and calculated the GWs generated by particular astrophysical systems [85]. This latter point was also addressed by Saul Teukolsky, who derived linear equations that describe the dynamical gravitational, electromagnetic, and neutrino-field perturbations of a rotating BH [126]. Teukolsky's formalism encapsulates all gravitational radiative degrees of freedom in a single master wave equation. In order to achieve some consolidation in the research program, Thorne published a review which presented the formalisms for gravitational radiation that had been developed by various groups us-

ing a unified notation [127]. A few years later, Sasaki and Nakamura [118] developed a novel approach to study gravitational perturbations of Kerr BHs. Unlike Teukolsky’s equations, their perturbation equations i) had a short-range potential; and ii) did not exhibit divergence associated with the source term. Teukolsky–Sasaki–Nakamura (TSN) is now a standard tool to compute GWs. One can use the TSN formalism to compute GWs as long as orbital evolution of the GW source is known.

By the time the TSN formalism was introduced, the motion of particles had been studied extensively. The early works of Lorentz, Abraham and Poincaré had shed light on the motion of an electric charge in flat spacetime. But it was Dirac [46] who made the first derivation of the relativistic equations of motion. The work of DeWitt and Brehme [45] generalized Dirac’s result to curved spacetimes, although it had a few inconsistencies that were later corrected by Hobbs [70]. The extension of this analysis to the motion of a point mass in a curved background spacetime was carried out by Mino, Sasaki, and Tanaka [98]. Their equations of motion were simultaneously derived by Quinn and Wald using an axiomatic approach [112]. These studies have shown that point scalar charges, point electric charges and point masses carry fields that behave as outgoing radiation in the wave zone. In the near-zone these fields generate a self-force that affects the motion of the particle and prevent it from following a geodesic of the background metric. This self-force has two components, i) a radiation–reaction part which is associated with dissipative transport of energy and angular momentum; and ii) a conservative piece which is not associated with energy or angular momentum transport, but that leads to a change in the phasing of the gravitational waveform. Deriving the self-force equations of motion was a remarkable achievement, but the actual computation of its conservative and radiative components is an outstanding challenge that has only been gradually overcome in the past few years. At present, the gravitational self-force has been computed for circular equatorial and generic orbits around Schwarzschild black holes [8; 10]. The scalar field self-force has also been computed for circular equatorial and eccentric equatorial orbits around Kerr black holes [131; 132]. Nonetheless, the computation of the gravitational self-force for test particles moving in a Kerr background still represents an exceptional theoretical and numerical challenge [109].

Parallel to the development of analytic and semi-analytic models for the emission of gravitational radiation from binary systems, the field of numerical relativity benefited from the rapid advance of electronic computation. In just 35 years, the pioneering work of Larry Smarr [121], who went on to found the National Center for Supercomputing Applications at Urbana–Champaign, USA, finally reached maturity when the first suc-

successful computational scheme for numerically solving the Einstein field equations for a BH binary was announced by Frans Pretorius [110]. Numerical relativity simulations of binary BH mergers close to and during the plunge phase of the merger have now demonstrated the domain of validity of PN and post-Minkowskian schemes developed by Blanchet and Damour [15; 16; 38; 101]. These simulations have also been useful to tune semi-analytic models, e.g., the effective one-body approach [25; 28; 105; 136] and “numerical kludge” schemes [5], to reproduce numerical calculations to high accuracy while being computationally inexpensive.

These waveform templates are essential for data analysis for the interferometric detectors that may provide the first direct detection of GWs within the coming decade. This has been achieved by the joint efforts of Ron Drever, Rochus Vogt, Rai Weiss, Kip Thorne and others to secure an unprecedented level of funding from the US National Science Foundation to launch the first large detector program—the laser interferometer GW observatory (LIGO). Similar efforts then followed with the construction of GEO 600 and Virgo in Europe, and TAMA in Japan.

The development of these ground-based detectors at the present scale has required large collaborations and more than thirty years of preparation. They are limited to frequencies above a few Hz because local disturbances in the Newtonian gravitational field are larger than the expected GWs at frequencies lower than this [90]. However, the three detector LIGO network—one at Livingstone, and two at Hanford—is currently being upgraded to push the seismic wall, which for Initial LIGO was at ~ 40 Hz, down to ~ 10 Hz. It is expected that within a few years of starting operation, ~ 2016 , the enhanced sensitivity of these detectors will make the detection of GWs a routine occurrence.

The existence of the seismic wall means that observation of GW signals in the frequency band 0.1 mHz–0.1 Hz requires a detector in space. The Laser Interferometer Space Antenna (LISA) was proposed to detect GW sources in this frequency band. LISA was a joint space mission between the European Space Agency (ESA) and NASA, which was recently included in the “Astro 2010” decadal survey as “a top priority to be implemented by NASA within the following decade”. Unfortunately, at the time of writing this thesis, NASA has temporarily suspended funding for research on LISA as a result of the recent economic downturn, and because the James Webb Space Telescope is substantially over budget. The future is not entirely gloomy, however. ESA will continue to push the project forward on its own, and, it is hoped that, as a result of the compelling science case for such a mission, LISA will recover from this setback.

If a low-frequency detector is eventually realised, the list of potential sources will

include the merger of BHs in the mass range $10^4 - 10^7 M_\odot$, and compact binary systems in our galaxy with periods of approximately a few hours, comprising relativistic objects like white dwarfs, NSs and BHs. It should also include extreme-mass-ratio inspirals (EMRIs), i.e., the inspiral of stellar mass compact objects (COs) into super-massive black holes (SMBHs), which should occur in the centres of galaxies where massive BHs are surrounded by stellar clusters that contain large numbers of NSs and stellar-mass BHs. In the following Section, I discuss the physical motivation to study these systems, and the tools that I will use in Chapter 2 to build an accurate waveform template to model the gravitational radiation emitted by these systems.

1.2 Extreme-mass-ratio inspirals

The realisation of a space-based low-frequency GW interferometer will constitute a very important step in the development of GW astronomy. Among the various GW sources that a low-frequency GW observatory may detect are extreme-mass-ratio inspirals (EMRIs). These are the inspirals of stellar mass COs into SMBHs. These events are expected to occur in systems in which massive BHs are surrounded by stellar clusters which contain large numbers of compact stellar remnants. In such systems, the heavier BHs sink toward the centre of the cluster as a result of mass segregation during random encounters among stars. Repeated encounters will gradually perturb the orbits of the inspiralling COs until one of them passes close to the central SMBH. If the impact parameter is sufficiently small, then enough orbital energy will be radiated in GWs on the first orbit that the remnant will end up on a bound orbit around the central SMBH. Thereafter, if the captured star is either a white dwarf, NS, BH, or a very low-mass main-sequence (MS) star, and the mass ratio of the system is of the order $\eta \sim 10^{-5}$, the inspiralling object's orbit will gradually decay via GW emission (MS stars are either not compact enough to withstand the tidal forces in the vicinity of the SMBH or not massive enough to produce waves of large enough amplitude). Eventually, the CO will end up on an orbit close to the SMBH, on which it will be radiating GWs continuously in the LISA band, and will generate several hundred thousand waveform cycles in the LISA band before crossing the horizon.

The GWs emitted by these sources will be rich with information. They will provide a very accurate map of the spacetime exterior to the large body, and the response of the SMBH's horizon to tidal forces [86; 115]. Furthermore, tests of the no-hair theorem will be possible as LISA will be able to measure the SMBH mass, spin and quadrupole moment to fractional accuracies of $\sim 10^{-3}$ [115]. Testing this theorem

with real data will provide the first tests of the predictions of general relativity for BH solutions. LISA observations could also lead to the discovery of non-BH systems, e.g., boson stars or naked singularities. The unprecedented accuracy with which EMRI observations will determine the masses and spins of systems will provide information about the astrophysical properties of BHs in the nearby universe, and will significantly improve our understanding of the stellar populations in the central parsecs of galactic nuclei by providing an accurate census of the distribution of types and masses of COs [61].

Nonetheless, detection of EMRIs will be difficult, since it is expected that their instantaneous signal amplitude will be about an order of magnitude below LISA’s projected instrumental noise (see Figure 1.1). Hence, in order to dig out the signals from the noisy LISA data, it will be essential to use intelligent matched filtering techniques. This will rely on the development of theoretical templates whose phase remains accurate to one cycle over the $\sim 10^5$ cycles of the waveform that LISA will detect, which are generated while the orbit of the stellar mass CO is in the strong curvature region, close to the large BH. In Chapter 2, I will outline an approach to develop accurate theoretical models to study the GW emission from EMRIs.

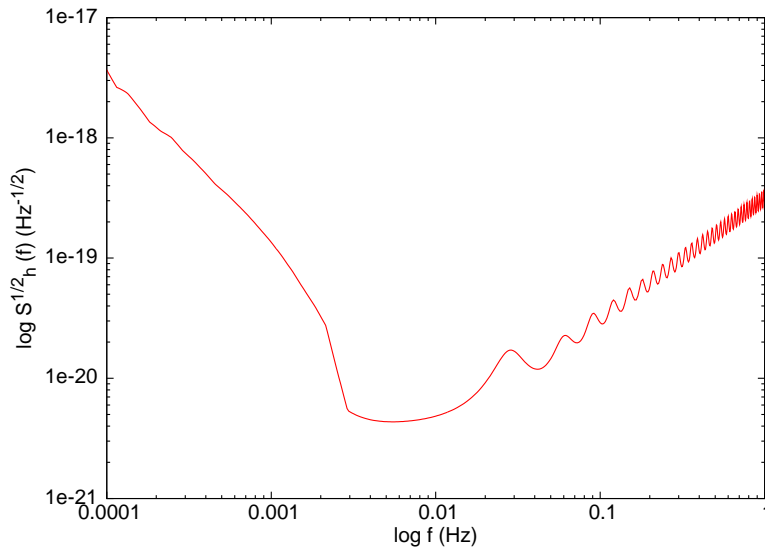


Figure 1.1: Total LISA noise curve, which includes instrumental noise, confusion noise from short-period galactic binaries, and confusion noise from extragalactic WD binaries [6].

For comparable mass binary systems, the early inspiral can be modeled using PN theory, and numerical relativity can be used to model the final orbits and merger. EMRI waveforms may not be computed in the same way, as the CO spends far too

many orbits in the strong curvature region close to the central SMBH. EMRIs will be visible to LISA for central BHs with masses in the range $10^4 - 10^7 M_\odot$, and out to redshifts $z \approx 1$ [3; 60], so the mass ratio for these EMRIs will be of order $\eta \sim 10^{-5}$. Hence, it is reasonable to treat the mass of the inspiralling CO as a small perturbation of the gravitational field of the central SMBH, and use black hole perturbation theory (BHPT) as the framework to study these systems.

Furthermore, because the mass ratio is very small, the orbital parameters evolve on a much longer time scale than the orbital periods, i.e., one can assume that the inspiralling CO instantaneously follows a Kerr space-time geodesic, and neglect back-reaction effects on an orbital timescale, i.e., one can assume adiabatic evolution.

A Kerr geodesic is characterized by three constants of motion, namely the energy, E , the angular momentum about the hole's spin axis, L_z , and the Carter constant, Q , which is a relativistic generalization of the third integral of motion and which is used to separate the equations of motion. In the spherical limit, i.e., for a non-rotating central BH, Q reduces to the square of the angular momentum projected into the equatorial plane. Over longer timescales, $\sim M/\eta$, radiation-reaction causes the orbit to evolve adiabatically. This can be characterized by changes in the geodesic orbital elements E, L_z and Q . As the CO nears an innermost stable orbit, this prescription breaks down and the inspiral ceases to be adiabatic. It then follows a geodesic plunge orbit and is swallowed by the central BH.

First order radiative BHPT in a Kerr background is described by the Teukolsky formalism. By construction this scheme includes the first order radiative piece of the self-force, which is associated with dissipative transport of energy and angular momentum. Unfortunately, Teukolsky-based waveforms are very computationally expensive to generate, and do not include conservative self-force corrections, which also lead to a change in the phasing of the gravitational waveform. However, there are various families of approximate waveforms that capture the main features of true signals and are much quicker to generate, e.g., the PN waveforms, which are both analytic and easy to generate. The PN waveform family developed by Barack and Cutler [6] for the EMRI case, is constructed considering the lowest-order quadrupole waveforms for eccentric binaries on Keplerian orbits, using the results of Peters and Matthews [108]. These orbits are corrected to include the effects of pericenter precession, Lense-Thirring precession, and inspiral due to radiation reaction. This waveform family has been extensively used for scoping out data analysis issues, e.g., computing the Fisher information matrix to estimate parameter measurement accuracies. However, a small BH in a close orbit about a much larger one is too relativistic a system for PN analyses to be valid. The

PN expansion is unlikely to be reliable in the EMRI limit, because the object spends so much time in the strong field region of the space-time where $v \sim c$, and it is in this zone where most of the GWs observable to LISA are generated. Thus, in order to have a more accurate modelling of GW emission before plunge, one needs to use a computationally inexpensive scheme that reproduces Teukolsky-based evolutions in the strong-field regime. Such a scheme has been developed and is referred to as a “numerical kludge” (NK) waveform [5; 63].

NK waveforms are constructed using an exact particle trajectory with a flat space-time wave-emission formula. This framework captures the main features of Teukolsky-based waveforms for geodesic orbits very accurately—the overlap between the two types of waveforms is greater than 0.95 over a considerable portion of the parameter space [5]. However, these models are incomplete in their treatment of the orbital evolution under the self-force, as they do not currently include conservative radiation-reaction terms, and the waveform-emission formula and phase space trajectories are only approximate.

The purpose of Chapter 2 is to improve the NK waveform family by means of including conservative self-force corrections, and shed some light on the importance of these corrections for waveform modelling, both in terms of source detection and parameter estimation. To this end, in Section 2.2 I will build asymptotic observables for the kludge waveform model, namely the orbital frequency and its first time derivative. I will present a scheme to effectively include both components of the self-force: radiative and conservative, to second and first order, respectively, by comparison to PN waveforms. I will also discuss the relative importance of the various conservative corrections to the phase evolution of the waveform signal. In section 2.3 I will use the kludge waveform model to assess the importance of the second order radiative piece that will be missing once first order accurate self-force waveforms are generated. I do this by comparing to self-force data obtained by Barack and Sago [8] for circular equatorial orbits around a Schwarzschild black hole. In Section 2.4 I will make use of the inspiral kludge waveforms including modulations from LISA’s response function to estimate the noise-induced parameter errors using the Fisher Matrix formalism. These provide confirmation and extension of the results previously obtained using the analytic kludge model of Barack and Cutler [6]. In Section 2.6 I will employ the recently developed formalism of Cutler and Vallisneri [35] to estimate the theoretical systematic parameter errors that would be introduced by waveform template inaccuracies. Specifically, I study the importance of the conservative corrections by computing the errors in the parameters that would arise from omitting conservative corrections from the model. Chapter 2 will conclude with a brief summary of the findings obtained from these studies.

In Chapter 3 I further extend the kludge model introduced in Chapter 2 to study the importance of including small body spin effects in the modelling of EMRIs and intermediate-mass-ratio inspirals (IMRIs), i.e., the inspirals of intermediate-mass black holes (IMBHs) into SMBHs. The following Section presents the physical motivation for this work, and describes the approach I will follow in Chapter 3 to address a few important issues associated with this problem.

1.3 Intermediate-mass-ratio inspirals in the context of space-based detectors

In Chapter 3 I will further extend the “numerical kludge” approach introduced in Chapter 2, to include an additional ingredient, namely, the spin of the inspiralling body for objects on Kerr circular-equatorial inspirals. The aim of this study will be to shed light on the importance of including this parameter in EMRI and IMRI models both for signal detection and parameter estimation.

This analysis is important because it is expected that most astrophysical black holes will have significant spin and therefore the true gravitational waveforms will exhibit small body spin effects. It has been argued that such effects will not play a significant role for signal detection and parameter estimation for EMRIs with mass ratios $\eta \sim 10^{-5}$ [6]. This is because the spin of the inspiralling object is suppressed by a factor of η in the equations of motion [117], and hence the inclusion of small body spin effects will modify the orbital evolution by at most a few radians over a year. Studies on the effect of the self-force on spinning objects that inspiral into Schwarzschild black holes have shown that the accurate determination of the local self-force may not be needed for a determination of the orbital evolution of EMRIs, and its omission will only introduce a small error in the determination of the spin rate of the companion [29]. However, the spin effects become more important as the mass ratio, η , is increased and may therefore be significant for IMRIs with $\eta \sim 10^{-3}$ (e.g., the inspiral of a $\sim 10^3 M_\odot$ IMBH into a $\sim 10^6 M_\odot$ SMBH).

Even if small body spin effects are only marginally important for detection, their inclusion in waveform templates may be important for parameter estimation. In that case, one needs to determine the mass ratio at which small body spin effects become important, i.e., when GW observations will be able to measure the spin of the inspiralling body. I address this question in Chapter 3, for the first time, by developing a “numerical kludge” waveform model that includes small body spin effects using the mathematical machinery developed by Saijo et al. [117], and by including conservative

self-force corrections for spin-orbit and spin-spin couplings using the same method that is employed to include the perturbative conservative corrections in Chapter 2. I present the mass-ratio threshold η above which low-frequency GW detectors like LISA will be able to accurately measure the spin of a BH inspiralling into a SMBH. I will show that future observations will not only provide an unprecedented census of the spin distribution of SMBHs, but could also yield an accurate census of the spin and mass distributions of IMBHs with mass $\mu \gtrsim 10^3 M_\odot$.

Chapter 3 is organized as follows. In Section 3.2 I will introduce the waveform model used to study the inspiral of spinning black holes into SMBHs. I construct kludge asymptotic observables to implement the radiative and conservative components of the self-force, including spin-orbit and spin-spin couplings, by comparison to PN results. In Section 3.3 I explore the accuracy with which LISA observations may be able to determine the parameters of a representative sample of binary systems. In Section 3.4 I again make use of the formalism developed by Cutler & Vallisneri [35] to estimate the theoretical or “model” errors that will arise from omitting these new conservative corrections in the waveform templates. Chapter 3 concludes with a summary of this work.

1.4 LISA descope studies

As mentioned earlier, the recent funding upheaval at NASA has forced ESA to explore ESA-only concepts for the LISA mission. In Chapter 4, I discuss a few of the alternatives that ESA is presently exploring for such a low-frequency GW detector. I present results on the accuracy with which these descoped detectors will be able to measure the parameters of EMRIs. The results presented therein suggest that EMRI science will not be seriously degraded for any of the descope concepts currently considered by ESA, except through a reduction in the number of events. Hence, these sources should still be included as an important part of the science goals of the new space-based mission that comes out of these descope studies.

This Chapter is the last one on the work that I have done related to the modelling of sources that may be detected via space-based detectors. In Chapters 5 and 6, I concentrate on sources that might be detected using ground-based detector networks. In these two Chapters I present two alternative waveform templates to model intermediate-mass-ratio inspirals (IMRIs), a GW source that may play an important role in the dynamics of globular clusters, and the formation of SMBHs. Waveform templates have not yet been developed for these sources, so it is timely and important

to do work in this particular area. In the following I will describe the appropriate framework for this analysis.

1.5 IMRIs in the context of ground-based interferometers

As mentioned above, the LIGO interferometer is currently undergoing an upgrade to provide a factor of ten improvement in sensitivity. This advanced LIGO detector, and the corresponding improved Virgo detector, should achieve sensitivity that stretches, at the low frequency end, down to the seismic limit at ~ 10 Hz. This seismic wall is caused by tectonic plate movements, cars, and ocean tides, amongst other sources. Thus, the detection of GW sources with masses in the range $100M_{\odot} \lesssim M \lesssim 10^3M_{\odot}$ will be beyond the reach of these advanced detectors. In order to detect such sources, it is necessary to build GW interferometers able to detect GWs with frequencies of ~ 1 Hz.

The Einstein Telescope (ET) is a proposed third generation ground-based GW detector for which the target is a sensitivity ten times better than that of the advanced detectors [58; 69]. It is hoped that by siting the instrument underground, the seismic and gravity gradient noises will be significantly reduced. In addition, it is hoped that the range of frequencies to which the detector is sensitive can be extended into the 1 – 10 Hz range, while also maintaining high frequency sensitivity up to 10 kHz. A design study for ET, which has just concluded, explored the design, cost, site selection, and the potential scientific impact of such an instrument, with a view to maximising the scientific output within a reasonable budget.

If the ET is realised, it will open up the possibility to study a wide variety of sources and address outstanding problems in fundamental physics, cosmology and astrophysics, e.g., to determine the mass and spin distributions of COs; study general relativistic instabilities in compact objects; solve the enigma of gamma-ray-bursts and shed light on the different classes; understand the mass-spectrum of compact stars and their populations; and measure cosmological parameters using GW sources as standard sirens [111].

The ET will be able to do the same type of science as the advanced detectors, but with much greater precision. The expected isotropic detection horizon (the angle-averaged distance to which a binary can be observed) for Advanced Virgo will be at ~ 150 Mpc ($z = 0.035$) for NS–NS binaries and ~ 310 Mpc ($z = 0.07$) for NS–BH binaries [113]. For Advanced LIGO, NS–NS signals will be in band for ~ 17 minutes and have a single detector detection horizon of ~ 200 Mpc ($z = 0.045$); NS–BH signals

will be in band for ~ 4 minutes, and have a detection horizon of ~ 420 Mpc ($z = 0.09$). In contrast, if ET’s seismic wall is pushed down to 5 Hz, NS–NS signals will be in band for ~ 2 hours, and NS–BH signals for ~ 25 minutes. If the seismic wall is further reduced down to 3 Hz/1 Hz, then NS–NS signals will be in band for ~ 7 hours/5 days, and NS–BH signals will be in band for ~ 2 hours/1 day, respectively. The ET detection horizon is expected to be at $z \simeq 1$ for NS–NS signals, and at $z \simeq 2$ for NS–BH signals [113].

In addition, there is also some science that only ET will be able to do. The 1–10 Hz frequency band lies below the range of future advanced ground–based interferometers, e.g., Advanced LIGO, and above the range of currently proposed space–based detectors, e.g., LISA [33]. On the other hand, the Japanese DECI-hertz Interferometer GW observatory (DECIGO) aims at detecting GW sources between 1mHz and 100Hz [65; 78]. Hence, the mergers seen by ET will be complementary to mergers between heavier black holes that will be seen by DECIGO ¹. If ET achieves good sensitivity in the 1–10 Hz band, it will be able to detect GWs generated by sources with mass from hundreds to a few thousand solar masses. Therefore, plausible sources will include IMBHs, which could be primordial, i.e., formed in the early Universe as seeds from which BHs in galaxies subsequently grow, or, alternatively, generated in the centre of dense globular clusters through runaway stellar collisions [64].

Interest in IMBHs has grown due to the observational evidence for their existence which has accumulated over the last decade. This evidence is of two different types. First, ultraluminous X–ray sources (ULXs) have been observed that are not associated with active galactic nuclei and yet have fluxes many times the angle–averaged flux of a $M < 20M_{\odot}$ BH accreting at the Eddington limit. Second, in several clusters, e.g., the globular clusters M15 and G1, the stellar kinematics shows evidence for an excess of dark mass in the centre. In M15, there is also evidence for rotation in the core at a speed that is comparable to the central stellar velocity dispersion. One possible explanation for this rotation would be the transferal of angular momentum from a BH binary to stars in the core through three body encounters. A binary comprising a $\sim 20M_{\odot}$ BH orbiting a 10^3M_{\odot} object at a semi-major axis of 10^{-3} pc would have enough angular momentum to account for the observed rotation [96].

¹The preconceptual design for this space-based antenna consists of three drag-free satellites, separated from each other by 1000 km. This configuration will provide accurate measurements of the parameters of BH mergers with $M \gtrsim 10^5M_{\odot}$. On the other hand, the full DECIGO mission, which aims to have four interferometers, two of them colocated in a “star-of-David” configuration to allow stochastic background measurements, will be able to determine the parameters of seed BH mergers with $M \lesssim 10^3M_{\odot}$ to great accuracy.

This evidence should further improve with future X-ray and optical observations, but a robust mass determination of an IMBH candidate will be needed for a solid identification. This may be possible using radial velocity measurements of companions to ULXs in binaries, but this technique can only yield a lower bound on the mass due to the unknown inclination of the system, and the companions are typically very faint.

In addition to the observational evidence, numerical simulations of globular clusters suggest that a fraction $\sim 10^{-6} - 10^{-4}$ of the $\sim 10^6$ initial stars that form a globular cluster will become stellar-mass BHs via normal stellar evolution [120]. Assuming a globular cluster with relaxation time of 1 Gyr [102], all these BHs should form within ~ 10 Myr, with the most massive BHs forming at around ~ 3 Myr [119]. These BHs should be more centrally concentrated than MS stars since there will be significant mass segregation of their higher mass progenitors [59], there will be preferential formation of stars near the cluster centre [100], and because BH birth kicks are not expected to displace BHs into the cluster halo [135]. Even if one assumes that the BHs are distributed throughout the cluster, mass segregation should be able to assemble a sub-cluster of BHs near the centre after at most ~ 100 Myr. During mass segregation, BH-MS binaries will undergo three body and four body interactions that will replace the MS stars by heavier BHs. Simulations [102; 125] suggest that, whether formed through successive BH mergers or stellar collisions, it is more likely to find an IMBH in a cluster with a dense core. This then means that IMBHs could exist in some tens of percent of current globular clusters. In these stellar environments, the first formation of an IMBH with mass $\sim 100M_{\odot}$ may take place ~ 10 Myr after the sub-cluster of BHs is formed. IMBHs formed through this channel have negligible cross section for direct collisions/plunges with other objects. However, they will readily swap into a binary, as the heaviest object in the cluster. These binaries can be hardened through three body interactions or the secular Kozai resonance. IMBH-CO binaries will eventually be driven to merger by GW emission, and the gravitational radiation generated during these final phases of evolution could be detected by ground-based laser interferometers. It has been estimated that in such environments the IMRI event rate for ET could be as high as a few hundred per year [64].

If IMBHs do exist, the numerical simulations suggest that they will merge with other IMBHs and smaller COs. These mergers will generate GWs whose frequency will be in the ET band, and which will provide very accurate mass measurements. Hence, it is very likely that the first convincing proof of the existence of IMBHs may come from these observations [96].

In order to explore the prospects for this science, it is necessary to develop accurate

waveform templates for IMRIs. This is a challenging endeavour because in this strong-field regime PN theory does not apply, and numerical relativity cannot be used due to the large number of orbits that must be modelled. Additionally, the mass ratio of these events is too large for BHPT. Thus, in order to make progress on this research program, I will introduce in Chapter 5 a waveform model to study the mergers of IMBHs with lower mass COs, which might be either NSs or stellar-mass BHs.

I will describe two alternative models for the gravitational waveform generated during an IMRI, and use them to estimate the SNR of events detected by ET. The low-frequency cut-off in the ET sensitivity will mean that only a short section of the inspiral phase will be observed for a typical ET IMRI event. A significant fraction of the total SNR will therefore come from the merger and ringdown, and so it is important to include them in the waveform model. For both models, I will make use of the “numerical kludge” [5] approach introduced in Chapter 2 to describe the inspiral phase. The two models will differ in the treatment of the merger. In the first model, which is valid for inspirals into IMBHs of arbitrary spin, I model the transition from adiabatic inspiral to plunge using the scheme developed by Ori and Thorne [104]. In the second model, which is used to cross-check the results in the non-spinning limit, I model the merger and plunge using the effective one-body (EOB) approach.

For the SNR calculations, I will assume that a network of ET-like detectors exists, rather than just a single detector. This will be necessary if one is to estimate the extrinsic parameters of IMRI events to any precision. The duration of an IMRI event will be between a few seconds (e.g., a $10M_{\odot} + 500M_{\odot}$ system) and a few minutes (e.g., a $1.4M_{\odot} + 100M_{\odot}$ system). Over such a short timescale, the event is effectively a burst in the detector and so a single ET cannot determine the sky position of the source. Hence, I will assume the existence of a detector network. Additionally, I will consider several different network configurations in order to assess how this affects the science, which will be useful input for future design decisions. This is an important problem because an accurate determination of the masses of a merging binary and a measurement of the luminosity distance at which the merger is taking place will be useful for extracting science from the observations.

I will present these results as follows. In Chapter 5, Section 5.2 will describe the assumptions adopted for the detector and detector network, and the binary systems that will be used in the analysis. In Sections 5.3- 5.5, I will present the IMRI waveform models, including the “numerical kludge” model that is used for the inspiral phase, the transition to plunge scheme developed by Ori and Thorne [104] for the merger, and the ringdown (RD) radiation. In Section 5.6 I also introduce the aspects of the EOB

model relevant for these studies. Section 5.7 will present an implementation of the ET response function, and a description of the properties of the resulting waveforms. I describe the orbital phase evolution up to the light ring (LR), i.e., the innermost unstable circular orbit for massless particles, and present gravitational waveforms including the final inspiral, merger and RD. This section also includes a comparison between the two models for inspirals into non-spinning IMBHs. In Section 5.8 I present ET signal-to-noise ratios for the sample binary systems. Using these results as input data, and assuming that the dominant mechanism that leads to the formation of IMRIs is three-body hardening of an IMBH-CO binary in a core-collapsed globular cluster, I will present estimates for the number of events per year that may be detected by the ET. This Chapter concludes with a brief summary of these findings. In Chapter 6, I make use of the IMRI waveform models developed in the preceding Chapter to obtain parameter estimation errors for a variety of binary systems, and also explore how the precision of parameter determination depends on the network configuration. This Chapter concludes with a discussion of the implications of these results.

A summary of the results presented in this thesis, and a brief outline of future work involving the extension of the models used in these studies, are the topic of the final concluding Chapter.

Chapter 2

Influence of conservative corrections on signal detection and parameter estimation for extreme-mass-ratio inspirals

2.1 Overview

In this Chapter, I will study the importance of including conservative self-force (SF) corrections in waveform templates for signal detection and parameter estimation for extreme-mass-ratio inspirals (EMRIs). The results presented in this Chapter were published in the article [72].

In order to ensure a self-contained presentation of the material, I start by describing a kludge waveform model for circular, equatorial EMRIs based on true Kerr geodesics. I then introduce the SF, and discuss the influence of its conservative and radiative components on the dynamics of a binary system. Following [5], I build kludge asymptotic observables including conservative corrections. Since the SF program has not yet succeeded in computing fully general relativistic SF results for Kerr inspirals, I derive the conservative corrections for the waveform model by ensuring that the kludge asymptotic observables reproduce post-Newtonian (PN) results in the weak-field regime.

Additionally, I use the kludge model and accurate first order SF results for Schwarzschild black holes to estimate the error that arises from omitting the second-order radiative piece of the SF. This analysis is important because this contributes observationally at

the same order as the first order conservative corrections, and one does not know *a priori* whether the contribution of this component will be as important as the conservative part, or whether its effects can be effectively ignored.

Thereafter, I will describe the basic elements of signal analysis, which will be relevant for the subsequent discussion on signal detection and parameter estimation. This includes the Fisher Matrix (FM) formalism, which is a scheme to estimate noise-induced errors. I also introduce a complementary formalism to estimate systematic errors that arise from the approximate nature of the waveform model [35].

Using the kludge model, I will present results of a Monte Carlo simulation of the parameter estimation errors, computed using the FM, and also estimate the “model errors” that arise from omitting the conservative correction terms included in the waveform template. I present results for three different types of system, namely the inspirals of black holes (BHs), neutron stars (NSs) and white dwarfs (WDs) into a super-massive black hole (SMBH). The analysis shows that, for a typical source, namely a $10M_{\odot}$ compact object captured by a 10^6M_{\odot} SMBH at a signal-to-noise ratio (SNR) of 30, it will be possible to determine the binary’s component masses to within a fractional error of $\sim 10^{-4}$, measure the SMBH spin parameter q to $\sim 10^{-4.5}$, and determine the location of the source on the sky and the spin orientation to within $\sim 10^{-3}$ steradians. I show that, for this model, omitting the conservative corrections leads to a small error over much of the parameter space, i.e., the ratio \mathcal{R} of the systematic model error to the noise-induced error is $\mathcal{R} \lesssim 1$ for all ten parameters in the model. For the few systems with larger errors, typically one still has $\mathcal{R} < 3$, and so the conservative corrections can be marginally ignored.

This analysis was the first of its kind to be done in the literature [72], and the results presented herein indicate that it may not be necessary to go beyond first order to recover accurate parameter estimates.

2.2 Kludge waveform

The waveform model I introduce in this Section is based on the numerical kludge approach described elsewhere [5; 63], but I summarise the formalism here.

The aim is to capture the main features of the waveform inspiral in the strong field regime. Because an accurate description of the orbital and phase evolution of the small body is not yet available, one can try to circumvent this problem in various steps. The first of them is an important observation: the system’s extreme mass ratio, $\eta = m/M \sim 10^{-5}$, guarantees that gravitational back-reaction effects occur on

2. Influence of conservative corrections on signal detection and parameter estimation for EMRIs

timescales much longer than any orbital timescale. Hence, one can assume that the inspiralling object instantaneously follows a Kerr space-time geodesic. Thus, I will compute the trajectory of the inspiralling body using the Boyer–Lindquist coordinates of the Kerr spacetime of the central BH. The differential equations that describe the geodesic motion of particles in a Kerr geometry are very well known [31; 99]

$$\Sigma \frac{dr}{d\tau} = \pm \sqrt{V_r}, \quad (2.1)$$

$$\Sigma \frac{d\theta}{d\tau} = \pm \sqrt{V_\theta}, \quad (2.2)$$

$$\Sigma \frac{d\phi}{d\tau} = V_\phi, \quad (2.3)$$

$$\Sigma \frac{dt}{d\tau} = V_t, \quad (2.4)$$

where the various potentials in Eqs. 2.1-2.4 are given by

$$V_r = [E(r^2 + a^2) - L_z a]^2 - \Delta [r^2 + (L_z - aE)^2 + Q], \quad (2.5)$$

$$V_\theta = Q - \cos^2 \theta \left[a^2(1 - E^2) + \frac{L_z^2}{\sin^2 \theta} \right], \quad (2.6)$$

$$V_\phi = \frac{L_z}{\sin^2 \theta} - aE + \frac{a}{\Delta} [E(r^2 + a^2) - L_z a], \quad (2.7)$$

$$V_t = a(L_z - aE \sin^2 \theta) + \frac{r^2 + a^2}{\Delta} [E(r^2 + a^2) - L_z a], \quad (2.8)$$

and $\Sigma = r^2 + a^2 \cos^2 \theta$, $\Delta = r^2 - 2Mr + a^2$. The constants E , L_z , Q are the three first integrals of the motion, namely, the specific orbital energy E ; the projection of the specific orbital angular momentum along the BH’s spin axis L_z ; and the Carter constant Q , a relativistic generalization of the third integral of motion which is used to separate the equations which describe orbits in an axisymmetric gravitational potential [5].

Because the waveform model I will develop in this Chapter will be used to study circular equatorial EMRIs, i.e, $\theta = \pi/2$, and $Q = 0$, the equations quoted above take a simple form, and the energy and angular momentum can be written in terms of the Boyer-Lindquist radius of the orbit, p , as follows [31],

$$\begin{aligned}\frac{E}{m} &= \frac{1 - 2(M/p) \pm (a/M)(M/p)^{3/2}}{\sqrt{1 - 3(M/p) \pm 2(a/M)(M/p)^{3/2}}}, \\ \frac{L_z}{mM} &= \pm \left(\frac{p}{M}\right)^{1/2} \frac{1 \mp 2(a/M)(M/p)^{3/2} + (a/M)^2(M/p)^2}{\sqrt{1 - 3(M/p) \pm 2(a/M)(M/p)^{3/2}}},\end{aligned}\quad (2.9)$$

where the upper (lower) sign is for prograde (retrograde) orbits, and a stands for the spin of the central BH. For convenience in the notation, I shall now introduce the spin parameter q , given by $q = a/M$. For these orbits, the inclination angle and eccentricity remain constant, i.e., circular-equatorial orbits remain circular-equatorial [80].

In order to obtain the orbital evolution of the compact object, one needs to evolve the geodesic parameters using the evolution of the energy, E , and angular momentum, L_z . One can evaluate these quantities by equating their rate of change with the flux carried away by the GWs, \dot{E} and \dot{L}_z . I have neglected the effect of black hole absorption, since it is found to appear at $\mathcal{O}(v^8)$ compared to the flux emitted to infinity, and it turns out to be negligible for the orbital evolution of coalescing compact binaries that may be detected by future laser GW interferometers (Note that if the central black hole is rotating, absorption appears at $\mathcal{O}(v^5)$) [97]. I will use the radiation fluxes derived by Gair & Glampedakis [63] to compute the CO’s inspiral evolution. These fluxes are based on 2.5PN expressions derived by Tagoshi [123]. However, they have been improved with higher order expressions that give better agreement with Teukolsky-based calculations, and satisfy various consistency conditions that ensure physical behaviour for near-circular and near-polar orbits. Furthermore, the scheme works very well even for strong-field orbits [63].

To evolve a circular orbit one needs to specify either the angular momentum or the energy flux, as they are related by the “circular goes to circular” rule [80]

$$\dot{E}(p) = \pm \frac{\sqrt{M}}{p^{3/2} \pm a\sqrt{M}} \dot{L}_z(p) = \Omega(p) \dot{L}_z(p), \quad (2.10)$$

where $d\phi/dt = \Omega(p)$, is the azimuthal velocity of the orbit. I have chosen to work with

2. Influence of conservative corrections on signal detection and parameter estimation for EMRIs

the evolution of L_z , which has the following form [63]

$$\dot{L}_z = -\frac{32}{5} \frac{m^2}{M} \left(\frac{M}{p}\right)^{7/2} \left\{ 1 - \frac{61}{12} q \left(\frac{M}{p}\right)^{3/2} - \frac{1247}{336} \left(\frac{M}{p}\right) + 4\pi \left(\frac{M}{p}\right)^{3/2} - \frac{44711}{9072} \left(\frac{M}{p}\right)^2 + \frac{33}{16} q^2 \left(\frac{M}{p}\right)^2 + \text{higher order Teukolsky fits} \right\}. \quad (2.11)$$

The “higher order Teukolsky fits” are given in [63]. I do not give these explicitly here, as they are not needed to derive the conservative corrections. However, I will include them to evolve the orbits and generate the waveforms.

The evolution in time of the radial coordinate is given by

$$\dot{p} = \frac{dp}{dE} \dot{E} = \frac{dp}{dL_z} \dot{L}_z. \quad (2.12)$$

Using the exact geodesic expression for dp/dL_z generates inspirals that are closer to Teukolsky based evolutions than expanding the above expression at 2PN order. However, I will need the 2PN expression in the following, which is

$$\frac{dp}{dt} = -\frac{64}{5} \eta \left(\frac{M}{p}\right)^3 \left\{ 1 - \frac{743}{336} \left(\frac{M}{p}\right) + \left(4\pi - \frac{133}{12} q\right) \left(\frac{M}{p}\right)^{3/2} + \left(\frac{34103}{18144} + \frac{81}{16} q^2\right) \left(\frac{M}{p}\right)^2 \right\}. \quad (2.13)$$

As before $\eta = m/M$. Up to this point the analysis has been incomplete as I have only considered the three integrals of motion. There are also three positional constants of the motion, which basically label the position of the test particle along the geodesic trajectory at some fiducial time. The evolution of these is non-trivial because the self-interaction has two main pieces. The only one I have considered so far is the dissipative or radiative SF and affects the evolution of the orbit. However, in real inspirals there is a second piece called the conservative SF, which affects the principal constants of the motion. In other words, it changes the frequency of an orbit at a given radius, but does not cause the orbit to evolve. One needs to include this piece of the SF as it could lead to several cycles of phase discrepancy in our kludge waveform over the inspiral.

The conservative SF has two parts. One part is oscillatory (for eccentric orbits) and averages to zero, whereas the other piece accumulates and affects the phasing of the waveform over time. I include this effect in the kludge by means of changing the ϕ

frequency. Specifically, I include this effect by re-writing the orbital frequency as

$$\frac{d\phi}{dt} = \left(\frac{d\phi}{dt}\right)_{\text{geo}} \left(1 + \delta\Omega\right). \quad (2.14)$$

This equation includes the phase derivative for a geodesic, labeled by the subscript “geo”, and a frequency shift which will depend on the instantaneous orbital parameters. A problem arises here because to compute the necessary frequency shifts within the appropriate framework, i.e., black hole perturbation theory (BHPT), would require SF calculations. At present, these are known for test-mass particles moving on circular and eccentric geodesic orbits around a Schwarzschild BH in the Lorentz gauge [8; 10]. But, there is an ongoing effort to extend such calculations to generic inspiral orbits in a Kerr background. The main challenge in this effort has to do with gauge freedoms as I will discuss later.

However, conservative corrections are known in the PN framework up to 2PN order, which include spin-orbit and spin-spin effects, and finite mass contributions [18]. One can combine these expressions with the radiative SF obtained by Tanaka et al. [124], based on the Teukolsky and Sasaki-Nakamura formalisms for perturbations around a Kerr BH, which includes terms of order q^2 . Equipped with these results, I will extend the method proposed by Babak et al. [5] to include conservative corrections in the kludge model. They computed the 1PN conservative correction for circular orbits in the Schwarzschild space-time, and I now extend that calculation to derive 2PN conservative corrections for circular orbits in the Kerr space-time.

The idea is to correct the kludge expressed in a particular coordinate system, in order to ensure that asymptotic observables are consistent with PN results in the weak field. In particular, I aim to modify the orbital frequency and its first time derivative. By modifying these two quantities, one can both identify coordinates between the two formalisms and find the missing conservative pieces.

From equation 2.10, at 2PN order the orbital frequency takes the form

$$\Omega = \frac{1}{M} \left(\frac{M}{p}\right)^{3/2} \left(1 - q \left(\frac{M}{p}\right)^{3/2} + O\left(\frac{M}{p}\right)^{5/2}\right), \quad (2.15)$$

2. Influence of conservative corrections on signal detection and parameter estimation for EMRIs

which I now augment by including conservative corrections

$$\begin{aligned}
\frac{d\phi}{dt} \equiv \Omega &= \frac{1}{M} \left(\frac{M}{p}\right)^{3/2} \left(1 - q \left(\frac{M}{p}\right)^{3/2}\right) (1 + \delta\Omega), \\
&= \frac{1}{M} \left(\frac{M}{p}\right)^{3/2} \left(1 - q \left(\frac{M}{p}\right)^{3/2}\right) \left\{1 + \right. \\
&\quad \left. + \eta \left(d_0 + d_1 \left(\frac{M}{p}\right) + (d_{1.5} + q f_{1.5}) \left(\frac{M}{p}\right)^{3/2} + d_2 \left(\frac{M}{p}\right)^2\right)\right\}. \tag{2.16}
\end{aligned}$$

I will use this expansion for Ω_{geo} only to derive the conservative corrections. As with dp/dL_z , it has been shown that more reliable waveforms can be obtained by including the full geodesic frequency where it is known, see 2.14, and this will be the approach used in section 2.4. It is inconsistent to include some pieces of the evolution at arbitrary PN order, while including the conservative corrections only at 2PN. However, the lower order effects that I am including with greater accuracy do have a more significant impact on the waveform. Moreover, it has been found in the past that including higher order terms where they are known is the right strategy to obtain accurate waveforms [63].

It is worth noting that the expansion in p is an expansion in $v^2 = M/p$. To derive the conservative corrections, I have chosen to leave the time derivative of the radial coordinate unchanged and given by equation 2.12/2.13. This amounts to a choice of gauge such that the η^2 piece of dp/dt vanishes. Differentiation of (2.16) then gives $d\Omega/dt$ for the kludge,

$$\begin{aligned}
\frac{d\Omega}{dt} &= \frac{96}{5} \frac{\eta}{M^2} \left(\frac{M}{p}\right)^{11/2} \left\{1 + \eta d_0 + \frac{M}{p} \left(-\frac{743}{336} + \eta \left(\frac{5}{3}d_1 - \frac{743}{336}d_0\right)\right) + \right. \\
&\quad + \left(\frac{M}{p}\right)^{3/2} \left(4\pi - \frac{157}{12}q + \eta \left(4\pi d_0 + 2d_{1.5} + q \left(2f_{1.5} - \frac{157}{12}d_0\right)\right)\right) \\
&\quad \left. + \left(\frac{M}{p}\right)^2 \left(\frac{34103}{18144} + \frac{81}{16}q^2 + \eta \left(\frac{34103}{18144}d_0 + \frac{81}{16}q^2d_0 - \frac{3715}{1008}d_1 + \frac{7}{3}d_2\right)\right)\right\}. \tag{2.17}
\end{aligned}$$

To relate the kludge coordinates with those used in the PN formalism one needs a coordinate transformation, i.e.,

$$\begin{aligned}
 p = & R \left\{ 1 + \left(\frac{M}{R} \right) b_1 + \left(\frac{M}{R} \right)^{3/2} (b_{1.5} + q s_{1.5}) + \left(\frac{M}{R} \right)^2 b_2 \right. \\
 & \left. + \eta \left(c_0 + \left(\frac{M}{R} \right) c_1 + \left(\frac{M}{R} \right)^{3/2} (c_{1.5} + q g_{1.5}) + \left(\frac{M}{R} \right)^2 c_2 \right) \right\}, \quad (2.18)
 \end{aligned}$$

where R denotes the PN semi-major axis. One can now substitute this expression for the coordinate transformation into relations 2.16 and 2.17.

The final stage of the computation is to compare the expressions for Ω and $\dot{\Omega}$, where a dot denotes d/dt , with the available PN expansions. The PN expansions are available to higher order in the mass ratio η , but I keep η only to the same order as the kludge, Eq. 2.17. The PN expressions for the orbital frequency and its first time derivative are given by [18]

$$\begin{aligned}
 \Omega_{PN}^2 = & \frac{m_T}{R^3} \left\{ 1 - \frac{m_T}{R} (3 - \eta) - \left(\frac{m_T}{R} \right)^{3/2} \left(2 \left(\frac{M}{m_T} \right)^2 + 3\eta \right) \hat{\mathbf{L}} \cdot \mathbf{q} \right. \\
 & \left. + \left(\frac{m_T}{R} \right)^2 \left(6 + \frac{41}{4}\eta \right) \right\}, \quad (2.19)
 \end{aligned}$$

where $m_T = M + m$ and $\hat{\mathbf{L}}$ is a unit vector directed along the orbital momentum. Additionally, [18]

$$\begin{aligned}
 \dot{\Omega}_{PN} = & \frac{96}{5} \eta m_T^{5/3} \omega^{11/3} \left\{ 1 - \left(\frac{743}{336} + \frac{11}{4}\eta \right) (m_T \omega)^{2/3} + (4\pi - \beta)(m_T \omega) \right. \\
 & \left. + \left(\frac{34103}{18144} + \frac{81}{16} q^2 + \eta \left(\frac{13661}{2016} + \zeta q^2 \right) \right) (m_T \omega)^{4/3} \right\}, \quad (2.20)
 \end{aligned}$$

where the spin-orbit parameter β is given by $\beta = 1/12 (113M^2/m_T^2 + 75\eta) \hat{\mathbf{L}} \cdot \mathbf{q}$ and the constant ζ will be determined from the kludge prescription. Note that I have assumed that the spin of the inspiralling BH is negligible with respect to the central object, and so I will ignore spin-spin interactions [3]. This assumption will be relaxed in the following Chapter to explore the influence of small body spin effects on signal detection and parameter estimation for massive binaries.

I shall now rewrite these expressions in a convenient way to take the EMRI limit,

2. Influence of conservative corrections on signal detection and parameter estimation for EMRIs

by writing $m_T = M(1 + \eta)$, i.e.,

$$\begin{aligned} \Omega_{PN} = & \frac{1}{M} \left(\frac{M}{R}\right)^{3/2} \left\{ 1 + \frac{\eta}{2} - \frac{M}{R} \left(\frac{3}{2} + \frac{7}{4}\eta\right) - q \left(\frac{M}{R}\right)^{3/2} \left(1 + \frac{3}{2}\eta\right) \right. \\ & \left. + \left(\frac{M}{R}\right)^2 \left(\frac{15}{8} + \frac{169}{16}\eta\right) \right\}, \end{aligned} \quad (2.21)$$

$$\begin{aligned} \dot{\Omega}_{PN} = & \frac{96}{5} \frac{\eta}{M^2} \left(\frac{M}{R}\right)^{11/2} \left\{ 1 + \frac{3}{2}\eta - \left(\frac{2591}{336} + \frac{13571}{672}\eta\right) \frac{M}{R} \right. \\ & + \left(4\pi - \frac{157}{12}q + \eta \left(12\pi - \frac{149}{6}q\right)\right) \left(\frac{M}{R}\right)^{3/2} \\ & \left. + \left(\frac{22115}{648} + \frac{81}{16}q^2 + \eta \left(\frac{87044}{567} + q^2 \left(\frac{567}{32} + \zeta\right)\right)\right) \left(\frac{M}{R}\right)^2 \right\}. \end{aligned} \quad (2.22)$$

A direct comparison between the two expressions for the orbital frequencies and their first time derivatives allows to solve simultaneously for b_1 , $b_{1.5}$, $s_{1.5}$, c_0 , c_1 , $c_{1.5}$, $g_{1.5}$, c_2 , d_0 , d_1 , $d_{1.5}$, $f_{1.5}$, and d_2 . One finds that the non-vanishing parameters are

$$\begin{aligned} b_1 = 1, \quad c_0 = -\frac{1}{4}, \quad c_1 = \frac{845}{448}, \quad d_0 = \frac{1}{8}, \quad d_1 = \frac{1975}{896} \\ c_{1.5} = -\frac{9}{5}\pi, \quad d_{1.5} = -\frac{27}{10}\pi, \quad f_{1.5} = -\frac{191}{160}, \quad g_{1.5} = -\frac{91}{240} \\ c_2 = -\frac{2065193}{677376}, \quad d_2 = \frac{1152343}{451584}. \end{aligned} \quad (2.23)$$

These parameters not only provide the missing conservative pieces, but also the value of the constant ζ of equation 2.22 and the coordinate transformation, which is given by $\zeta = -243/32$. Therefore, the first time derivative of the PN orbital frequency at 2nd order, including spin effects and conservative corrections, is given by

$$\begin{aligned}
 \dot{\Omega}_{PN} = & \frac{96}{5} \frac{\eta}{M^2} \left(\frac{M}{R}\right)^{11/2} \left\{ 1 + \frac{3}{2}\eta - \left(\frac{2591}{336} + \frac{13571}{672}\eta\right) \frac{M}{R} \right. \\
 & + \left(4\pi - \frac{157}{12}q + \eta \left(12\pi - \frac{149}{6}q \right) \right) \left(\frac{M}{R}\right)^{3/2} \\
 & \left. + \left(\frac{22115}{648} + \frac{81}{16}q^2 + \eta \left(\frac{87044}{567} + \frac{81}{8}q^2 \right) \right) \left(\frac{M}{R}\right)^2 \right\}. \quad (2.24)
 \end{aligned}$$

Having obtained the conservative pieces, one can now assess how important they are in determining the phasing of the waveform. To do so, I will first look at the number of cycles that the orbiting stellar-mass compact object performs in the last year of inspiral before plunge, and how many of these are contributed by each term in Ω . I will focus on this particular period of time, as that is when most of the GWs are radiated in the LISA band.

In Figure 2.1, I show the number of cycles in the last year of inspiral including the contributions from 1PN, 1.5PN and 2PN conservative corrections. I consider six different binary systems which consist of a central Kerr BH of specific mass $\bar{M} = M/M_{\odot} = \{10^5, 10^6, 10^7\}$, and an inspiralling compact object of specific mass $\bar{m} = m/M_{\odot} = \{1, 10\}$. I have considered both prograde and retrograde orbits.

As mentioned before, even though the GW signals are instantaneously below instrumental and confusion noise, one should be able to detect the signals with high SNR observing them for η^{-1} cycles, and using matched filtering. This requires the template waveform to match the true signal to better than half a cycle over the observation. In Figure 2.2 I assess the importance of including the conservative corrections by showing how long all of the conservative pieces combined take to contribute one cycle to the GW phasing. I consider both prograde and retrograde orbits for all of the binary systems shown in Figure 2.1.

From Figure 2.2, one learns that for a binary system of $10 + 10^5$ solar masses, the conservative corrections contribute with one cycle in about 60 days when $q = -0.9$. In all other cases it takes longer. The next step is to assess the importance of the highest order conservative term, i.e., the 2PN term. I do this by playing the same game as above, but considering the 2PN term only. This is shown in Figure 2.3.

Figure 2.3 shows that the 2PN conservative contribution does not have a significant impact on the number of cycles. In fact, referring to the $10 + 10^5$ binary system considered above, one observes that the 2PN term needs about 141 years to contribute

2. Influence of conservative corrections on signal detection and parameter estimation for EMRIs

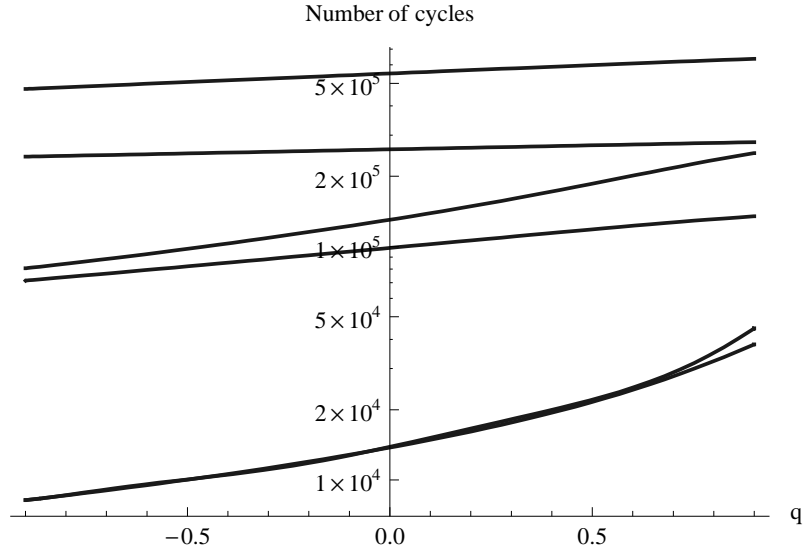


Figure 2.1: Number of gravitational waveform cycles spent during the last year of inspiral before plunge by a stellar-mass compact object of specific mass, \bar{m} , that falls on to a central Kerr BH of specific mass, \bar{M} . The number of cycles is derived including conservative corrections up to order 2PN. I show results for both prograde ($q > 0$) and retrograde ($q < 0$) orbits for the following binary systems, $\{\bar{M}, \bar{m}\} = (\{10^5, 1\}, \{10^5, 10\}, \{10^6, 1\}, \{10^6, 10\}, \{10^7, 1\}, \{10^7, 10\})$, from top to bottom, respectively.

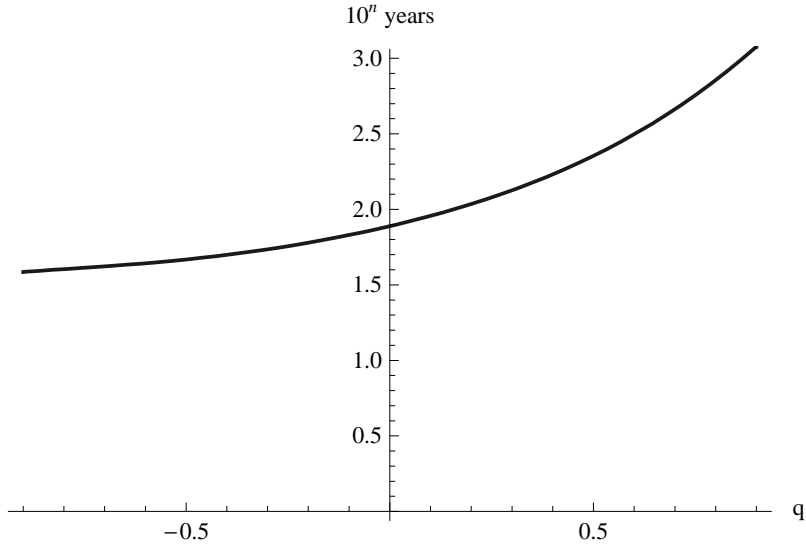


Figure 2.2: Time in years taken by the conservative pieces to contribute one cycle to the GW phasing for a given binary system as a function of q . The curve has the same shape for all binary systems. The vertical scale changes according to the binary system under consideration, and is expressed in units of 10^n years, where n depends on the system. Hence if $\{\bar{M}, \bar{m}, n\}$ defines our system, I show the cases: $\{10^7, 1, 4\}, \{10^7, 10, 3\}, \{10^6, 1, 2\}, \{10^6, 10, 1\}, \{10^5, 1, 0\}, \{10^5, 10, -1\}$.

with one cycle for a value of $q = 0.9$. In any other case, it takes longer. One also observes in Figure 2.2 that the number of years increases as q increases, whereas Figure 2.3 shows the opposite behaviour. This arises because all of the conservative pieces have a positive contribution, apart from the 1.5PN term. Indeed, this term is the dominant one. Were it not included in the kludge, the number of years taken by the conservative pieces to complete a cycle would be much smaller. However, because the 1.5PN term balances and even overcomes the other positive contributions, one gets the behaviour portrayed in Figure 2.2. Roughly speaking, an effect will have to be included in a matched filtering template if it contributes of the order of one cycle over the observation. These results suggest that it will be necessary to include conservative corrections in our waveform model, but it may not be necessary to go beyond 2PN order.

2.3 A comparison with the SF formalism for non-spinning BHs

The conservative pieces that I have included in the model, Eq. (2.23), were obtained in the PN framework. In the future, one would want to obtain a more accurate solution

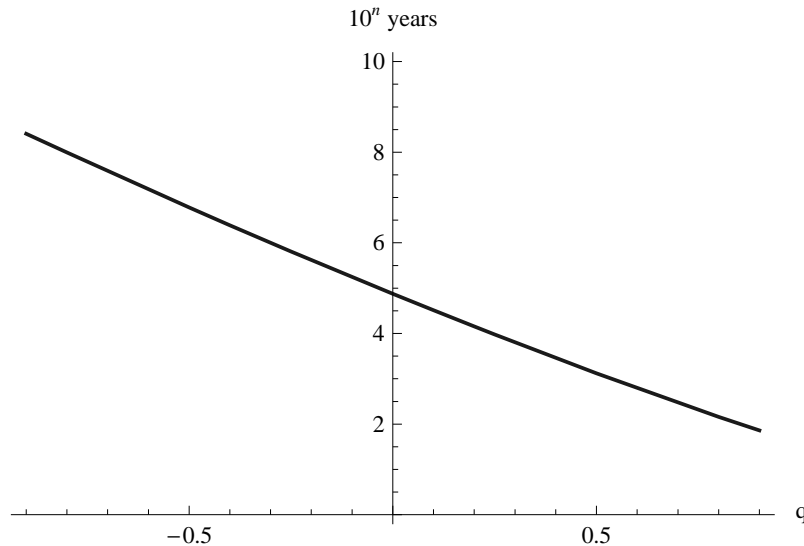


Figure 2.3: This graphic shows the time in years taken by the 2PN conservative piece to contribute one cycle to the GW phasing for a given binary system as a function of q . The notation is as for Figure 2.2, and I show the following $\{\bar{M}, \bar{m}, n\}$ cases: $\{10^7, 1, 7\}$, $\{10^7, 10, 6\}$, $\{10^6, 1, 5\}$, $\{10^6, 10, 4\}$, $\{10^5, 1, 3\}$, $\{10^5, 10, 2\}$.

for the conservative corrections using fits to SF calculations, once these are available. It is worth pointing out that, as shown above, second order radiative corrections contribute to the phase evolution at the same level as first order conservative corrections. The model I have developed includes both corrections, and so I can use it to assess the relative contribution from the first order conservative SF, and the second order dissipative SF. To do so, I will use the SF results recently obtained by Barack and Sago [8] for a circular orbit around a Schwarzschild BH.

The main complication in SF calculations comes from gauge freedom —the gauges in which the local and global fields are most easily computed are different. Barack et al. [8] found a way to circumvent this problem in the non-rotating case by solving both the perturbation equations for the global retarded field in the Lorenz gauge. In the kludge prescription, by choosing only to modify Ω and not dL_z/dt when comparing to the PN model, I have effectively chosen a gauge in which the η^2 corrections to the radiative part of the SF vanish.

2.3.1 Assessing SF calculations using the kludge model

I can compare SF results to the kludge results in the same way that I computed the conservative corrections above, namely by comparing asymptotic observables —the orbital frequency and its first time derivative. The second order piece of $d\Omega/dt$ as a function of Ω depends on both the first order conservative and the second order radiative SF corrections, and therefore cannot be determined completely from the first order SF. What I want to study now is whether first order accurate SF calculations will be sufficient for parameter estimation with LISA, by assessing the importance of the second order radiative piece to the orbital phase evolution.

Following [8], the orbital frequency of an orbit in the Schwarzschild metric under the influence of the radial SF, F_r , is

$$\Omega_{\text{SF}} = \Omega_0 \left[1 - \left(\frac{r(r-3M)}{2Mm} \right) F_r \right] \left(1 - \frac{m}{\sqrt{r(r-3M)}} \right), \quad (2.25)$$

where $\Omega_0 = \sqrt{M/r^3}$, and r stands for the radial coordinate in the SF framework

Barack and Sago [8] gave a fit to F^r , but the terms they proposed were not motivated by PN expansions. For easier comparison to my results, I now derive an alternative fit

2. Influence of conservative corrections on signal detection and parameter estimation for EMRIs

to their results of the form

$$F^r(r \gg M) \simeq \frac{m^2}{r^2} \left[a_0 + a_1 \frac{M}{r} + a_{1.5} \left(\frac{M}{r} \right)^{3/2} + a_2 \left(\frac{M}{r} \right)^2 \right], \quad (2.26)$$

where the various coefficients have the values

$$a_0 = 2.01638, \quad a_1 = -8.98147, \quad a_{1.5} = 12.20270, \quad a_2 = -16.51406. \quad (2.27)$$

This fit reproduces the numerical data within the numerical accuracy considered by Barack et al. [8] in the range $8M < r < 150M$. Note that the leading term $F^r \simeq 2.016m^2/r_0^2 \simeq 2m^2/r_0^2$ is consistent with the Keplerian SF which describes the back-reaction effect that arises from the motion of the BH around its center of mass.

To fit the data in the range $6M < r < 8M$ I use the expression

$$F^r(r \geq 6M) \simeq \frac{m^2}{r^2} \left[b_0 + b_1 \frac{M}{r} + b_{1.5} \left(\frac{M}{r} \right)^{3/2} + b_2 \left(\frac{M}{r} \right)^2 \right], \quad (2.28)$$

where the various coefficients are given by

$$b_0 = 2.44194, \quad b_1 = -29.44529, \quad b_{1.5} = 89.73089, \quad b_2 = -99.32447. \quad (2.29)$$

One can now plug these fits into Eq. (2.25) to obtain Ω_{SF} .

$$\Omega_{\text{SF}} = \Omega_0 \left[1 + \eta \left(\lambda_0 + \lambda_1 \frac{M}{r} + \lambda_{1.5} \left(\frac{M}{r} \right)^{3/2} + \lambda_2 \left(\frac{M}{r} \right)^2 \right) \right], \quad (2.30)$$

where the various coefficients have the values

$$6M < r < 8M : \quad \lambda_0 = -1.22097, \quad \lambda_1 = 14.9436, \quad \lambda_{1.5} = -44.8654, \\ \lambda_2 = 35.3815; \quad (2.31)$$

$$r > 8M : \quad \hat{\lambda}_0 = -1.00819, \quad \hat{\lambda}_1 = 4.49892, \quad \hat{\lambda}_{1.5} = -6.10135, \\ \hat{\lambda}_2 = 4.2826. \quad (2.32)$$

To compare the SF orbital frequency, Eq. (2.30), to the kludge Ω , Eq. (2.16), I need the coordinate transformation that relates the kludge radial coordinate p to that

2. Influence of conservative corrections on signal detection and parameter estimation for EMRIs

of the SF formalism, r . To that effect I use a transformation of the form

$$p = r \left\{ 1 + \alpha_1 \frac{M}{r} + \alpha_{1.5} \left(\frac{M}{r} \right)^{3/2} + \alpha_2 \left(\frac{M}{r} \right)^2 + \eta \left(\beta_0 + \beta_1 \frac{M}{r} + \beta_{1.5} \left(\frac{M}{r} \right)^{3/2} + \beta_2 \left(\frac{M}{r} \right)^2 \right) \right\}. \quad (2.33)$$

The non-vanishing coefficients are given by

$$6M < r < 8M : \quad \beta_0 = 0.89731, \quad \beta_1 = -8.4929, \quad \beta_{1.5} = 24.25543, \\ \beta_2 = -22.2198 \quad (2.34)$$

$$r > 8M : \quad \beta_0 = 0.75546, \quad \beta_1 = -1.52978, \quad \beta_{1.5} = -1.58730, \\ \beta_2 = -1.15393. \quad (2.35)$$

Using the coordinate transformations, Eqs. (2.33), (2.34), (2.35), in Eq. (2.16) recovers Eq. (2.25).

Under the influence of the conservative SF, the angular momentum of an orbit undergoes a shift

$$L = L_0 \left(1 - \frac{r^2}{2Mm} F^r \right), \quad (2.36)$$

where $L_0 = \sqrt{Mr^2/(r-3M)}$. The first order radiative SF is given by Eq. (2.11), but with p , the kludge radial coordinate, replaced by r , the SF radial coordinate. As before, the evolution of \dot{r} is best expressed as $\dot{r} = \dot{L}_z / (dr/dL_z)$ with

$$\frac{1}{M} \frac{dL_z}{dr} = \frac{1}{2(r/M-3)^{3/2}} \left(\frac{r}{M} - 6 + \frac{\eta}{2} \left(\epsilon_{-1} \frac{r}{M} + \epsilon_0 + \epsilon_{0.5} \left(\frac{M}{r} \right)^{1/2} + \epsilon_1 \left(\frac{M}{r} \right) + \epsilon_{1.5} \left(\frac{M}{r} \right)^{3/2} + \epsilon_2 \left(\frac{M}{r} \right)^2 \right) \right), \quad (2.37)$$

where the various coefficients can be found to be

$$6M < r < 8M : \quad \epsilon_{-1} = -2.44194, \quad \epsilon_0 = -14.7936, \quad \epsilon_{0.5} = 179.462, \\ \epsilon_1 = -297.973, \quad \epsilon_{1.5} = -269.193, \quad \epsilon_2 = 595.947; \quad (2.38)$$

$$r > 8M : \quad \epsilon_{-1} = -2.01638, \quad \epsilon_0 = 3.11681, \quad \epsilon_{0.5} = 24.4054 \\ \epsilon_1 = -49.5422, \quad \epsilon_{1.5} = -36.6081, \quad \epsilon_2 = 99.0843. \quad (2.39)$$

2. Influence of conservative corrections on signal detection and parameter estimation for EMRIs

By construction, in this gauge, one is missing a contribution from the second order part of \dot{L}_z . However, I have already computed a similar expression within the kludge approach, Eq. (2.12), which includes that contribution. Using the coordinate transformation, Eqs (2.33)–(2.35), I can use the kludge result to find the second order piece of \dot{L}_z in the SF gauge

$$\delta\dot{L}_z = -\frac{32}{5}\eta^2 \left(\frac{M}{r}\right)^{7/2} \left\{ l_0 + l_1 \left(\frac{M}{r}\right) + l_{1.5} \left(\frac{M}{r}\right)^{3/2} + l_2 \left(\frac{M}{r}\right)^2 \right\}$$

where $6M < r < 8M$: $l_0 = -4.0379$, $l_1 = 48.0413$, $l_{1.5} = -140.422$,
 $l_2 = -57.544$;
 $r > 8M$: $l_0 = -3.3995$, $l_1 = 20.7749$, $l_{1.5} = -52.1948$,
 $l_2 = 1.5371$. (2.40)

The importance of the second order radiative piece of the SF is readily assessed by computing the difference between an evolution using only Eq. (2.11) for \dot{L}_z , and one that also includes the second order correction above. One can now compute the number of cycles that the stellar mass CO performs before plunge for various binary systems in three separate cases — 1) ignoring all η^2 corrections to \dot{r} (i.e., setting $\delta\dot{L}_z$ and the ϵ coefficients in Eq. (2.37) to zero); 2) ignoring the second order radiative contribution (i.e., use $\delta\dot{L}_z = 0$ and the ϵ coefficients from Eqs. (2.38)–(2.39)); 3) including all second order corrections (i.e., as (2) but now with $\delta\dot{L}_z$ from Eq. (2.40)). The results are given in Table 2.1. From this Table one can see that the second order radiative bit, which is missing from the SF formalism, appears to be relatively unimportant for the GW phasing. This is because the number of gravitational waveform cycles changes very little as one changes the approximation used to compute them.

M/M_\odot	0.6	1.4	10
Number of cycles with no 2PN order corrections	133312.6	127503.0	98642.5
Number of cycles with no 2PN order radiative corrections	133311.9	127502.1	98645.8
Number of cycles with all 2PN order corrections	133312.2	127502.6	98643.3

Table 2.1: In this table I present the number of gravitational waveform cycles that are generated during the last year of inspiral of COs with masses of $0.6M_\odot$, $1.4M_\odot$ and $10M_\odot$ into a 10^6M_\odot Schwarzschild BH. I consider three different approximations, as described in the text.

2.4 Noise induced parameter errors

2.4.1 Waveform prescription

In order to explore the parameter estimation accuracy which LISA observations are likely to achieve, one needs waveforms in addition to the orbital phase evolution. In the spirit of the numerical kludge prescription I will use the linearized scheme for waveform generation.

The starting point of the linearized scheme is to take the Einstein field equations,

$$R_{\mu\nu} - \frac{1}{2}g_{\mu\nu}R = 8\pi\mathcal{T}_{\mu\nu},$$

and study them around the flat-space metric $\eta_{\mu\nu}$, i.e.,

$$g_{\mu\nu} = \eta_{\mu\nu} + h_{\mu\nu}, \tag{2.41}$$

where $h_{\mu\nu}$ are small metric perturbations, $|h_{\mu\nu}| \ll 1$. To recast the Einstein field equations in the weak-field regime, it is convenient to introduce the trace-reversed metric perturbation, i.e.,

$$\bar{h}^{\mu\nu} \equiv h^{\mu\nu} - (1/2)\eta^{\mu\nu}h, \text{ and, } h = \eta^{\mu\nu}h_{\mu\nu}, \tag{2.42}$$

where $\bar{h}^{\mu\nu}$ represents the gravitational field. Additionally, imposing the Lorenz gauge condition $\partial_\alpha \bar{h}^{\mu\alpha} = 0$, the linearized equations take the form

$$\square \bar{h}^{\mu\nu} = -16\pi\mathcal{T}^{\mu\nu}, \tag{2.43}$$

and $\square = \nabla^2 - \partial_t^2$ denotes the usual flat space wave operator. Since the flat-space d'Alembertian \square commutes with ∂_μ , the Lorenz gauge and relation 2.43 imply that the effective energy-momentum tensor $\mathcal{T}^{\mu\nu}$ satisfies

$$\mathcal{T}^{\mu\nu}{}_{,\nu} = 0. \tag{2.44}$$

This latter relation indicates that in a self-consistent approach, the energy-momentum tensor is flat-spaced conserved. Additionally, if the motion of the source is only negligibly influenced by gravity, then the effective energy-momentum tensor $\mathcal{T}^{\mu\nu}$ can be taken to be equal to the energy-momentum tensor of the matter source $T^{\mu\nu}$.

2. Influence of conservative corrections on signal detection and parameter estimation for EMRIs

Because the aim of developing this kludge waveform model is to detect GWs at large distances outside the source, i.e., $T^{\mu\nu} = 0$, Eq. 2.43 takes the form

$$\square \bar{h}^{\mu\nu} = 0. \quad (2.45)$$

From this relation one concludes that in the linearized regime, GWs travel at the speed of light. One also notes that in this case, the relation $\partial_\alpha \bar{h}^{\mu\alpha} = 0$ is not spoiled by a further coordinate transformation $x^\mu \rightarrow x^\mu + \chi^\mu(x)$, as long as $\square \chi_\mu = 0$. This is because under this coordinate transformation, $h^{\mu\nu} \rightarrow h^{\mu\nu} - (\partial_\mu \chi_\nu + \partial_\nu \chi_\mu)$. In terms of $\bar{h}^{\mu\nu}$, this transformation takes the form $\bar{h}^{\mu\nu} \rightarrow \bar{h}^{\mu\nu} - (\partial_\mu \chi_\nu + \partial_\nu \chi_\mu - \eta_{\mu\nu} \partial_\rho \chi^\rho)$. Therefore

$$\partial^\nu \bar{h}^{\mu\nu} \rightarrow \partial^\nu \bar{h}^{\mu\nu} - \square \chi_\mu.$$

Since $\square \chi_\mu = 0$, and the d’Alambertian commutes with ∂_μ , then

$$\square \chi_{\mu\nu} = \square (\partial_\mu \chi_\nu - \partial_\nu \chi_\mu - \eta_{\mu\nu} \partial_\rho \chi^\rho) = 0.$$

Hence, the residual gauge freedom associated with the four independent arbitrary functions χ_μ can be chosen so as to impose four conditions on $h^{\mu\nu}$. For instance, one can choose χ^0 so that the trace $\bar{h} = 0$. Hence, the trace-reversed metric takes the form $\bar{h}^{\mu\nu} = h^{\mu\nu}$. Additionally, choosing the three functions χ^i so that $h^{0i} = 0$, the time component of the Lorenz gauge reads $\partial^0 h_{00} + \partial^i h_{0i} = 0$. But, $h^{0i} = 0$. So the time component of the Lorenz gauge implies that the h_{00} component is constant in time. This component corresponds to the Newtonian potential of the source that generated the GW. On the other hand, because the GW itself is the time dependent component, the condition $\partial^0 h_{00} = 0$, effectively means $h_{00} = 0$. These considerations allow one to set $h_{0\mu} = 0$.

The spatial component of the Lorenz gauge reads $\partial^i h_{0i} + \partial^i h_{ij} = 0$. Since $h_{0i} = 0$, and $\bar{h} = 0$, then one gets $\partial^i h_{ij} = 0$, $h_i^i = 0$, respectively. In summary, the equations $\square \chi_{\mu\nu} = 0$, $\square \bar{h}^{\mu\nu} = 0$ imply

$$h^{0\mu} = 0, \quad h_i^i = 0, \quad \partial^i h_{ij} = 0. \quad (2.46)$$

These conditions define the transverse–traceless (TT) gauge. In this gauge the time–space components of the Riemann curvature tensor satisfy the condition

$$R_{j0k0} = -\frac{1}{2} h_{jk,00}^{TT}. \quad (2.47)$$

Because the Riemann curvature tensor is gauge-invariant, Eq. 2.47 indicates that the TT gauge provides the minimum number of degrees of freedom for $h^{\mu\nu}$, i.e., two. Furthermore, this relation shows that gravitational information is in the form of spacetime curvature.

Using the projection operator $P_{ij} = \eta_{ij} - \hat{n}_i\hat{n}_j$, with \hat{n}_i the unit vector in the direction of propagation, one can write the metric perturbations, $h_{ij}(t)$, in the TT gauge as follows [99]

$$h_{ij}^{TT}(t) = \frac{2}{D} \left(P_{ik}P_{jl} - \frac{1}{2}P_{ij}P_{kl} \right) \ddot{I}^{kl}, \quad (2.48)$$

where D is the distance to the source, and \ddot{I}^{kl} is the second time derivative of the inertia tensor. This relation shows that when a system of masses is accelerated, then, according to relation 2.47, fluctuations in curvature are generated, which propagate away from the system carrying energy.

In the EMRI framework, the inertia tensor takes the form $I^{kl} = mr^i(t)r^j(t)$, where $r^i(t)$ represents the position vector of the compact object with respect to the SMBH in the pseudo-flat space.

2.4.2 Implementation of LISA's response function

Following [34], the LISA response may be written as

$$h_\alpha(t) = \frac{\sqrt{3}}{2D} \left[F_\alpha^+(t)A^+(t) + F_\alpha^\times(t)A^\times(t) \right], \quad (2.49)$$

where $\alpha = I, II$ refers to the two independent Michelson-like detectors that constitute the LISA response at low frequencies. The functions $A^{+,\times}(t)$ are the polarization coefficients given by

$$A^+ = -a_+[1 + (\hat{a} \cdot \hat{n})^2], \quad A^\times = 2a_\times(\hat{a} \cdot \hat{n}), \quad (2.50)$$

where \hat{a} is a unit vector along the SMBH's spin direction, and a_+, a_\times are given by

$$a_+ = \frac{1}{2} \left(\ddot{I}^{11} - \ddot{I}^{22} \right), \quad a_\times = \ddot{I}^{12}.$$

2. Influence of conservative corrections on signal detection and parameter estimation for EMRIs

The antenna pattern functions $F_\alpha^{+\times}$ are given by

$$\begin{aligned} F_I^+ &= \frac{1}{2}(1 + \cos^2 \theta) \cos(2\phi) \cos(2\psi) - \cos \theta \sin(2\phi) \sin(2\psi), \\ F_I^\times &= \frac{1}{2}(1 + \cos^2 \theta) \cos(2\phi) \sin(2\psi) + \cos \theta \sin(2\phi) \cos(2\psi), \end{aligned} \quad (2.51)$$

$$\begin{aligned} F_{II}^+ &= \frac{1}{2}(1 + \cos^2 \theta) \sin(2\phi) \cos(2\psi) + \cos \theta \cos(2\phi) \sin(2\psi), \\ F_{II}^\times &= \frac{1}{2}(1 + \cos^2 \theta) \sin(2\phi) \sin(2\psi) - \cos \theta \cos(2\phi) \cos(2\psi). \end{aligned} \quad (2.52)$$

The various angles in the previous expressions represent the source's sky location in a detector based coordinate system, (θ, ϕ) , and the polarization angle of the wavefront, ψ . These can be re-written in a fixed, ecliptic-based coordinate system. If one denotes the source co-latitude and azimuth angles and the direction of \hat{a} in this fixed coordinate system by (θ_S, ϕ_S) and (θ_K, ϕ_K) respectively, then

$$\begin{aligned} \cos \theta(t) &= \frac{1}{2} \cos \theta_S - \frac{\sqrt{3}}{2} \sin \theta_S \cos[\bar{\phi}_0 + 2\pi(t/T) - \phi_S], \\ \phi(t) &= \bar{\alpha}_0 + 2\pi(t/T) + \tan^{-1} \left\{ \frac{\sqrt{3} \cos \theta_S + \sin \theta_S \cos[\bar{\phi}_0 + 2\pi(t/T) - \phi_S]}{2 \sin \theta_S \sin[\bar{\phi}_0 + 2\pi(t/T) - \phi_S]} \right\}, \\ \tan \psi &= \left\{ \frac{1}{2} \cos \theta_K - \frac{\sqrt{3}}{2} \sin \theta_K \cos[\bar{\phi}_0 + 2\pi(t/T) - \phi_K] \right. \\ &\quad \left. - \cos \theta(t) [\cos \theta_K \cos \theta_S + \sin \theta_K \sin \theta_S \cos(\phi_K - \phi_S)] \right\} / \\ &\quad \left\{ \frac{1}{2} \sin \theta_K \sin \theta_S \sin(\phi_K - \phi_S) - \frac{\sqrt{3}}{2} \cos(\bar{\phi}_0 + 2\pi t/T) \right. \\ &\quad \left. \{ \cos \theta_K \sin \theta_S \sin \phi_S - \cos \theta_S \sin \theta_K \sin \phi_K \} \right. \\ &\quad \left. - \frac{\sqrt{3}}{2} \sin(\bar{\phi}_0 + 2\pi t/T) (\cos \theta_S \sin \theta_K \cos \phi_K - \cos \theta_K \sin \theta_S \cos \phi_S) \right\}, \end{aligned} \quad (2.53)$$

where $\bar{\phi}_0, \bar{\alpha}_0$ are constant angles which represent the orbital and rotational phase of the detector at $t = 0$. Following [6], I will set both of these to zero in the subsequent analysis. Additionally, T is the orbital period, which is 1 year. Barack and Cutler [6] write these expressions in terms of θ_L, ϕ_L , which specify the direction of the compact object's orbital angular momentum in the ecliptic-based system. In the case I consider, the orbits are circular and equatorial, so the angular momentum vector of the orbiting

body does not precess about the SMBH's spin \hat{a} and $\theta_K = \theta_L, \phi_K = \phi_L$.

The last ingredient to be included in the detector response is the Doppler phase modulation. If $\Phi(t)$ denotes the phase of the waveform, the inclusion of the Doppler modulation shifts the phase as follows [6]

$$\Phi(t) \rightarrow \Phi(t) + 2\frac{d\phi}{dt}R \sin\theta_S \cos[2\pi(t/T) - \phi_S], \quad (2.54)$$

where $R = 1\text{AU}/c = 499.00478\text{s}$ and $d\phi/dt$ is the azimuthal velocity of the orbit, cf. (2.10).

2.4.3 Signal analysis

This section contains an overview of the basic elements of signal analysis that I will use to estimate the accuracies with which LISA measurements will be able to determine the parameters of spinning binary systems.

The measured strain, $s(t)$, in a GW detector is a time series that contains both a true GW signal, $h(t)$, and instrumental noise, $n(t)$. In the context of LISA, the output of the equivalent two arm Michelson detectors can be represented as

$$s_\alpha(t) = h_\alpha(t) + n_\alpha(t), \quad \alpha = \text{I, II}. \quad (2.55)$$

Given two time series, one can define the overlap as

$$(\mathbf{p} | \mathbf{q}) \equiv 2 \sum_\alpha \int_0^\infty [\tilde{p}_\alpha^*(f)\tilde{q}_\alpha(f) + \tilde{p}_\alpha(f)\tilde{q}_\alpha^*(f)] / S_n(f) df, \quad (2.56)$$

where $S_n(f)$ stands for the one-sided spectral density of the instrumental noise. Assuming that each Fourier component of the noise, $\tilde{n}_\alpha(f)$, is Gaussian distributed, and uncorrelated with other Fourier components (i.e., the noise is stationary), the ensemble average of the Fourier components of the noise has the property

$$\langle \tilde{n}_\alpha(f) \tilde{n}_\beta(f')^* \rangle = \frac{1}{2} \delta(f - f') S_n(f) \delta_{\alpha\beta}. \quad (2.57)$$

The former relation defines the spectral density $S_n(f)$, which incidentally is the same in the two detectors. Furthermore, the probability distribution function for the noise $n(t)$ is given by

$$p(\mathbf{n} = \mathbf{n}_0) \propto \exp\left(-\frac{(\mathbf{n}_0 | \mathbf{n}_0)}{2}\right). \quad (2.58)$$

2. Influence of conservative corrections on signal detection and parameter estimation for EMRIs

One can interpret Eq. (2.58) as the probability that the actual noise realization is \mathbf{n}_0 . Assuming that one has made a detection, i.e., the output of the detector is given by $\mathbf{s}(t) = \mathbf{h}(t; \theta_{\text{true}}) + \mathbf{n}_0(t)$, where $\mathbf{n}_0(\mathbf{t})$ is the specific realization of the noise and θ_{true} is the unknown true value of the parameters of the source, the likelihood of measuring the output signal is

$$\Lambda(\mathbf{s} | \theta_{\text{true}}) \propto \exp\left(-\frac{\mathbf{s} - \mathbf{h}(\theta_{\text{true}}) | \mathbf{s} - \mathbf{h}(\theta_{\text{true}})}{2}\right). \quad (2.59)$$

In order to reconstruct the most probable value of the parameters of the source, and compute their respective errors, one needs to calculate the probability of the parameters given the data, i.e., the posterior probability, which, according to Bayes's theorem, is given by the product of the likelihood function, Eq. 2.59, and the prior probability $p_0(\theta_{\text{true}})$, i.e.,

$$p(\mathbf{h}(\theta_{\text{true}}) | \mathbf{s}) = N p_0(\theta_{\text{true}}) \exp\left(\left(\mathbf{h}(\theta_{\text{true}}) | \mathbf{s}\right) - \frac{1}{2} \left(\mathbf{h}(\theta_{\text{true}}) | \mathbf{h}(\theta_{\text{true}})\right)\right), \quad (2.60)$$

where the factor $(\mathbf{s} | \mathbf{s})/2$ has been absorbed into the normalization factor N . For a given measured signal $\mathbf{s}(\mathbf{t})$, the gravitational waveform $\mathbf{h}(\mathbf{t})$ that best fits the data is the one that minimizes the quantity $(\mathbf{s} - \mathbf{h} | \mathbf{s} - \mathbf{h})$. This condition is also satisfied by the maximum likelihood estimators of the parameters, and corresponds to the point in parameter space with the highest SNR in a matched filtering search, namely,

$$\frac{S}{N} [h(\theta^i)] = \frac{(\mathbf{s} | \mathbf{h})}{\sqrt{(\mathbf{h} | \mathbf{h})}}. \quad (2.61)$$

In the limit of high SNR, a locally flat prior would be a reasonable assumption because the best-fit parameters will have a Gaussian distribution centered on the correct values. Hence, one can expand Eq. (2.60) about the peak, $\hat{\theta} = \theta_{\text{true}}$, by setting $\theta^i = \hat{\theta}^i + \Delta\theta^i$, and find

$$p(\Delta\theta | s) = \mathcal{N} e^{-\frac{1}{2} \Gamma_{ij} \Delta\theta^i \Delta\theta^j}, \quad \Gamma_{ij} \equiv \left(\frac{\partial \mathbf{h}}{\partial \lambda^i} \middle| \frac{\partial \mathbf{h}}{\partial \lambda^j} \right)_{|\theta=\hat{\theta}}, \quad (2.62)$$

where $p(\Delta\theta | s)$ is the Gaussian probability distribution of the parameter estimation errors $\Delta\theta$, and Γ_{ij} is the Fisher Information Matrix. Additionally, for large SNR, the covariance of the posterior probability distribution, $(\Gamma^{-1})^{ij}$, gives the expectation value

2. Influence of conservative corrections on signal detection and parameter estimation for EMRIs

of the errors $\Delta\theta^i$

$$\langle \Delta\theta^i \Delta\theta^j \rangle = (\Gamma^{-1})^{ij} + \mathcal{O}(\text{SNR})^{-1}. \quad (2.63)$$

In the subsequent analysis, I will use a simplified definition of the inner product, Eq. (2.56), which is based on the following observation: for white noise, i.e., $S_n(f) = \text{const.}$, so by Parseval's theorem Eq. (2.56) takes the simple form $2S_n^{-1} \sum_{\alpha} \int_{-\infty}^{\infty} p_{\alpha}(t)q_{\alpha}(t)dt$. Following Barack & Cutler [6], one can define the “noise-weighted” waveform as follows

$$\hat{h}_{\alpha}(t) \equiv \frac{h_{\alpha}(t)}{\sqrt{S_h(f(t))}}, \quad f(t) = \frac{1}{\pi} \frac{d\phi}{dt}, \quad (2.64)$$

and rewrite the Fisher matrix approximately as

$$\Gamma_{ab} = 2 \sum_{\alpha} \int_0^T \partial_a \hat{h}_{\alpha}(t) \partial_b \hat{h}_{\alpha}(t) dt. \quad (2.65)$$

2.4.4 Noise model

The function $S_h(f)$ is the total LISA noise, which has three components: instrumental noise, confusion noise from short-period galactic binaries, and confusion noise from extragalactic binaries. I use the same prescription as in Barack and Cutler [6], namely

$$S_h(f(t)) = \min\{S_h^{\text{inst}}(f)/\exp(-\kappa T_{\text{mission}}^{-1} dN/df) + S_h^{\text{exgal}}(f), S_h^{\text{inst}}(f) + S_h^{\text{gal}}(f) + S_h^{\text{exgal}}(f)\}, \quad (2.66)$$

where the various components have the following analytic forms [6]

$$\begin{aligned} S_h^{\text{inst}}(f) &= 9.18 \times 10^{-52} f^{-4} + 1.59 \times 10^{-41} + 9.18 \times 10^{-38} f^2 \text{ Hz}^{-1}, \\ S_h^{\text{gal}}(f) &= 2.1 \times 10^{-45} \left(\frac{f}{1\text{Hz}}\right)^{-7/3} \text{ Hz}^{-1}, \\ S_h^{\text{ex. gal}} &= 4.2 \times 10^{-47} \left(\frac{f}{1\text{Hz}}\right)^{-7/3} \text{ Hz}^{-1}. \end{aligned} \quad (2.67)$$

Here dN/df is the number density of galactic WD binaries per unit GW frequency, and κ is the average number of frequency bins that are lost when each galactic binary is fitted out. I use

$$\frac{dN}{df} = 2 \times 10^{-3} \text{ Hz}^{-1} \left(\frac{1\text{Hz}}{f}\right)^{11/3}, \quad \kappa T_{\text{mission}}^{-1} = 1.5/\text{yr}, \quad (2.68)$$

2. Influence of conservative corrections on signal detection and parameter estimation for EMRIs

with $T_{\text{mission}} = 3$ yr, and $\kappa = 4.5$.

Using 2.66, one can generate the total noise curve, which includes instrumental noise, confusion noise from short-period galactic binaries, and confusion noise from extragalactic WD binaries, for any CO species. Fig. 2.4 presents the total LISA noise curve for BH inspirals onto SMBHs during the last year before plunge.

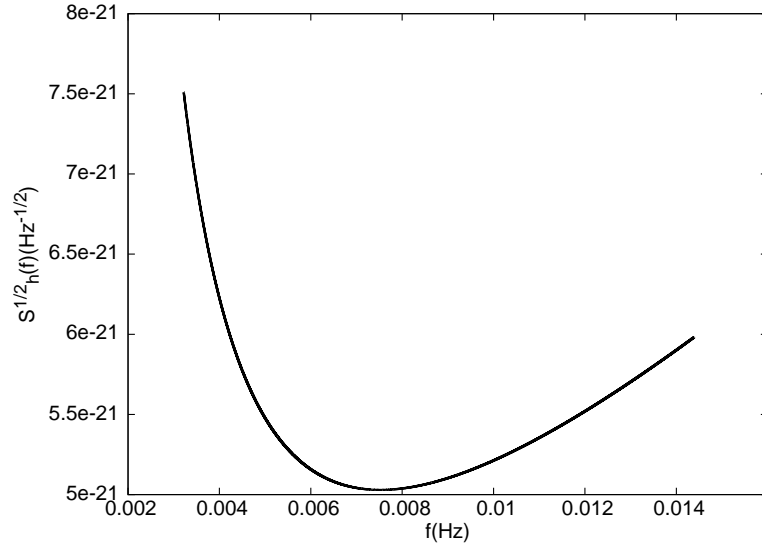


Figure 2.4: Total LISA noise curve, which includes instrumental noise, confusion noise from short-period galactic binaries, and confusion noise from extragalactic WD binaries, for BH inspirals into SMBHs during the last year before plunge.

2.5 Parameter estimation error results

To estimate noise-induced errors, I fixed the values of the intrinsic parameters of the source, and carried out a Monte Carlo simulation over values of the extrinsic parameters using the inverse FM. The error estimate is SNR dependent, but I quote results at fixed SNR= 30. I first compute the FM for a source at $D = 1\text{Gpc}$, and the corresponding SNR from the expression

$$\text{SNR}^2 = 2 \sum_{\alpha=I,II} \int_{t_{\text{init}}}^{t_{\text{LSO}}} \hat{h}_{\alpha}^2(t) dt. \quad (2.69)$$

I then multiply the errors from the inverse FM by $(\text{SNR}/30)$ to normalise to SNR= 30. I considered one year observations and chose the initial radial coordinate, p_0 , such that the compact object would reach the last stable orbit after one year of inspiral. The FM has ten dimensions. Four of these are intrinsic parameters, namely $\ln m, \ln M, q, p_0$. The other six are extrinsic or phase parameters. The physical meaning of the parameters is summarized in Table 2.2.

For these Monte Carlo simulations, I used the \dot{L}_z expression, Eq. (2.11), including Teukolsky fits to compute the inspiral trajectory $r(t)$, and took $\dot{\phi}(t)$ as a function of r from Eq. (2.14), including the conservative corrections. In this way, I included lower order effects as accurately as possible as discussed earlier.

The results of the Monte Carlo simulations are summarized in Tables 2.3, 2.4 and 2.5. I considered “typical” systems with $M = 10^6 M_{\odot}$, $q = 0.9$ and three different values of $m = 0.6M_{\odot}, 1.4M_{\odot}, 10M_{\odot}$ to represent inspirals of WDs, NSs and BHs, respectively. For comparison to the SF, I also considered a case with $q = 0$, for which I also ignored q as a parameter in the FM. The tables list the mean, standard deviation, median, lower and upper quartiles of the distribution of FM errors computed in the Monte Carlo simulation. In Figure 2.5 I show sample histograms of the FM errors in the intrinsic parameters computed from the Monte Carlo simulation for the $m = 10M_{\odot}$ system.

For the $m = 10M_{\odot}$ case I also carried out Monte Carlo simulations with (a) \dot{L}_z truncated at 2PN order, which did not significantly affect the results for the $q = 0$ case, but made the $q = 0.9$ errors greater by about an order of magnitude; and (b) p evolved directly via the 2PN expression, Eq. (2.13), rather than evolving L_z , which made the errors for the $q = 0$ case about an order of magnitude greater, but which did not significantly change the $q = 0.9$ results.

The Tables show estimates for the noise-induced parameter errors if the last year of inspiral is observed. However, LISA may observe a binary system in various stages

2. Influence of conservative corrections on signal detection and parameter estimation for EMRIs

$\ln m$	mass of CO
$\ln M$	mass of SMBH
q	magnitude of (specific) spin angular momentum of SMBH
p_0	Initial radius of CO orbit
ϕ_0	Initial phase of CO orbit
θ_S	source sky colatitude in an ecliptic-based system
ϕ_S	source sky azimuth in an ecliptic-based system
θ_K	direction of SMBH spin (colatitude)
ϕ_K	direction of SMBH spin (azimuth)
$\ln D$	distance to source

Table 2.2: This table describes the meaning of the parameters used in our model. The angles (θ_S, ϕ_S) and (θ_K, ϕ_K) are defined in a fixed ecliptic-based coordinate system.

Model		Statistics of distribution of $\log_{10}(\Delta X)$ for error, ΔX , in parameter $X =$									
		$\ln m$	$\ln M$	q	p_0	ϕ_0	θ_S	ϕ_S	θ_K	ϕ_K	$\ln D$
Kludge ($q=0.9$)	Mean	-4.04	-3.73	-4.53	-3.88	-0.99	-1.63	-1.74	-1.15	-1.03	-1.58
	St. Dev.	0.121	0.125	0.129	0.125	0.470	0.171	0.209	0.458	0.459	0.391
	L. Qt.	-4.14	-3.82	-4.60	-3.96	-1.35	-1.76	-1.90	-1.53	-1.42	-1.85
	Med.	-4.04	-3.72	-4.52	-3.87	-1.17	-1.63	-1.76	-1.27	-1.14	-1.72
	U. Qt.	-3.94	-3.63	-4.43	-3.77	-0.68	-1.50	-1.65	-0.81	-0.70	-1.41
Self- Force ($q=0$)	Mean	-4.37	-4.79	N/A	-4.96	-0.70	-1.57	-1.64	-0.90	-0.76	-1.26
	St. Dev.	0.128	0.124	N/A	0.124	0.904	0.136	0.204	0.770	0.783	0.407
	L. Qt.	-4.44	-4.85	N/A	-5.02	-1.33	-1.66	-1.78	-1.48	-1.35	-1.54
	Med.	-4.34	-4.77	N/A	-4.94	-1.05	-1.54	-1.66	-1.13	-0.95	-1.40
	U. Qt.	-4.27	-4.69	N/A	-4.86	-0.36	-1.45	-1.55	-0.54	-0.41	-1.12

Table 2.3: Summary of Monte Carlo over FM errors for BH systems ($m = 10M_\odot$). The Table shows the mean, standard deviation, median and quartiles of the distribution of the logarithm to base ten of the error in each parameter. Results are given both for the kludge model (with conservative corrections to 1.5PN order) and for the SF model, as indicated. The angles $\bar{\phi}_0$ and $\bar{\alpha}_0$, specifying LISA's position and orientation at $t = 0$, are set to zero.

of evolution. Figures 2.6 and 2.7 show how the error estimates vary as a function of the time remaining until plunge at the start of the observation. These results assume a one year LISA observation with fixed parameters $m = 10M_\odot$, $M = 10^6M_\odot$, $q = 0.9$, $\Phi_0 = 0$, $\theta_S = \pi/4$, $\phi_S = 0$, $\theta_K = \pi/8$, $\phi_K = 0$. The results are presented in two ways, (1) the distance to the source is adjusted to keep the total SNR= 30 over the observation; (2) the distance to the source is fixed and chosen so that the SNR= 30 over a one year observation starting one year before plunge.

The results for BH systems, $m = 10M_\odot$, are broadly consistent with existing results in the literature [6]. Typically, an EMRI observation can determine the CO and SMBH masses and the SMBH spin within fractional errors of $\sim 10^{-4}$, $10^{-3.5}$ and $10^{-4.5}$, respectively. LISA observations may also determine the location of the source in the sky to within 10^{-3} steradians, and determine the SMBH spin orientation to within $10^{-3.5}$,

2. Influence of conservative corrections on signal detection and parameter estimation for EMRIs

Model		Statistics of distribution of $\log_{10}(\Delta X)$ for error, ΔX , in parameter $X =$									
		$\ln m$	$\ln M$	q	p_0	ϕ_0	θ_S	ϕ_S	θ_K	ϕ_K	$\ln D$
Kludge ($q=0.9$)	Mean	-4.60	-3.94	-4.59	-4.06	-0.75	-1.71	-1.88	-0.96	-0.82	-0.92
	St. Dev.	0.109	0.118	0.122	0.118	0.882	0.199	0.212	0.766	0.797	0.399
	L. Qt.	-4.70	-4.02	-4.65	-4.14	-1.36	-1.87	-2.03	-1.56	-1.40	-1.19
	Med.	-4.61	-3.94	-4.58	-4.05	-1.09	-1.71	-1.89	-1.19	-1.03	-1.06
	U. Qt.	-4.52	-3.85	-4.49	-3.97	-0.42	-1.54	-1.77	-0.60	-0.45	-0.79
Self Force ($q=0$)	Mean	-4.12	-4.87	N/A	-5.06	-0.76	-1.63	-1.71	-0.94	-0.80	-0.62
	St. Dev.	0.136	0.130	N/A	0.131	0.852	0.155	0.217	0.731	0.767	0.379
	L. Qt.	-4.19	-4.95	N/A	-5.13	-1.37	-1.74	-1.86	-1.52	-1.40	-0.88
	Med.	-4.10	-4.86	N/A	-5.04	-1.08	-1.61	-1.73	-1.17	-1.01	-0.76
	U. Qt.	-4.02	-4.78	N/A	-4.96	-0.41	-1.49	-1.62	-0.58	-0.40	-0.48

Table 2.4: As Table 2.3, but for neutron star inspirals ($m = 1.4M_\odot$).

Model		Statistics of distribution of $\log_{10}(\Delta X)$ for error, ΔX , in parameter $X =$									
		$\ln m$	$\ln M$	q	p_0	ϕ_0	θ_S	ϕ_S	θ_K	ϕ_K	$\ln D$
Kludge ($q=0.9$)	Mean	-4.78	-3.93	-4.52	-4.03	-0.73	-1.74	-1.88	-0.94	-0.80	-0.57
	St. Dev.	0.119	0.182	0.195	0.182	0.892	0.211	0.228	0.781	0.813	0.410
	L. Qt.	-4.82	-4.00	-4.57	-4.10	-1.36	-1.89	-2.04	-1.56	-1.43	-0.85
	Med.	-4.76	-3.91	-4.49	-4.01	-1.07	-1.74	-1.90	-1.15	-1.01	-0.71
	U. Qt.	-4.70	-3.83	-4.41	-3.93	-0.36	-1.56	-1.77	-0.55	-0.41	-0.43
Self Force ($q=0$)	Mean	-3.99	-4.90	N/A	-5.08	-0.70	-1.64	-1.74	-0.90	-0.77	-0.26
	St. Dev.	0.139	0.132	N/A	0.133	0.928	0.157	0.196	0.799	0.819	0.424
	L. Qt.	-4.05	-4.98	N/A	-5.16	-1.37	-1.76	-1.89	-1.52	-1.39	-0.56
	Med.	-3.96	-4.88	N/A	-5.06	-1.05	-1.63	-1.74	-1.13	-0.98	-0.42
	U. Qt.	-3.88	-4.80	N/A	-4.98	-0.29	-1.51	-1.64	-0.48	-0.36	-0.11

Table 2.5: As Table 2.3, but for WD inspirals ($m = 0.6M_\odot$).

steradians. However, these results are based on a different waveform model. The model I have used in these studies is based on true geodesics of the Kerr space-time, so among other things it renders a more accurate frequency at plunge. The various other modifications, such as the inclusion of the conservative SF corrections, hopefully means this model is providing reliable and independent error estimates. One thing that is significantly different in these results is the estimate of LISA's ability to determine parameters for the NS and WD systems. The error estimates for these systems are even smaller than those for the BHs. The improvement arises because, by evolving L_z rather than p , the approach to the innermost stable circular orbit (ISCO) shows the proper rapid change in p , which carries more information about the intrinsic parameters. This rapid inspiral to ISCO is missed in PN evolutions. In a sense, these results are optimistic as, given the event rate [60], one is unlikely to observe such systems in the last year before plunge, and the SNR is likely to be lower, while I have normalised all results to SNR= 30. These results are nonetheless interesting.

In the Monte Carlo simulations that used an evolution of p instead of L_z (case (b))

2. Influence of conservative corrections on signal detection and parameter estimation for EMRIs

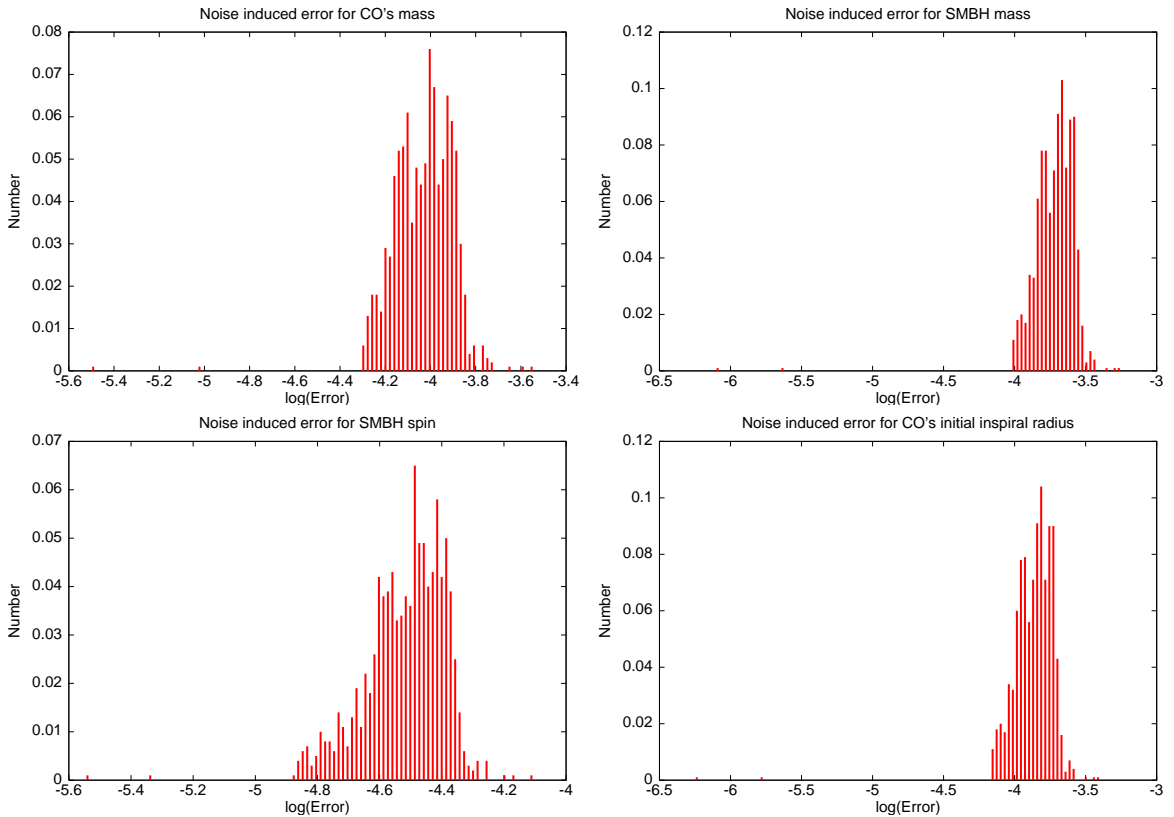


Figure 2.5: Distributions of errors in the intrinsic parameters as computed from the Monte Carlo simulations of the inverse FM. The Figure shows the system with $m = 10M_{\odot}$, $M = 10^6 M_{\odot}$, $q = 0.9$ and show the errors in $\ln(m)$, $\ln(M)$, $\ln(q)$ and $\ln(p_0)$ respectively.

mentioned above), I found results that were close to the ones quoted here and were also in good agreement with the results obtained by Barack and Cutler’s [6]. However, there were subtle differences. In particular, the distribution of the errors, cf., Figure 2.5, is much broader when using the 2PN p evolution. In addition, the error estimate for the SMBH spin is an order of magnitude worse using the 2PN p evolution.

These various results provide reassurance that the estimates from the kludge model and those by Barack & Cutler [6], may provide a fair reflection of what will be achieved in practice with LISA. My Monte Carlo results are also the first of their kind for the EMRI problem to appear in the literature and illustrate the spread in errors that arise from randomisation of the extrinsic source parameters. The variation in the parameter determination accuracy as a function of time remaining until plunge indicates that the accuracy of determination of the intrinsic parameters depends significantly on which part of the inspiral is observed, while the determination of the extrinsic parameters

2. Influence of conservative corrections on signal detection and parameter estimation for EMRIs

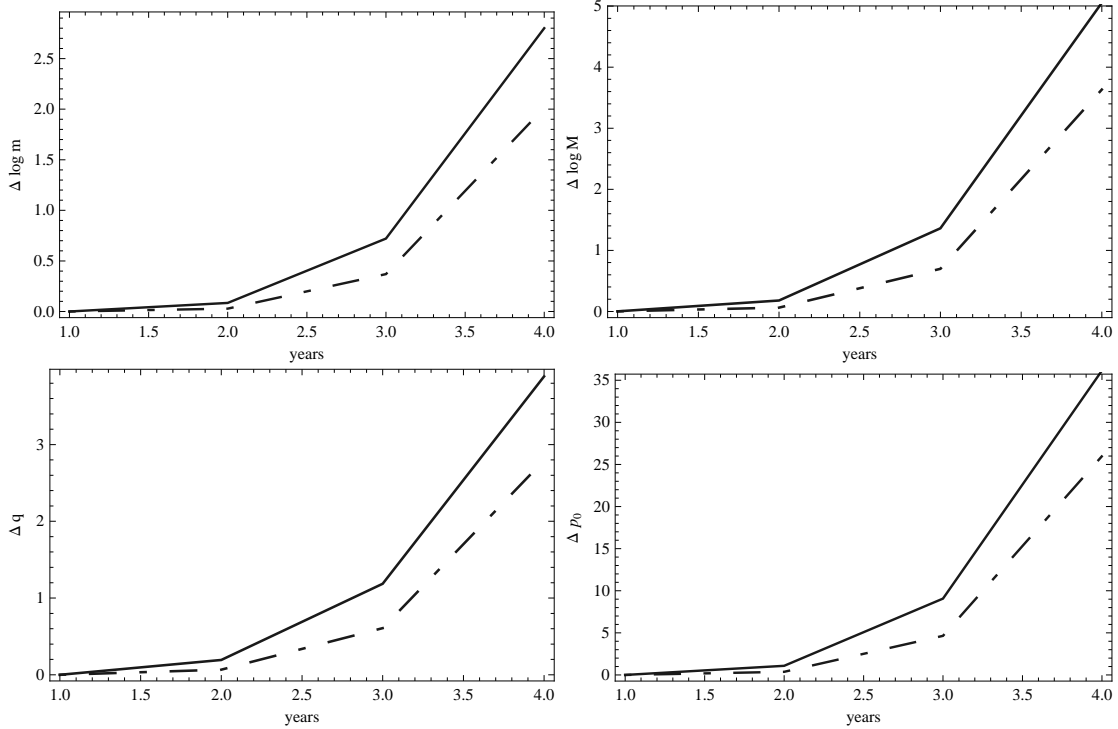


Figure 2.6: Plots of noise-induced errors in a one year observation as a function of time remaining until plunge at the start of the observation. Two cases are illustrated, namely (1) the distance to the source is normalized by means of weighting the noise errors by a factor of $\text{SNR}/30$ (solid line), (2) the distance to the source is fixed as in (1) but only for the last year before plunge (dot-dash line). The plots correspond to a $10M_{\odot}$ CO orbiting around a 10^6M_{\odot} SMBH with spin parameter $q = 0.9$. The various extrinsic parameters have been set as follows: $\Phi_0 = 0$, $\theta_S = \pi/4$, $\phi_S = 0$, $\theta_K = \pi/8$, $\phi_K = 0$. These four plots show the errors in the intrinsic parameters.

2. Influence of conservative corrections on signal detection and parameter estimation for EMRIs

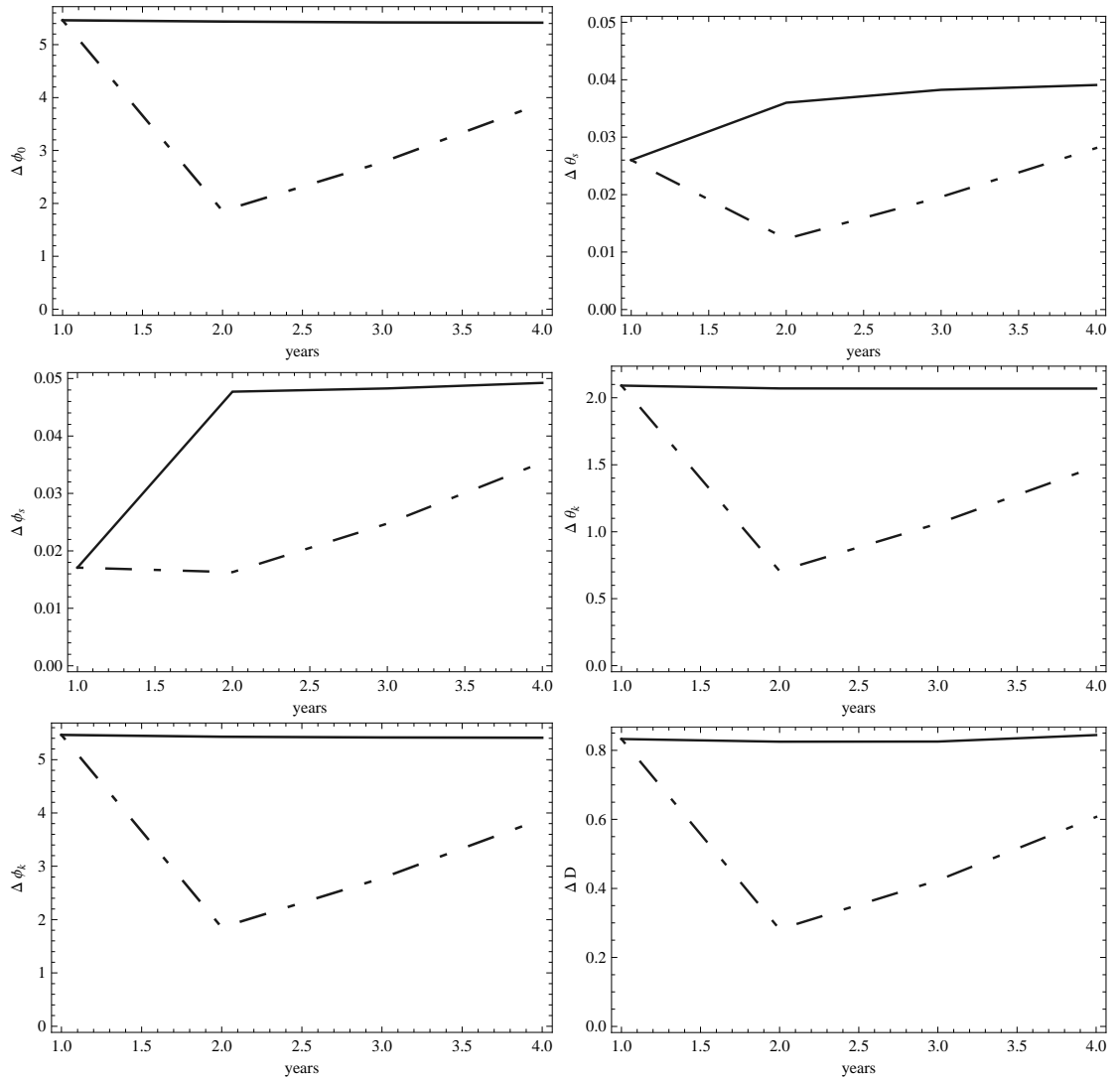


Figure 2.7: Same as in Figure 2.6, but for extrinsic parameters.

is equally good no matter which part of the inspiral is detected. This makes sense, as most of the orbital evolution takes place during the last year of inspiral and so the signature of the intrinsic parameters is most strongly present there. In contrast, the determination of the extrinsic parameters, such as the position in the sky and orientation of the SMBH spin, comes primarily from the modulations induced in the waveform by the detector motion, and so do not change significantly provided a full year of inspiral is observed.

2.6 Model-induced parameter errors

The FM gives an estimate of the errors that arise due to noise in the detector. But that is not the only source of error. The kludge I have built is only approximate, and hence the kludge waveform that is the best-fit to the data may have different parameters to the true waveform, introducing another parameter error. These errors are referred to as “model errors”. Cutler and Vallisneri [35] developed a framework to estimate the magnitude of these errors. The scheme relies on knowing what the “true” signal is, which at present is beyond one’s knowledge. However, one can use this formalism to assess the importance of the various terms that have been included in the waveform model. In this section, I look specifically at what effect ignoring the conservative SF corrections will have on parameter determination.

The noise error scales as $1/\text{SNR}$ (cf. (2.63)), but the model errors are independent of SNR. Therefore, it might be the case that for the EMRI systems with highest SNR, theoretical errors could dominate the total parameter-estimation error. In general, if crossing a term out in the model gives rise to a parameter error that is comparable to or smaller than the noise-induced error, then one can safely ignore that term in the search template. Because I want to estimate theoretically what error would result from omitting conservative corrections from the waveform model, or by using a model with incomplete conservative corrections, I will take the “true” waveform, h_{GR} , to be the kludge waveform including all conservative pieces, and then I will search for h_{GR} using approximate templates, h_{AP} , that include none or only part of the conservative corrections.

In order to ensure a self-contained presentation of the material, I briefly sketch the Cutler and Vallisneri model error formalism [35].

Consider two manifolds embedded in the vector spaces of data streams. One of them is covered by the true waveforms $\{h_{\text{GR}}(\theta^i)\}$, and the other one by the approximate waveforms $\{h_{\text{AP}}(\theta^i)\}$. Given a signal $\mathbf{s} = \mathbf{h}_{\text{GR}}(\hat{\theta}^i) + \mathbf{n}$, the best fit θ^i is determined by

2. Influence of conservative corrections on signal detection and parameter estimation for EMRIs

the condition

$$\left(\partial_j \mathbf{h}_{\text{AP}}(\theta^i) \Big|_{\mathbf{s} - \mathbf{h}_{\text{AP}}(\theta^i)}\right) = 0. \quad (2.70)$$

Furthermore, at first order in the error $\Delta\theta^i(\mathbf{n}) \equiv \theta^i(\mathbf{n}) - \hat{\theta}^i$, Eq. (2.70) takes the form

$$\Delta\theta^i = \left(\Gamma^{-1}(\theta)\right)^{ij} \left(\partial_j \mathbf{h}_{\text{AP}}(\theta) \Big|_{\mathbf{n}}\right) + \left(\Gamma^{-1}(\theta)\right)^{ij} \left(\partial_j \mathbf{h}_{\text{AP}}(\theta) \Big|_{\mathbf{h}_{\text{GR}}(\hat{\theta}) - \mathbf{h}_{\text{AP}}(\hat{\theta})}\right), \quad (2.71)$$

where the Fisher matrix is evaluated using the approximate waveforms

$$\Gamma_{ij}(\theta) \equiv (\partial_i \mathbf{h}_{\text{AP}}(\theta) | \partial_j \mathbf{h}_{\text{AP}}(\theta)).$$

Relation (2.71) clearly shows that, at leading order, $\Delta\theta^i$ is the sum of two contributions. The first one is due to noise in the detector, $\Delta_n\theta^i$, whereas the second one, $\Delta_{\text{th}}\theta^i$, is the contribution due to the inaccurate waveform. These are given, respectively, by

$$\Delta_n\theta^i = \left(\Gamma^{-1}(\theta)\right)^{ij} \left(\partial_j \mathbf{h}_{\text{AP}}(\theta) \Big|_{\mathbf{n}}\right), \quad \Delta_{\text{th}}\theta^i = \left(\Gamma^{-1}(\theta)\right)^{ij} \left(\partial_j \mathbf{h}_{\text{AP}}(\theta) \Big|_{\mathbf{h}_{\text{GR}}(\hat{\theta}) - \mathbf{h}_{\text{AP}}(\hat{\theta})}\right). \quad (2.72)$$

If one knew both $\hat{\theta}$ and the noise realization \mathbf{n} , then these equations would allow the determination of θ . However, experimentally one is only able to determine the $\mathbf{h}_{\text{AP}}(\theta)$ that is the best fit waveform for a given data stream, \mathbf{s} , and one is unsure about the error $\Delta\theta \equiv \theta - \hat{\theta}$. In addition, one does not know $\hat{\theta}$ in Eq. (2.72). At leading order, one can replace, $\mathbf{h}_{\text{GR}}(\hat{\theta}) - \mathbf{h}_{\text{AP}}(\hat{\theta})$ by $\mathbf{h}_{\text{GR}}(\theta) - \mathbf{h}_{\text{AP}}(\theta)$, obtaining

$$\Delta_{\text{th}}\theta^i = \left(\Gamma^{-1}(\theta)\right)^{ij} \left(\partial_j \mathbf{h}_{\text{AP}}(\theta) \Big|_{\mathbf{h}_{\text{GR}}(\theta) - \mathbf{h}_{\text{AP}}(\theta)}\right). \quad (2.73)$$

This relation is both noise and SNR independent. This property, along with the fact that $\Delta_{\text{th}}\theta^i$ is not averaged out if the same event is measured by a large number of nearly identical detectors leads one to consider $\Delta_{\text{th}}\theta^i$ as a systematic error.

Cutler and Vallisneri [35] found that the leading order approximation, Eq. (2.73), was not very good, unless the waveform is re-written in an amplitude-phase form

$$\tilde{h}^\alpha(f) = A^\alpha(f) e^{i\Psi^\alpha(f)}. \quad (2.74)$$

The amplitude A and phase Ψ are given by

$$A_I = \frac{\sqrt{3}m}{2D} \sqrt{A_+^2 F_{I,+}^2 + A_\times^2 F_{I,\times}^2}, \quad \Psi_I = 2\phi + \psi_I, \quad (2.75)$$

$$A_{II} = \frac{\sqrt{3}m}{2D} \sqrt{A_+^2 F_{II,+}^2 + A_\times^2 F_{II,\times}^2}, \quad \Psi_{II} = 2\phi + \psi_{II}, \quad (2.76)$$

2. Influence of conservative corrections on signal detection and parameter estimation for EMRIs

where $A_{+, \times}$ are given by (2.50) with $A_+ = A_\times = 2p^2 \dot{\phi}^2$, $F_{\{I, II; +, \times\}}$ are given by (2.51) and (2.52), and the other various quantities are given by

$$\psi_I = \arctan\left(-\frac{A_\times F_{I, \times}}{A_+ F_{I, +}}\right), \quad \psi_{II} = \arctan\left(-\frac{A_\times F_{II, \times}}{A_+ F_{II, +}}\right). \quad (2.77)$$

The first order approximation to this expression

$$\Delta_{\text{th}} \theta^i \approx (\Gamma^{-1}(\theta))^{ij} \left(\underbrace{[\Delta \mathbf{A} + i \mathbf{A} \Delta \Psi] e^{i\Psi}}_{\text{at } \theta} \Big| \partial_j \mathbf{h}_{\text{AP}}(\theta) \right), \quad (2.78)$$

was found to give reliable results when compared to more accurately computed error estimates [35], so I use this form again here. Equation (2.78) behaves better than Eq. (2.73) since the difference between two waveforms, $\mathbf{h}_{\text{AP}}(\theta) - \mathbf{h}_{\text{AP}}(\hat{\theta})$, is not very well approximated by the first term in its Taylor expansion. The differences in both the amplitude and phase of the waveform are individually well approximated by the linear terms in the Taylor series [35]. In fact, (2.73) is reliable only as long as the phase difference between the two waveforms is much less than one radian, i.e. $\Delta \theta^j \partial_j \Psi_{\text{AP}}(\theta) \ll 1$, whereas for (2.78) one just requires $\Delta \theta^i \Delta \theta^j \partial_i \partial_j \Psi_{\text{AP}}(\theta) \ll 1$. This condition is much less restrictive than the former one.

In the following analysis, I use equation (2.78) to estimate the magnitude of the parameter errors that arise from inaccuracies in the template waveform. At present, accurate waveforms including all first order conservative SF corrections are not known. But, I can estimate how relevant these corrections are for parameter estimation by turning them on and off from my kludge waveform template. This will allow me to compute the ratio \mathcal{R} of the model error to the noise-induced errors that arises from omitting the conservative part of the SF for each of the 10 parameters in the model. This ratio \mathcal{R} will shed light on the importance of the conservative corrections for parameter determination. If $\mathcal{R} \lesssim 1$, then the estimates obtained from a model that ignores the conservative piece should still be reliable, but if $\mathcal{R} \gg 1$ then it is clear that the model errors will be a limiting factor to accurately measure the parameters of the source. The ratio of parameter errors to FM errors obtained from a Monte Carlo simulation are summarized in Tables 2.6, 2.7 and 2.8. As before I have evaluated these model-induced parameter errors using expression (2.12) to evolve p , and using the full Teukolsky fit expression for \dot{L}_z , Eq. (2.11). I have also done Monte Carlo simulations with \dot{L}_z truncated at 2PN order, and evolving p at 2PN order directly using Eq. (2.13). The results were largely consistent between all three simulations.

2. Influence of conservative corrections on signal detection and parameter estimation for EMRIs

I quote results for the same three test systems considered previously, and consider five different comparisons — for the first two I took the “true” waveform to be the kludge waveform with 2PN conservative corrections, and took the template to be a kludge waveform with either no conservative corrections (“0PN”) or with conservative corrections to 1.5PN order (“1.5PN”); for the latter three comparisons I used the SF model in the three varieties listed in Table 2.1 — (1) $\delta\dot{L}_z = 0$ and all $\epsilon_i = 0$ in Eq. (2.37) (“1st order”); (2) $\delta\dot{L}_z = 0$ and the ϵ coefficients set to the values in Eqs. (2.38)–(2.39) (“incomplete”); (3) as (2) but now with $\delta\dot{L}_z$ from Eq. (2.40) (“2nd order”) — and did pairwise comparisons.

Model		Statistics of distribution of $\log_{10}(\Delta X)$ for error, ΔX , in parameter $X =$									
		$\ln m$	$\ln M$	q	p_0	ϕ_0	θ_S	ϕ_S	θ_K	ϕ_K	$\ln D$
Kludge 2PN vs 0PN	Mean	-0.50	-0.26	-0.31	-0.26	-0.28	-0.30	-0.37	-0.12	-0.09	-0.16
	St. Dev.	0.583	0.441	0.590	0.481	0.778	0.606	0.623	0.703	0.718	0.824
	L. Qt.	-0.85	-0.60	-0.70	-0.59	-0.54	-0.56	-0.61	-0.47	-0.46	-0.56
	Med.	-0.42	-0.15	-0.20	-0.15	-0.15	-0.16	-0.23	0.04	0.03	0.02
	U. Qt.	-0.09	0.17	0.11	0.19	0.16	0.10	0.09	0.38	0.36	0.43
Kludge 2PN vs 1.5PN	Mean	-0.70	-0.49	-0.47	-0.48	-0.42	-0.53	-0.62	-0.32	-0.27	-0.42
	St. Dev.	0.578	0.564	0.603	0.610	0.720	0.619	0.617	0.763	0.740	0.813
	L. Qt.	-0.98	-0.73	-0.77	-0.72	-0.65	-0.72	-0.83	-0.60	-0.51	-0.68
	Med.	-0.59	-0.35	-0.38	-0.37	-0.28	-0.35	-0.44	-0.19	-0.09	-0.17
	U. Qt.	-0.31	-0.02	-0.01	0.00	-0.01	-0.13	-0.15	0.14	0.20	0.16
Self Force “incomplete” vs “1st order”	Mean	-0.04	0.00	N/A	-0.13	-0.41	-0.60	-0.37	-0.38	-0.31	-0.67
	St. Dev.	0.455	0.454	N/A	0.454	0.454	0.594	0.523	0.553	0.610	0.572
	L. Qt.	-0.20	-0.16	N/A	-0.15	-0.65	-0.92	-0.74	-0.59	-0.49	-0.63
	Med.	0.09	0.06	N/A	0.05	-0.35	-0.48	-0.16	-0.29	-0.27	-0.54
	U. Qt.	0.23	0.28	N/A	0.27	-0.25	-0.25	0.00	-0.13	-0.11	-0.47
Self Force “2nd order” vs “1st order”	Mean	-0.15	-0.14	N/A	-0.16	-0.23	-0.26	-0.26	-0.05	-0.08	-0.05
	St. Dev.	0.446	0.489	N/A	0.485	0.735	0.375	0.521	0.678	0.639	0.681
	L. Qt.	-0.37	-0.44	N/A	-0.46	-0.63	-0.49	-0.47	-0.52	-0.60	-0.51
	Med.	-0.15	-0.11	N/A	-0.13	-0.11	-0.25	-0.07	0.02	0.00	-0.02
	U. Qt.	0.16	0.21	N/A	0.34	0.34	0.02	0.11	0.45	0.47	0.50
Self Force “2nd order” vs “incomplete”	Mean	0.11	0.08	N/A	0.04	0.13	0.14	0.06	0.28	0.33	0.22
	St. Dev.	0.553	0.619	N/A	0.625	0.747	0.531	0.639	0.705	0.717	0.863
	L. Qt.	-0.26	-0.30	N/A	-0.36	-0.26	-0.20	-0.37	-0.20	-0.17	-0.30
	Med.	0.17	0.08	N/A	0.09	0.20	0.16	0.21	0.32	0.43	0.35
	U. Qt.	0.46	0.47	N/A	0.46	0.66	0.53	0.50	0.85	0.87	0.84

Table 2.6: Summary of Monte Carlo simulation results for the ratio of model errors to FM errors for BH systems ($m = 10M_\odot$) using the Teukolsky fit expression for dL_z/dt . The Tables shows the mean, standard deviation, median and quartiles of the distribution of the logarithm to base ten of the ratio for each parameter. Results are given for various comparisons, as indicated and described in the text. A comparison “A vs B” uses model A as the true waveform, and model B as the search template.

Figure 2.8 shows the full distribution of the error ratio, \mathcal{R} , for the intrinsic parameters, as computed from the Monte Carlo simulation. These are shown for the BH systems in the kludge 2PN vs 1.5PN comparison. These plots show that, in this par-

2. Influence of conservative corrections on signal detection and parameter estimation for EMRIs

Model		Statistics of distribution of $\log_{10}(\Delta X)$ for error, ΔX , in parameter $X =$									
		$\ln m$	$\ln M$	q	p_0	ϕ_0	θ_S	ϕ_S	θ_K	ϕ_K	$\ln D$
Kludge 2PN vs 0PN	Mean	-0.43	-0.35	-0.33	-0.36	-0.35	-0.33	-0.36	-0.23	-0.21	0.37
	St. Dev.	0.563	0.587	0.586	0.626	0.728	0.589	0.601	0.728	0.754	0.832
	L. Qt.	-0.75	-0.62	-0.60	-0.62	-0.59	-0.55	-0.58	-0.48	-0.44	0.05
	Med.	-0.30	-0.20	-0.19	-0.20	-0.19	-0.18	-0.20	-0.10	-0.04	0.57
	U. Qt.	-0.00	0.06	0.08	0.06	0.08	0.07	0.03	0.23	0.23	0.89
Kludge 2PN vs 1.5PN	Mean	-0.80	-0.67	-0.68	-0.68	-0.73	-0.68	-0.71	-0.57	-0.56	0.02
	St. Dev.	0.576	0.551	0.657	0.573	0.744	0.598	0.623	0.711	0.760	0.817
	L. Qt.	-1.09	-0.90	-0.88	-0.90	-0.98	-0.90	-0.91	-0.83	-0.77	-0.23
	Med.	-0.66	-0.53	-0.50	-0.54	-0.57	-0.51	-0.56	-0.43	-0.40	0.21
	U. Qt.	-0.37	-0.29	-0.28	-0.29	-0.31	-0.26	-0.33	-0.15	-0.12	0.52
Self Force “incomplete” vs “1st order”	Mean	-0.90	-0.84	N/A	-0.84	-1.02	-1.11	-1.08	-1.23	-1.19	-1.21
	St. Dev.	0.456	0.403	N/A	0.404	0.642	0.543	0.521	0.563	0.569	0.544
	L. Qt.	-1.06	-1.01	N/A	-1.03	-1.25	-1.37	-1.23	-1.41	-1.44	-1.32
	Med.	-0.85	-0.78	N/A	-0.82	-0.92	-1.08	-0.99	-1.17	-1.15	-1.16
	U. Qt.	-0.62	-0.58	N/A	-0.57	-0.69	-0.93	-0.81	-0.94	-0.95	-0.91
Self Force “2nd order” vs “1st order”	Mean	-0.95	-0.98	N/A	-0.99	-1.13	-1.37	-1.23	-1.90	-1.88	-1.76
	St. Dev.	0.556	0.557	N/A	0.584	0.680	0.571	0.507	0.672	0.614	0.580
	L. Qt.	-1.14	-1.07	N/A	-1.09	-1.47	-1.77	-1.48	-2.19	-2.27	-1.97
	Med.	-0.89	-0.94	N/A	-0.91	-1.04	-1.23	-1.19	-1.76	-1.75	-1.69
	U. Qt.	-0.73	-0.69	N/A	-0.79	-0.85	-0.89	-0.91	-1.41	-1.44	-1.42
Self Force “2nd order” vs “incomplete”	Mean	-0.76	-0.82	N/A	-0.84	-0.83	-0.84	-0.80	-0.66	-0.63	-0.69
	St. Dev.	0.434	0.603	N/A	0.626	0.697	0.572	0.634	0.716	0.732	0.803
	L. Qt.	-0.98	-1.20	N/A	-1.20	-1.19	-1.09	-1.10	-0.99	-0.92	-0.99
	Med.	-0.64	-0.70	N/A	-0.75	-0.73	-0.69	-0.66	-0.53	-0.47	-0.56
	U. Qt.	-0.39	-0.29	N/A	-0.38	-0.36	-0.48	-0.41	-0.16	-0.12	-0.21

Table 2.7: As Table 2.6, but for NS inspirals ($m = 1.4M_\odot$).

ticular case, the vast majority of sources fulfill the condition that the model errors are smaller than the noise induced errors. For those binary systems that do not fulfill this condition, the upper bound on the error ratio $\mathcal{R} \lesssim 3$. Tables 2.6, 2.7 and 2.8 indicate that, for both kludge model comparisons, the ratio $\mathcal{R} \lesssim 1$ for all parameters at most points in the parameter space for all three types of inspiral. In fact, for any of the model parameters, less than 0.15% of points in the Monte Carlo runs had $2 < \mathcal{R} < 3$. These results suggest that including conservative corrections is not essential for accurate parameter determination, but including them up to 2PN order will certainly reduce the model errors further.

Things are not so clear cut for the SF comparisons, however. For the NS and WD inspirals, the ratio $\mathcal{R} \lesssim 1$ for practically every element of the parameter space. In fact, for any parameter, less than 0.1% of points of the Monte Carlo runs satisfy $2 < \mathcal{R} < 3$. For BHs, the model errors appear generally larger, with ratios typically greater than 1 in the comparisons to the “2nd order” model that was built from the kludge. One thing that must be born in mind for these comparisons is that the kludge model was

2. Influence of conservative corrections on signal detection and parameter estimation for EMRIs

Model		Statistics of distribution of $\log_{10}(\Delta X)$ for error, ΔX , in parameter $X =$									
		$\ln m$	$\ln M$	q	p_0	ϕ_0	θ_S	ϕ_S	θ_K	ϕ_K	$\ln D$
Kludge 2PN vs 0PN	Mean	-0.37	-0.52	-0.52	-0.53	-0.55	-0.49	-0.52	-0.43	-0.39	0.17
	St. Dev.	0.526	0.589	0.661	0.614	0.782	0.657	0.643	0.786	0.772	0.878
	L. Qt.	-0.57	-0.72	-0.70	-0.73	-0.78	-0.69	-0.71	-0.65	-0.60	-0.07
	Med.	-0.22	-0.38	-0.36	-0.38	-0.38	-0.31	-0.35	-0.25	-0.22	0.41
	U. Qt.	0.00	-0.13	-0.12	-0.13	-0.11	-0.07	-0.12	0.03	0.06	0.71
Kludge 2PN vs 1.5PN	Mean	-0.71	-0.85	-0.86	-0.86	-0.96	-0.87	-0.86	-0.81	-0.79	-0.22
	St. Dev.	0.491	0.518	0.589	0.530	0.781	0.632	0.628	0.790	0.769	0.870
	L. Qt.	-0.88	-1.06	-1.05	-1.06	-1.20	-1.09	-1.00	-1.04	-1.00	-0.48
	Med.	-0.59	-0.76	-0.74	-0.76	-0.79	-0.70	-0.71	-0.65	-0.63	-0.01
	U. Qt.	-0.38	-0.49	-0.48	-0.49	-0.51	-0.46	-0.48	-0.33	-0.34	0.32
Self Force “incomplete” vs “1st order”	Mean	-1.27	-1.21	N/A	-1.22	-1.32	-1.34	-1.30	-1.19	-1.15	-1.22
	St. Dev.	0.596	0.586	N/A	0.591	0.797	0.608	0.601	0.792	0.720	0.773
	L. Qt.	-1.54	-1.57	N/A	-1.54	-1.62	-1.55	-1.52	-1.43	-1.42	-1.56
	Med.	-1.16	-1.13	N/A	-1.14	-1.19	-1.24	-1.16	-1.02	-1.05	-1.05
	U. Qt.	-0.83	-0.73	N/A	-0.74	-0.91	-0.93	-0.85	-0.70	-0.68	-0.61
Self Force “2nd order” vs “1st order”	Mean	-1.65	-1.55	N/A	-1.65	-2.19	-2.22	-2.12	-2.05	-2.02	-1.96
	St. Dev.	0.425	0.442	N/A	0.447	0.581	0.523	0.537	0.645	0.575	0.683
	L. Qt.	-1.79	-1.67	N/A	-1.79	-2.60	-2.57	-2.49	-2.47	-2.45	-2.25
	Med.	-1.59	-1.47	N/A	-1.55	-2.11	-2.07	-1.99	-1.94	-1.90	-1.99
	U. Qt.	-1.36	-1.30	N/A	-1.37	-1.61	-1.75	-1.66	-1.49	-1.58	-1.47
Self Force “2nd order” vs “incomplete”	Mean	-1.24	-1.31	N/A	-1.32	-1.34	-1.37	-1.33	-1.19	-1.14	-1.22
	St. Dev.	0.454	0.519	N/A	0.604	0.697	0.541	0.589	0.721	0.651	0.753
	L. Qt.	-1.45	-1.61	N/A	-1.61	-1.64	-1.58	-1.60	-1.47	-1.42	-1.54
	Med.	-1.19	-1.23	N/A	-1.26	-1.21	-1.26	-1.20	-1.05	-1.04	-1.06
	U. Qt.	-0.94	-0.85	N/A	-0.86	-0.94	-1.02	-0.90	-0.76	-0.74	-0.75

Table 2.8: As Table 2.6, but for WD inspirals ($m = 0.6M_\odot$).

constructed by comparison to a weak-field PN expansion, but I am now comparing it to fully accurate SF computations in the strong-field. Thus, the reason for the apparently larger discrepancy may be that the kludge model is not accurate enough in this regime. This was the reason why I also did the “incomplete” vs “1st order” comparisons for the SF models. These expressions do not use the kludge model, but are in the spirit of the other kludge comparisons in that I am crossing out the last term in the model and looking at what effect this has. These results show generally smaller errors, with more than 50% of points having $\mathcal{R} < 1$. The conclusion is that, in the worst case, a template that omits conservative corrections will identify parameters that are (conservatively) within 10 FM errors of the true parameters, and this region of parameter space can then be followed up using more accurate waveforms, if these are available. Furthermore, the kludge model with 2PN conservative corrections is a reasonably good approximation to the SF model, since although the ratios for those comparisons are larger, they are still manageably small.

The last two rows of the tables also indicate that it may be better to work con-

2. Influence of conservative corrections on signal detection and parameter estimation for EMRIs

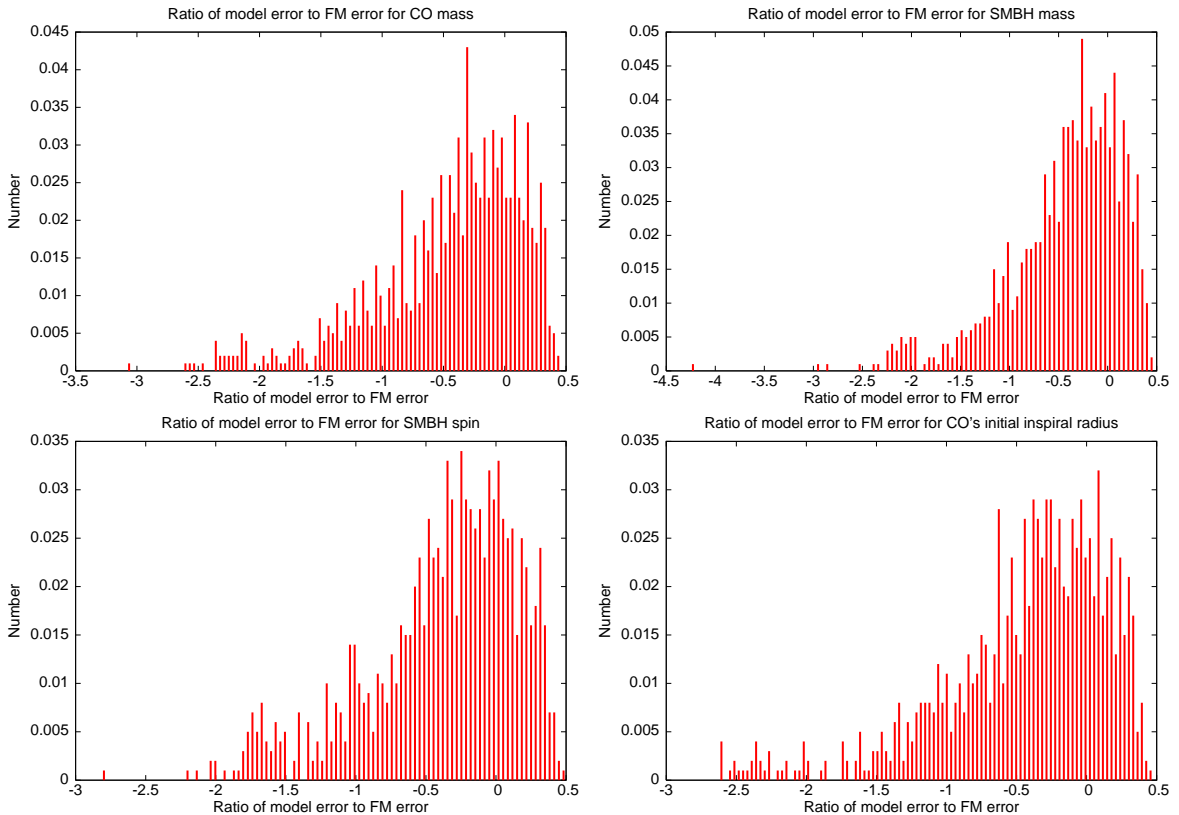


Figure 2.8: Distribution of the ratio of the model induced error to the noise induced FM error for the intrinsic parameters. This data is for the BH inspiral system ($m = 10M_{\odot}$) for the kludge 2PN vs 1.5PN comparison.

sistently to a certain order in mass ratio, rather than to include an incomplete term at higher order. The “incomplete” model includes second order in η corrections to the evolution of the orbital radius that arise from the first order conservative part of the SF, but not those that arise from the second order radiative part. The “1st order” model includes no second order corrections to the rate of change of radius. The tables indicate that the “1st order” model actually leads to smaller parameter errors (when searching for the kludge waveform) than the “incomplete” model, although the difference between the two cases is relatively small.

Another thing to point out, is that I have normalised all the results to $\text{SNR} = 30$. This is an estimate of the threshold SNR that will be required for EMRI detection [3], but nearby events may have SNR as high as several hundred [62]. For such systems, the noise induced errors will be smaller than those quoted here by a factor of $\text{SNR}/30$, while the model induced errors will be the same. Thus, for accurate parameter determination

2. Influence of conservative corrections on signal detection and parameter estimation for EMRIs

for the loudest sources LISA detects, these results suggest that it will almost certainly be necessary to include first-order conservative and, if possible, second-order radiative terms in the model.

Figures 2.9 and 2.10 show how the model and FM errors vary for a one year observation as a function of the time remaining until plunge at the start of the observation. This is for a BH inspiral, $m = 10M_\odot$, with the following fixed values of the extrinsic parameters, $\Phi_0 = 0, \theta_S = \pi/4, \phi_S = 0, \theta_K = \pi/8, \phi_K = 0$. In each plot, the noise errors are weighted by a factor $\text{SNR}/30$ to ensure the SNR is 30 over the one year observation.

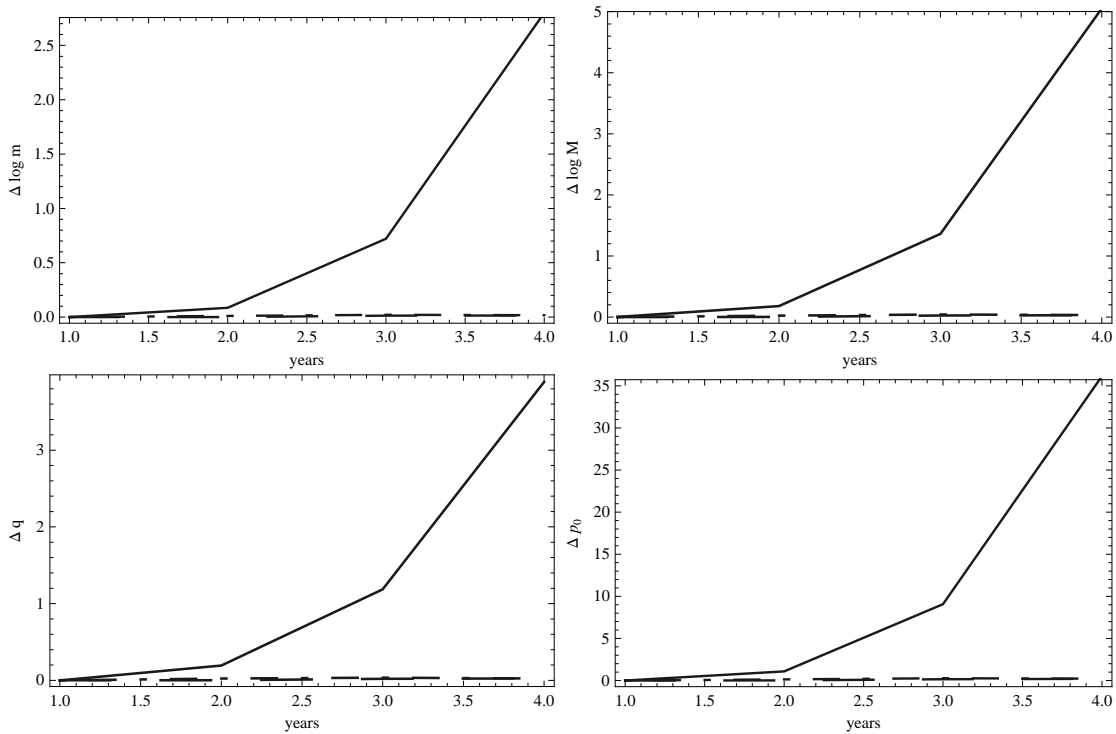


Figure 2.9: The panels show how the noise induced and model errors vary in a one year observation as a function of the time remaining until plunge at the start of the observation. I show noise induced errors (solid lines), and model errors for two cases, namely $(h_{\text{GR}}, h_{\text{AP}}) = (2\text{PN}, 0\text{PN})$ (dashed lines), and $(h_{\text{GR}}, h_{\text{AP}}) = (2\text{PN}, 1.5\text{PN})$ (dot-dash lines). This is for a $10M_\odot$ CO inspiralling into a 10^6M_\odot SMBH with spin parameter $q = 0.9$. The various extrinsic parameters have been set as follows: $\Phi_0 = 0, \theta_S = \pi/4, \phi_S = 0, \theta_K = \pi/8, \phi_K = 0$. The noise induced errors have been re-normalised to a signal to noise ratio of 30 over the year of observation. These four plots show the errors in the intrinsic parameters of the system.

2. Influence of conservative corrections on signal detection and parameter estimation for EMRIs

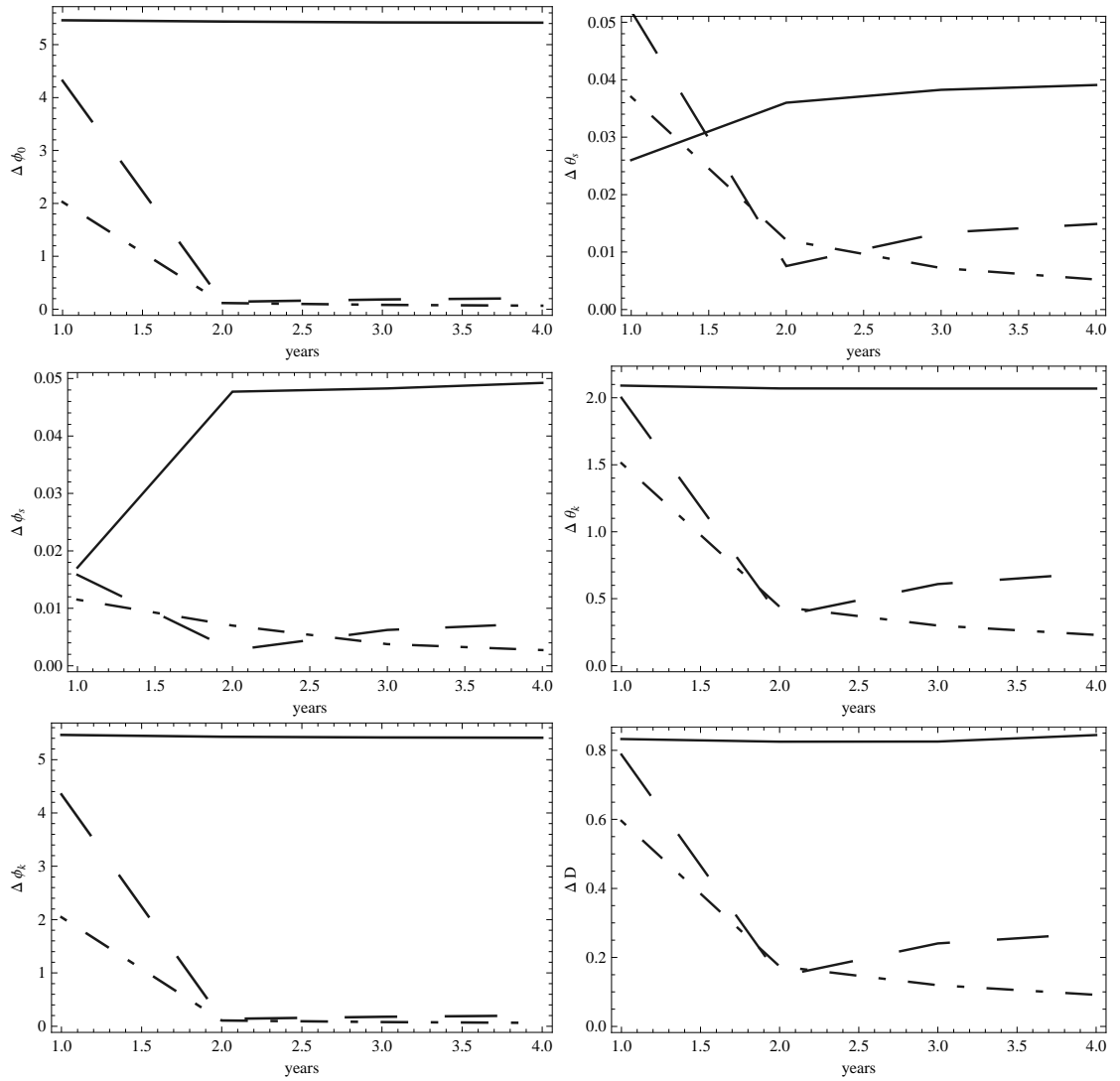


Figure 2.10: As Figure 2.9 but I now show the errors in the extrinsic parameters.

Figures 2.9 and 2.10 suggest that, for this typical source, (1) the noise induced errors in the intrinsic parameters increase quickly if one observes only an earlier part of the inspiral, while the model errors only increase by a small amount. Hence, one would only expect to be model-error dominated when observing the last year if at all; (2) noise and model errors for the extrinsic parameters do not change substantially as one varies the initial time; (3) the theoretical errors decrease as one includes more conservative corrections.

It is worth pointing out that the results quoted in Tables 2.6, 2.7, and 2.8 were obtained from Fisher Matrices which were nicely convergent over several orders of magnitude in the offset used to compute the numerical waveform derivatives. The noise-induced and model errors obtained from the inverses of these matrices also exhibited good convergent behaviour. This is a relevant observation as the matrices I have dealt with have very large condition numbers — the ratio of the largest to smallest eigenvalues. Typically, I found that using an LU decomposition, i.e., writing the FM as the product of a lower triangular matrix and an upper triangular matrix, the inverse Fisher matrices converged to $\lesssim 8\%$ over three orders of magnitude in the numerical offsets.

2.7 Conclusions

In this Chapter, I have introduced an improved kludge model of GW emission for circular-equatorial EMRIs, which includes conservative SF corrections up to 2PN order. I have also obtained a 2PN expression for $\dot{\Omega}$, which includes both the conservative SF at first order in η , and quadratic terms of the spin parameter q at 2PN order. Previous expressions included either conservative corrections [18], or quadratic terms of the spin parameter [124], but not both. This model indicates that the inclusion of conservative corrections has a relatively small impact on the waveform phasing, and so these corrections may not be essential for source detection. But, it will be useful to include them for parameter estimation. At this PN order, the model provides parameter determination accuracy estimates for BH inspiral systems, $m = 10M_{\odot}$, that are broadly consistent with previous results derived by Barack and Cutler [6]. For a typical source at SNR of 30, a LISA EMRI observation should be able to determine the CO and SMBH masses and the SMBH spin magnitude to within fractional errors of $\sim 10^{-4}$, $10^{-3.5}$ and $10^{-4.5}$, respectively. LISA may also be able to determine the location of the source in the sky, and the SMBH spin orientation to within $\sim 10^{-3}$ steradians. This improved model introduced here should be more reliable than the

PN model used in [6] to model the GW emission in the strong field regime. This is because the kludge model I have built is based on true Kerr geodesics, and also includes conservative corrections in a physically consistent way. Furthermore, I have computed the inspiral trajectory of the CO evolving its geodesic parameters using the most accurate prescription for the radiative flux of the angular momentum, \dot{L}_z . The fact that I get results that are consistent with those already available in the literature provides reassurance that both estimates will be a reasonable reflection of the precision that a detector like LISA will ultimately achieve. I have also obtained new results for NS and WD inspirals that indicate LISA will also be able to return highly accurate parameters for these systems, provided that the last year of inspiral is observed.

I have also studied in detail the importance of the first order conservative part and the second-order radiative part of the SF for parameter estimation accuracy using the formalism of Cutler and Vallisneri [35]. I have found that, for these sources, the model errors that arise from omitting these SF terms are generally smaller than the parameter errors that arise from instrumental noise when the source has SNR= 30. In the Monte Carlo simulations, no points had model-error to noise-error ratios $\mathcal{R} \gtrsim 3$, and less than 0.15% of the points in the Monte Carlo runs lay in the range $2 < \mathcal{R} < 3$.

I have also compared these results with recently published SF calculations, that include all first order terms, but nothing at higher order. This comparison allowed me to assess the relative importance of the first order conservative and second order radiative parts of the SF. I found that these affect the orbital evolution in the same way. Additionally, this exercise showed that the missing terms were not necessary for accurate parameter estimation for the inspirals of NSs or WDs. However, the results for the inspirals of BHs were less conclusive —model errors were typically a few times the expected parameter errors from instrumental noise. This could be attributed to the fact that I derived the kludge corrections by comparison to PN expressions in the weak field, and then used them to test the SF results in the strong field. Comparing the SF waveform to a truncated version of the same did indicate slightly smaller error ratios, although these were still somewhat bigger than in the calculations based entirely on the kludge waveforms.

These results are the first attempt to assess the necessity of including conservative corrections in templates for parameter estimation with LISA. They are not absolutely conclusive since they show neither that the model errors are always completely negligible nor that the model errors always overwhelm the errors from instrumental noise. Instead, I find that the two errors are generally comparable. This suggests that search templates can certainly ignore conservative corrections, but it may be necessary to

follow-up with more accurate templates to get more precise parameter estimates. The potential problem is that these results suggest that the second order radiative part of the SF may be as important as the first order conservative piece. Nonetheless, for all the cases I have considered, the model errors are only a few times the noise errors. This in turn implies that a) one will obtain good estimates of the source parameters, although quoted error bounds must allow for the model error; b) if more accurate templates are available, one will only need to use these (presumably computationally more expensive templates) in an area of parameter space approximately ten times the error box predicted by the FM.

The results presented in this Chapter are not the full story. I have only considered circular equatorial EMRIs. If non-standard EMRI channels operate efficiently, these may make up a significant fraction of LISA events [3]. However, it is expected that orbits will generically be both eccentric and inclined to the equatorial plane. Although I hope these results to be representative of the general case, this needs to be properly explored in the future to verify these conclusions in a more general context.

Chapter 3

The importance of including small body spin effects in the modelling of extreme and intermediate mass-ratio inspirals

3.1 Overview

In this Chapter I will study the ability of future low-frequency gravitational wave (GW) detectors to measure the spin of stellar mass and intermediate mass black holes (IMBHs) that inspiral into spinning super-massive black holes (SMBHs). To do this, I will present a kludge waveform model that includes the spin of the small body, using the equations of motion derived by Saijo et al. [117] for spinning black hole binaries, augmented with spin-orbit and spin-spin couplings taken from perturbative and PN calculations, and the associated conservative self-force (SF) corrections which are derived by comparison to post-Newtonian (PN) results. I model the inspiral phase using accurate fluxes which include perturbative corrections for the spin of the inspiralling body, spin-spin couplings and higher-order fits to solutions of the Teukolsky equation for inspirals of non-spinning objects. I present results of Monte Carlo simulations of the parameter estimation errors, computed using the Fisher Matrix formalism, and also the systematic errors that arise when the conservative corrections are omitted from the waveform template for the inspirals of spinning stellar mass and IMBHs into spinning SMBHs. The analysis shows that, for intermediate-mass-ratio inspirals (IMRIs) with mass ratios $\eta \gtrsim 10^{-3}$,

3. The importance of including small body spin effects in the modelling of EMRIs and IMRIs

GW observations will be able not only to provide a very accurate census of the mass and spin distributions of the central SMBHs, but could also yield accurate measurements for the mass and spin distributions of the inspiralling black holes. These studies also show that, for EMRIs with $\eta \sim 10^{-5}$, LISA observations will not be able to determine the spin magnitude of the inspiralling black hole, and the measurement of the other waveform parameters will not be significantly degraded by the presence of spin. Finally, I will show that the model errors which arise from ignoring conservative corrections become significant for mass-ratios above $\sim 10^{-4}$, but including these corrections up to second PN order may be sufficient to reduce the corresponding systematic errors to an acceptable level.

3.2 Kludge waveform with small body spin effects

The numerical kludge waveform model introduced in Chapter 2, and originally developed by Babak et al. [5], has been very successful as a model for the GW emission from EMRIs, as it is able to capture the main features of the inspiral waveform in the strong field regime.

This model has already been used to explore the accuracy with which LISA will be able to measure the parameters of Kerr circular equatorial EMRIs [72], and to estimate the importance of conservative and radiative SF corrections on parameter estimation and detection. In the kludge models to date, the spin of the stellar mass CO was ignored. For the purpose of providing a better theoretical template, and to find out under which circumstances the spin of the CO can be measured, in this section I will develop a new kludge model that incorporates this additional parameter.

To achieve this, I will augment the standard “numerical kludge” model using the equations of motion of a spinning particle in the equatorial plane ($\theta = \pi/2$) of a Kerr BH, as derived by Saijo et al. [117]. I will include small body spin corrections of two different natures: i) first-order conservative corrections to amend the orbital phase evolution, and; ii) second order radiative corrections in the fluxes of energy and angular momentum to evolve the geodesic parameters of the inspiralling object.

For a particle with spin angular momentum $\mathbf{S}_1 = s\mu\hat{\mathbf{z}}$, aligned with the central Kerr BH spin ($\mathbf{S}_2 = aM\hat{\mathbf{z}}$) and the orbital angular momentum L_z , the spin vectors remain constant and the equations of motion take a form similar to the Kerr geodesic equations, namely, [117],

3. The importance of including small body spin effects in the modelling of EMRIs and IMRIs

$$\Sigma_s \Lambda_s \frac{dt}{d\tau} = a \left(1 + \frac{3Ms^2}{p\Sigma_s} \right) [\tilde{J}_z - (a+s)\tilde{E}] + \frac{p^2 + a^2}{\Delta} P_s, \quad (3.1)$$

$$\Sigma_s \Lambda_s \frac{d\varphi}{d\tau} = \left(1 + \frac{3Ms^2}{p\Sigma_s} \right) [\tilde{J}_z - (a+s)\tilde{E}] + \frac{a}{\Delta} P_s, \quad (3.2)$$

$$\Sigma_s \Lambda_s \frac{dp}{d\tau} = \pm \sqrt{R_s}, \quad (3.3)$$

where

$$\begin{aligned} \Sigma_s &= p^2 \left(1 - \frac{Ms^2}{p^3} \right), \\ \Lambda_s &= 1 - \frac{3Ms^2 p [\tilde{J}_z - (a+s)\tilde{E}]^2}{\Sigma_s^3}, \\ R_s &= P_s^2 - \Delta \left\{ \frac{\Sigma_s^2}{p^2} + [\tilde{J}_z - (a+s)\tilde{E}]^2 \right\}, \\ P_s &= \left[(p^2 + a^2) + as \left(1 + \frac{M}{p} \right) \right] \tilde{E} - \left(a + s \frac{M}{p} \right) \tilde{J}_z, \\ \Delta &= p^2 - 2Mp + a^2, \end{aligned} \quad (3.4)$$

and (t, p, θ, φ) are Boyer-Lindquist coordinates, τ is the particle's proper time, and $\tilde{E} \equiv E/\mu$ and $\tilde{J}_z \equiv J_z/\mu$ are the conserved energy and total angular momentum, respectively (see Eqs. (2.10) of [117]). The radial motion of the spinning particle can be understood by re-writing the function R_s in the form

$$R_s = B(p)[\tilde{E} - \tilde{E}_1(p, \tilde{J}_z)][\tilde{E} - \tilde{E}_2(p, \tilde{J}_z)], \quad (3.5)$$

where the roots $\tilde{E}_{1,2}$ of $R_s = 0$ are found by solving

$$\alpha \tilde{E}^2 - 2\beta \tilde{E} + \gamma = 0, \quad \text{with} \quad (3.6)$$

$$\begin{aligned} \alpha &= \left[(p^2 + a^2) + as \left(1 + \frac{M}{p} \right) \right]^2 - \Delta(a+s)^2, \\ \beta &= \left\{ \left(a + s \frac{M}{p} \right) \left[(p^2 + a^2) + as \left(1 + \frac{M}{p} \right) \right] - \Delta(a+s) \right\} \tilde{J}_z, \\ \gamma &= \left(a + s \frac{M}{p} \right)^2 \tilde{J}_z^2 - \Delta \left[p^2 \left(1 - \frac{Ms^2}{p^3} \right)^2 + \tilde{J}_z^2 \right]. \end{aligned} \quad (3.7)$$

3. The importance of including small body spin effects in the modelling of EMRIs and IMRIs

The effective potential is defined as the minimum allowed value of the particle energy at radius p and so Eq. (3.6) implies,

$$V_{\text{eff}} = \frac{\beta + \sqrt{\beta^2 - \alpha\gamma}}{\alpha}. \quad (3.8)$$

Note that I have taken the positive square root to ensure that the specific particle's energy $\tilde{E} \rightarrow \infty$ when $r \rightarrow \infty$.

One can now derive the expressions for the energy and angular momentum of a spinning particle, following a circular equatorial orbit by ensuring that the function $R_s(p)$, and its radial gradient, $R'_s(p)$, vanish at the same point.

The equations of motion derived by Saijo et al. [117] are valid only to linear order in the spin of the small body so I shall quote the expressions for the energy and angular momentum of the spinning particle at the same order, namely,

$$\begin{aligned} \frac{E}{\mu} &= \frac{r^2 - 2r \pm (q + \hat{s}/r)\sqrt{r + 3q\hat{s}/r} - 5q\hat{s}/2r}{r\sqrt{r^2 - 3r \pm (2q + \frac{3\hat{s}}{r})\sqrt{r + 3q\hat{s}/r} - 6q\hat{s}/r}}, \\ \frac{L_z}{\mu M} &= \frac{\pm\sqrt{r + 3q\hat{s}/r}(r^2 + q^2 + q\hat{s}(r+1)/r) - 2rq + \hat{s}r(r - \frac{7}{2})}{r\sqrt{r^2 - 3r \pm (2q + 3\hat{s}/r)\sqrt{r + 3q\hat{s}/r} - 6q\hat{s}/r}}, \end{aligned} \quad (3.9)$$

where $r = p/M$, $\hat{s} = s/M = \eta\chi$, with χ the dimensionless spin parameter of the inspiralling black hole, and $q = a/M$, with a the spin of the central black hole.

Furthermore, for Schwarzschild black holes, $q = 0$, one finds that at linear order in \hat{s} ,

$$\left. \frac{E}{\mu} \right|_{q \rightarrow 0} = \frac{r - 2}{\sqrt{r(r - 3)}} - \frac{\eta\chi}{2r(r - 3)^{3/2}} + O(\hat{s}^2), \quad (3.10)$$

$$\left. \frac{L_z}{\mu M} \right|_{q \rightarrow 0} = \frac{r}{\sqrt{r - 3}} + \frac{\eta\chi}{2} \frac{(r - 2)(2r - 9)}{\sqrt{r}(r - 3)^{3/2}} + O(\hat{s}^2). \quad (3.11)$$

Eq. (3.10) corrects a typo in Eq. (B18) of [56].

To obtain the orbital evolution of the CO, one needs to calculate the evolution of the energy E and angular momentum L_z . These quantities can be evaluated by equating their rate of change with the flux carried away by the GWs, \dot{E} and \dot{L}_z . I will use the radiation fluxes derived by Gair & Glampedakis [63], augmented with accurate black

3. The importance of including small body spin effects in the modelling of EMRIs and IMRIs

hole perturbation theory (BHPT) results that include small body spin corrections [124], i.e.,

$$\begin{aligned}
 \dot{E} &= -\frac{32}{5} \frac{\mu^2}{M} \left(\frac{1}{r}\right)^5 \left\{ 1 - \frac{1247}{336} \left(\frac{1}{r}\right) + \left(4\pi - \frac{73}{12}q - \frac{25}{4}\eta\chi\right) \left(\frac{1}{r}\right)^{3/2} + \right. \\
 &\quad \left. \left(-\frac{44711}{9072} + \frac{33}{16}q^2 + \frac{71}{8}q\eta\chi\right) \left(\frac{1}{r}\right)^2 + \text{higher order Teukolsky fits} \right\}, \\
 \dot{L}_z &= -\frac{32}{5} \frac{\mu^2}{M} \left(\frac{1}{r}\right)^{7/2} \left\{ 1 - \frac{1247}{336} \left(\frac{1}{r}\right) + \left(4\pi - \frac{61}{12}q - \frac{19}{4}\eta\chi\right) \left(\frac{1}{r}\right)^{3/2} + \right. \\
 &\quad \left. \left(-\frac{44711}{9072} + \frac{33}{16}q^2 + \frac{59}{8}q\eta\chi\right) \left(\frac{1}{r}\right)^2 + \text{higher order Teukolsky fits} \right\}.
 \end{aligned} \tag{3.12}$$

The ‘‘higher order Teukolsky fits’’ are given in [63]. As in Chapter 2, I do not give these explicitly here, as they are not needed to derive the conservative corrections. However, I will include them to evolve orbits and generate waveforms.

To evolve a circular orbit for a spinless particle in a Kerr background, one needs only to specify the angular momentum or the energy flux, as they are related by the ‘circular goes to circular’ rule [80]

$$\dot{E}(r, \chi \rightarrow 0) = \pm \frac{1}{r^{3/2} \pm q} \dot{L}_z(r, \chi \rightarrow 0) = \Omega(r, \chi \rightarrow 0) \dot{L}_z(r, \chi \rightarrow 0), \tag{3.13}$$

where $d\phi/dt = \Omega(r)$, is the azimuthal velocity of the orbit. One can use exactly the same scheme for spinning particles, as Tanaka et al. [124] showed that the assumption that a circular orbit remains circular under radiation reaction is consistent with the energy and angular momentum loss rates at linear order in the spin of the particle. Thus, Eq. (3.13) now reads [97; 124]

$$\dot{E}(r) = \pm \frac{1}{r^{3/2} \pm q} \left(1 - \frac{3}{2}\eta\chi \frac{\pm\sqrt{r} - q}{r^2 \pm q\sqrt{r}} \right) \dot{L}_z(r). \tag{3.14}$$

Furthermore, the evolution in time of the radial coordinate is given by

$$\dot{r} = \frac{dr}{dE} \dot{E} = \frac{dr}{dL_z} \dot{L}_z. \tag{3.15}$$

In the non-spinning case, $\chi = 0$, using the exact geodesic expression for dr/dL_z gener-

3. The importance of including small body spin effects in the modelling of EMRIs and IMRIs

ates inspirals that are closer to Teukolsky based evolutions than expanding the above expression at 2PN order [72] and I will adopt this approach here as well. However, I will need the 2PN expression in the following, which is

$$\begin{aligned} \frac{dr}{dt} = & -\frac{64}{5} \frac{\eta}{M} \left(\frac{1}{r}\right)^3 \left\{ 1 - \frac{743}{336} \left(\frac{1}{r}\right) + \left(4\pi - \frac{133}{12}q - \frac{35\eta\chi}{4}\right) \left(\frac{1}{r}\right)^{3/2} \right. \\ & \left. + \left(\frac{34103}{18144} + \frac{81}{16}q^2 + \frac{95q\eta\chi}{8}\right) \left(\frac{1}{r}\right)^2 \right\}. \end{aligned} \quad (3.16)$$

As before, $\eta = m/M$. In the same spirit of the analysis carried out in Chapter 2, I shall now introduce conservative SF corrections in the equations of motion. To that effect, I will amend the evolution equation for the ϕ frequency as follows,

$$\frac{d\phi}{dt} = \left(\frac{d\phi}{dt}\right)_{\text{geo}} \left(1 + \delta\Omega\right). \quad (3.17)$$

This equation includes the phase derivative for a geodesic, labeled by the subscript “geo” which is given implicitly in Eq. (3.14), and a frequency shift which will depend on the instantaneous orbital parameters. A problem arises here because to compute the necessary frequency shifts within our framework, i.e., BHPT, would require SF calculations. At present, Barack & Sago have computed gravitational SF corrections for particles moving on circular and eccentric bound geodesic orbits around a Schwarzschild BH in the Lorenz gauge [8; 10]. Warburton & Barack have recently computed the SF on a scalar charge for Kerr circular and eccentric equatorial orbits in the same gauge [131; 132]. The extension of this work to Kerr eccentric inclined geodesic orbits is still a challenging endeavour mainly because there is not a formal framework to deal with Lorenz-gauge metric perturbations in the frequency domain — the natural arena in which to carry out these calculations.

However, conservative corrections in the PN framework up to 2PN order which include spin-orbit, spin-spin couplings and finite mass contributions [18] are already known. One can combine these expressions with the radiative SF obtained by Tanaka et al. [124] based on the Teukolsky and Sasaki-Nakamura formalisms for perturbations around a Kerr BH, which includes terms of order q^2 , $\eta\chi$, $q\eta\chi$. Using these results, I will extend the method originally proposed by Babak et al. [5], who computed the 1PN conservative correction for circular orbits in the Schwarzschild space-time. The extension of this idea has been introduced in the previous Chapter, in which I included conservative corrections in a kludge model at 2PN order for Kerr circular-equatorial

3. The importance of including small body spin effects in the modelling of EMRIs and IMRIs

orbits. In this Section I shall extend the latter model by including small body spin effects at 2PN order and their corresponding conservative corrections.

The idea is to correct the kludge expressed in a particular coordinate system, in order to ensure that asymptotic observables are consistent with PN results in the weak field. In particular, I aim to modify the orbital frequency and its first time derivative. By modifying these two quantities, one can both identify coordinates between the two formalisms and find the missing conservative pieces.

From equation (3.14), the orbital frequency, at 2PN order, takes the form

$$\Omega = \frac{1}{M} \left(\frac{1}{r}\right)^{3/2} \left(1 - \left(q + \frac{3}{2}\eta\chi\right) \left(\frac{1}{r}\right)^{3/2} + \frac{3}{2}q\eta\chi \left(\frac{1}{r}\right)^2 + O\left(\frac{1}{r}\right)^{5/2}\right). \quad (3.18)$$

In order to include the conservative piece of the SF, one can recast Eq. 3.18 as follows

$$\begin{aligned} \Omega &= \frac{1}{M} \left(\frac{1}{r}\right)^{3/2} \left(1 - \left(q + \frac{3}{2}\eta\chi\right) \left(\frac{1}{r}\right)^{3/2} + \frac{3}{2}q\eta\chi \left(\frac{1}{r}\right)^2\right) \left(1 + \delta\Omega\right), \\ &= \frac{1}{M} \left(\frac{1}{r}\right)^{3/2} \left(1 - \left(q + \frac{3}{2}\eta\chi\right) \left(\frac{1}{r}\right)^{3/2} + \frac{3}{2}q\eta\chi \left(\frac{1}{r}\right)^2\right) \left\{1 + \right. \\ &\quad \left. + \eta \left(d_0 + d_1 \left(\frac{1}{r}\right) + (d_{1.5} + q f_{1.5} + \chi g_{1.5}) \left(\frac{1}{r}\right)^{3/2} + (d_2 + k_2 q\chi) \left(\frac{1}{r}\right)^2\right)\right\}. \end{aligned} \quad (3.19)$$

I will use this expansion for Ω_{geo} only to derive the conservative corrections. As discussed in Chapter 2, more reliable waveforms can be obtained by including the full geodesic frequency where it is known, and this will be the approach used in Section 3.3.

The expansion in r is an expansion in $v^2 = 1/r$. To derive the conservative corrections, I choose to leave the time derivative of the radial coordinate unchanged and given by equation (3.15)/(3.16). This amounts to a choice of gauge in which the η^2 terms of dr/dt that are not proportional to χ vanish. Differentiation of (3.19) then gives $d\Omega/dt$ for the kludge,

3. The importance of including small body spin effects in the modelling of EMRIs and IMRIs

$$\begin{aligned}
\frac{d\Omega}{dt} = & \frac{96}{5} \frac{\eta}{M^2} \left(\frac{1}{r}\right)^{11/2} \left\{ 1 + \eta d_0 + \frac{1}{r} \left(-\frac{743}{336} + \eta \left(\frac{5}{3} d_1 - \frac{743}{336} d_0 \right) \right) + \right. \\
& + \left(\frac{1}{r} \right)^{3/2} \left[4\pi - \frac{157}{12} q + \eta \left\{ (4\pi d_0 + 2d_{1.5} + q \left(2f_{1.5} - \frac{157}{12} d_0 \right) + \right. \right. \\
& + \left. \left. \chi \left(-\frac{47}{4} + 2g_{1.5} \right) \right\} \right] + \left(\frac{1}{r} \right)^2 \left[\frac{34103}{18144} + \frac{81}{16} q^2 \right. \\
& \left. \left. + \eta \left\{ \frac{34103}{18144} d_0 + \frac{81}{16} q^2 d_0 - \frac{3715}{1008} d_1 + \frac{7}{3} d_2 + \left(\frac{123}{8} + \frac{7}{3} k_2 \right) q\chi \right\} \right] \right\}, \tag{3.20}
\end{aligned}$$

where I have used $\hat{s} = \eta\chi$, with $\chi = S_1/\mu^2$. In order to relate the kludge coordinates with those used in the PN formalism, one needs a coordinate transformation, namely,

$$\begin{aligned}
r = & \frac{R}{M} \left\{ 1 + \left(\frac{M}{R} \right) b_1 + \left(\frac{M}{R} \right)^{3/2} (b_{1.5} + q w_{1.5} + \eta\chi v_{1.5}) + \left(\frac{M}{R} \right)^2 (b_2 + b_{2.1} q \eta\chi) \right. \\
& \left. + \eta \left(c_0 + \left(\frac{M}{R} \right) c_1 + \left(\frac{M}{R} \right)^{3/2} (c_{1.5} + q l_{1.5} + \gamma\chi) + \left(\frac{M}{R} \right)^2 (c_2 + c_{2.1} q \chi) \right) \right\}, \tag{3.21}
\end{aligned}$$

where R denotes the PN semi-major axis. One can now substitute this expression for the coordinate transformation into relations (3.19) and (3.20).

The final stage of the computation is to compare the expressions for Ω and $\dot{\Omega}$, where a dot denotes d/dt , with the available PN expansions. The PN expansions are available to higher order in the mass ratio η , but I keep η only to the same order as the kludge, Eq. (3.20). The PN expressions for the orbital frequency and its first time derivative are given by

$$\begin{aligned}
\Omega_{PN}^2 = & \frac{m_{\Gamma}}{R^3} \left\{ 1 - \frac{m_{\Gamma}}{R} (3 - \eta) - \left(\frac{m_{\Gamma}}{R} \right)^{3/2} \sum_i \left(2 \left(\frac{m_i}{m_{\Gamma}} \right)^2 + 3\eta \right) \hat{\mathbf{L}} \cdot \boldsymbol{\chi}_i \right. \\
& \left. + \left(\frac{m_{\Gamma}}{R} \right)^2 \left(6 + \frac{41}{4} \eta - \frac{3\eta}{2} (\boldsymbol{\chi}_1 \cdot \boldsymbol{\chi}_2 - 3\hat{\mathbf{L}} \cdot \boldsymbol{\chi}_1 \hat{\mathbf{L}} \cdot \boldsymbol{\chi}_2) \right) \right\}, \tag{3.22}
\end{aligned}$$

3. The importance of including small body spin effects in the modelling of EMRIs and IMRIs

where $m_T = M + m$, $\hat{\mathbf{L}}$ is a unit vector directed along the orbital momentum, and $\boldsymbol{\chi} = \boldsymbol{\chi}_1 = \mathbf{S}_1/\mu^2$, $\mathbf{q} = \boldsymbol{\chi}_2 = \mathbf{S}_2/M^2$. Additionally,

$$\begin{aligned} \dot{\Omega}_{PN} = & \frac{96}{5} \eta m_T^{5/3} \omega^{11/3} \left\{ 1 - \left(\frac{743}{336} + \frac{11}{4} \eta \right) (m_T \omega)^{2/3} + (4\pi - \beta) (m_T \omega) \right. \\ & \left. + \left(\frac{34103}{18144} + \frac{81}{16} q^2 + \sigma + \eta \left(\frac{13661}{2016} + \zeta q^2 \right) \right) (m_T \omega)^{4/3} \right\}, \end{aligned} \quad (3.23)$$

where the constant ζ was determined in [72], and has the value $\zeta = -243/32$. This term guarantees that the PN framework and the perturbative approach coincide in the test mass particle limit $\eta \rightarrow 0$. The spin-orbit β and spin-spin parameters σ are given by

$$\begin{aligned} \beta &= \frac{1}{12} \sum_i \left(113 \frac{m_i^2}{m_T^2} + 75\eta \right) \hat{\mathbf{L}} \cdot \boldsymbol{\chi}_i, \\ \sigma &= \frac{\eta}{48} \left(-247 \boldsymbol{\chi}_1 \cdot \boldsymbol{\chi}_2 + 721 \hat{\mathbf{L}} \cdot \boldsymbol{\chi}_1 \hat{\mathbf{L}} \cdot \boldsymbol{\chi}_2 \right). \end{aligned} \quad (3.24)$$

To be consistent with the perturbative approach outlined above, I shall assume that the spin of the small particle is perpendicular to the equatorial plane (this guarantees that the orbit remains circular-equatorial), and parallel to the momentum of the central Kerr black hole. For prograde orbits, the spin and spin-spin corrections will play a more significant role, and so the following analysis will focus on those.

One can rewrite the previous PN expressions in a convenient way to take the small mass-ratio limit, by writing $m_T = M(1 + \eta)$, giving

$$\begin{aligned} \Omega_{PN} = & \frac{1}{M} \left(\frac{M}{R} \right)^{3/2} \left\{ 1 + \frac{\eta}{2} - \frac{M}{R} \left(\frac{3}{2} + \frac{7}{4} \eta \right) - \left(\frac{M}{R} \right)^{3/2} \left(q + \eta \left(\frac{3}{2} q + \frac{3}{2} \chi \right) \right) \right. \\ & \left. + \left(\frac{M}{R} \right)^2 \left(\frac{15}{8} + \eta \left(\frac{169}{16} + \frac{3}{2} q \chi \right) \right) \right\}, \end{aligned} \quad (3.25)$$

3. The importance of including small body spin effects in the modelling of EMRIs and IMRIs

$$\begin{aligned}
\dot{\Omega}_{PN} = & \frac{96}{5} \frac{\eta}{M^2} \left(\frac{M}{R}\right)^{11/2} \left\{ 1 + \frac{3}{2}\eta - \left(\frac{2591}{336} + \frac{13571}{672}\eta\right) \frac{M}{R} \right. \\
& + \left(4\pi - \frac{157}{12}q + \eta\left(12\pi - \frac{149}{6}q - \frac{47}{4}\chi\right)\right) \left(\frac{M}{R}\right)^{3/2} \\
& \left. + \left(\frac{22115}{648} + \frac{81}{16}q^2 + \eta\left(\frac{87044}{567} + \frac{81}{8}q^2 + \frac{123}{8}q\chi\right)\right) \left(\frac{M}{R}\right)^2 \right\}.
\end{aligned} \tag{3.26}$$

A direct comparison between the expressions for the orbital frequencies and their first time derivatives is sufficient to solve simultaneously for the various coefficients of Eqs. (3.19), (3.20) and (3.21). The non-vanishing parameters are

$$\begin{aligned}
b_1 = 1, \quad c_0 = -\frac{1}{4}, \quad c_1 = \frac{845}{448}, \quad d_0 = \frac{1}{8}, \quad d_1 = \frac{1975}{896} \\
c_{1.5} = -\frac{9}{5}\pi, \quad d_{1.5} = -\frac{27}{10}\pi, \quad f_{1.5} = -\frac{191}{160}, \quad l_{1.5} = -\frac{91}{240} \\
c_2 = -\frac{2065193}{677376}, \quad d_2 = \frac{1152343}{451584}.
\end{aligned} \tag{3.27}$$

Having found the required corrections, I will now explore whether small body spin effects are important for signal detection. Previous studies have ignored this effect, in particular for EMRIs, since it is expected to be small for mass ratios $\eta \sim 10^{-5}$. However, even though an accurate measurement of the spin of the small body will be unlikely for these systems, I will discuss whether this additional parameter has a bearing on the accuracy with which other parameters can be determined. Furthermore, I will study various systems to find the mass ratio threshold at which the small spin parameter starts to be measurable through GW observations, and will also explore whether small object spin conservative corrections are relevant for parameter estimation and detection.

To carry out these studies, I will make use of the waveform model introduced in Section 2.4.1. Since this work will assume the existence of a low-frequency GW detector, I will use the LISA's response function described in Section 2.4.2.

Having incorporated the detector's response function in the waveform model, one can use the Fisher Matrix Formalism, developed in Section 2.4.3, to explore the accuracy with which GW observations will be able to determine the system parameters.

3.3 Parameter estimation error results

In this Section I explore the accuracy with which LISA observations will be able to measure the spin of the inspiralling object. To effectively address this problem, I will estimate noise-induced errors for a variety of binary systems using the formalism described in Sections 2.4.2 – 2.4.4. To estimate the noise-induced errors, I will use the inverse Fisher Matrix (see Eq. (2.65)). I have verified that the Fisher Matrices used in these studies were convergent over several orders of magnitude in the offset used to compute the numerical waveform derivatives. The same convergent behaviour was exhibited by the associated inverse matrices.

The noise-induced errors will be quoted for fixed values of the intrinsic parameters of the source, but with a Monte Carlo simulation over possible values of the extrinsic parameters. I compute the Fisher Matrix for a source at $D = 1\text{Gpc}$, and the corresponding SNR using the expression

$$\text{SNR}^2 = 2 \sum_{\alpha=I,II} \int_{t_{\text{init}}}^{t_{\text{LSO}}} \hat{h}_{\alpha}^2(t) dt. \quad (3.28)$$

I then re-normalise the results to a fixed SNR. The choice of this fixed SNR detection threshold is based on the information obtained from the MC SNR distributions.

3.3.1 Determination of SNR detection thresholds

To estimate the “typical” SNR of a source, I did a Monte Carlo simulation in which the extrinsic parameters of each source were chosen randomly. I then considered the SNRs of events distributed uniformly out to a redshift of $z = 1$, and which are detected in a certain time window at the detector, namely, one year. Finally, I looked at how the SNRs of those detected events were distributed. I have chosen events uniformly distributed out to redshift of $z = 1$, because this might be more representative of the real universe. The intrinsic parameters of the source were fixed, with redshifted masses equal to the quoted values, e.g., $10M_{\odot} + 10^6M_{\odot}$ etc. For each source, I computed the SNR accumulated in a one year observation prior to plunge. This was accomplished by choosing the initial radial coordinate, p_0 , such that the inspiralling BH reached the last stable orbit after one year of inspiral.

Figure 3.1 presents the normalized cumulative distribution function for the SNR of a cosmological population of binary systems with central BHs of redshifted mass 10^6M_{\odot} , and spin parameter $q = 0.9$. The inspiralling BHs have specific spin parameter $\chi = 0.9$, and redshifted masses $\mu = 10M_{\odot}$, $\mu = 10^2M_{\odot}$, $\mu = 10^3M_{\odot}$, and $\mu = 5 \times 10^3M_{\odot}$.

3. The importance of including small body spin effects in the modelling of EMRIs and IMRIs

Figure 3.2 presents the normalized cumulative distribution function for the SNR of the more massive cosmological population of binary systems shown in Figure 3.1, but for three additional combinations of the spin magnitudes of the binary components.

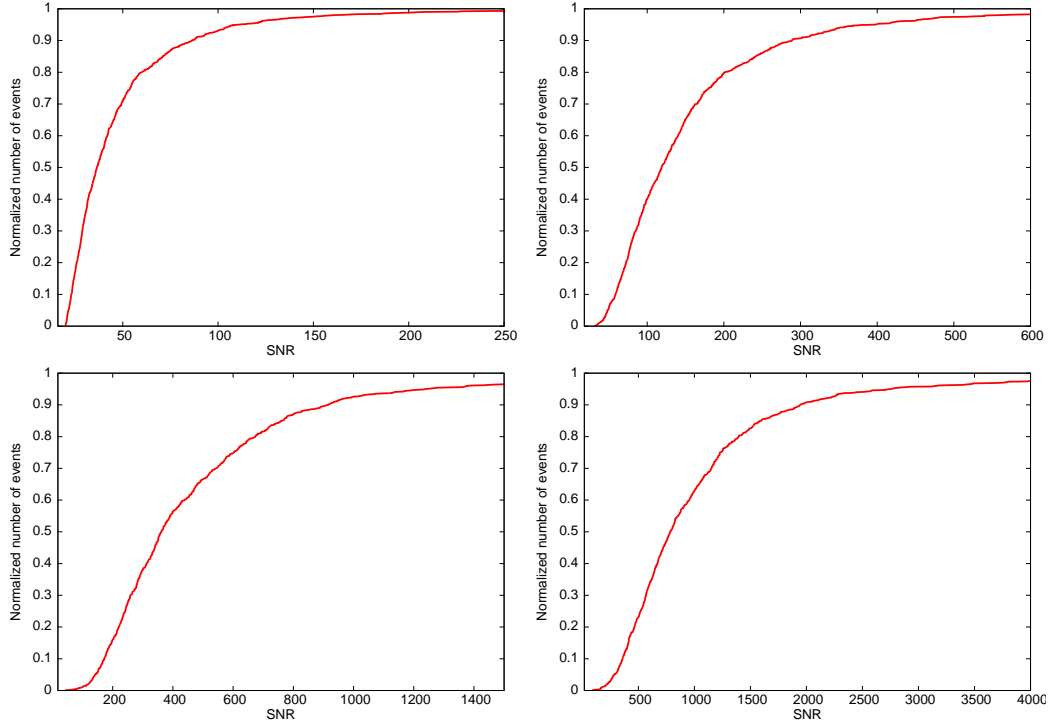


Figure 3.1: The normalized cumulative distribution function for the signal-to-noise ratio of a cosmological population of binary systems with central BHs of redshifted mass $M = 10^6 M_\odot$, and spin parameter $q = 0.9$. The inspiralling BHs have specific spin parameter $\chi = 0.9$, and redshifted masses $\mu = 10 M_\odot$ (top left panel), $\mu = 10^2 M_\odot$ (top right), $\mu = 10^3 M_\odot$ (bottom left), and $\mu = 5 \times 10^3 M_\odot$ (bottom right).

The way to interpret the normalised cumulative distributions of Figures 3.1, 3.2 is the following: the value of the cumulative distribution at a given SNR_t , indicates the fraction of events with $\text{SNR} < \text{SNR}_t$. Hence, for the least massive system, the cumulative distribution indicates that $\sim 50\%$ of events in the Monte Carlo sample have $\text{SNR} \sim 30$. This “median” SNR will be used as the “typical” SNR for the binary systems considered in these studies.

Thus, based on Figures 3.1 and 3.2, I will normalise our results to the following reference SNRs: for the inspiralling BHs with masses $\mu = 10 M_\odot, 10^2 M_\odot, 10^3 M_\odot, 5 \times 10^3 M_\odot$, and spin magnitude $\chi = 0.9$, I will use a fixed SNR detection threshold of 30, 150, 400, 1000, respectively. For the more massive system, $5 \times 10^3 M_\odot + 10^6 M_\odot$, Figure 3.2 suggests that for the combination of spin magnitudes $q = 0.9, \chi = 0.1$, one

3. The importance of including small body spin effects in the modelling of EMRIs and IMRIs

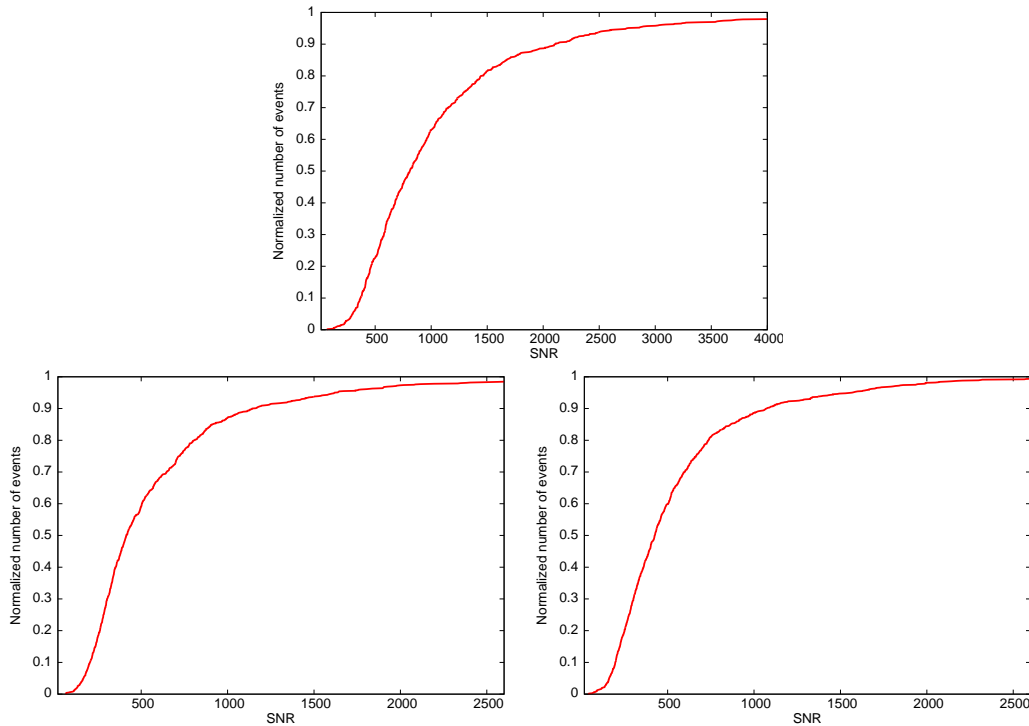


Figure 3.2: Normalized cumulative distribution function for the signal-to-noise ratio of a cosmological population of binary systems with BHs of redshifted mass $5 \times 10^3 M_\odot + 10^6 M_\odot$. The panels show results for three different combinations of the spin magnitudes of the central and inspiralling BHs, q, χ , namely: top panel $q = 0.9, \chi = 0.1$; bottom-left panel $q = 0.1, \chi = 0.9$; bottom-right panel $q = 0.1, \chi = 0.1$.

may use a fixed SNR threshold of 1000; whereas for the combination $q = 0.1, \chi = 0.9$, and $q = 0.1, \chi = 0.1$, one can use SNR= 500.

Figures 3.1, 3.2 provide information that can be used to renormalise the results presented later in the Chapter, in Tables 2.3-3.6, to a cosmological population of sources.

3.3.2 Parameter estimation results

The parameter space I have considered is 11-dimensional. Five of these are intrinsic parameters, namely $\ln m, \ln M, q, \chi, p_0$, where χ is the dimensionless spin parameter of the inspiralling BH. The other six are extrinsic or phase parameters. I summarize the physical meaning of the parameters in Table 3.1.

The results of the Monte Carlo simulations are summarized in Tables 3.2, 3.3, 3.4, 3.5 and 3.6. As mentioned above, these Tables present results for a variety of binary systems. All of them have a central $M = 10^6 M_\odot$ BH with spin parameter $q = 0.9$, and

3. The importance of including small body spin effects in the modelling of EMRIs and IMRIs

$\ln \mu$	mass of inspiralling object
$\ln M$	mass of central SMBH
q	magnitude of (specific) spin angular momentum of SMBH
χ	magnitude of (specific) spin angular momentum of inspiralling object
p_0	Initial radius of inspiralling object's orbit
ϕ_0	Initial phase of inspiralling object's orbit
θ_S	source sky colatitude in an ecliptic-based system
ϕ_S	source sky azimuth in an ecliptic-based system
θ_K	direction of SMBH spin (colatitude)
ϕ_K	direction of SMBH spin (azimuth)
$\ln D$	distance to source

Table 3.1: This table describes the meaning of the parameters used in our model. The angles (θ_S, ϕ_S) and (θ_K, ϕ_K) are defined in a fixed ecliptic-based coordinate system.

four different types of inspiralling BHs with masses $\mu = 10M_\odot, 10^2M_\odot, 10^3M_\odot, 5 \times 10^3M_\odot$, and spin parameter $\chi = 0.9$. For completeness in the analysis, and to explore the trend with the spin of the small/big body, I have also considered three additional cases for the more massive systems in Tables 3.5 and 3.6, namely, $q = 0.9, \chi = 0.1$; $q = 0.1, \chi = 0.9$; and $q = \chi = 0.1$, using the same component masses.

Model		Distribution of $\log_{10}(\Delta X)$ in error, ΔX , for parameter $X =$										
		$\ln(m)$	$\ln(M)$	q	χ	t_0	ϕ_0	θ_S	ϕ_S	θ_K	ϕ_K	$\ln(D)$
$q = 0.9$	Mean	-3.99	-3.58	-4.13	1.68	-3.31	-0.99	-1.54	-1.58	-1.14	-1.07	-1.09
	St. Dev.	0.110	0.122	0.114	0.098	0.124	0.453	0.133	0.199	0.433	0.456	0.311
	L. Qt.	-4.08	-3.61	-4.34	1.63	-3.35	-1.35	-1.63	-1.71	-1.49	-1.40	-1.37
$\chi = 0.9$	Med.	-3.99	-3.55	-4.08	1.68	-3.29	-1.16	-1.53	-1.62	-1.24	-1.08	-1.16
	U. Qt.	-3.89	-3.51	-3.95	1.74	-3.23	-0.85	-1.49	-1.51	-0.85	-0.79	-0.88

Table 3.2: Summary of results of the Monte Carlo simulation of Fisher Matrix errors for spinning BH systems with specific spin parameters $q = \chi = 0.9$, and masses $\mu = 10M_\odot$, $M = 10^6M_\odot$. The Table shows the mean, standard deviation, median and quartiles of the distribution of the logarithm to base ten of the error in each parameter. Results are given for the kludge model with conservative corrections to 2PN order. The angles $\bar{\phi}_0$ and $\bar{\alpha}_0$, specifying LISA's position and orientation at $t = 0$, are set to zero. Note that the results have been normalised to fixed SNR= 30.

Model		Distribution of $\log_{10}(\Delta X)$ in error, ΔX , for parameter $X =$										
		$\ln(m)$	$\ln(M)$	q	χ	t_0	ϕ_0	θ_S	ϕ_S	θ_K	ϕ_K	$\ln(D)$
$q = 0.9$	Mean	-3.78	-3.62	-4.98	0.19	-2.76	-1.60	-2.04	-2.00	-1.81	-1.68	-1.78
	St. Dev.	0.074	0.075	0.112	0.068	0.075	0.330	0.206	0.246	0.361	0.396	0.270
	L. Qt.	-3.84	-3.68	-5.06	0.14	-2.82	-1.86	-2.20	-2.18	-2.08	-1.98	-2.02
$\chi = 0.9$	Med.	-3.79	-3.63	-4.98	0.19	-2.77	-1.66	-2.03	-2.01	-1.89	-1.74	-1.85
	U. Qt.	-3.74	-3.57	-4.88	0.25	-2.71	-1.43	-1.87	-1.88	-1.56	-1.40	-1.58

Table 3.3: As Table 3.2, but for an inspiralling BH with mass $\mu = 100M_\odot$. Results are quoted at a fixed SNR of 150.

Model		Distribution of $\log_{10}(\Delta X)$ in error, ΔX , for parameter $X =$										
		$\ln(m)$	$\ln(M)$	q	χ	p_0	ϕ_0	θ_S	ϕ_S	θ_K	ϕ_K	$\ln(D)$
$q = 0.9$	Mean	-3.33	-3.15	-4.62	-0.52	-2.03	-1.39	-1.88	-1.84	-1.67	-1.56	-1.73
	St. Dev.	0.096	0.097	0.091	0.084	0.097	0.407	0.344	0.363	0.444	0.470	0.321
$\chi = 0.9$	L. Qt.	-3.41	-3.23	-4.70	-0.59	-2.11	-1.66	-2.15	-2.06	-1.95	-1.87	-1.94
	Med.	-3.38	-3.20	-4.67	-0.55	-2.08	-1.50	-1.82	-1.79	-1.72	-1.62	-1.82
	U. Qt.	-3.24	-3.06	-4.54	-0.45	-1.93	-1.26	-1.60	-1.68	-1.43	-1.30	-1.55

Table 3.4: As Table 3.2, but for an inspiralling BH with mass $\mu = 10^3 M_\odot$. Results are quoted at a fixed SNR of 400.

Model		Distribution of $\log_{10}(\Delta X)$ in error, ΔX , for parameter $X =$										
		$\ln(m)$	$\ln(M)$	q	χ	p_0	ϕ_0	θ_S	ϕ_S	θ_K	ϕ_K	$\ln(D)$
$q = 0.9$	Mean	-3.12	-2.94	-4.38	-1.07	-1.60	-1.48	-2.06	-2.07	-1.85	-1.71	-1.90
	St. Dev.	0.089	0.089	0.083	0.081	0.089	0.417	0.379	0.391	0.434	0.468	0.326
$\chi = 0.9$	L. Qt.	-3.14	-2.99	-4.40	-1.09	-1.65	-1.91	-2.39	-2.23	-2.13	-2.00	-2.10
	Med.	-3.13	-2.94	-4.38	-1.06	-1.64	-1.72	-2.07	-2.02	-1.89	-1.73	-1.95
	U. Qt.	-3.03	-2.84	-4.37	-1.02	-1.54	-1.42	-1.87	-1.74	-1.62	-1.53	-1.71
$q = 0.9$	Mean	-2.62	-2.44	-3.92	-0.60	-1.19	-1.49	-2.09	-2.04	-1.75	-1.62	-1.81
	St. Dev.	0.181	0.185	0.176	0.172	0.205	0.359	0.440	0.365	0.398	0.444	0.411
$\chi = 0.1$	L. Qt.	-2.77	-2.59	-4.07	-0.70	-1.31	-1.96	-2.44	-2.32	-2.12	-2.09	-2.10
	Med.	-2.60	-2.41	-3.90	-0.61	-1.21	-1.66	-2.06	-2.03	-1.82	-1.77	-1.89
	U. Qt.	-2.46	-2.29	-3.77	-0.44	-1.09	-1.36	-1.78	-1.69	-1.60	-1.41	-1.67

Table 3.5: As Table 2.3, but for an inspiralling BH with mass $\mu = 5 \times 10^3 M_\odot$. Results are quoted at a fixed SNR of 1000.

Model		Distribution of $\log_{10}(\Delta X)$ in error, ΔX , for parameter $X =$										
		$\ln(m)$	$\ln(M)$	q	χ	p_0	ϕ_0	θ_S	ϕ_S	θ_K	ϕ_K	$\ln(D)$
$q = 0.1$	Mean	-3.09	-2.92	-2.61	-0.15	-1.62	-1.58	-1.99	-1.89	-1.75	-1.63	-1.79
	St. Dev.	0.071	0.072	0.064	0.062	0.072	0.365	0.401	0.416	0.387	0.416	0.283
$\chi = 0.9$	L. Qt.	-3.16	-2.99	-2.66	-0.20	-1.68	-1.82	-2.25	-2.15	-2.00	-1.92	-1.98
	Med.	-3.09	-2.93	-2.62	-0.16	-1.62	-1.66	-1.87	-1.85	-1.77	-1.64	-1.83
	U. Qt.	-3.01	-2.85	-2.56	-0.11	-1.56	-1.41	-1.67	-1.64	-1.54	-1.38	-1.62
$q = 0.1$	Mean	-3.09	-2.92	-2.61	-0.15	-1.62	-1.68	-1.99	-1.90	-1.85	-1.71	-1.86
	St. Dev.	0.069	0.070	0.064	0.060	0.070	0.282	0.397	0.444	0.348	0.385	0.254
$\chi = 0.1$	L. Qt.	-3.15	-2.98	-2.66	-0.20	-1.68	-1.86	-1.21	-2.12	-2.07	-1.96	-2.01
	Med.	-3.09	-2.92	-2.61	-0.16	-1.62	-1.68	-1.89	-1.83	-1.83	-1.71	-1.89
	U. Qt.	-3.03	-2.86	-2.56	-0.11	-1.56	-1.54	-1.68	-1.59	-1.61	-1.48	-1.72

Table 3.6: As Table 3.5, but for a slowly rotating central BH with spin parameter $q = 0.1$. Results are quoted at a fixed SNR of 500.

3. The importance of including small body spin effects in the modelling of EMRIs and IMRIs

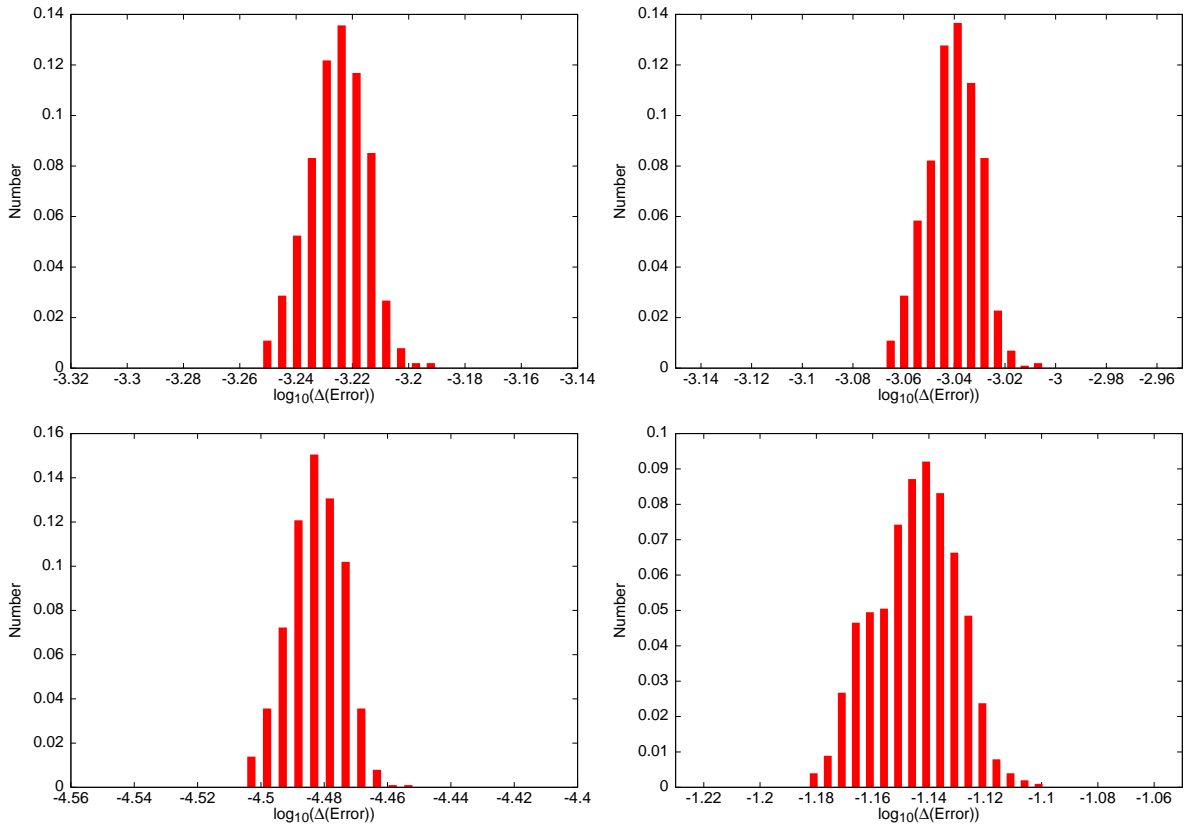


Figure 3.3: Distribution of parameter measurement error estimates, Δ , computed in the Monte Carlo simulations for the system with $\mu = 5 \times 10^3 M_{\odot}$, $M = 10^6 M_{\odot}$, $q = 0.9$, $\chi = 0.9$. The panels show, from left to right, the error distributions for, top row: $\Delta(\log_{10}(\ln \mu))$, $\Delta(\log_{10}(\ln M))$; and bottom row: $\Delta(\log_{10}(q))$ and $\Delta(\log_{10}(\chi))$ respectively. Results are quoted at fixed SNR of 1000.

The results quoted in Table 2.3 provide a cross-check of the analysis carried out in the context of EMRIs in Chapter 2, in which I ignored the spin of the CO. These results also show that i) including the spin of the small CO for EMRIs with mass ratios $\eta \lesssim 10^{-5}$ will not significantly affect parameter determination or detection and, ii) GW observations will not be able to constrain at all the spin parameter of the inspiralling BH for systems of this mass ratio. These results are consistent with the arguments presented by Barack & Cutler [6] in the sense that including small body spin effects for EMRIs has a minor effect on the orbital evolution of the system.

For systems with mass ratios $\eta \sim 10^{-4}$, Table 3.3 shows that attempts to measure the spin of inspiralling BHs in this regime will not yield much information. In addition, Table 3.4 suggests that the determination of the spin of the inspiralling BH might be feasible for systems with mass ratios $\eta \sim 10^{-3}$. At fixed SNR of 400, GW observations

3. The importance of including small body spin effects in the modelling of EMRIs and IMRIs

will be able to determine the spin parameter of inspiralling BHs for systems with component masses $10^3 M_\odot + 10^6 M_\odot$ to an accuracy better than $\sim 28\%$.

This latter estimate will be further improved for inspiralling BHs of mass $\mu = 5 \times 10^3 M_\odot$. For these systems, Table 3.5 and Figure 2.5 show that, at fixed SNR=1000, LISA measurements will be able to determine the spinning BH mass, SMBH mass, SMBH spin parameter, and BH spin parameter within fractional errors of $\sim 10^{-3}$, 10^{-3} , 10^{-4} , and 10%. One also expects to determine the location of the source in the sky to within $10^{-4.3}$ steradians, and determine the SMBH spin orientation to within $10^{-3.7}$ steradians.

These results suggest that the inclusion of small body spin effects becomes relevant for signal analysis for massive binaries with mass ratios $\eta \gtrsim 10^{-3}$. Having found this threshold, one can explore the trend with the spin of the small/big body in this best case. Tables 3.5 and 3.6 present four different combinations of the spin parameters of the more massive binary's components. For $q = \chi = 0.9$, Table 3.5 suggests that GW observations will be able to measure the spin of the inspiraling body to a precision of a few percent. For $q = 0.9$, $\chi = 0.1$, this same Table shows that when the inspiralling body is slowly rotating, the accuracy with which one can determine the intrinsic parameters of the system decreases by roughly a factor of ~ 3 . In this latter case, the small body spin magnitude can be measured within a fractional error of 25%. Furthermore, the accuracy with which the extrinsic parameters can be determined remains basically unchanged. Hence, for binaries with $\eta \gtrsim 10^{-3}$, the determination of the intrinsic parameters is best accomplished when both binary components are rapidly rotating.

Table 3.6 shows that when the central SMBH is slowly rotating i) the accuracy with which the intrinsic parameters of the system can be determined is not very sensitive to the spin of the inspiralling body; ii) GW observations will not provide an accurate measurement of the spin of the inspiralling object.

This suggests that spin couplings play an important role in the orbital evolution of massive rapidly rotating objects, and this effect is reflected in the accuracy with which GW observations will be able to determine the intrinsic parameters of the system. These findings also confirm the fact that spin couplings are expected to be important when the inspiralling objects probe strong-field regions of the central SMBH. Put in different words, when both components of the binary are rapidly rotating, and, in particular, when the SMBH is rapidly rotating.

These results suggest that GW observations in the low-frequency band could be useful not only to measure the spin distribution of SMBHs with unprecedented accuracy,

3. The importance of including small body spin effects in the modelling of EMRIs and IMRIs

but also to provide information on the spin distribution of any intermediate mass BHs that exist in the centres of galaxies.

Another point that deserves consideration is the fact that the errors reported in the Tables 2.3-3.6 seem to get steadily worse at larger fixed SNRs. This is due to the fact that the more massive the binary system is, the less time the inspiralling object spends close to the central SMBH. To illustrate this, the inspiralling BH of the system $\mu = 10M_{\odot} + 10^6M_{\odot}$ with $q = \chi = 0.9$, spends the last six months of inspiral within the region $p \in (\sim 6.01M \rightarrow \sim 2.32M)$. In contrast, the inspiralling object of the more massive system with $q = \chi = 0.9$, spends the last six months probing a more extended region, $p \in (\sim 29.52M \rightarrow \sim 2.31M)$, and hence spends less time close to the innermost stable circular orbit (ISCO) of the central BH. Furthermore, the number of cycles completed over the last year of inspiral by the more massive system amounts to $\sim 10\%$ the number of cycles completed by the less massive system.

3.4 Model-induced parameter errors

Up to this point, I have used the Fisher Matrix formalism described in Section 2.4.3 to estimate errors that arise due to noise in the detector. I shall now explore errors that arise from the approximate nature of the kludge waveform model.

In the absence of noise, for a particular true signal, $\mathbf{s}(\mathbf{t})$, the kludge waveform model, $\mathbf{h}(\mathbf{t})$, that is the best match to the data may have different parameters to the true waveform. This in turn introduces another parameter error, which is usually referred to as “model” error.

Using the framework developed by Cutler and Vallisneri [35], and the analysis on model errors for EMRIs in the context of spinless particles introduced in Section 2.6, I will present results on the magnitude of the model errors that could arise in the EMRIs and IMRIs in which the inspiral component has significant spin.

The aim of this analysis is to find out whether including conservative corrections is important for detection and parameter estimation. To address this problem, I will build waveform templates that include all, only part, or none of the conservative pieces derived in Section 3.2. The kludge waveform templates that include all of the conservative corrections at 2PN order will be taken as the “true” waveforms $h_{\mathbf{GR}}$. I then estimate the model errors by searching for $h_{\mathbf{GR}}$ using templates, $h_{\mathbf{AP}}$, that include none or only part of the conservative corrections. The rule of thumb will be that if crossing a term out in the model gives rise to a parameter error that is comparable to or smaller than the noise-induced error, then one can safely ignore that term in the

3. The importance of including small body spin effects in the modelling of EMRIs and IMRIs

search template.

By re-writing the waveform in an amplitude–phase approximation, namely, $\tilde{h}^\alpha(f) = A^\alpha(f)e^{i\Psi^\alpha(f)}$, where A and Ψ stand for the amplitude and the phase of the waveform, respectively, (see Eq. 2.76), one can derive a reliable prescription for the computation of model errors,

$$\Delta_{\text{th}}\theta^i \approx (\Gamma^{-1}(\theta))^{ij} \left(\underbrace{[\Delta\mathbf{A} + i\mathbf{A}\Delta\Psi]}_{\text{at } \theta} e^{i\Psi} \Big| \partial_j \mathbf{h}_{\text{AP}}(\theta) \right). \quad (3.29)$$

I will use this approximation, (3.29), to estimate the magnitude of the parameter errors that arise from inaccuracies in the template waveform. At present, accurate waveforms including all first order conservative SF corrections are not known. In Chapter 2, I introduced a waveform model that included conservative SF corrections at 2PN for Kerr circular–equatorial EMRIs. The conservative corrections used in that model were derived using the same method employed in Section 3.2, since accurate fully relativistic conservative SF corrections are not currently available for COs moving in the background of Kerr black holes. The extension of this analysis to the gravitational case is now under investigation. Furthermore, the computation of conservative corrections for the case I consider in these studies, namely, spinning BHs moving in the background of a Kerr black hole, is beyond the scope of the current SF program, which is focused on inspiralling objects that are non-spinning. Nonetheless, one can use the kludge model to assess the importance of conservative corrections for detection and parameter estimation.

I will compute the model error that arises when one omits part or all of the conservative corrections in the waveform template and calculate the ratio, \mathcal{R} , of this error to the error that arises from noise in the detector. This ratio will indicate the importance of including the conservative corrections for parameter determination. If $\mathcal{R} \lesssim 1$, then the estimates obtained from a model that ignores the conservative piece should still be reliable, but if $\mathcal{R} \gg 1$ then it is clear that one must include the conservative corrections. The ratios of parameter errors to Fisher Matrix errors obtained from the Monte Carlo simulations over extrinsic parameters are summarized in Tables 3.7, 3.8, 3.9, 3.10, and 3.11.

I quote results for the same four test systems that were studied previously, and consider two different comparisons, namely, I take the “true” waveform to be the kludge waveform with 2PN conservative corrections, and the template to be a kludge waveform with either no conservative corrections (“0PN”) or with conservative corrections to 1.5PN order (“1.5PN”), and do pairwise comparisons.

Model		\log_{10} of the ratio \mathcal{R} of model to noise-induced error for parameter $X =$										
		$\ln(m)$	$\ln(M)$	q	χ	p_0	ϕ_0	θ_S	ϕ_S	θ_K	ϕ_K	$\ln(D)$
2PN vs 0PN	Mean	-0.50	-0.26	-0.31	-0.35	-0.26	-0.28	-0.30	-0.37	-0.12	-0.09	-0.16
	St. Dev.	0.583	0.441	0.590	0.622	0.481	0.778	0.606	0.623	0.703	0.718	0.824
	L. Qt.	-0.85	-0.60	-0.70	-0.74	-0.59	-0.54	-0.56	-0.61	-0.47	-0.46	-0.56
	Med.	-0.42	-0.15	-0.20	-0.17	-0.15	-0.15	-0.16	-0.23	0.04	0.03	0.02
	U. Qt.	-0.09	0.17	0.11	0.15	0.19	0.16	0.10	0.09	0.38	0.36	0.43
2PN vs 1.5PN	Mean	-0.70	-0.49	-0.47	-0.52	-0.48	-0.42	-0.53	-0.62	-0.32	-0.27	-0.42
	St. Dev.	0.578	0.564	0.603	0.626	0.610	0.720	0.619	0.617	0.763	0.740	0.813
	L. Qt.	-0.98	-0.73	-0.77	-0.79	-0.72	-0.65	-0.72	-0.83	-0.60	-0.51	-0.68
	Med.	-0.59	-0.35	-0.37	-0.38	-0.32	-0.28	-0.35	-0.44	-0.19	-0.09	-0.17
	U. Qt.	-0.31	-0.02	-0.01	-0.05	0.00	-0.01	-0.13	-0.15	0.14	0.20	0.16

Table 3.7: Summary of Monte Carlo simulation results for the ratio of model errors to noise-induced errors, computed using the Fisher Matrix, for spinning BH systems with $\mu = 10M_{\odot}$. The Table shows the mean, standard deviation, median and quartiles of the distribution of the logarithm to base ten of the ratio for each parameter. Results are given for various comparisons, as indicated and described in the text. A comparison “A vs B” uses model A as the true waveform, and model B as the search template. Note that the noise-induced errors are quoted at a fixed SNR= 30.

Model		\log_{10} of the ratio \mathcal{R} of model to noise-induced error for parameter $X =$										
		$\ln(m)$	$\ln(M)$	q	χ	p_0	ϕ_0	θ_S	ϕ_S	θ_K	ϕ_K	$\ln(D)$
2PN vs 0PN	Mean	0.33	0.37	0.65	0.47	0.32	0.62	0.48	0.53	0.65	0.65	0.61
	St. Dev.	0.645	0.561	0.555	0.638	0.564	0.738	0.654	0.657	0.710	0.707	0.659
	L. Qt.	0.07	0.05	0.37	0.16	0.05	0.31	0.18	0.29	0.23	0.29	0.08
	Med.	0.49	0.50	0.71	0.67	0.48	0.79	0.63	0.67	0.83	0.82	0.79
	U. Qt.	0.74	0.74	1.06	0.92	0.74	1.08	1.04	0.98	1.25	1.21	1.27
2PN vs 1.5PN	Mean	0.16	0.14	0.60	0.34	0.09	0.46	0.42	0.42	0.61	0.64	0.56
	St. Dev.	0.521	0.564	0.536	0.667	0.635	0.743	0.703	0.692	0.688	0.662	0.776
	L. Qt.	-0.11	-0.17	0.24	0.02	-0.18	0.09	0.06	0.03	0.19	0.23	0.15
	Med.	0.30	0.30	0.69	0.48	0.27	0.61	0.51	0.55	0.81	0.79	0.78
	U. Qt.	0.58	0.58	1.01	0.78	0.60	1.02	0.84	0.97	1.12	1.11	1.17

Table 3.8: As Table 3.7, but for a spinning BH with mass $\mu = 100M_\odot$. Noise-induced errors are quoted at a fixed SNR= 150.

Model		\log_{10} of the ratio \mathcal{R} of model to noise-induced error for parameter $X =$										
		$\ln(m)$	$\ln(M)$	q	χ	p_0	ϕ_0	θ_S	ϕ_S	θ_K	ϕ_K	$\ln(D)$
2PN vs 0PN	Mean	1.28	1.30	1.50	1.38	1.30	1.81	1.63	1.68	1.90	1.91	1.90
	St. Dev.	0.599	0.651	0.494	0.651	0.563	0.715	0.725	0.643	0.664	0.673	0.725
	L. Qt.	0.89	0.92	1.22	0.98	0.93	1.24	1.15	1.21	1.26	1.24	1.21
	Med.	1.30	1.40	1.47	1.51	1.40	1.79	1.69	1.76	1.96	1.99	1.98
	U. Qt.	1.75	1.75	1.80	1.88	1.76	2.52	2.23	2.20	2.67	2.69	2.75
2PN vs 1.5PN	Mean	0.24	0.24	0.58	0.44	0.25	0.66	0.77	0.69	0.80	0.84	0.81
	St. Dev.	0.629	0.614	0.519	0.611	0.596	0.759	0.724	0.708	0.740	0.691	0.737
	L. Qt.	-0.25	-0.24	0.35	-0.04	-0.27	0.04	0.05	0.09	-0.03	0.03	-0.01
	Med.	0.41	0.40	0.57	0.53	0.44	0.70	0.91	0.73	0.94	0.95	0.92
	U. Qt.	0.79	0.77	0.87	0.97	0.79	1.36	1.61	1.44	1.65	1.75	1.74

Table 3.9: As Table 3.7, but for a spinning BH with mass $\mu = 10^3M_\odot$. Noise-induced errors are quoted at a fixed SNR= 400.

Model		\log_{10} of the ratio \mathcal{R} of model to noise-induced error for parameter $X =$										
		$\ln(m)$	$\ln(M)$	q	χ	p_0	ϕ_0	θ_S	ϕ_S	θ_K	ϕ_K	$\ln(D)$
2PN vs 0PN	Mean	1.72	1.73	1.82	1.83	1.73	2.47	2.24	2.22	2.54	2.54	2.56
	St. Dev.	0.709	0.686	0.597	0.614	0.677	0.708	0.679	0.731	0.752	0.789	0.826
	L. Qt.	1.29	1.25	1.52	1.35	1.29	1.92	1.74	1.80	1.90	1.90	1.91
	Med.	1.81	1.78	1.85	1.92	1.77	2.43	2.24	2.33	2.56	2.56	2.54
	U. Qt.	2.21	2.21	2.18	2.32	2.21	3.04	2.64	2.81	3.29	3.34	3.35
2PN vs 1.5PN	Mean	0.38	0.39	0.76	0.49	0.39	1.04	0.93	0.90	1.04	1.11	1.10
	St. Dev.	0.719	0.604	0.490	0.585	0.594	0.720	0.715	0.637	0.799	0.735	0.816
	L. Qt.	-0.18	-0.16	0.56	-0.11	-0.18	0.40	0.38	0.30	0.39	-0.02	0.35
	Med.	0.47	0.45	0.82	0.64	0.51	0.96	1.00	0.98	1.08	1.17	1.11
	U. Qt.	0.90	0.87	1.04	1.04	0.84	1.77	1.54	1.45	1.78	1.93	1.94
2PN vs 1.5PN	Mean	0.50	0.50	0.77	0.63	0.50	1.06	0.97	0.92	1.11	1.14	1.10
	St. Dev.	0.708	0.622	0.405	0.612	0.621	0.731	0.632	0.680	0.701	0.703	0.795
	L. Qt.	0.02	0.01	0.58	0.14	0.03	0.39	0.38	0.28	0.34	0.36	0.30
	Med.	0.63	0.63	0.78	0.77	0.62	1.00	1.00	0.97	1.12	1.16	1.18
	U. Qt.	0.98	0.98	1.02	1.11	0.97	1.73	1.68	1.60	2.00	2.01	1.99

Table 3.10: As Table 3.7, but for a spinning BH with mass $\mu = 5 \times 10^3 M_\odot$. Noise-induced errors are quoted at a fixed SNR= 1000.

Model		\log_{10} of the ratio \mathcal{R} of model to noise-induced error for parameter $X =$										
		$\ln(m)$	$\ln(M)$	q	χ	p_0	ϕ_0	θ_S	ϕ_S	θ_K	ϕ_K	$\ln(D)$
2PN vs 1.5PN	Mean	0.41	0.40	0.49	0.49	0.38	0.79	0.66	0.62	0.88	0.91	0.87
	St. Dev.	0.597	0.615	0.517	0.643	0.607	0.698	0.739	0.723	0.776	0.801	0.799
	L. Qt.	0.05	0.05	0.15	0.13	0.02	0.22	0.17	0.09	0.16	0.21	0.12
	Med.	0.46	0.46	0.60	0.58	0.45	0.81	0.73	0.69	0.93	0.92	0.99
	U. Qt.	0.78	0.75	0.90	0.87	0.75	1.47	1.23	1.19	1.81	1.75	1.74
2PN vs 1.5PN	Mean	0.43	0.41	0.51	0.50	0.41	0.78	0.66	0.64	0.90	0.93	0.92
	St. Dev.	0.624	0.619	0.632	0.681	0.609	0.702	0.757	0.695	0.758	0.749	0.784
	L. Qt.	0.06	0.03	0.17	0.17	0.03	0.18	0.20	0.15	0.18	0.22	0.19
	Med.	0.51	0.48	0.63	0.64	0.46	0.79	0.74	0.74	0.94	1.00	0.96
	U. Qt.	0.81	0.83	0.95	0.93	0.83	1.49	1.28	1.24	1.79	1.83	1.85

Table 3.11: As Table 3.10, but for a central SMBH with spin parameter $q = 0.1$. Noise-induced errors are quoted at a fixed SNR= 500.

Model		\log_{10} of the ratio \mathcal{R} of model to noise-induced error for parameter $X =$										
		$\ln(m)$	$\ln(M)$	q	χ	p_0	ϕ_0	θ_S	ϕ_S	θ_K	ϕ_K	$\ln(D)$
$\chi = 0.9$ vs $\chi = 0$	Mean	0.64	1.12	0.87	6.21	1.88	3.41	3.20	3.21	3.72	3.98	3.79
	St. Dev.	0.519	0.569	0.610	0.603	0.629	0.725	0.617	0.574	0.697	0.621	0.649
	L. Qt.	0.37	0.99	0.63	5.94	1.70	3.33	3.00	2.99	3.31	3.50	3.34
	U. Qt.	0.98	1.43	1.29	6.58	2.21	3.55	3.41	3.44	4.16	4.33	4.39

Table 3.12: Model errors that arise from omitting the spin of the inspiralling object for systems with component masses $[5 \times 10^3 + 10^6] M_\odot$.

3. The importance of including small body spin effects in the modelling of EMRIs and IMRIs

Tables 2.6–3.11 show that the ratio \mathcal{R} of model errors to noise-induced errors is smaller when \mathbf{h}_{AP} tends to \mathbf{h}_{GR} . This feature is particularly evident for more massive binaries, but I must emphasise that I have renormalized these results to a fixed SNR whose value depends on the binary under consideration. Table 2.6 shows that for the binary systems $10M_{\odot} + 10^6M_{\odot}$, the vast majority of sources fulfill the condition that the model errors are smaller than the noise-induced errors. The ratio for the spin of the inspiralling object is similar to the ratio of other intrinsic parameters. However, one should bear in mind that this value is the ratio of two large numbers. As indicated in Section 3.3, the median of its noise-induced error is of the order of $\sim 10^{1.6}$, whereas its model error is of the order of $\sim 10^{1.2}$. Hence, the ratio looks small, but this is not an indication that this parameter can be accurately measured for EMRIs.

Tables 3.8–3.11 indicate that, for louder sources, i.e., more massive BH binaries, model errors are likely to be larger than the statistical errors. This feature had already been pointed out by Cutler & Vallisneri [35] for the inspiral of non-spinning massive BH binaries. In their studies, they used a simple PN model with no spin corrections, for sources with a duration of 1 year, which were truncated at the ISCO of non-spinning BHs, i.e., $p = 6M$. I have now extended that initial calculation by i) building a more accurate waveform model using the equations of motion derived by Saijo et al. [117] for spinning inspiralling objects; ii) augmenting this model with spin-orbit and spin-spin couplings taken from perturbative and PN calculations to amend the equations of motion; and iii) modelling the inspiral phase using the most accurate fluxes available which include perturbative corrections for the spin of the inspiralling body, spin-spin couplings and higher-order fits to Teukolsky calculations. Additionally, I have used a consistent prescription for the computation of the ISCO at which I truncate the waveforms. Small body spin effects produce fairly negligible changes in the value of ISCO for IMRIs, but I have included these in order to be consistent throughout.

There are two reasons why the model error to noise-error ratio appears to increase as the mass of the inspiralling body increases. Firstly, I am using a higher reference SNR to quote the noise errors for the more massive systems, since these are intrinsically louder. At higher SNR, the noise-induced error decreases while the model error is fixed. Nonetheless, if one renormalises the results in the tables to a fixed SNR, across all sources, one still sees that the error ratio, \mathcal{R} , for the 2PN to 0PN comparison tends to increase as the mass ratio η is increased. This is to be expected, since the corrections that I am omitting in the comparison are proportional to the mass ratio and therefore should have a greater impact for higher mass systems.

Tables 3.8–3.11 also show that for the 2PN vs 1.5PN comparisons, the error ratio,

3. The importance of including small body spin effects in the modelling of EMRIs and IMRIs

\mathcal{R} , increases, but it remains small as the mass ratio increases at fixed SNR. The results in Table 3.10 for $\chi = 0.9$ show that, for the 2PN vs 1.5PN comparison, the error ratio $\mathcal{R} \lesssim 4$ in all cases, which is a manageably small value. For this same case, the value of \mathcal{R} is a factor of $\sim 20/30$ larger for the intrinsic/extrinsic parameters for the 2PN vs 0PN comparison. These results then suggest that a model that includes conservative corrections at 2PN order might be sufficient for parameter estimation, since the relative importance of the 1.5PN \rightarrow 2PN change is small, even for the most massive systems. More work is required to confirm this, by comparing this 2PN to a higher order (3PN or 3.5PN) model, but the results presented here seem promising.

Table 3.12 shows the model errors that would arise if one did not include the spin of the inspiralling body in the waveform template, but it was included in the “true” waveform. I show results for the system with component masses $[5 \times 10^3 + 10^6]M_\odot$ since the spin has the biggest impact in that case. This exercise is important in order to understand how much the parameter estimation one could achieve from a GW observation would be degraded if one did not use spinning templates in the search. This table shows that not including small body spin corrections could significantly degrade the accuracy with which the CO mass, SMBH mass and SMBH spin may be determined, since the model errors associated with these parameters are a factor of $\sim 6, 18, 11$, bigger than the noise-induced errors, respectively. In addition, the large quoted error associated with the small body spin parameter χ , is merely an indication that one cannot determine that parameter using a waveform template that does not include it in the first place. These results indicate that the small body spin corrections in IMRIs should not be ignored in detection templates, since doing so may significantly degrade our determination of the system parameters.

In summary, this analysis shows that, for systems with more massive inspiraling objects, model errors will be a limiting factor in determining the system parameters, and that the small object spin should not be ignored. However, if the waveform template includes conservative corrections up to at least 2PN order, this may be sufficient to reduce systematic errors to an acceptable level. Such templates should be able to constrain a source to a sufficiently small region of the parameter space, and then one could follow it up using more accurate and computationally expensive waveform templates, if available.

3.5 Conclusions

I have developed a kludge waveform model that includes small body spin corrections in order to explore the ability of a future low-frequency gravitational wave detector, such as LISA, to measure the spin of black holes inspiralling into much more massive Kerr black holes. This model uses the equations of motion derived by Saijo et al. [117], and includes first-order conservative SF corrections to compute the evolution of the inspiralling object’s orbital frequency. The trajectory of the inspiralling object is computed using accurate prescriptions for the fluxes of energy and angular momentum [63], augmented with perturbative results that include spin-orbit and spin-spin couplings [124].

This analysis has demonstrated that LISA observations will not be able to measure the spin of stellar mass COs inspiralling into SMBHs, i.e., systems with mass ratio $\eta \lesssim 10^{-3}$. This result is in accord with arguments presented elsewhere [6]. However, including small body spin effects will be relevant for signal detection and parameter estimation for binaries with mass ratio $\eta \gtrsim 10^{-3}$. At a fixed SNR of 1000, a LISA observation of a binary with masses $5 \times 10^3 M_\odot + 10^6 M_\odot$ whose components have specific spin parameters $q = \chi = 0.9$, will be able to determine the CO and SMBH masses, the SMBH spin magnitude and the inspiralling BH spin magnitude, χ , to within fractional errors of $\sim 10^{-3}$, 10^{-3} , 10^{-4} , $\sim 10\%$, respectively. One also expects to determine the location of the source in the sky and the SMBH spin orientation to within $\sim 10^{-4}$ steradians. Small body spin effects will be more noticeable when both components of a massive binary are rapidly rotating, but these effects will not have a significant impact on parameter estimation when the central SMBH is slowly rotating.

I have also studied in detail the importance of the first-order conservative part of the SF for parameter estimation using the formalism developed by Cutler & Vallisneri [35]. I have found that for a source with component masses $5 \times 10^3 M_\odot + 10^6 M_\odot$, the relative error when using a 1.5PN template to detect a 2PN signal is small at fixed SNR. Indeed, for the 2PN vs 1.5PN comparison, the ratio \mathcal{R} of the model errors to the noise-induced errors is of order $\mathcal{R} \lesssim 4$ for the intrinsic parameters. In contrast, when comparing 0PN to 2PN templates, this error ratio \mathcal{R} increases by a factor of $\sim 20/30$ for intrinsic/extrinsic parameters. This suggests that including these corrections up to 2PN order may be sufficient to reduce these systematic errors to an acceptable level. I also investigated the importance of including the spin of the small body in the waveform model. For systems with more massive inspiralling objects, the model error that arises from omitting the spin can be one to two orders of magnitude larger than the noise-

3. The importance of including small body spin effects in the modelling of EMRIs and IMRIs

induced error. This suggests that including the spin in waveform templates will be important for such systems.

These results are an extension of the analysis initially carried out by Cutler & Vallisneri [35], but these studies include various ingredients that were not originally considered, namely, the waveform is not purely PN. Rather, it is based on accurate equations of motion for modelling circular-equatorial spinning BH binary systems. This model can also probe regions much closer to the outer horizon of the central Kerr black hole, and hence, test the accuracy of this model in the strong field.

The $5 \times 10^3 M_\odot + 10^6 M_\odot$ system described here can be considered to be an intermediate-mass-ratio inspiral (IMRI). IMRIs in which a stellar mass object falls into an intermediate-mass-black hole might be detected by future ground-based detectors, such as the Einstein Telescope [58]. In the following two Chapters I will assess the capability of the Einstein Telescope to determine the parameters of such systems, when the inspiralling black hole is non-spinning. The small-body-spin corrections in the model described here could be used to augment the IMRI model that is introduced in Chapter 5 to assess the importance and measurability of the small body spin effects in such systems. This project should be pursued in the future in conjunction with the result that will be presented in Chapters 5 and 6.

Chapter 4

Extreme–mass–ratio inspirals in the context of LISA descope studies

4.1 Overview

The LISA science requirements and the conceptual design for the mission went through a refining period in 1993. As a Cornerstone mission within ESA’s former Horizon 2000 Plus programme, the LISA mission would have consisted of six spacecraft. In order to reduce costs, while also maintaining all the scientific capabilities of a six spacecraft mission, a three spacecraft configuration was studied by the science team. The outcome of this study was a conceptual design for LISA consisting of a three arm mission in which the pair of spacecraft at each vertex of the triangular configuration would be replaced by a single spacecraft, housing two instruments. This concept remained fairly stable for about a decade. However, given current NASA budgetary constraints, ESA is now exploring possible simplifications of the mission architecture and re-defining the science goals of the mission within these constraints. In this Chapter I will describe a few alternatives that are under investigation, and I will discuss the impact of these simplifications on the science return in the context of EMRIs.

4.2 LISA descope studies

When LISA was included in the Astro2010 decadal review as a major NASA space mission to be completed within the following decade, its conceptual design consisted of

an equilateral triangle with an arm length of 5 million km, oriented at an angle of 60 degrees with respect to the plane of the Earth’s orbit. Each vertex of this triangle would have a spacecraft housing two telescopes with associated lasers and two free-floating cubes made of a gold-platinum alloy. These test-masses would act as reflectors for the laser beams, and would provide the reference for measuring the distance between the spacecraft.

This ambitious conceptual design is too expensive to be funded by a single space agency. Hence, NASA’s temporary withdrawal from the project has compelled ESA to explore options for the mission that can be realised with a budget of €850m. It is worth exploring these descopes due to the compelling science case of the LISA mission, but with the understanding that a revision of the science goals will be necessary.

A few alternative descope concepts that ESA is currently exploring are summarised in Table 4.1.

Configuration	Descope configurations			
	Laser Power [W]	Telescope Diameter [m]	Arm length [Gm]	Acceleration noise
C1	0.05	0.4	1.0	LPF
C2	2.0	0.4	1.0	DRS
C3	0.7	0.25	1.0	DRS
C4	0.7	0.25	3.0	DRS
C5	2.0	0.28	2.0	DRS

Table 4.1: Specifications of the descope configurations. The acceleration noise LPF corresponds to the acceleration noise target for LISA pathfinder, DRS is the LISA acceleration noise specification.

An analytic fit to the spectral density of the acceleration noise models LPF and DRS, mentioned in Table 4.1, is given by

$$\begin{aligned}
 \text{LPF : } \quad S_h &= 8.17 \times 10^{-48} \left(\frac{1}{f} + \frac{1.8 \times 10^{-4}}{f^2} \right)^2 \text{ Hz}^{-1}, \\
 \text{DRS : } \quad S_h &= 6 \times 10^{-48} \text{ Hz}^{-1},
 \end{aligned}
 \tag{4.1}$$

where f stands for the frequency. Using these analytic fits, I have generated the corresponding noise curves for configurations C1-C5 in Figure 4.1.

The alternative configurations described in Table 4.1 will save money in various ways. The best saving will come from reducing the number of laser links along the arms of the antenna from six to four. This simplification in the architecture may reduce costs by up to €0.25b. Furthermore, launching this simplified “mother-daughter” configuration will be cheaper, since it will require less propellant than a six-link configuration that

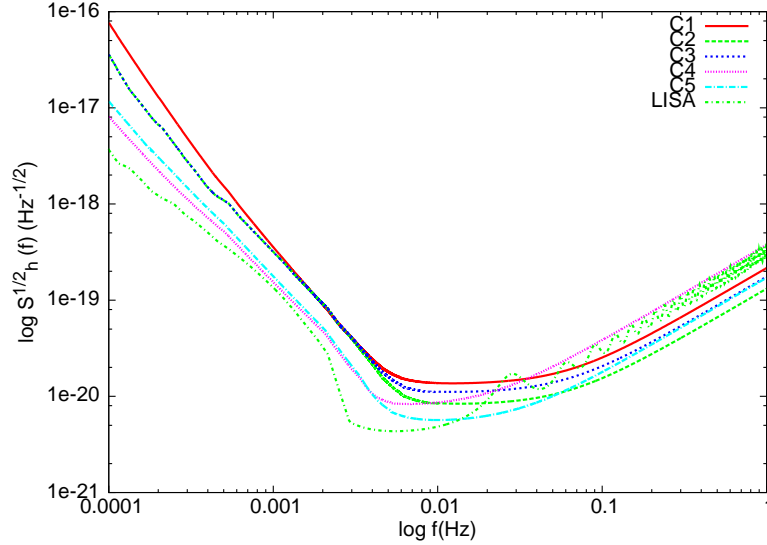


Figure 4.1: Total noise curves for the five descope configurations described in Table 4.1. The total LISA noise curve has been included for reference.

has three satellites with the same specifications. The reduction in the arm length of the antenna will also reduce costs, since less propellant will be needed to maintain the three satellites in a stable configuration. Furthermore, using less powerful lasers will save costs in a twofold way, namely, smaller satellites will be needed to house them, and, in turn, less propellant will be required to put the antenna in orbit.

The aim of this Chapter is to explore the science return that could be obtained with these alternative concepts in the context of EMRIs assuming two different configurations for the antenna, namely, i) an effective two Michelson detector in which the three spacecraft have the same specifications, so there are six laser links, two along each arm; and ii) a mother-daughter configuration in which there are only four links, two along each mother to daughter arm, which is equivalent to a single Michelson detector.

Using the formalism described in Sections 2.2, 2.4.1-2.4.4, I will now present results of the accuracy with which these descope detectors will be able to measure the parameters of EMRIs.

4.3 Parameter estimation results

Table 4.2 presents results for the parameter estimation errors for EMRIs for the five descope configurations described in Table 4.1, assuming an effective two Michelson interferometer, and normalised to a fixed signal-to-noise ratio (SNR) of 30. These

results show that i) there are very little changes in science capability for all the missions concepts; and more importantly, ii) these results are comparable to those shown in Table 2.3. Thus, this study suggests that if an EMRI event is observed by any of the descope missions currently explored by ESA, GW observations made with these detectors will be able to measure the system parameters to great accuracy, except for a loss in the number of events and SNR for an event at a given distance.

Table 4.3 presents results for the parameter estimation errors assuming a four-link configuration, once again quoted at a fixed SNR=30. These results show that for this configuration, any of the descope concepts would still be able to do EMRI science with great accuracy, apart from a minor decrease in the ability to constrain the extrinsic parameters. It should also be noted that in this configuration — a single Michelson interferometer — it is no longer possible to measure polarisation.

4. EMRIs in the LISA descope study

Model		Statistics of distribution of $\log_{10}(\Delta X)$ for error, ΔX , in parameter $X =$									
		$\ln m$	$\ln M$	q	p_0	ϕ_0	θ_S	ϕ_S	θ_K	ϕ_K	$\ln D$
LISA baseline	Mean	-4.04	-3.73	-4.53	-3.88	-0.99	-1.63	-1.74	-1.15	-1.03	-1.58
	St. Dev.	0.121	0.125	0.129	0.125	0.470	0.171	0.209	0.458	0.459	0.391
	L. Qt.	-4.14	-3.82	-4.60	-3.96	-1.35	-1.76	-1.90	-1.53	-1.42	-1.85
	Med.	-4.04	-3.73	-4.52	-3.87	-1.17	-1.63	-1.76	-1.27	-1.14	-1.72
	U. Qt.	-3.94	-3.63	-4.43	-3.77	-0.68	-1.50	-1.65	-0.81	-0.70	-1.41
C1	Mean	-4.11	-3.79	-4.62	-3.15	-0.96	-1.60	-1.73	-1.15	-1.01	-1.09
	St. Dev.	0.104	0.108	0.113	0.108	0.463	0.174	0.173	0.462	0.493	0.323
	L. Qt.	-4.19	-3.86	-4.68	-3.22	-1.31	-1.72	-1.86	-1.54	-1.42	-1.38
	Med.	-4.10	-3.78	-4.60	-3.14	-1.14	-1.59	-1.72	-1.26	-1.12	-1.17
	U. Qt.	-4.02	-3.70	-4.52	-3.07	-0.71	-1.46	-1.62	-0.84	-0.69	-0.87
C2	Mean	-4.14	-3.80	-4.62	-3.17	-0.92	-1.56	-1.67	-1.12	-1.02	-1.09
	St. Dev.	0.093	0.097	0.103	0.097	0.450	0.176	0.211	0.466	0.472	0.318
	L. Qt.	-4.20	-3.87	-4.68	-3.23	-1.25	-1.68	-1.81	-1.53	-1.43	-1.38
	Med.	-4.14	-3.79	-4.61	-3.16	-1.07	-1.56	-1.69	-1.23	-1.11	-1.16
	U. Qt.	-4.07	-3.73	-4.55	-3.10	-0.67	-1.44	-1.57	-0.80	-0.69	-0.86
C3	Mean	-4.12	-3.79	-4.62	-3.16	-0.96	-1.59	-1.72	-1.11	-0.99	-1.05
	St. Dev.	0.099	0.112	0.108	0.100	0.426	0.174	0.159	0.491	0.512	0.344
	L. Qt.	-4.18	-3.85	-4.67	-3.22	-1.30	-1.71	-1.84	-1.52	-1.38	-1.37
	Med.	-4.12	-3.79	-4.60	-3.15	-1.09	-1.58	-1.71	-1.19	-1.09	-1.13
	U. Qt.	-4.05	-3.72	-4.53	-3.09	-0.70	-1.47	-1.60	-0.79	-0.69	-0.85
C4	Mean	-4.04	-3.73	-4.57	-3.10	-0.97	-1.62	-1.75	-1.14	-1.01	-1.09
	St. Dev.	0.113	0.115	0.118	0.111	0.418	0.175	0.144	0.472	0.499	0.327
	L. Qt.	-4.13	-3.81	-4.64	-3.18	-1.33	-1.75	-1.86	-1.54	-1.41	-1.38
	Med.	-4.14	-3.72	-4.55	-3.09	-1.00	-1.61	-1.74	-1.25	-1.11	-1.16
	U. Qt.	-3.95	-3.63	-4.47	-3.00	-0.75	-1.48	-1.65	-0.79	-0.67	-0.85
C5	Mean	-4.11	-3.78	-4.61	-3.15	-0.99	-1.61	-1.74	-1.15	-1.02	-1.09
	St. Dev.	0.101	0.105	0.111	0.103	0.433	0.168	0.201	0.458	0.478	0.359
	L. Qt.	-4.18	-3.85	-4.68	-3.22	-1.31	-1.72	-1.85	-1.52	-1.41	-1.37
	Med.	-4.10	-3.77	-4.59	-3.14	-1.03	-1.59	-1.72	-1.26	-1.10	-1.16
	U. Qt.	-4.03	-3.69	-4.52	-3.07	-0.77	-1.47	-1.64	-0.81	-0.69	-0.87

Table 4.2: Summary of Monte Carlo over FM errors for BH systems ($m = 10M_\odot$) that inspiral into a 10^6M_\odot SMBH with spin parameter $q = 0.9$. The Table shows the mean, standard deviation, median and quartiles of the distribution of the logarithm to base ten of the error in each parameter. The labels C1-C5 correspond to the LISA descope configurations listed in Table 4.1. The results are quoted at a fixed SNR=30.

4. EMRIs in the LISA descope study

Model		Statistics of distribution of $\log_{10}(\Delta X)$ for error, ΔX , in parameter $X =$									
		$\ln m$	$\ln M$	q	p_0	ϕ_0	θ_S	ϕ_S	θ_K	ϕ_K	$\ln D$
C1	Mean	-4.08	-3.75	-4.58	-3.12	-0.79	-1.54	-1.67	-0.92	-0.77	-0.90
	St. Dev.	0.117	0.121	0.126	0.113	0.518	0.195	0.188	0.553	0.551	0.404
	L. Qt.	-4.17	-3.83	-4.65	-3.20	-1.21	-1.68	-1.82	-1.36	-1.21	-1.25
	Med.	-4.08	-3.75	-4.56	-3.12	-0.93	-1.54	-1.68	-1.00	-0.85	-0.96
	U. Qt.	-4.00	-3.66	-4.47	-3.03	-0.41	-1.40	-1.56	-0.52	-0.38	-0.58
C2	Mean	-4.10	-3.77	-4.58	-3.13	-0.80	-1.52	-1.64	-0.93	-0.80	-0.92
	St. Dev.	0.114	0.117	0.120	0.116	0.478	0.198	0.172	0.506	0.483	0.357
	L. Qt.	-4.18	-3.84	-4.65	-3.21	-1.18	-1.64	-1.77	-1.35	-1.21	-1.23
	Med.	-4.10	-3.76	-4.57	-3.13	-0.90	-1.52	-1.65	-0.97	-0.87	-0.95
	U. Qt.	-4.03	-3.69	-4.50	-3.06	-0.46	-1.37	-1.54	-0.55	-0.45	-0.64
C3	Mean	-4.09	-3.75	-4.57	-3.12	-0.82	-1.53	-1.65	-0.91	-0.83	-0.93
	St. Dev.	0.118	0.120	0.122	0.120	0.478	0.183	0.178	0.544	0.474	0.360
	L. Qt.	-4.17	-3.83	-4.66	-3.20	-1.19	-1.65	-1.79	-1.35	-1.18	-1.26
	Med.	-4.09	-3.75	-4.56	-3.12	-0.93	-1.53	-1.66	-0.97	-0.85	-0.97
	U. Qt.	-4.00	-3.66	-4.48	-3.03	-0.51	-1.41	-1.55	-0.53	-0.50	-0.65
C4	Mean	-4.00	-3.67	-4.52	-3.05	-0.81	-1.58	-1.68	-0.93	-0.82	-0.92
	St. Dev.	0.141	0.141	0.140	0.141	0.499	0.177	0.185	0.539	0.493	0.390
	L. Qt.	-4.11	-3.78	-4.61	-3.15	-1.25	-1.71	-1.83	-1.42	-1.27	-1.28
	Med.	-4.01	-3.69	-4.53	-3.06	-0.94	-1.58	-1.70	-1.00	-0.90	-0.98
	U. Qt.	-3.90	-3.59	-4.43	-2.96	-0.48	-1.45	-1.56	-0.55	-0.49	-0.63
C5	Mean	-4.08	-3.74	-4.57	-3.11	-0.82	-1.55	-1.65	-0.90	-0.80	-0.93
	St. Dev.	0.117	0.119	0.122	0.119	0.505	0.176	0.189	0.521	0.493	0.368
	L. Qt.	-4.16	-3.82	-4.64	-3.19	-1.21	-1.68	-1.81	-1.34	-1.15	-1.22
	Med.	-4.08	-3.74	-4.56	-3.11	-0.93	-1.54	-1.66	-1.00	-0.83	-0.99
	U. Qt.	-4.00	-3.66	-4.48	-3.02	-0.50	-1.41	-1.53	-0.50	-0.46	-0.65

Table 4.3: As Table 4.2, but assuming the four-link configuration, which has the equivalent response to a single Michelson interferometer.

4.4 Conclusions

In this Chapter I have briefly explored the accuracy with which a few proposed descoped configurations of the LISA mission, currently being considered by ESA, will be able to do EMRI science. This study is important because, as discussed in Chapter 2, it is hoped that LISA observations of EMRIs can be used to measure the astrophysical parameters of supermassive black holes in the $z < 1$ universe to great accuracy. In addition, it is hoped that GW observations of these systems can provide information about the compact object population in the nuclei of galaxies, and GW data from these events can be used to test the nature of gravity at the high-energy regime.

EMRI science will be degraded by the fact that the number of detectable events will be lower, and the SNR of an event at a given redshift will be lower. However, every detected event will provide precise parameter estimates. Therefore, these studies suggest that EMRIs should still form an integral part of the science goals of the future space-based mission that comes out of these descope studies.

Chapter 5

Source modelling of intermediate–mass–ratio inspirals

5.1 Overview

In part two of this thesis, comprising Chapters 5 and 6, I will present the results of the studies I carried out on source modelling and signal analysis for intermediate–mass–ratio inspirals (IMRIs) in the context of ground–based detector networks. An IMRI is the inspiral of a NS or stellar-mass BH into an intermediate mass black hole (IMBH). The aim of these studies was to shed light on the science that could be done with the proposed third generation ground–based detector the Einstein Telescope (ET), and to provide useful input that will feed into the final design of this instrument.

Developing waveform templates for IMRIs is an important endeavour that involves the modelling of sources in a dynamical regime that has not been extensively explored in the past. The potential payoff of this work is great, as these sources could be detected by advanced GW interferometers, and hence provide the first direct evidence for the existence of IMBHs.

In this Chapter, I will focus on the development of models for IMRI waveforms for circular and equatorial inspirals. I consider two approximations for the waveforms, which both incorporate the inspiral, merger and ringdown phases in a consistent way. One approximation, valid for IMBHs of arbitrary spin, uses the transition model of Ori and Thorne [104] to describe the merger, and this is then matched smoothly onto a ringdown waveform. The second approximation uses the Effective One Body (EOB) approach to model the merger phase of the waveform, and is valid for non-spinning IMBHs.

After introducing the waveform models, I will use them to compute signal-to-noise ratios (SNRs) for IMRI sources detectable by ET. I also show that the two models make predictions for non-spinning inspirals that are consistent to about ten percent. These results were published in the article [73].

5.2 Assumptions

5.2.1 Einstein Telescope Design

The ET is a proposed third generation GW interferometer for which the target is a sensitivity ten times better than that of advanced detectors [58; 69]. It is expected that by siting the interferometer underground, both the seismic and gravity gradients will be significantly reduced, and the range of frequencies to which the interferometer is sensitive can be extended into the 1-10 Hz range, while also maintaining high frequency sensitivity up to 10 kHz. ET’s currently favoured design is a triangular configuration, with three 10 km long arms, and containing three independent detectors with 60° opening angles. This design has the capability to measure polarization at a single site, has lower infrastructure costs, and its sensitivity is a factor $\sqrt{3}/2\sqrt{2} \approx 1.06$ higher than the two right-angle interferometer configuration [64].

In this and the following Chapter, I take the response of a “single ET” to be that of two right-angle interferometers, coplanar and colocated, but rotated 45° with respect to each other. Assuming uncorrelated noise, this set-up is equivalent to ET’s triangular configuration, but as mentioned above, its sensitivity is a factor $\sqrt{3}/2\sqrt{2} \approx 1.06$ smaller. I shall ignore this factor since it is small compared to other uncertainties in the design.

In these studies, I will consider the “ET B” sensitivity curve, which at the current stage of the design study is the official sensitivity curve for ET [77]. The corresponding amplitude spectrum is shown in Figure 5.1.

An analytic fit to the ET-B spectral density is given by [77]

$$S_h^{1/2}(f) = \begin{cases} S_0^{1/2} [a_1 x^{b_1} + a_2 x^{b_2} + a_3 x^{b_3} + a_4 x^{b_4}] & \text{if } f \geq f_s, \\ \infty & \text{if } f < f_s, \end{cases} \quad (5.1)$$

where $x = f/f_0$, f stands for the frequency, $f_0 = 100\text{Hz}$, $S_0 = 10^{-50}\text{Hz}^{-1}$, and f_s is a low frequency cut-off that can be varied, and below which the sensitivity curve can be

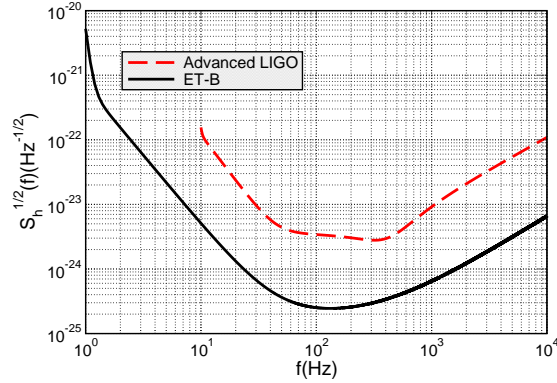


Figure 5.1: Sensitivity curve for the Einstein Telescope, as described in the text. The Advanced LIGO noise curve is also shown for reference.

considered infinite for practical purposes. The various coefficients take the values

$$\begin{aligned}
 a_1 &= 2.39 \times 10^{-27}, & b_1 &= -15.64, \\
 a_2 &= 0.349, & b_2 &= -2.145, \\
 a_3 &= 1.76, & b_3 &= -0.12, \\
 a_4 &= 0.409, & b_4 &= 1.10.
 \end{aligned} \tag{5.2}$$

Although it is hoped that ET will have sensitivity down to 1Hz, it is not yet clear whether this will be achievable, and 3Hz might be more realistic. To be conservative, for the results described in this Chapter, I use a cut-off at 5Hz and started the inspiral evolution at the point when the GWs emitted by the IMRI swept through a frequency of 5Hz. For completeness, I also quote a few results using frequency cut-offs at 3Hz and 1Hz.

As mentioned in Section 1.5, parameter estimation will require the existence of more than one, well-separated, detector. Hence, I will assume the existence of a detector network comprising three detectors sited at the current geographic locations of Virgo, Perth (Australia) and LIGO Livingston. I shall consider five configurations, C1–C5, for a few sample systems. These configurations are C1: one ET at the geographic location of Virgo; C2: as configuration C1 plus a right-angle detector at the location of LIGO Livingston; C3: as configuration C1 plus another ET at the location of LIGO Livingston; C4: as configuration C2 plus another right-angle detector in Perth; and C5: as configuration C3 plus another ET in Perth.

In both this Chapter, and the next in the series, I shall first quote results for the most optimistic configuration C5, i.e., a network of three detectors each with the sensitivity

of a single ET, and then I will go on to compare these with more modest configurations. The aim of this presentation is to exhibit the best performance achievable with a third generation ground-based detector network, but also to set the appropriate framework for the following Chapter, in which the assumption of a detector network will be required for the parameter estimation studies. This presentation is in the spirit of the philosophy currently followed in other studies, of first exploring the best performance achievable by detector networks, both in terms of detection and parameter estimation, for binary inspirals and burst-like events [1; 55; 133]. A 3 ET detector network is extremely optimistic, but I will show that more modest configurations will still produce fairly competitive results.

5.2.2 Sample IMRI systems

I present results for twelve different binary systems. I take four combinations for the component masses, namely $1.4M_{\odot} + 100M_{\odot}$, $1.4M_{\odot} + 500M_{\odot}$, $10M_{\odot} + 100M_{\odot}$ and $10M_{\odot} + 500M_{\odot}$, and three different values for the spin parameter of the central IMBH, $q = 0, 0.3, 0.9$. The twelve sample binaries are all possible combinations of the masses with the spin parameters.

5.3 IMRI waveform modelling - Inspiral phase

For comparable mass binary systems, the early inspiral phase is well modelled using PN theory and the final few cycles can now be computed accurately using numerical relativity (NR) [43]. By contrast, EMRI systems, with mass ratio $\eta = m_1 m_2 / (m_1 + m_2)^2 \sim 10^{-5}$, emit thousands of cycles in a regime where the velocity is a significant fraction of the speed of light. PN theory therefore does not apply, while NR cannot be used due to the large number of orbits that must be modelled. However, EMRIs can be accurately modelled using black hole perturbation theory (BHPT), treating the mass ratio as a small expansion parameter.

IMRIs lie somewhere between these two regimes, with mass ratios at which none of the preceding techniques have been tested. Accurate IMRI waveforms are therefore not known at present, and so I will construct two models using the best information currently available. For the inspiral phase, I will use the “numerical kludge” model introduced in Chapter 2, but augmented with higher-order-in-mass-ratio PN corrections. For the merger phase, I will consider two independent models—one prescription for spinning IMBHs, and an independent approach in the non-spinning limit—which are matched onto the standard prescription for the ringdown phase. I will cross-check

the predictions of these models in the non-spinning limit to test the robustness of the results. While the resulting models may not represent the exact waveform of true IMRI sources, they will capture the main features of the signals and so should make reliable predictions for the SNRs and parameter accuracies that ET observations will achieve.

As described in Chapter 2, the “numerical kludge” waveform model was developed in the context of EMRI systems and has various nice features: a) the waveforms have been checked against more accurate, Teukolsky-based, waveforms for test-particles on geodesic orbits and the overlap exceeds 0.95 over a large portion of the parameter space [5]; b) they are computationally inexpensive; c) conservative self-force corrections to this model have been derived for Kerr circular equatorial orbits at 2PN order [72]. This model is not complete as conservative corrections are not yet known for generic orbits, the phase space trajectories are approximate —although they have been matched to Teukolsky based evolutions—, and the waveform is constructed from the trajectory using a flat-spacetime wave-emission formula. Despite these various approximations, the numerical kludge waveforms should capture the main features of the inspiral waveform accurately.

During the inspiral phase, radiation-reaction drives the motion of the CO. On short timescales, the small object follows an approximately geodesic orbit in the spacetime of the larger body. Over longer timescales, radiation-reaction causes the orbit to evolve adiabatically. This evolution can be characterized by changes in the geodesic orbital elements, namely the energy, E , angular momentum, L_z , and the Carter constant, Q . The models I will develop are valid for circular equatorial IMRIs, so I will only need to consider changes in the energy and angular momentum, since for equatorial orbits $Q = 0$.

The orbital evolution of the CO is obtained by equating the rate of loss of energy E and angular momentum L_z with the corresponding fluxes carried to infinity by the GWs, namely \dot{E} and \dot{L}_z . These fluxes of energy and angular momentum must satisfy a consistency relation to ensure that circular orbits remain circular under radiation reaction [80], i.e.,

$$\dot{E}(p) = \pm \frac{\sqrt{M}}{p^{3/2} \pm a\sqrt{M}} \dot{L}_z(p) = \Omega(p) \dot{L}_z(p). \quad (5.3)$$

To evolve the geodesic parameters I will use the prescription

$$\dot{p} = \frac{dp}{dE} \dot{E} = \frac{dp}{dL_z} \dot{L}_z, \quad (5.4)$$

where the angular momentum, L_z , which is evolved using a PN expansion augmented with fits to more accurate fluxes computed using the Teukolsky equation, is given by relation 2.11.

Additionally, the azimuthal velocity of the orbit, $d\phi/dt = \Omega(p)$, which includes conservative self-force corrections at 2PN order has the following form

$$\begin{aligned}\Omega(p) &= \pm \frac{\sqrt{M}}{p^{3/2} \pm a\sqrt{M}} \left(1 + \delta\Omega \right), \\ &= \Omega_{\text{Kerr}} \left\{ 1 + \eta \left(d_0 + d_1 \left(\frac{M}{p} \right) + (d_{1.5} + q l_{1.5}) \left(\frac{M}{p} \right)^{3/2} + d_2 \left(\frac{M}{p} \right)^2 \right) \right\},\end{aligned}\tag{5.5}$$

where the various coefficients are given by

$$d_0 = \frac{1}{8}, \quad d_1 = \frac{1975}{896}, \quad d_{1.5} = -\frac{27}{10}\pi, \quad l_{1.5} = -\frac{191}{160}, \quad d_2 = \frac{1152343}{451584}.\tag{5.6}$$

These are the ingredients to build the inspiral part of the IMRI waveform models. I should point out that I will not explore the relative importance of the various terms that enter these expressions, but leave that exercise for future work.

Once the inspiral trajectory has been computed, the inspiral waveform can be obtained from an expansion of the form

$$h(t) = -(h_+ - ih_\times) = \sum_{\ell=2}^{\infty} \sum_{m=-\ell}^{\ell} h^{\ell m} {}_{-2}Y_{\ell m}(\theta, \Phi),\tag{5.7}$$

where the spin-weight -2 spherical harmonics ${}_{-2}Y_{\ell m}(\theta, \Phi)$ are given in terms of the Wigner d functions by

$${}_{-s}Y_{\ell m}(\theta, \Phi) = (-1)^s \sqrt{\frac{2\ell+1}{4\pi}} d_{ms}^{\ell}(\theta) e^{im\Phi},\tag{5.8}$$

$$\begin{aligned}\text{with } d_{ms}^{\ell}(\theta) &= \sqrt{(\ell+m)!(\ell-m)!(\ell+s)!(\ell-s)!} \\ &\times \sum_{k=k_i}^{k_f} \frac{(-1)^k (\sin \frac{\theta}{2})^{2k+s-m} (\cos \frac{\theta}{2})^{2\ell+m-s-2k}}{k!(\ell+m-k)!(\ell-s-k)!(s-m+k)!},\end{aligned}\tag{5.9}$$

where $k_i = \max(0, m-s)$ and $k_f = \min(\ell+m, \ell-s)$. Additionally, the complex

conjugates of the spin-weighted spherical harmonics satisfy

$${}_s Y^{\ell m*}(\theta, \Phi) = (-1)^{s+m} {}_{-s} Y^{\ell -m}(\theta, \Phi). \quad (5.10)$$

I shall include only the modes $(\ell, m) = (2, \pm 2)$, which means that, at leading order, the components of the waveform are

$$h_+(t) = \frac{4\mu [\Omega(t) p(t)]^2}{D} \left(\frac{1 + \cos^2 \theta}{2} \right) \cos [2(\phi(t) + \Phi)], \quad (5.11)$$

$$h_\times(t) = \frac{4\mu [\Omega(t) p(t)]^2}{D} \cos \theta \sin [2(\phi(t) + \Phi)], \quad (5.12)$$

where $\Omega(t) = d\phi/dt$ is the orbital frequency, $p(t)$ is the radius of the orbit, and D is the distance to the source.

This model provides a description of the inspiral only, but it ceases to be valid when the CO approaches the ISCO and adiabaticity begins to break down. One requires a different model for the evolution of the CO through the ISCO all the way down to the light ring (LR), where one should match it on to ringdown radiation.

5.4 Transition and plunge phases for an initially spinning IMBH

The approach I adopt to describe the merger waveform is based on a scheme developed by Ori & Thorne [104]. This describes the transition from inspiral to plunge for circular-equatorial inspirals into a massive spinning BH in the extreme-mass-ratio limit. To be consistent with their notation, I have re-expressed the Boyer–Lindquist coordinates (t, p, θ, ϕ) in dimensionless form using the transformations $\tilde{r} = p/M$ and $\tilde{t} = t/M$.

As described in Section 5.3, during the inspiral phase, the CO moves on a circular geodesic orbit with dimensionless angular velocity

$$\tilde{\Omega} \equiv M\Omega = \frac{d\phi}{d\tilde{t}} = \frac{1}{\tilde{r}^{3/2} + q}. \quad (5.13)$$

As the CO inspirals onto the spinning IMBH, it radiates energy which is carried away by GWs. The radiation flux can be written as

$$\dot{E}_{\text{GW}} = -\dot{E} = \frac{32}{5} \eta^2 \tilde{\Omega}^{10/3} \dot{\tilde{E}}, \quad (5.14)$$

with $\dot{\mathcal{E}}$ being a general relativistic correction to the Newtonian, quadrupole-moment formula.

The adiabatic inspiral phase evolution continues until the CO approaches the ISCO. As discussed previously, the adiabatic prescription breaks down somewhat before ISCO, as the orbit starts to evolve more quickly and the instantaneous-geodesic approximation is no longer valid. Hence, one needs to find some point near the ISCO, $\tilde{r}_{\text{trans}} \gtrsim \tilde{r}_{\text{ISCO}}$, that joins smoothly the adiabatic inspiral of Section 5.3 onto the transition phase. This choice must ensure a continuous and smooth matching of the inspiral and transition waveforms. The transition radius, \tilde{r}_{trans} , is the point at which $\dot{\tilde{r}}_{\text{inspiral}}$ becomes “too fast”. “Too fast” obviously has a different meaning according to the binary system under consideration, as it depends on the mass-ratio η . However, the transition solution described in the following provides a unique solution that should match smoothly onto the inspiral. In practice, the chosen matching radius for each binary system ensures that: i) the transition from inspiral to plunge of the radial, Eqs. 5.4, 5.54, and azimuthal, Eqs. 5.5, 5.53, coordinates is smooth; ii) the transition from inspiral, Eqs. 5.11, 5.74, to plunge, Eqs. 5.12, 5.75, of the waveform is smooth; and iii) the choice of \tilde{r}_{trans} is robust, i.e., conditions i) and ii) are met in a vicinity around the precise value of r_{trans} . Furthermore, I have verified that the phasing and the amplitude of the resulting waveform are robust to small changes of the exact choice of \tilde{r}_{trans} .

At the transition point, the circular geodesic has dimensionless angular velocity, energy and angular momentum given by

$$\tilde{\Omega}_{\text{trans}} \equiv M\Omega = \frac{1}{\tilde{r}_{\text{trans}}^{3/2} + q}, \quad (5.15)$$

$$\tilde{E}_{\text{trans}} \equiv \frac{E_{\text{trans}}}{\mu} = \frac{E_{\text{trans}}}{\eta M} = \frac{1 - 2/\tilde{r}_{\text{trans}} + q/\tilde{r}_{\text{trans}}^{3/2}}{\sqrt{1 - 3/\tilde{r}_{\text{trans}} + 2q/\tilde{r}_{\text{trans}}^{3/2}}}, \quad (5.16)$$

$$\tilde{L}_{\text{trans}} \equiv \frac{L_{\text{trans}}}{\mu M} = \tilde{r}_{\text{trans}}^{1/2} \frac{1 - 2q/\tilde{r}_{\text{trans}}^{3/2} + q^2/\tilde{r}_{\text{trans}}^2}{\sqrt{1 - 3/\tilde{r}_{\text{trans}} + 2q/\tilde{r}_{\text{trans}}^{3/2}}}. \quad (5.17)$$

The values of these quantities for the binary systems under consideration are given in Table 5.1. I have also included the values of these quantities evaluated at ISCO for reference.

As the CO enters the transition regime, the geodesic motion ceases to be adiabatic but radiation reaction continues to drive the orbital evolution. In this regime the CO still moves on a nearly circular orbit with radius close to \tilde{r}_{trans} . Additionally, since the

Binary systems	$q = 0.9$			$q = 0.3$		
	\tilde{L}_{trans}	\tilde{E}_{trans}	\tilde{r}_{trans}	\tilde{L}_{trans}	\tilde{E}_{trans}	\tilde{r}_{trans}
[10+100] M_{\odot}	2.113	0.8470	2.533	3.155	0.9308	5.145
[1.4+100] M_{\odot}	2.111	0.8466	2.515	3.155	0.9308	5.129
ISCO	2.100	0.8442	2.321	3.154	0.9306	4.979
[10+500] M_{\odot}	2.109	0.8463	2.498	3.155	0.9308	5.120
[1.4+500] M_{\odot}	2.109	0.8463	2.497	3.155	0.9308	5.119

Table 5.1: Dimensionless values for the energy \tilde{E}_{trans} and angular momentum \tilde{L}_{trans} as defined in Eqs. 5.16, 5.17 at the point of transition \tilde{r}_{trans} . The values for the energy and angular momentum at ISCO have been included for reference.

radiation reaction is proportional to the mass ratio and is therefore weak, the angular velocity and proper time can be approximated by [104]

$$\frac{d\phi}{d\tilde{t}} \equiv \tilde{\Omega} \simeq \tilde{\Omega}_{\text{trans}} , \quad (5.18)$$

$$\frac{d\tilde{r}}{d\tilde{t}} \simeq \left(\frac{d\tilde{r}}{d\tilde{t}} \right)_{\text{trans}} = \frac{\sqrt{1 - 3/\tilde{r}_{\text{trans}} + 2q/\tilde{r}_{\text{trans}}^{3/2}}}{1 + q/\tilde{r}_{\text{trans}}^{3/2}} . \quad (5.19)$$

In the vicinity of \tilde{r}_{trans} , the CO's energy and angular momentum can be written as

$$\tilde{E} = \tilde{E}_{\text{trans}} + \tilde{\Omega}_{\text{trans}}\xi , \quad \tilde{L} = \tilde{L}_{\text{trans}} + \xi , \quad (5.20)$$

where

$$\frac{d\xi}{d\tilde{r}} = -\kappa\eta , \quad \text{and} \quad (5.21)$$

$$\kappa = \frac{32}{5} \tilde{\Omega}_{\text{trans}}^{7/3} \frac{1 + q/\tilde{r}_{\text{trans}}^{3/2}}{\sqrt{1 - 3/\tilde{r}_{\text{trans}} + 2q/\tilde{r}_{\text{trans}}^{3/2}}} \dot{\tilde{c}}_{\text{trans}} . \quad (5.22)$$

To make further progress, it is useful to recast the effective potential, $V(\tilde{r}, \tilde{E}, \tilde{L})$, describing the radial motion for geodesics

$$V(\tilde{r}, \tilde{E}, \tilde{L}) = \tilde{E}^2 - \frac{1}{\tilde{r}^4} \left\{ [\tilde{E}(\tilde{r}^2 + q^2) - \tilde{L}q]^2 - (\tilde{r}^2 - 2\tilde{r} + q^2)[\tilde{r}^2 + (\tilde{L} - \tilde{E}q)^2] \right\} , \quad (5.23)$$

as a function of \tilde{r} and $\xi \equiv \tilde{L} - \tilde{L}_{\text{trans}}$. It is convenient to introduce the variable

$R \equiv \tilde{r} - \tilde{r}_{\text{trans}}$ to parametrise the CO's location during the transition regime. Both R and ξ are small and therefore one can expand the effective potential in terms of these two variables

$$V(R, \xi) = \frac{2\alpha}{3}R^3 - 2\beta R\xi + \text{constant}, \quad (5.24)$$

where α and β are constants to be computed below. This new expression for the effective potential can be plugged into the equation describing the radial evolution in the transition regime, namely,

$$\frac{d^2\tilde{r}}{d\tilde{\tau}^2} = -\frac{1}{2}\frac{\partial V(\tilde{r}, \xi)}{\partial\tilde{r}} + \eta\tilde{F}_{\text{self}}. \quad (5.25)$$

The radial self-force $\eta\tilde{F}_{\text{self}}$ is approximately non-dissipative and hence can be ignored. Absorbing this term into $-\frac{1}{2}\partial V/\partial\tilde{r}$ effectively amounts to changes in \tilde{r}_{trans} , \tilde{E}_{trans} , \tilde{L}_{trans} and α by fractional amounts proportional to η . Likewise, these various quantities change by order $O(\eta)$ as a result of the CO's perturbation of the BH's spacetime geometry [9]. I shall ignore these small corrections in the following analysis.

Once the effective potential 5.24 is plugged into the equation of motion 5.25, and the proper time $\tilde{\tau} \equiv 0$ at the moment when $\xi = 0$, one obtains [104]

$$\frac{d^2R}{d\tilde{\tau}^2} = -\alpha R^2 - \eta\beta\kappa\tilde{\tau}, \quad (5.26)$$

where the constants α, β are given by

$$\alpha = \frac{1}{4} \left(\frac{\partial^3 V(\tilde{r}, \tilde{E}, \tilde{L})}{\partial\tilde{r}^3} \right)_{\text{trans}}, \quad (5.27)$$

$$\beta = -\frac{1}{2} \left(\frac{\partial^2 V(\tilde{r}, \tilde{E}, \tilde{L})}{\partial\tilde{L}\partial\tilde{r}} + \tilde{\Omega} \frac{\partial^2 V(\tilde{r}, \tilde{E}, \tilde{L})}{\partial\tilde{E}\partial\tilde{r}} \right)_{\text{trans}}. \quad (5.28)$$

Eventually the transition regime ends, radiation reaction is no longer important and pure plunge takes over. Thereafter, the CO plunges towards the BH with nearly constant energy and angular momentum given by [104]

$$\begin{aligned} \tilde{L}_{\text{fin}} - \tilde{L}_{\text{trans}} &= -(\kappa\tau_0 T_{\text{plunge}})\eta^{4/5}, \\ \tilde{E}_{\text{fin}} - \tilde{E}_{\text{trans}} &= -\tilde{\Omega}_{\text{trans}}(\kappa\tau_0 T_{\text{plunge}})\eta^{4/5}, \end{aligned} \quad (5.29)$$

where,

$$T_{\text{plunge}} = 3.412, \quad \tau_o = (\alpha\beta\kappa)^{-1/5}. \quad (5.30)$$

During the plunge phase, the evolution is given by the Kerr geodesic equations [99], i.e.,

$$\frac{d^2\tilde{r}}{d\tilde{\tau}^2} = \frac{6\tilde{E}_{\text{fin}}\tilde{L}_{\text{fin}}q + \tilde{L}_{\text{fin}}^2(\tilde{r}-3) + (q^2 - \tilde{r})\tilde{r} - \tilde{E}_{\text{fin}}^2q^2(\tilde{r}+3)}{\tilde{r}^4}, \quad (5.31)$$

$$\frac{d\phi}{d\tilde{t}} = \frac{\tilde{L}_{\text{fin}}(\tilde{r}-2) + 2\tilde{E}_{\text{fin}}q}{\tilde{E}_{\text{fin}}(\tilde{r}^3 + (2+\tilde{r})q^2) - 2q\tilde{L}_{\text{fin}}}, \quad (5.32)$$

$$\frac{d\tilde{r}}{d\tilde{t}} = \frac{\tilde{r}(q^2 + \tilde{r}(\tilde{r}-2))}{\tilde{E}_{\text{fin}}(\tilde{r}^3 + (2+\tilde{r})q^2) - 2q\tilde{L}_{\text{fin}}}. \quad (5.33)$$

Notice that the plunge angular frequency 5.32 is entirely determined by the values of the energy and angular momentum 5.29. Hence, to match the transition regime onto the plunge regime, one only needs find the point $\tilde{r}_{\text{plunge}}$ at which the transition angular frequency 5.13 and the plunge angular frequency 5.32 smoothly match for these specific values of energy and angular momentum 5.29.

These are all the ingredients required to build the waveform model from inspiral to plunge. For the inspiral waveform the cross and plus polarizations are given by 5.11, 5.12, which provide a good approximation before \tilde{r}_{trans} . Thereafter the particle is no longer on a circular orbit. Hence, I will use the following expressions

$$\begin{aligned} h_+(t) &= \frac{\mu}{2D} \left[\left\{ 1 - 2\cos 2\theta \cos^2[\phi(t) + \Phi] - 3\cos[2(\phi(t) + \Phi)] \right\} \dot{r}^2 \right. \\ &+ (3 + \cos 2\theta) \left\{ 2\cos[2(\phi(t) + \Phi)]\phi^2(t) + \sin[2(\phi(t) + \Phi)]\phi(t) \right\} r^2 + \\ &\quad \left\{ 4(3 + \cos 2\theta) \sin[2(\phi(t) + \Phi)]\phi(t)\dot{r} \right. \\ &\left. + (1 - 2\cos 2\theta \cos^2[\phi(t) + \Phi] - 3\cos[2(\phi(t) + \Phi)])\dot{r} \right\} r \Big], \quad (5.34) \end{aligned}$$

$$\begin{aligned} h_\times(t) &= \frac{-2\mu \cos \theta}{D} \left[\sin[2(\phi(t) + \Phi)]\dot{r}^2 \right. \\ &+ \left\{ \cos[2(\phi(t) + \Phi)]\phi(t) - 2\sin[2(\phi(t) + \Phi)]\phi^2(t) \right\} r^2 \\ &\left. + \left\{ 4\cos[2(\phi(t) + \Phi)]\phi(t)\dot{r} + \sin[2(\phi(t) + \Phi)]\dot{r} \right\} r \right], \quad (5.35) \end{aligned}$$

where μ is the mass of the CO and D is the distance to the source. These are flat-spacetime emission formulae applied to a geodesic in curved space and so is in keeping with the ‘‘numerical kludge’’ approach to waveform generation. This approximation is vindicated by the similarity of the results to the EOB waveforms which I will demon-

strate later.

This “transition” waveform model provides a consistent modelling for the gravitational radiation emitted from the early stages of inspiral evolution all the way down to the horizon. However, I will attach the final part of the waveform, i.e., the ringdown part, at the effective LR. The following section describes the method for attaching the plunge phase onto a ringdown waveform. The method is generic, i.e, it is applicable both for “transition” model, and for the EOB scheme which I introduce in Section 5.6.

5.5 Ringdown waveform

The ringdown radiation originates from the distorted Kerr BH that is the end product of the merger, and consists of a superposition of quasinormal modes (QNMs), labelled by indices (ℓ, m, n) , where (ℓ, m) specifies the mode and n the tone. Each mode has a complex frequency $\hat{\omega}$, whose real part is the oscillation frequency and whose imaginary part is the inverse of the damping time [24],

$$\hat{\omega} = \omega_{\ell mn} - i/\tau_{\ell mn}. \quad (5.36)$$

These two observables are uniquely determined by the mass and angular momentum of the newly formed Kerr BH. Recent numerical simulations have shown that the total mass-energy radiated during the merger of two equal-mass maximally spinning BHs ranges from 0.6% – 5% of the total rest mass energy. The energy released in IMRI ringdown radiation will be much lower, as it is suppressed by the mass ratio η .

It would be reasonable to ignore the change in mass of the IMBH and approximate the final mass and spin by the initial values for the central BH. But, for completeness, I will use a one-parameter fit, derived within the framework of the EOB formalism, as an approximation for the final mass M_f of the BH even though this does not account for the IMBH spin [27],

$$M_f/M = 1 + (\sqrt{8/9} - 1)\eta - 0.498(\pm 0.027)\eta^2. \quad (5.37)$$

This fit is consistent with NR simulations to about $\sim 2\%$ accuracy for mass ratios $\eta \gtrsim 0.16$ [40]. Additionally, the extrapolation to smaller values of η is consistent with NR simulations [13] and test-mass limit predictions [40]. The coefficient of the linear term has been calibrated to reproduce results in the test-mass particle limit.

I will also use the fit by Rezzolla, et. al. [114], to compute the final spin of the

post-merger BH

$$a_f/M_f = q_f = q + s_4 q^2 \eta + s_5 q \eta^2 + t_0 q \eta + 2\sqrt{3} \eta + t_2 \eta^2 + t_3 \eta^3, \quad (5.38)$$

in which the coefficients, obtained via a least-squares fit to available data, are

$$\begin{aligned} s_4 &= -0.129 \pm 0.012, & s_5 &= 0.384 \pm 0.261, \\ t_0 &= -2.686 \pm 0.065, & t_2 &= -3.454 \pm 0.132, & t_3 &= 2.353 \pm 0.548. \end{aligned} \quad (5.39)$$

This fit was derived by using available data for spin parameters $q \lesssim 0.8$ and mass ratios $\eta \gtrsim 0.16$ along with exact results which hold in the extreme-mass-ratio limit, i.e., $\eta \rightarrow 0$. For $q = 1$, the fit 5.38 is a non-monotonic function with maximum $q_f = 1.029$ for $\eta \simeq 0.093$, but this fit should be valid for the systems I consider here, for which $\eta \lesssim 0.08$ and $q \leq 0.9$. At present one does not have a good idea as to plausible values of q for the systems that will be detected by ET. If the dominant process by which IMBHs acquire spin is through the capture of COs, their angular momenta will undergo a damped random walk [95], [75]. This process was studied in detail by Mandel [91], who computed the probability distribution for the spin of IMBHs that gain mass following a series of minor mergers. This work suggested that IMBHs with masses in the $\sim 10^2$ – $10^4 M_\odot$ range would have spin parameter $q \sim 0.3$.

Given the mass and spin of the final Kerr BH, one can uniquely determine the complex ringdown frequencies 5.36. I do this by building an interpolation function based on the data provided in Table 2 of Berti, et. al. [14], and evaluating this function for the final IMBH spin. Following Berti, et. al. [14], and Buonanno, et. al. [24], I construct a ringdown waveform that includes the fundamental mode ($\ell = 2, m = 2, n = 0$) and two overtones ($n = 1, 2$). In order to be consistent, I also include the “twin” modes with frequency $\omega'_{\ell mn} = -\omega_{\ell - mn}$ and a different damping $\tau'_{\ell mn} = \tau_{\ell - mn}$. I include the “twin modes” since a mode with a given (ℓ, m) will always consist of a superposition of two different exponentials. It might be the case that one of the exponentials has a shorter damping time or is less excited in the given physical situation and hence become “invisible”, but formally one cannot have an isolated “ $\ell = m = 2$ ” frequency with a positive real part. Furthermore, a single-mode expansion restricts attention to circularly polarized GWs. These considerations are not important for non-spinning BHs, as the two mirror solutions are degenerate in the modulus of the frequency and in the damping time. Adding BH rotation acts in a similar way to an external magnetic field on the energy levels of an atom, causing a Zeeman splitting effect of the QNM

frequencies.

The ringdown waveform is given by

$$\begin{aligned}
 h(t) = -(h_+ - ih_\times) &= \frac{M_f}{D} \sum_{lmn} \left\{ \mathcal{A}_{\ell mn} e^{-i(\omega_{\ell mn} t + \phi_{\ell mn})} e^{-t/\tau_{\ell mn}} S_{\ell m}(a\omega_{\ell mn}) \right. \\
 &\quad \left. + \mathcal{A}'_{\ell mn} e^{i(\omega_{\ell mn} t + \phi'_{\ell mn})} e^{-t/\tau_{\ell mn}} S_{\ell m}^*(a\omega_{\ell mn}) \right\}, \quad (5.40)
 \end{aligned}$$

in which M_f and D are the mass of the Kerr BH formed after merger and the distance to the source, respectively.

The spheroidal harmonics of spin-weight -2 , ${}_{-2}S_{\ell m}$ obey the equation

$$\begin{aligned}
 \left[\frac{1}{\sin \theta} \frac{d}{d\theta} \left\{ \sin \theta \frac{d}{d\theta} \right\} - a^2 \omega^2 \sin^2 \theta - \frac{(m - 2 \cos \theta)^2}{\sin^2 \theta} \right. \\
 \left. + 4a\omega \cos \theta - 2 + 2ma\omega + \lambda \right] {}_{-2}S_{\ell m}(a\omega) = 0. \quad (5.41)
 \end{aligned}$$

Expanding ${}_{-2}S_{\ell m}(a\omega)$ and the eigenvalue λ [97]

$$\begin{aligned}
 {}_{-2}S_{\ell m}(a\omega) &= {}_{-2}Y_{\ell m} + a\omega S_{\ell m}^{(1)} + (a\omega)^2 S_{\ell m}^{(2)} + O((a\omega)^3), \\
 \lambda &= \lambda_0 + a\omega \lambda_1 + a^2 \omega^2 \lambda_2 + O((a\omega)^3), \quad (5.42)
 \end{aligned}$$

where ${}_{-2}Y_{\ell m}$ are the spherical harmonics of spin weight $s = -2$. The normalizations of ${}_{-2}Y_{\ell m}$ and ${}_{-2}S_{\ell m}(a\omega)$ are fixed by

$$\int_0^\pi |{}_{-2}Y_{\ell m}|^2 \sin \theta d\theta = \int_0^\pi |{}_{-2}S_{\ell m}(a\omega)|^2 \sin \theta d\theta = 1. \quad (5.43)$$

After plugging 5.42 into 5.41 and collecting terms, one obtains the zero and first order corrections to the eigenvalue λ , i.e.,

$$\lambda_0 = (\ell - 1)(\ell + 2), \quad \lambda_1 = -2m \frac{\ell(\ell + 1) + 4}{\ell(\ell + 1)}.$$

The first order correction to ${}_{-2}S_{\ell m}(a\omega)$ is given by

$$S_{\ell m}^{(1)} = \sum_{\ell'} c_{\ell m}^{\ell'} {}_{-2}Y_{\ell' m}, \quad (5.44)$$

where the non-zero coefficients $c_{\ell m}^\ell$ are

$$\begin{aligned} c_{\ell m}^{\ell+1} &= \frac{2}{(\ell+1)^2} \left[\frac{(\ell+3)(\ell-1)(\ell+m+1)(\ell-m+1)}{(2\ell+1)(2\ell+3)} \right]^{1/2}, \\ c_{\ell m}^{\ell-1} &= -\frac{2}{\ell^2} \left[\frac{(\ell+2)(\ell-2)(\ell+m)(\ell-m)}{(2\ell+1)(2\ell-1)} \right]^{1/2}. \end{aligned} \quad (5.45)$$

This first order approximation will suffice for this analysis since $a\omega \ll 1$ in Eq. 5.41 for the systems I shall consider. Using these relations one can split 5.40 into plus and cross polarizations, which can then be matched onto the corresponding components of the plunge waveforms. This matching requires the determination of 24 constants, 12 for each polarization, but the equations can be rewritten as two 6D systems of equations. I do this matching at the time when the particle reaches the LR.

The approach to determine the various amplitudes and ringdown phases of Eq. 5.40 is the following: use the plunge waveform to compute ten points before and after the LR to build an interpolation function. This function can be used to match onto the various QNMs by imposing continuity of the waveform and all the necessary higher order time derivatives. I first match the plunge waveform onto the leading ringdown tone $n = 0$ at the point where the orbital frequency (5.32, 5.53) peaks, t_{peak} . This fixes 2 constants per polarization. I then use these values as seeds to compute the amplitudes and phases of the first overtone at a time $t_{\text{peak}} + dt$. Finally, I use the values of the amplitudes and phases of the leading tone and first overtone to determine the four remaining constants at a time $t_{\text{peak}} + 2dt$.

In terms of the relative SNRs contributed by the different tones, I have found that the leading tone along with its twin mode are the major contributors. These two modes contribute more than 90% of the SNR for the various binary systems under consideration. The remaining two overtones and their twin modes do not contribute substantially to SNR, but I have included them for completeness and to achieve the best possible modelling of the ringdown waveform.

5.6 Plunge and merger waveform from the effective one-body approach

In order to cross-check the predictions of the IMRI “transition model” in the non-spinning limit, I have used an independent approach to model the plunge and merger phases, which is based on the EOB formalism. Note, however, that the ringdown waveform presented in Section 5.5 is generic and can be applied to this new prescription.

Therefore, within this framework, a complete waveform model consists of the inspiral waveform described in Section 5.3, the plunge and merger waveform to be discussed below, and the ringdown waveform described in Section 5.5.

Although I use the EOB model only in the non-spinning limit, an extension of the EOB scheme does exist which includes leading-order spin-orbit and spin-spin effects of a binary system for an “effective test particle” moving in a Kerr-type metric [36], and next-to-leading-order spin-orbit couplings [39]. However, it has been recently found [105] that it is not straightforward to include higher-order non-spinning PN couplings, such as the 4PN and 5PN adjustable parameters that were recently calibrated to NR simulations for non-spinning systems [28; 42], using these Hamiltonians [36; 39]. Additionally, the EOB Hamiltonian in [39] does not reduce to the Hamiltonian of a spinning test particle in Kerr spacetime. This issue was recently resolved in [12], in which a canonical Hamiltonian was derived for a spinning test particle in a generic curved spacetime at linear order in the particle spin. The construction of an improved EOB Hamiltonian based on the results of [12] has recently been obtained [11]. The Hamiltonian derived in [39] has recently been used in an exploratory study to calibrate the EOB parameters using NR simulations of spinning, non-precessing, equal mass BHs. This is the same approach that was previously used with great success for non-spinning BH systems, e.g., to derive fits for the final mass and spin of a BH after merger that are consistent with NR to about $\sim 2\%$ accuracy [40]. I used the non-spinning EOB model only in this work because that model is more mature. However, the EOB model has recently been used to model circular-equatorial EMRIs around spinning supermassive BHs, using fits of various PN parameters to Teukolsky-based waveforms [136]. Comparisons between an IMRI model based on this spinning EOB framework and the waveforms constructed using the transition model should be pursued in the future.

The standard analytic method to study the two-body dynamics of comparable-mass BHs is the PN framework, which is an expansion in the characteristic orbital velocity v/c . Accurate equations of motion at 2.5PN order were derived in the 1980’s [37]. At present, corrections at 3.5PN-level in the equations of motion are available [83; 101; 106], and the diffeomorphism-invariant dimensional regularization method proposed by Blanchet et al., [17] has allowed the modelling of GWs emitted by inspiralling non-spinning compact binaries up to 3.5PN order of accuracy. The PN formalism is reliable as long as the PN expansion parameter $\delta = M/d \ll 1/6$, where M is the total mass of the binary system and d is the separation between the two BHs, i.e., only during the early inspiral stage. Once $\delta \gtrsim 1/12$, one requires an alternative description of

the motion and radiation to accurately model the final stages of inspiral plus merger and ringdown [43]. NR is the best candidate to model these various evolution phases for comparable-mass BHs. However, the need to compute thousands of waveform templates to carry out matched filtering searches makes NR an impractical tool due to the high computational cost of producing individual waveforms.

In order to circumvent this problem, Buonanno & Damour [25] introduced a framework to study the entire waveform using conservative dynamics at 2PN order. This scheme provides an accurate model from the early stages of inspiral down to the last stable orbit (LSO). Inside the LSO, the scheme includes a non-perturbative plunge prescription that is valid down to the LR and, thereafter, the model can be matched onto ringdown radiation. The basic claim for the validity of the EOB approach is that it is possible to use analytical tools to obtain a sufficiently accurate waveform from inspiral to ringdown. Instead of using PN expansions in the original form, resummation methods (a non-polynomial function of the symmetric mass ratio $\eta = m_1 m_2 / M^2$, which incorporates some of the expected non-perturbative features of the exact results) can be used to improve the convergence properties of the PN expansions. In the test-mass limit, $\eta \rightarrow 0$, the two basic ingredients of a GW signal, the two-body energy and the GW energy flux, are first resummed. The resulting EOB model is constructed to exactly recover geodesic motion in the test-mass limit. It is expected that the resummed quantities may also provide a good description for the comparable-mass case, since this is in effect a smooth deformation of the test-mass limit. The intrinsic flexibility of the model allowed a natural extension to higher order [19] once the 3PN calculation was completed. The success of this approach has been vindicated by recent advances in NR, as it has been possible to construct EOB waveforms that match the results of the numerical simulations very well [43].

One of the central features of the EOB approach is its success at encoding the conservative part of the relative orbital dynamics into the dynamics of an effective particle, i.e., to map the *real* conservative two-body dynamics at the highest PN order available, onto an *effective* one-body problem, in which a test particle of mass $\mu = m_1 m_2 / M$ moves in some effective background metric $g_{\mu\nu}^{\text{eff}}$. In the particular case of non-spinning binaries, and ignoring radiation-reaction effects, the best effective metric was found to be a deformation of the Schwarzschild metric, with η playing the role of a deformation parameter.

In order to be self-contained in the subsequent discussion, I introduce the mathematical machinery required to construct the plunge waveform model. I first show how to obtain the cross and plus polarizations for the plunge phase evolution, and then I

go on to explain how one can match the inspiral waveform model of Section 5.3 onto this plunge waveform.

Using the phase space variables (r, ϕ, p_r, p_ϕ) , one can write the effective EOB Hamiltonian for non-spinning binaries at 3PN order as follows

$$H_{\text{eff}}(\mathbf{r}, \mathbf{p}) = \mu \hat{H}_{\text{eff}}(\mathbf{r}, \mathbf{p}) = \mu \sqrt{A(r) \left[1 + \mathbf{p}^2 + \left(\frac{A(r)}{D(r)} - 1 \right) (\mathbf{n} \cdot \mathbf{p})^2 + \frac{1}{r^2} (z_1 (\mathbf{p}^2)^2 + z_2 \mathbf{p}^2 (\mathbf{n} \cdot \mathbf{p})^2 + z_3 (\mathbf{n} \cdot \mathbf{p})^4) \right]}, \quad (5.46)$$

where $\mathbf{n} = \mathbf{r}/r$, $\mu = m_1 m_2 / M$, and $r = |\mathbf{r}|$. It is convenient to replace the radial momentum p_r by the momentum conjugate to the tortoise radial coordinate $r_* = \int dr (B(r)/A(r))^{1/2}$, where $A(r)$, $B(r)$ are metric functions which will be defined below. It is convenient to do this because p_{r_*} tends to a finite value after merger, whereas p_r diverges at the event horizon. Such a coordinate transformation allows a more controlled treatment of the late part of the EOB dynamics [43]. Under this coordinate transformation the EOB Hamiltonian takes the form

$$\hat{H}_{\text{eff}} = \sqrt{p_{r_*}^2 + A(r) \left(1 + \frac{p_\phi^2}{r^2} + z_3 \frac{p_{r_*}^4}{r^2} \right)}, \quad (5.47)$$

and the mapping between the real and effective EOB Hamiltonian is given by

$$\hat{H}_{\text{EOB}}(r, p_{r_*}, p_\phi) = \frac{H_{\text{real}}}{\mu} = \frac{1}{\eta} \sqrt{1 + 2\eta (\hat{H}_{\text{eff}} - 1)}, \quad (5.48)$$

where $\hat{H}_{\text{real}} = H_{\text{real}}/\mu$. This relation holds true at 2PN and 3PN order. The arbitrary coefficients z_1, z_2 and z_3 in Eq. 5.46 are subject to the constraint

$$8z_1 + 4z_2 + 3z_3 = 6(4 - 3\eta)\eta. \quad (5.49)$$

It is possible to determine these coefficients by means of a fit to numerical results for comparable mass systems. One should bear in mind that in so doing, the coefficients must reproduce exact results in the test-mass limit. To achieve this, one has to ensure that z_1, z_2 and z_3 must go to zero as $\eta \rightarrow 0$. On the other hand, Damour, et al., [44], found that the terms proportional to z_2, z_3 in Eq. 5.46 are very small for quasicircular orbits. They also noticed the convenience of setting $z_1 = 0$ because, in any other case,

z_1 could be suitably chosen so as to cancel the 3PN contribution in the metric coefficient $A(r)$. Hence, I shall follow the general philosophy adopted by Damour et. al. [44], and Buonanno et. al., [23] and set $z_1 = z_2 = 0$, $z_3 = 2(4 - 3\eta)\eta$.

Additionally, in order to ensure the existence and η -continuity of a LSO, as well as the existence and η -continuity of an η -deformed analog of the LR, the metric coefficient $A(r)$ must be Padé resummed,

$$A_{P_3^1}^{3\text{PN}}(r) = \frac{r^2 [(a_4(\eta) + 8\eta - 16) + r(8 - 2\eta)]}{r^3(8 - 2\eta) + r^2[a_4(\eta) + 4\eta] + r[2a_4(\eta) + 8\eta] + 4[\eta^2 + a_4(\eta)]}, \quad (5.50)$$

where

$$a_4(\eta) = \left[\left(\frac{94}{3} - \frac{41}{32}\pi^2 \right) \eta \right]. \quad (5.51)$$

The LR in the test-mass limit is the solution to $d/dr(A(r)/r^2) = 0$. For $\eta \neq 0$, the η -deformed LR is obtained by solving $d/dr(A(r, \eta)/r^2) = 0$. The existence of this “deformed” LR guarantees that in its vicinity the orbital frequency Ω reaches a maximum. Additionally, the Padé resummation of the metric coefficient $D(r)$ ensures an η -continuity in the plunging phase. Its Padé resummed form at 3PN is given by

$$D_{P_3^0}^{3\text{PN}}(r) = \frac{r^3}{r^3 + 6\eta r + 2\eta(26 - 3\eta)}. \quad (5.52)$$

Using reduced quantities $\hat{H}_{\text{real}} = H_{\text{real}}/\mu$, $\hat{t} = t/M$, $\hat{\Omega} = \Omega M$, the EOB equations of motion that describe the orbital evolution from the LSO to the LR are [27],

$$\frac{d\phi}{d\hat{t}} = \frac{Ap_\phi}{\eta r^2 \hat{H} \hat{H}_{\text{eff}}} \equiv \hat{\Omega}, \quad (5.53)$$

$$\frac{dr}{d\hat{t}} = \left(\frac{A}{B} \right)^{1/2} \frac{1}{\eta \hat{H} \hat{H}_{\text{eff}}} \left(p_{r_*} + z_3 \frac{2A}{r^2} p_{r_*}^3 \right), \quad (5.54)$$

$$\frac{dp_\phi}{d\hat{t}} = \hat{\mathcal{F}}_\phi, \quad (5.55)$$

$$\frac{dp_{r_*}}{d\hat{t}} = - \left(\frac{A}{B} \right)^{1/2} \frac{1}{2\eta \hat{H} \hat{H}_{\text{eff}}} \left\{ A' + \frac{p_\phi^2}{r^2} \left(A' - \frac{2A}{r} \right) + z_3 \left(\frac{A'}{r^2} - \frac{2A}{r^3} \right) p_{r_*}^4 \right\}, \quad (5.56)$$

where $\hat{\mathcal{F}}_\phi$ is the ϕ component of the radiation-reaction force, and $D(r) = A(r)B(r)$.

I use this set of equations only to model the waveform evolution from the LSO onwards. Hence, it is reasonable to assume that the two-body dynamics is no longer

driven by radiation–reaction, but occurs along a geodesic with constant angular momentum p_ϕ given by [27]

$$p_\phi^2 = - \left[\frac{A'(u)}{(u^2 A(u))'} \right]_{\text{LSO}}, \quad (5.57)$$

where $u = 1/r$ and the prime denotes d/du . The motion during plunge remains quasi-circular in the sense that $p_r^2/B(r) \ll p_\phi^2/r^2$.

In the limit $\eta \rightarrow 0$, one knows that circular orbits in a Schwarzschild geometry satisfy the Kepler law $\Omega^2 r^3 = 1$. It is common to use $v_\Omega \equiv \Omega^{1/3}$ or $x_\Omega \equiv \Omega^{2/3}$ to describe all PN corrections whether they are proportional to the square of the linear azimuthal velocity ($v_\phi = \Omega r$) or to the gravitational potential ($U = 1/r$). In order to generalise this to the case $\eta \neq 0$, it is necessary to introduce the functions

$$\psi(r, p_\phi) = \frac{2}{r^2} \left(\frac{dA(r)}{dr} \right)^{-1} \left[1 + 2\eta \left(\sqrt{A(r) \left(1 + \frac{p_\phi^2}{r^2} \right)} - 1 \right) \right], \quad (5.58)$$

$$r_\Omega = r \psi(r, p_\phi), \quad (5.59)$$

so that this modified radius r_Ω is related to Ω by the standard Kepler law $\Omega^2 r_\Omega^3 = 1$. This expression holds true during plunge, while the combination $K = \Omega^2 r^3$ becomes of order 0.5 at the effective LR. I use this modified relation, $\Omega^2 r_\Omega^3 = 1$, to determine Ω inside the LSO. Finally, I use Eqs. (4.51) of [26] to determine the value of p_r at the LSO, i.e.,

$$p_r = \left[\frac{1}{C_r} (A_r)^{-2/5} (B_r)^{3/5} \frac{d\rho}{d\tau} \right]_{\text{LSO}}, \quad (5.60)$$

where

$$C_r^{\text{LSO}} = \left[\frac{1}{p_r} \frac{\partial \hat{H}_{\text{EOB}}}{\partial p_r}(r, p_r, p_\phi) \right]_{p_r \rightarrow 0}, \quad (5.61)$$

$$A_r^{\text{LSO}} = C_r^{\text{LSO}} \left(\frac{\partial^3 \hat{H}_{\text{EOB}}(r, p_r = 0, p_\phi)}{\partial r^3} \right)_{\text{LSO}}, \quad (5.62)$$

$$B_r^{\text{LSO}} = C_r^{\text{LSO}} \left[\left(\frac{\partial^2 \hat{H}_{\text{EOB}}(r, p_r = 0, p_\phi)}{\partial r \partial p_\phi} \right) \hat{\mathcal{F}}_\phi \right]_{\text{LSO}}, \quad (5.63)$$

$$\frac{d^2 \rho}{d\tau^2} + \frac{1}{2} \rho^2 = -\tau, \quad (5.64)$$

and the “universal ρ -equation” is solved by fixing the initial values of ρ , $\dot{\rho}$ in the adiabatic limit, i.e., by ignoring the right hand side term in Eq. 5.64

$$\rho_{\text{adiab}} = \sqrt{-2\tau}, \quad \left(\frac{d\rho}{d\tau} \right)_{\text{adiab}} = -\frac{1}{\rho_{\text{adiab}}}.$$

Finally, one can obtain p_{r*} using the transformation $p_r = (dr_*/dr)p_{r*}$, with $r_* = \int dr (B(r)/A(r))^{1/2}$. Having found p_{r*} , one can in turn solve the set of Eqs. 5.53, 5.54 and 5.56 for the plunge phase.

Once the orbital evolution has been determined, the EOB waveform is given in terms of spin-weight -2 spherical harmonics $_{-2}Y_{\ell m}(\theta, \Phi)$ through the relation

$$h_{\ell m} \equiv -(h_+ - ih_\times)_{\ell m} = - \int d\Omega \, _{-2}Y_{\ell m}^*(\theta, \Phi) (h_+ - ih_\times). \quad (5.65)$$

For consistency with the modelling of the inspiral phase, I shall include only the two modes $(\ell, m) = (2, \pm 2)$. At leading PN order the two modes h_{22} and h_{2-2} are given by

$$\frac{D}{M} h_{22}^{\text{EOB}}(t) = -8 \sqrt{\frac{\pi}{5}} \eta (r_\Omega(t) \Omega(t))^2 F_{22}(t) e^{-2i\phi(t)}, \quad (5.66)$$

$$h_{2-2}^{\text{EOB}}(t) = h_{22}^*(t), \quad (5.67)$$

where D is the distance to the source, M is the total mass of the binary system and $\phi(t)$ is the binary orbital phase. The factor F_{22} is a resummed version of all the PN corrections and is given by

$$F_{22}(t) = \hat{H}_{\text{eff}} T_{22}(t) \rho_{22}^2(x(t)) e^{i\delta_{22}(t)}, \quad (5.68)$$

where $x(t) = r_\Omega^{-1}$, and $T_{\ell m}(t)$ is a resummed version of an infinite number of logarithmic terms that enter the transfer function between the near-zone and far-zone waveforms. These terms arise due to tail effects connected to the wave propagation in a Schwarzschild background of mass $M_{\text{ADM}} = H_{\text{EOB}}^{\text{real}}$ [43]. The factor $\delta_{\ell m}$ is a supplementary phase which corrects the phase effects not included in the complex tail factor $T_{\ell m}$.

Finally, in order to enhance the agreement between the EOB model and numerically computed waveforms near the end of inspiral and during the beginning of plunge, I have introduced the resummed quantity $\rho_{\ell m}$, which enters the waveform only through its ℓ -th power, $\rho_{\ell m}^\ell$. Previous waveform models have utilised a different PN improving factor F_{22} (see Eq. 5.68), namely, $F_{22}(t) = \hat{H}_{\text{eff}} T_{22}(t) f_{22}(x(t)) e^{i\delta_{22}(t)}$, where f_{22} is a PN-expanded amplitude factor. The Taylor-expanded $f_{\ell m}$'s produce results that are incompatible with numerical data close to the LSO. This problem arises because the $f_{\ell m}$'s have coefficients that grow linearly with ℓ , and these terms are problematic for the accuracy of PN-expansions, as shown in [38]. Replacing $f_{\ell m}$ by its ℓ -th root $\rho_{\ell m} = [f_{\ell m}]^{1/\ell}$ seems to be a cure for these accuracy problems and improves agreement with NR in the strong-field/fast-motion regime [43]. The explicit forms of the various quantities introduced above are [38; 41],

$$T_{22} = \frac{\Gamma(3 - 2i\hat{k})}{\Gamma(3)} e^{\pi\hat{k}} e^{2i\hat{k}\log(2kr_0)}, \quad (5.69)$$

$$\delta_{22} = \frac{7}{3} H_{\text{real}} \Omega + \frac{428}{105} \pi (H_{\text{real}} \Omega)^2 - 24\eta x^{5/2}, \quad (5.70)$$

$$\begin{aligned} \rho_{22}(x; \nu) = & 1 + \left(\frac{55\nu}{84} - \frac{43}{42} \right) x + \left(\frac{19583\nu^2}{42336} - \frac{33025\nu}{21168} - \frac{20555}{10584} \right) x^2 \\ & + \left\{ \frac{10620745\nu^3}{39118464} - \frac{6292061\nu^2}{3259872} + \frac{41\pi^2\nu}{192} - \frac{48993925\nu}{9779616} - \frac{428}{105} \text{eulerlog}_2(x) + \right. \\ & \left. \frac{1556919113}{122245200} \right\} x^3 + \left\{ \frac{9202}{2205} \text{eulerlog}_2(x) - \frac{387216563023}{160190110080} \right\} x^4 \\ & + \left\{ \frac{439877}{55566} \text{eulerlog}_2(x) - \frac{16094530514677}{533967033600} \right\} x^5 + \mathcal{O}(x^6), \end{aligned} \quad (5.71)$$

in which

$$\begin{aligned}
 \hat{k} &\equiv GH_{\text{real}}m\Omega, & k &= m\Omega, \\
 r_0 &= 2M, & x(t) &= \frac{1}{r_\Omega}, \\
 \text{eulerlog}_2(x) &= \gamma_E + 2 \log 2 + \frac{1}{2} \log x, & \text{with } \gamma_E &= 0.577215,
 \end{aligned} \tag{5.72}$$

with M being the total mass of the binary as before.

In order to facilitate the matching between the inspiral and plunge waveforms, one can rewrite the factor $F_{22}(t) = G(t) e^{i\epsilon(t)}$, where both $G(t)$ and $\epsilon(t)$ are real quantities. The waveform can then be written as

$$\begin{aligned}
 h(t) &\equiv -(h_+ - ih_\times) \\
 &= {}_{-2}Y_{22}(\theta, \Phi) h_{22}(t) + {}_{-2}Y_{2-2}(\theta, \Phi) h_{2-2}(t).
 \end{aligned} \tag{5.73}$$

Using Eq. 5.73, the cross and plus waveform components for the plunge and merger can be written as

$$h_+(t) = \frac{4\mu G(t) [\Omega(t) r_\Omega(t)]^2}{D} \left(\frac{1 + \cos^2 \theta}{2} \right) \cos \left[2(\phi(t) + \Phi - \frac{1}{2}\epsilon(t)) \right], \tag{5.74}$$

$$h_\times(t) = \frac{4\mu G(t) [\Omega(t) r_\Omega(t)]^2}{D} \cos \theta \sin \left[2(\phi(t) + \Phi - \frac{1}{2}\epsilon(t)) \right]. \tag{5.75}$$

Now that I have found explicit expressions for the plus and cross polarizations of the plunge waveform, I match these on to the inspiral waveform following the scheme described in Section 5.4.

Table 5.2 presents the values of the energy and angular momentum, as defined in Eq. 2.9, evaluated at the transition point, r_{trans} .

Binary systems	\tilde{L}_{trans}	\tilde{E}_{trans}	r_{trans}
[10+100] M_\odot	3.4648	0.9429	6.125
[1.4+100] M_\odot	3.4646	0.9428	6.107
ISCO	3.4641	0.9428	6.000
[10+500] M_\odot	3.4646	0.9428	6.100
[1.4+500] M_\odot	3.4645	0.9428	6.093

Table 5.2: Dimensionless values for the energy \tilde{E}_{trans} and angular momentum \tilde{L}_{trans} , as defined in Eqs. 5.16, 5.17, at the point of transition r_{trans} . The values for the energy and angular momentum at ISCO have been included for reference.

By construction, the plunge waveform is a good description of the waveform all the way to the event horizon. However, as for the transition model, I have attached a set of QNMs at the effective LR. Following Buonanno, et. al. [27], I attach the ringdown modes at the time when the orbital frequency 5.53 peaks. The frequency of these ringdown modes depends on the mass and spin of the newly formed Kerr BH after merger, which can be estimated using the following EOB-based fit for mass and spin of the post-merger Kerr BH [27]

$$M_f/M = 1 + (\sqrt{8/9} - 1)\eta - 0.498(\pm 0.027)\eta^2, \quad (5.76)$$

$$a_f/M_f = q_f = \sqrt{12}\eta - 2.900(\pm 0.065)\eta^2. \quad (5.77)$$

This one-parameter fit for the spin of the newly formed Kerr BH, Eq. 5.77, differs from the zero-spin limit of the spin-dependent expression used for the “transition model”, Eq. 5.38. The two expressions render similar results, but I will use Eq. 5.77 to estimate the final spin of the post-merger Kerr BH in the context of the EOB-based waveform model. The reason for doing this is to develop a model that is purely based on EOB-results, hence ensuring consistency in the modelling, and because this is the conservative approach.

I will use the EOB model both as a consistency check of the transition model, and to assess the level of uncertainty in my results. The latter is best accomplished by using the EOB-based fit for the final spin to make the waveform as different as possible from non-EOB-based results available in the literature. I have verified that the waveform models are not particularly sensitive to this choice, and the level of consistency I quote later encodes this uncertainty. The matching onto QNMs is obtained as before by imposing continuity of the EOB waveform, Eqs. 5.74 and 5.75, and all the higher order time derivatives that are necessary to determine the amplitudes and phases of the leading ringdown tone, two overtones and their respective twin modes. The strategy to carry out this matching was described in Section 5.5.

5.7 Dynamics of the waveform models

I shall now combine the ingredients of the preceding sections to generate complete waveforms for twelve test systems, which have mass ratios $\eta = 0.0192 (10M_\odot + 500M_\odot)$, $\eta = 0.0028 (1.4M_\odot + 500M_\odot)$, $\eta = 0.0826 (10M_\odot + 100M_\odot)$ and $\eta = 0.0136 (1.4M_\odot + 100M_\odot)$, and the three different spin parameters, namely, $q = 0, 0.3, 0.9$. For the zero

spin case, I will compare the EOB model to the transition model as a consistency check. The final ingredient to be included in the model is the response function and the noise model for the ET detector.

5.7.1 Implementation of the response function

The ET response may be written as

$$h_\alpha(t) = \frac{1}{D} \left[F_\alpha^+(t) h^+(t) + F_\alpha^\times(t) h^\times(t) \right], \quad (5.78)$$

where $\alpha = I, II$ refers to the two independent right-angle Michelson-like detectors. Any number of coplanar and colocated detectors with uncorrelated noise have an equivalent GW response to that of two right-angle interferometers offset by 45° to one another, and it is these putative detectors that I have labeled as I and II . The functions $h^{+\times}(t)$ are the two independent polarizations of the gravitational waveform. The antenna pattern functions $F_\alpha^{+\times}$ are given by Eqs. 2.51 and 2.52 of Chapter 2.

The various angles in these relations represent, (a) the source's sky location in a detector based coordinate system (θ, ϕ) , and (b) the polarization angle of the wavefront (ψ) . These can be re-written in a fixed, ecliptic-based coordinate system. If one denotes the source co-latitude and azimuth angles in the ecliptic coordinate system by (θ_S, ϕ_S) , and the direction of the IMBH's spin \hat{a} by (θ_K, ϕ_K) , then one can use the following expressions to determine $\theta(t)$, $\psi(t)$, $\phi(t)$ [4],

$$\begin{aligned} \cos \theta(t) &= \hat{\mathbf{n}} \cdot \hat{\mathbf{z}}, \\ \tan \phi(t) &= -\frac{\mathbf{l}_1 \cdot \hat{\mathbf{n}}}{\mathbf{l}_2 \cdot \hat{\mathbf{n}}}, \\ \tan \psi(t) &= \frac{\hat{\mathbf{L}} \cdot \hat{\mathbf{z}} - (\hat{\mathbf{L}} \cdot \hat{\mathbf{n}})(\hat{\mathbf{z}} \cdot \mathbf{n})}{\hat{\mathbf{n}} \cdot (\hat{\mathbf{L}} \times \hat{\mathbf{z}})}, \end{aligned} \quad (5.79)$$

where \mathbf{l}_i stand for the unit vectors along the detector's arms, and $\hat{\mathbf{z}}$ represents the normal to the detector plane. Additionally, $\hat{\mathbf{n}}$ and $\hat{\mathbf{L}}$ are the unit vector pointing toward the source binary and the orbital angular momentum, respectively,

$$\hat{\mathbf{n}} = \begin{pmatrix} \sin \theta_S \cos \phi_S \\ \sin \theta_S \sin \phi_S \\ \cos \theta_S \end{pmatrix}, \quad \hat{\mathbf{L}} = \begin{pmatrix} \sin \theta_K \cos \phi_K \\ \sin \theta_K \sin \phi_K \\ \cos \theta_K \end{pmatrix}.$$

Furthermore, if $\Phi(t)$ denotes the phase of the waveform at the centre of the Earth, there

is also a shift in the waveform phase due to the difference in location of the detector. This can be included as a phase shift [6]

$$\Phi(t) \rightarrow \Phi(t) + 2 \frac{d\phi}{dt} R \sin \theta_S \cos[2\pi(t/T) - \phi_S], \quad (5.80)$$

where $R = R_{\oplus}/c = 0.02125$ s, and $d\phi/dt$ is the azimuthal velocity of the orbit. This term is different for different detectors in a network, and encodes the time delay information that allows source triangulation using the network.

5.7.2 Noise model

The SNR for a given waveform is determined by an integral in Fourier space, weighted by the power spectral density (PSD) of the detector. For a monochromatic source, one can approximate this integral as a time domain integral by defining a noise-weighted waveform

$$\hat{h}_\alpha(t) \equiv \frac{h_\alpha(t)}{\sqrt{S_h(f(t))}}, \quad f(t) = \frac{1}{\pi} \frac{d\phi}{dt}. \quad (5.81)$$

Where the PSD, $S_h(f)$, is evaluated at the instantaneous GW frequency, $f(t)$. This is a good approximation during the inspiral, during which the frequency is given by Eq. 5.5, and for the ringdown, during which the PSD factor takes the form $S_h(f(t)) = S_h(f_{\ell mn})$, with $f_{\ell mn} = \omega_{\ell mn}/2\pi$ [14]. Since the distorted Kerr BH will predominantly be emitting GWs at the leading mode $\ell = m = 2, n = 0$, I have set $S_h(f(t)) = S_h(f_{220})$ during the ringdown phase. In the merger and plunge phase, this approximation is not appropriate, but this phase is short and so I use the same approximation, taking the instantaneous frequency from 5.53 in the EOB case and 5.32 in the transition model. Treated in this way, there is a small jump in the frequency used to evaluate the PSD when the orbit passes from plunge to ringdown, so I use interpolation to ensure a smooth transition. In the regime where this approximation is used, the PSD is quite flat (see Figure 5.1) so one does not expect significant errors from using this approach. Furthermore, I have checked that this treatment of the detector noise generates results that are consistent with results computed directly in the frequency domain.

5.7.3 Sample waveforms

In this Section I put at work the machinery developed in Sections 5.3–5.6 to generate a few sample noise-weighted waveforms. Figure 5.2 presents complete gravitational waveforms for two sample systems. These waveforms exhibit the expected behaviour,

i.e., a gradual chirping signal with increasing frequency and amplitude, which peaks at the merger and is damped exponentially afterwards. The ringdown radiation is weaker for the lower mass inspirals, $m = 1.4M_\odot$, as one would expect since the radiated energy scales as η^2 .

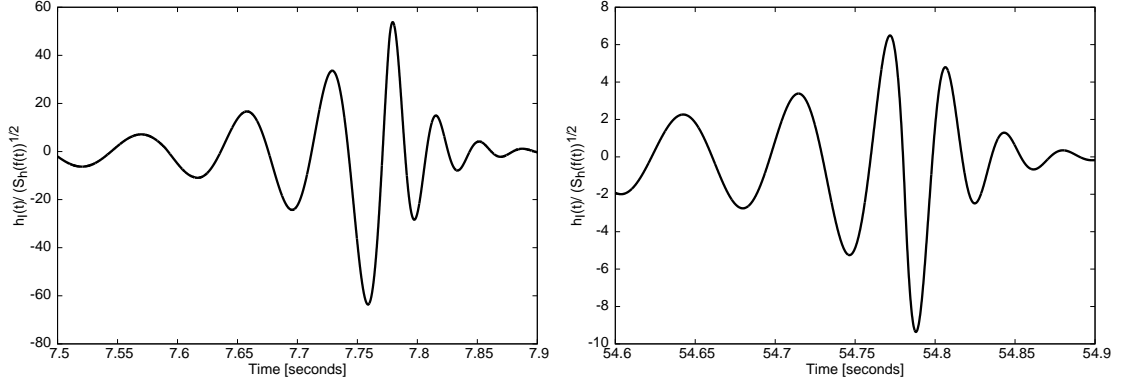


Figure 5.2: Complete gravitational waveforms in the interferometer ‘I’ for COs of masses $10 M_\odot$ (left panel) and $1.4M_\odot$ (right panel), orbiting around a $500M_\odot$ BH with spin parameter $q = 0.3$. The gravitational waveform shows the last stage of inspiral, plus the transition, plunge and ringdown phases. The various extrinsic parameters were chosen randomly.

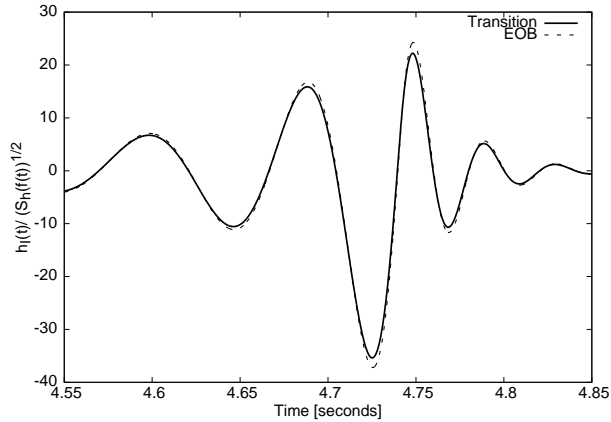


Figure 5.3: Gravitational waveforms emitted during the final stage of inspiral, merger and ringdown for a $10 M_\odot$ CO orbiting around a $500M_\odot$ BH, as computed using the EOB model and the transition waveform with $q = 0$. As for Figure 5.2, the various extrinsic parameters were chosen randomly.

In Figure 5.3 I compare the waveforms generated by the EOB and transition models. Since these were designed to yield accurate results in the test-mass limit, one expects good agreement for small η , but perhaps a larger deviation for large η . In fact, the models agree well even for the larger value of η . The phase is in very good agreement,

which is important for matched filtering, and the amplitude agrees to better than 10%. This provides confidence in the results I present below, and the difference provides a guide to the overall level of uncertainty that one might expect in the SNRs which are presented in the next section.

The full parameter space of the waveform is ten dimensional and these parameters are defined in Table 5.3. For the SNR calculations, I fix the intrinsic parameters (the first four parameters of Table 5.3) and the distance to the source, and then run a Monte Carlo over the values of the remaining five extrinsic parameters.

$\ln m$	mass of CO
$\ln M$	mass of SMBH
q	magnitude of (specific) spin angular momentum of SMBH
t_0	time at which orbital frequency sweeps through a reference value
ϕ_0	initial phase of CO orbit
θ_S	source sky colatitude in an ecliptic-based system
ϕ_S	source sky azimuth in an ecliptic-based system
θ_K	direction of SMBH spin (colatitude)
ϕ_K	direction of SMBH spin (azimuth)
$\ln D$	distance to source

Table 5.3: This table shows the physical meaning of the parameters used in the waveform models. The various angles (θ_S, ϕ_S) and (θ_K, ϕ_K) are defined in an ecliptic-based coordinate system.

5.8 SNRs for spinning and non-spinning binaries

To compute the SNRs of the sample systems, I use the signal analysis scheme introduced in Section 2.4.3. The optimal value of the SNR can be obtained using the relation

$$\text{SNR}^2 = 2 \sum_{\alpha=I,II} \int_{t_{\text{init}}}^{t_{\text{LSO}}} \hat{h}_{\alpha}^2(t) dt. \quad (5.82)$$

The SNRs to be quoted below have been obtained for twelve binary systems at a fixed distance $D = 6.63481$ Gpc, or, alternatively at redshift $z = 1$. As mentioned earlier, the triangular design of ET, consisting of three interferometers with 60° opening angles, generates a response equivalent to two co-located interferometers with 90° opening angles, but rotated 45° with respect to each other, and with SNR that is a factor $3/(2\sqrt{2}) \sim 1.06$ higher. I have not included this factor in the quoted SNRs, given the uncertainties in the ET design that exist at this stage. The distribution of SNRs over random choices of the extrinsic parameters are summarised in Figures 5.4–5.7, while the statistics of the SNR distributions are given in Tables 5.4 and 5.5.

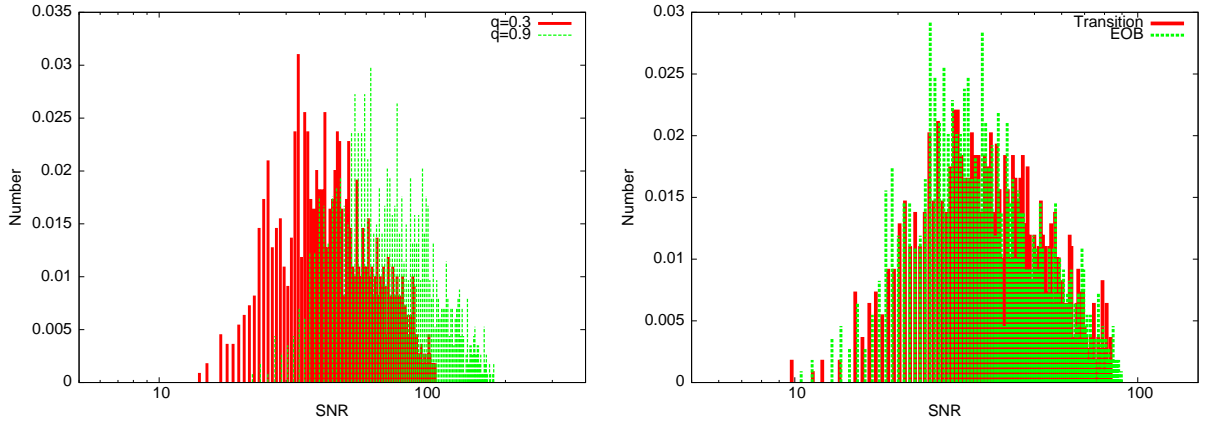


Figure 5.4: The left panel shows the SNR distributions in a Monte Carlo simulation over extrinsic parameters for a $10 M_{\odot} + 100 M_{\odot}$ binary, with IMBH spin parameter $q = 0.9, 0.3$. The right panel shows the SNR distributions for the same binary system using the transition waveform model in the $q = 0$ limit, along with its EOB counterpart. Note that the SNR distributions have been computed at a fixed distance $D = 6.63481$ Gpc, or, equivalently, at a fixed redshift $z = 1$.

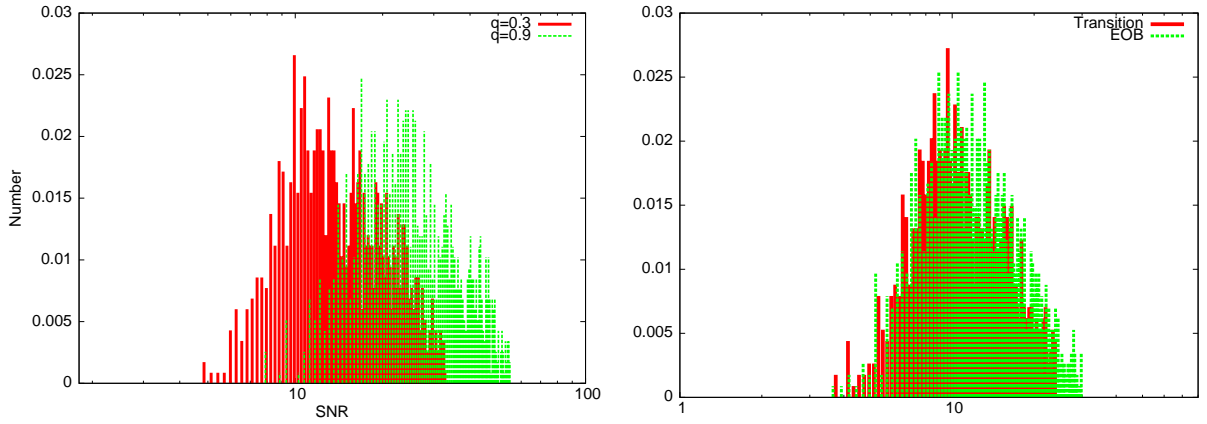


Figure 5.5: As Figure 5.4, but now for binaries with masses $1.4 M_{\odot} + 100 M_{\odot}$.

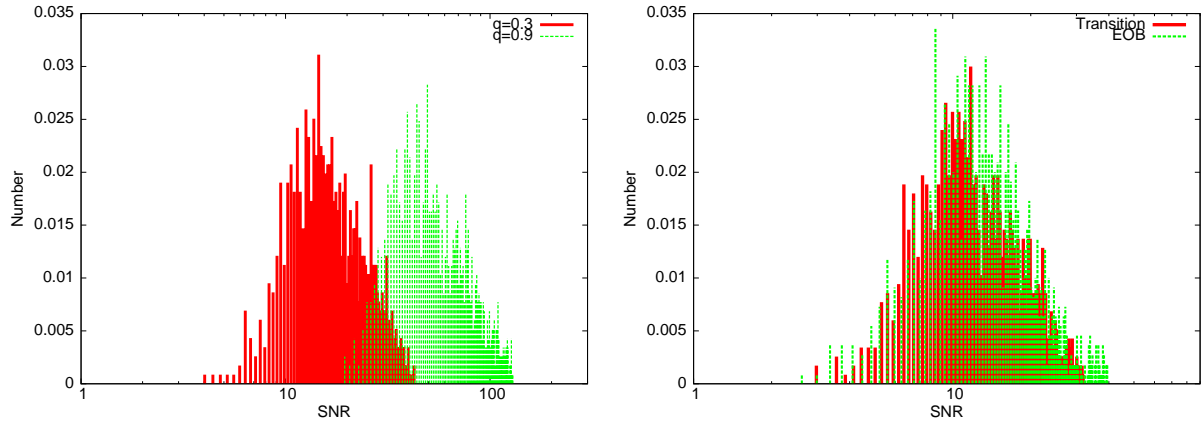


Figure 5.6: As Figure 5.4, but now for binaries with component masses $10 M_{\odot} + 500 M_{\odot}$.

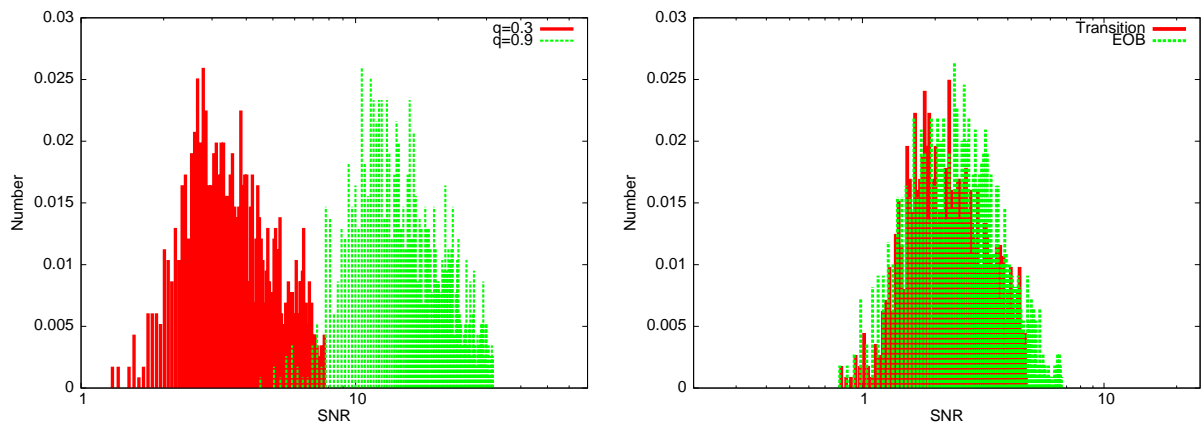


Figure 5.7: As Figure 5.6, but now for binaries with masses $1.4 M_{\odot} + 500 M_{\odot}$.

5. Source modelling of IMRIs

Stats	$m = 10M_{\odot}$				$m = 1.4M_{\odot}$			
	$q = 0.9$	$q = 0.3$	$q = 0$	EOB	$q = 0.9$	$q = 0.3$	$q = 0$	EOB
Mean	74.645	46.774	37.844	38.282	24.099	14.388	11.272	11.967
St. Dev.	31.030	20.665	12.401	14.450	9.113	5.149	4.101	4.103
L. Qt.	55.081	33.266	27.606	27.669	18.113	10.740	8.337	8.933
U. Qt.	103.276	65.163	52.000	51.642	32.584	19.454	15.205	16.144
Med.	73.451	46.026	37.844	38.107	24.266	14.289	11.041	11.995

Table 5.4: Summary statistics of the SNR distributions for binary systems with a central IMBH of mass $M = 100M_{\odot}$, and various choices for IMBH spin, q , and CO mass, m . The Table shows the mean, standard deviation, median and quartiles of the distribution of the SNR for each system. The SNR distributions have been computed at a fixed distance $D = 6.63481$ Gpc.

Stats	$m = 10M_{\odot}$				$m = 1.4M_{\odot}$			
	$q = 0.9$	$q = 0.3$	$q = 0$	EOB	$q = 0.9$	$q = 0.3$	$q = 0$	EOB
Mean	55.463	18.408	12.853	13.677	15.417	3.908	2.570	2.729
St. Dev.	21.337	6.723	4.271	4.716	5.571	1.256	1.102	1.113
L.Qt.	39.811	13.583	9.484	9.908	11.508	2.884	1.932	2.084
U.Qt.	74.645	25.645	17.579	19.099	20.845	5.272	3.327	3.707
Med.	55.590	18.408	12.764	13.836	15.668	3.882	2.636	2.723

Table 5.5: As Table 5.4, but now for binary systems with a central IMBH of mass $M = 500M_{\odot}$.

The results shown on Tables 5.4 and 5.5 can be better visualized by plotting the mean of the SNR distributions as a function of the spin parameter q , which is shown in Figure 5.8. This figure shows that binaries with rapidly spinning IMBHs, $q \sim 0.9$, and large mass ratios, $\eta \sim 0.08$, will be relatively loud. At a fixed SNR detection threshold of 10, this implies that such sources would be seen to distances $D \gtrsim 6.6$ Gpc. In contrast, for binaries with slowly rotating IMBHs, $q \sim 0.3$, and small mass ratios, $\eta \sim 0.003$, will only be visible at distances $D \lesssim 6.6$ Gpc.

In order to understand the implication of these results, one can use the data summarized in Tables 5.4 and 5.5 to estimate the number of events per year that may be detected by the ET. To do so I will follow the procedure outlined in Section 3.3 of [64]. The basic idea is the following: fix an SNR detection threshold, $\rho_{\text{thresh}} = 10$, then estimate the luminosity distance, $D_L(z)$, at which a given source can be detected, using the simple prescription $D_L = \rho(6.63481)/\rho_{\text{thresh}}$, where $\rho(6.63481)$ is the SNR of the source at a distance of 6.63481 Gpc, which can be obtained from Tables 5.4 and 5.5. Thereafter, use the concordance cosmology to convert this luminosity distance estimate into a redshift estimate, z , by inverting the following expression,

$$D_L(z) = D_H(1+z) \left\{ \int_0^z \frac{dz'}{[\Omega_M(1+z')^3 + \Omega_\Lambda]^{1/2}} \right\}. \quad (5.83)$$

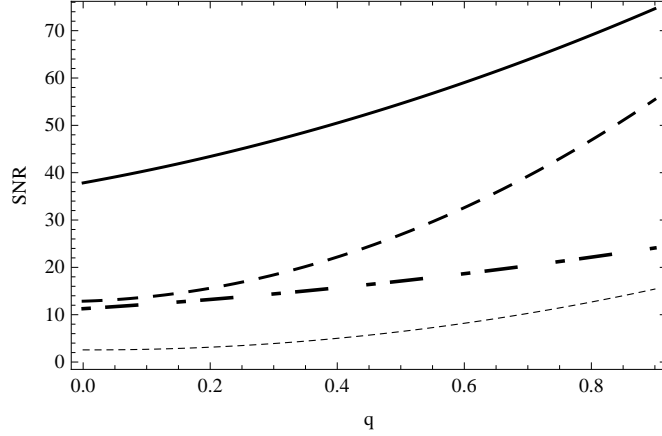


Figure 5.8: The plot shows the mean value of the SNR distribution as a function of the spin parameter q . From top to bottom, the various lines correspond to binaries of mass-ratio η , namely, solid line $\eta = 0.0826$ ($[10+100]M_\odot$), dashed line $\eta = 0.0192$ ($[10+500]M_\odot$), dash-dot line $\eta = 0.0136$ ($[1.4+100]M_\odot$) and dotted line $\eta = 0.0028$ ($[1.4+500]M_\odot$).

Note that I have assumed a flat universe $\Omega_k = 0$, and used $\Omega_M = 0.27$, $\Omega_\Lambda = 0.73$, $H_0 = 72 \text{ km s}^{-1} \text{ Mpc}^{-1}$; and $D_H = c/H_0 \approx 4170 \text{ Mpc}$. Under these assumptions, one can compute the co-moving volume, V_c , within which the source can be detected, using the relation [71],

$$V_c = \frac{4\pi D_H^3}{3} \left\{ \int_0^z \frac{dz'}{[\Omega_M(1+z')^3 + \Omega_\Lambda]^{1/2}} \right\}^3. \quad (5.84)$$

In a previous study on the possible detection of IMRIs of COs into IMBHs with Advanced LIGO [92], it was found that binary tightening via three-body interactions was the dominant mechanism that led to the formation of IMRIs. In this mechanism, the merger time for an IMRI can be estimated as the sum of the hardening timescale, T_{harden} , and the gravitational-wave merger timescale, T_{GW} , i.e, $T_{\text{merge}} = T_{\text{harden}} + T_{\text{GW}}$ [64], where

$$T_{\text{harden}} \approx 2 \times 10^8 \frac{10^{5.5} \text{ pc}^{-3}}{n} \frac{10^{13} \text{ cm}}{a} \frac{\sigma}{10 \text{ km/s}} \frac{0.5 M_\odot}{m_*} \text{ yr}, \quad (5.85)$$

$$T_{\text{GW}} \approx 10^8 \frac{M_\odot}{m} \left(\frac{100 M_\odot}{M} \right)^2 \left(\frac{a}{10^{13} \text{ cm}} \right)^4 \text{ yr}, \quad (5.86)$$

in which a is the semi-major axis of the binary, n is the number density of stars in a globular cluster, σ is the velocity dispersion, and m_* stands for the mass of stars

that interact with the binary. In practice, I set n , σ and m_* to their fiducial values, and minimize $T_{\text{merge}} = T_{\text{harden}} + T_{\text{GW}}$ over a to estimate the CO–IMBH coalescence rate. The rate at which IMRIs occur per globular cluster can then be approximated by $1/T_{\text{merge}}$.

The SNRs I have computed correspond to the SNRs of systems with *redshifted masses*, $M_z = M(1+z)$, $m_z = m(1+z)$, equal to those specified on the first two columns of Table 5.6. Hence, the maximum detectable redshift, z , estimated from the SNR distributions can be used to work out the intrinsic source–frame masses of these systems. In the case of ET, which can detect sources out to cosmological redshifts, $z \gtrsim 1$, these intrinsic masses may not correspond to astrophysically interesting systems. However, by considering a range of redshifted masses and computing for each one an event rate, under the assumption that all IMRI systems were of that particular intrinsic type, one can still obtain a rough estimate of the event rate.

Following [64], I assume that 10% of clusters form an IMBH and are sufficiently dense to host an IMRI. I also assume that such globular clusters have a fixed comoving density of $\sim 0.3\text{Mpc}^{-3}$. The rate of detectable events for a particular type of system can then be estimated as $\sim 0.3(V_c/\text{Mpc}^3)/[T_{\text{merge}}(1+z)]$ [64].

Table 5.6 presents estimates, for each of the fiducial systems, of the maximum detectable redshift, the intrinsic masses that the source represents at that redshift, the corresponding merger time through binary hardening, the co-moving volume within that redshift, and the IMRI event rate assuming all IMRI sources were of that type. Note that the latter assumption means that the entries in this table are not independent of each other, i.e., the total number of events is not given by the sum of the last column, but is somewhere in the range of rates tabulated. Even though the astrophysical properties of IMBHs, e.g., their mass and spin distributions, are currently very uncertain, one can still draw conservative predictions from Table 5.6. First of all, it is worth pointing out that these event rate estimates compare fairly well with those of [64], but are a bit larger since I have used a more accurate waveform model that includes the spin of the IMBH. Additionally, these results suggest that IMRIs could be seen at redshifts $z \sim 1\text{--}6$, depending on the mass of the IMBHs that exist, and there could be as many as a few hundred systems observed. If IMRIs had component masses $2M_\odot + 100M_\odot$, then they could be seen out to $z \sim 4$, and one would expect a few hundred events. However, if IMRIs tended to be $1M_\odot + 400M_\odot$ systems, one would only see ~ 10 events out to $z \sim 0.3$. The greatest uncertainty in these figures comes from the unknown number of IMBHs that exist in the Universe, and these uncertainties are not folded into the numbers in Table 5.6. If IMBHs are rare, then the IMRI rate

5. Source modelling of IMRIs

could be orders of magnitude lower.

M_z/M_\odot	m_z/M_\odot	q	D/Gpc	z	M/M_\odot	m/M_\odot	$T_{\text{merge}}/\text{yr}$	V_c/Mpc^3	Events/yr
100	10	0.9	49.29	5.15	16.3	1.6	5.40×10^8	2.16×10^{12}	195
100	10	0.3	31.03	3.49	22.3	2.2	4.47×10^8	1.38×10^{12}	206
100	10	0	25.01	2.92	25.5	2.5	4.12×10^8	1.09×10^{12}	201
100	1.4	0.9	15.93	2.02	33.1	0.5	5.13×10^8	6.15×10^{11}	119
100	1.4	0.3	9.47	1.33	42.9	0.6	4.46×10^8	2.82×10^{11}	81
100	1.4	0	7.47	1.10	47.6	0.7	4.15×10^8	1.88×10^{11}	64
500	10	0.9	36.75	4.02	99.6	2.0	2.50×10^8	1.64×10^{12}	392
500	10	0.3	12.30	1.64	189.3	3.8	1.70×10^8	4.24×10^{11}	283
500	10	0	8.51	1.22	225.2	4.5	1.54×10^8	2.35×10^{11}	207
500	1.4	0.9	10.19	1.41	207.5	0.6	2.37×10^8	3.16×10^{10}	16
500	1.4	0.3	2.55	0.46	342.5	1.0	1.75×10^8	2.24×10^{10}	26
500	1.4	0	1.66	0.32	378.8	1.1	1.65×10^8	8.35×10^9	11

Table 5.6: “3 ET detector network” average range, corresponding redshift, source-frame masses, merger timescale, co-moving volume within range, and detectable event rate for several combinations of plausible redshifted CO and IMBH masses.

As discussed earlier, there is currently some uncertainty about the low-frequency sensitivity that ET will achieve. The preceding results assumed a frequency cut-off at 5Hz, but it is informative to consider how the SNR changes if this frequency cut-off is pushed down to 3Hz or even 1Hz. Table 5.7 shows how the SNR changes as a function of the cut-off frequency for the sample binaries under consideration. In each case I have chosen a particular random, but fixed, set of extrinsic parameters that is representative of the events that lie around the peak of the SNR distribution for the binary.

Binary	q = 0.9			q = 0.3			q = 0		
	5Hz	3Hz	1Hz	5Hz	3Hz	1Hz	5Hz	3Hz	1Hz
[10 + 100] M_\odot	72.111	79.799	86.896	52.240	56.885	63.680	42.855	45.186	48.306
[10 + 500] M_\odot	55.286	58.325	63.293	19.364	20.701	22.961	15.276	15.959	16.331
[1.4 + 100] M_\odot	20.941	21.878	23.714	16.711	17.418	18.030	11.351	11.952	12.123
[1.4 + 500] M_\odot	13.274	13.804	13.932	4.207	4.256	4.613	2.610	2.792	3.029

Table 5.7: SNR of a source as a function of the low frequency cut-off. For each binary, the extrinsic parameters have been chosen randomly, but kept fixed as the cut-off frequency was varied.

Table 5.7 suggests that if ET achieves frequency sensitivity down to 1Hz, it will have greater sensitivity to systems containing more massive compact objects. This will facilitate the extraction of these signals from the data, and will allow the possibility of detecting these sources at higher redshift. In order to cross-check the reliability of the results quoted in Table 5.7, I run a full Monte Carlo for the system [10 + 100] M_\odot , with IMBH spin parameter $q = 0.3$, and at a frequency cut-off of 1Hz. Figure 5.9 presents these results, and confirms that Table 5.7 is a fair representation of what may

be achieved by ET at lower frequencies.

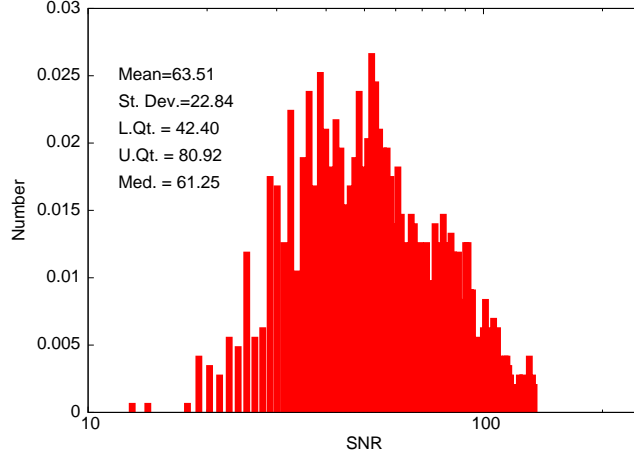


Figure 5.9: The panel shows the SNR distribution for a $10M_{\odot} + 100M_{\odot}$ binary with IMBH spin parameter $q = 0.3$, at a frequency cut-off of 1Hz. Note that the SNR distribution has been computed at a fixed distance $D = 6.63481$ Gpc, or, equivalently, at a fixed redshift $z = 1$. The statistics of the SNR distribution are summarized at the top-left of the panel.

The results contained in Table 5.7 can be used to explore the redshift at which the loudest sources may be seen if ET achieved a frequency cut-off of 1Hz. Table 5.6 shows that the systems with redshifted masses, $m_z + M_z$, of $[10 + 100]M_{\odot}$, $[10 + 500]M_{\odot}$, with $q = 0.9$, could be seen up to redshift $z \sim 5$, $z \sim 4$, respectively. Using Eq. 5.83, and assuming a cut-off at 1Hz, these same systems could be detected up to redshift $z \sim 6$, $z \sim 5$, respectively. Table 5.8 summarizes these results for the loudest sources from Table 5.6. The event rate estimate only changes appreciably for the $q = 0.3$ case (since the intrinsic masses for the systems are also changing), but as $q = 0.3$ may be a good estimate for the typical spin of an IMRI, there could be a significant scientific gain from pushing the lower frequency cut-off to 1Hz. A more systematic study, which fixes the intrinsic masses of the events as opposed to the redshifted masses, is needed to fully explore the implications of the cut-off frequency on the expected IMRI detection rate.

There is another important consequence of a lower low-frequency cut-off. As discussed previously, the binary systems considered here are very short lived. However, by pushing the seismic wall down to 1Hz, these binaries stay longer in the sensitivity band of the detector, as indicated in Table 5.9. In this scenario, it should be possible to obtain better parameter estimation accuracies, in particular for the extrinsic parameters. I will show that this is indeed the case in the following Chapter.

5. Source modelling of IMRIs

M_z/M_\odot	m_z/M_\odot	q	D/Gpc	z	M/M_\odot	m/M_\odot	$T_{\text{merge}}/\text{yr}$	V_c/Mpc^3	Events/yr
100	10	0.9	57.72	5.9	14.5	1.4	5.81×10^8	2.47×10^{12}	187
100	10	0.3	42.46	4.6	17.8	1.8	4.47×10^8	1.92×10^{12}	202
500	10	0.9	41.79	4.5	90.9	1.8	2.62×10^8	1.87×10^{12}	385
500	10	0.3	15.26	2.2	156.2	3.1	1.70×10^8	7.08×10^{11}	346

Table 5.8: “3 ET detector network” average range, corresponding redshift, source-frame masses, merger timescale, co-moving volume within range, and detectable event rate for several combinations of plausible redshifted CO and IMBH masses. The cut-off frequency has been set at 1Hz.

Binary	$q = 0.9$			$q = 0.3$			$q = 0$		
	5Hz	3Hz	1Hz	5Hz	3Hz	1Hz	5Hz	3Hz	1Hz
$[10 + 100]M_\odot$	45.0	169.2	3093.7	42.1	161.5	3048.5	38.9	157.3	3025.8
$[10 + 500]M_\odot$	16.3	61.2	1099.3	8.3	43.9	1010.1	5.4	35.6	963.2
$[1.4 + 100]M_\odot$	319.9	1209.0	22089.1	291.0	1152.4	21776.9	275.9	1123.7	21614.1
$[1.4 + 500]M_\odot$	112.5	436.1	7851.8	55.6	311.2	7221.9	34.0	252.5	6879.9

Table 5.9: Summary of how the time spent in band of a source changes as the low-frequency sensitivity cut-off changes from 5Hz to 3Hz to 1Hz. The time is reported in seconds. For each binary, the extrinsic parameters have been chosen randomly, but kept fixed as the cut-off frequency was varied.

Table 5.9 shows that pushing the frequency cut-off to 1Hz will boost the time spent in band of the shortest-lived events by a factor ~ 200 . The systems $[1.4 + 100]M_\odot$ could spend up to 6 hours in band. In the following Chapter, I will show that even with a 5Hz cut-off, it is possible to pinpoint the location of these sources in the sky, and constrain their luminosity distance to about $\sim 10\%$, at SNR of 30, using a 3 ET detector network. Pushing the seismic limit down to 1Hz would further improve these estimates.

All the results obtained up to this point have assumed that one will be able to detect IMRIs using a 3 ET detector network. Hence, the previous results may be considered as upper limits for event rates per year, SNRs, horizon distances etc. I shall now relax this assumption and explore more modest scenarios, i.e., the configurations C1–C5 outlined in Section 5.2.1. To recap, these are, C1: one ET at the geographic location of Virgo; C2: as configuration C1 plus a right-angle detector at the location of LIGO Livingston; C3: as configuration C1 plus another ET at the location of LIGO Livingston; C4: as configuration C2 plus another right-angle detector in Perth; and C5: as configuration C3 plus another ET in Perth. Note that configuration C5 corresponds to the 3ET detector network used in the previous studies.

In the following, I quote results for IMBHs with spin parameter $q \sim 0.3$ only, since, as argued earlier, this could be a reasonable fiducial value for IMBH spin. Table 5.10 presents SNRs for IMRIs with a central $M = 100M_\odot$ IMBH with spin parameter

$q = 0.3$, for five different configuration.

Stats	$m = 10M_{\odot}$					$m = 1.4M_{\odot}$				
	C1	C2	C3	C4	C5	C1	C2	C3	C4	C5
Mean	26.242	34.119	40.179	40.458	46.774	8.222	10.740	12.589	12.823	14.388
St. Dev.	14.785	16.623	18.912	19.015	20.665	3.113	3.485	4.102	4.408	5.149
L.Qt.	18.239	24.660	28.708	29.242	33.266	5.754	8.054	9.333	9.311	10.740
U. Qt.	38.282	48.195	57.148	55.719	65.163	11.169	14.928	16.711	16.634	19.454
Med.	26.424	33.884	39.719	40.365	46.026	8.017	10.666	12.162	12.445	14.289

Table 5.10: As Table 5.4, but for binary systems with a central IMBH of mass $M = 100M_{\odot}$ and spin parameter $q = 0.3$, and assuming five different configurations for the detector network, C1–C5 as described in Section 5.2.1. Configuration C5 is the network of three ETs which has been used for all results elsewhere in this Chapter.

Stats	$m = 10M_{\odot}$					$m = 1.4M_{\odot}$				
	C1	C2	C3	C4	C5	C1	C2	C3	C4	C5
Mean	9.528	12.677	14.825	14.894	18.408	2.084	2.685	3.141	3.177	3.908
St.Dev.	4.432	4.866	5.551	5.346	6.723	1.102	1.117	1.164	1.129	1.256
L.Qt.	6.683	8.974	10.328	12.677	13.583	1.517	2.032	2.333	2.382	2.884
U.Qt.	13.868	17.742	20.370	20.045	25.645	2.844	3.589	4.188	4.207	5.272
Med.	9.638	12.853	14.521	14.689	18.408	2.109	2.704	3.090	3.126	3.882

Table 5.11: As Table 5.10, but for binary systems with a central IMBH of mass $M = 500M_{\odot}$ and spin parameter $q = 0.3$.

Tables 5.10 and 5.11 indicate that the SNR corresponding to a 3 ET detector network is, roughly speaking, a factor of $\sqrt{3}$ and $\sqrt{3/2}$ greater than the SNR associated with a single ET and a 2 ET network, respectively. This is an expected scaling since, despite the different locations of the detectors, the SNR scales approximately as the square root of the number of detectors. Furthermore, the SNR associated with configuration C4 is similar to that of configuration C5. C4 is somewhat less ambitious than a 3ET network, and hence might be more likely to be realised in the future. In the following Chapter, I present parameter estimation results for these same configurations which show that for slowly rotating IMBHs, network C4 will suffice for determining the system parameters with an accuracy that is comparable to configuration C5, at a source SNR of 30.

The above discussion indicates that IMRI sources detected by ET may shed some light on the astrophysical properties of IMBHs, e.g., their mass and spin distributions, and to find out whether dynamical interactions in dense stellar systems do indeed lead to the formation of IMBHs.

Additionally, the mergers detected by ET will be complementary to mergers between heavier BHs that will be seen by future low-frequency space-based detectors. These

various instruments will provide a measurement of the rate of BH mergers in various mass ranges, which will be useful to place constraints on models of BH growth [64].

5.9 Conclusions

In this Chapter I developed two waveform models for circular equatorial IMRIs. One model, valid for inspirals into IMBHs of arbitrary spin, is based on the transition-to-plunge scheme of Ori and Thorne [104] to smoothly match the inspiral onto a plunge waveform and ringdown. The second approach, at present valid only for non-spinning IMBHs, uses the EOB formalism to match a merger and ringdown onto the inspiral waveform. I have shown that the two distinct waveform families are in good agreement in the $q = 0$ limit, particularly in the small η regime. The agreement in phasing all the way from inspiral to ringdown is particularly good and this is important as a good phase model will be crucial for the detection of these systems via matched filtering and to extract parameter information from the detector measurements.

I have also used these models to compute SNRs for various binary systems using five different detector networks. Assuming a 3 ET detector network, I showed that the two models make predictions that are consistent to about ten percent in the non-spinning limit. Additionally, I found that at a low-frequency sensitivity cut-off of 5Hz, and at redshift $z = 1$, typical SNRs for IMRI systems with masses $1.4M_{\odot}+100M_{\odot}$, $10M_{\odot}+100M_{\odot}$, $1.4M_{\odot}+500M_{\odot}$ and $10M_{\odot}+500M_{\odot}$ will be in the range ~ 10 –25, ~ 40 –80, ~ 3 –15 and ~ 10 –60 respectively. Using the SNR distributions as input data, I also estimated the horizon distance at which these various sources could be seen. This results suggest that ET could detect as many as several hundred of these systems, up to a redshift $z \lesssim 5$, although the exact number will depend on the intrinsic distribution of masses and spins for the IMRI systems. If the ET sensitivity extends down to 1Hz, these same systems could be detected up to redshift $z \lesssim 6$.

For completeness, I also explored more modest network configurations consisting of 1 ET only, 1 ET plus 1 right-angle detector, 2 ETs and 1 ET plus 2 right-angle detectors to compute SNR distributions for four combinations of source masses $1.4M_{\odot}+100M_{\odot}$, $10M_{\odot}+100M_{\odot}$, $1.4M_{\odot}+500M_{\odot}$, $10M_{\odot}+500M_{\odot}$, but with fixed IMBH spin parameter $q = 0.3$. I chose this spin since it is a reasonable estimate of the spin parameter of an IMBH that has grown primarily through a series of minor mergers. A network consisting of one ET and two right-angle interferometers will have almost as great a sensitivity to IMRIs as the highly-ambitious 3-ET network, and this result will be important when a third-generation detector network is planned.

IMRI detections will probe the existence and properties of IMBHs, and their number density over cosmic history. This in turn will provide information about how these objects form and evolve. Since IMRIs will primarily be observed from globular clusters, IMRI observations will shed light on the efficiency of formation of IMBHs in cluster environments, the number density of cluster IMBHs and the rate at which IMBH-IMBH binaries could form through the globular cluster channel [64]. Understanding the properties of globular cluster IMBHs through the IMRI channel could therefore help identify candidate primordial IMBHs, which will have important consequences for hierarchical models of structure growth. These studies indicate that ET might detect as many as several hundred IMRI events, which could be used to extract this physics. In the following Chapter I will study the precision with which the parameters of IMRI systems might be estimated using the ET detector.

Chapter 6

Parameter estimation using intermediate–mass–ratio inspirals

6.1 Overview

In this Chapter I will explore the precision with which the Einstein Telescope (ET) will be able to measure the parameters of IMRIs. I will make use of the waveform models developed in Chapter 5 to carry out a Monte Carlo simulation of parameter estimation errors over choices of the extrinsic parameters of the source. I will present results for the same binary systems considered in Chapter 5. For completeness, I will also present results for several different possible configurations of a third generation detector network to assess how the precision of parameter determination depends on the network configuration. The results presented in this Chapter were published in the article [74].

6.2 Assumptions

For consistency with the analysis carried out in Chapter 5, I will follow the assumptions listed in Section 5.2.1. Additionally, I will use the “ET B” sensitivity curve (see Figure 5.1) to obtain the various results presented in this Chapter.

Because the IMRI signals considered in these studies are short–lived, I will assume that one of the detector networks described in Section 5.2.1 is available to enable extrinsic parameter estimation for the sources.

6.3 Signal analysis

As mentioned in Chapter 2, assuming a flat prior (or a locally-flat prior which would be a reasonable assumption for a signal of high SNR), the covariance of the posterior probability distribution, $(\Gamma^{-1})^{ij}$, gives the expectation value of the errors $\Delta\theta^i$

$$\langle \Delta\theta^i \Delta\theta^j \rangle = (\Gamma^{-1})^{ij} + \mathcal{O}(\text{SNR})^{-1}. \quad (6.1)$$

However, as discussed in Chapter 5, some of the binaries considered in these studies have relatively low SNR, and it is known that in such situations the Fisher Matrix may overestimate measurement accuracies. In order to address this problem, Vallisneri [130] developed a mismatch criterion to determine whether Fisher Matrix results are reliable in a particular context. The idea is to compute the ratio $r(\theta, A)$ of the linearized signal amplitude (LSA) likelihood to the exact likelihood. This ratio r is given by [130]

$$|\log r(\theta, A)| = (\Delta\theta_j h_j - \Delta h(\theta), \Delta\theta_k h_k - \Delta h(\theta)), \quad (6.2)$$

where A represents the signal strength, $\Delta h(\theta) = h(\theta) - h(\hat{\theta})$, with $\theta = \hat{\theta} + \Delta\theta$, and $\hat{\theta}$ the observed location of maximum LSA likelihood for a given experiment. I have used the consistency criterion, Eq. (6.2), to explore the $1\text{-}\sigma$ likelihood surface predicted by the Fisher Matrix to verify that the mismatch between the LSA and the exact likelihoods is small. Ratios below a fiducial value, say $|\log r(\theta, A)| \sim 0.1$, are considered acceptable [130].

As an example of typical results obtained from this analysis, for $(10M_\odot, 100M_\odot)$ binaries with $q = 0.3$ at a fixed redshift $z = 1$, I have found that systems near the lower quartile of the distribution had $|\log r(\theta, A)| \sim 0.2$. From this threshold onwards, the ratio r decreased gradually so that at the upper quartile of the distribution $|\log r(\theta, A)| \sim 0.04$. This indicates that the results I get should be a reasonable estimate of the measurement precisions achievable for IMRIs using ET. These results may be somewhat optimistic and at some point should be verified using Monte Carlo simulations to recover the full posterior probability distributions. Such an exercise is beyond the scope of this present work. Nonetheless, the results should be fairly accurate, and I will show in Section 6.4 that, where comparisons can be made, my results are in good accord with results available in the literature that have been derived for other types of binaries, and using different waveform models.

The Fisher matrix for a network of detectors is given by the sum of the individual Fisher Matrices for each detector. When modelling the response of the various detec-

tors, it is necessary to account for their relative positions on the surface of the Earth, as the corresponding time delays are what allow source triangulation. In computing the waveforms used in the Fisher Matrix, I found it convenient to use two different timesteps in order to separately resolve the (slow) inspiral and (fast) merger/ringdown phases. I checked that varying the choice of timesteps and the location of the transition between the two timesteps did not significantly affect the results for any of the systems considered. I will discuss the convergence of the Fisher Matrices further in Section 6.4.

6.4 Parameter estimation error results

The parameter space of the signals I consider is 10 dimensional, as described in Table 5.3.

To explore parameter estimation errors using the inverse Fisher Matrix, I fix the values of the intrinsic parameters of the source, and carry out a Monte Carlo simulation over possible values for the extrinsic parameters. The parameter errors scale with the SNR of the source as $1/\text{SNR}$, so I can quote results at a fixed SNR, and these may be easily extrapolated to other SNRs. I have chosen a reference SNR of 30, as this would represent a very robust detection for which the Fisher Matrix prediction is likely to be a good estimate. To obtain this reference result, I first compute the Fisher Matrix for a source at a fixed distance, $D = 6.6348\text{Gpc}$, and obtain the SNR at that distance from the expression 5.82.

Thereafter, I multiply the errors estimated from the Fisher Matrix by $(\text{SNR}/30)$ to normalise to the reference SNR of 30. I assume that the observation starts when the GWs from the inspiral reach a frequency of 5Hz, and finishes when the ringdown waveform is no longer contributing to the SNR.

6.4.1 Dependence of parameter estimation errors on system parameters

For completeness with the results presented in Chapter 5, I have considered the twelve different binary systems described in Section 6.2. For the binaries whose central IMBH has spin parameter $q = 0.3, 0.9$, I present results computed from the transition waveform model. For the non-spinning systems, $q = 0$, I present results from both the transition model and the EOB model.

The Tables 6.1–6.4 list the mean, standard deviation, median and lower and upper quartiles of the distribution of the Fisher Matrix errors computed in the Monte Carlo

simulation. There is one table for each of the four mass combinations. All of these results have been computed at the fixed reference SNR of 30. These results assume that the detection is made using the optimistic 3 ET network configuration, and hence should be considered as upper bounds on the accuracy with which ET may be able to measure the various parameters.

Figure 6.1 shows the intrinsic parameter error distributions of the binary with component masses $m = 10M_{\odot}$, $M = 100M_{\odot}$, and IMBH spin parameter $q = 0.9$. This Figure, and Table 6.1, indicate that a network of 3 ETs might be able to determine the location of the source in the sky to an accuracy of $\sim 10^{-3}$ steradians, i.e., ~ 4 square degrees, at a fixed SNR of 30. It is worth pointing out that this estimate is the statistical mean of the Monte Carlo distribution.

Recent work has shown that for the existing LIGO–Virgo detector network, and assuming a uniform distribution of sources across the sky, at a network SNR of around 15, 50% of inspiral sources should be located within 23 sq-degs (best case) at the 95% confidence level. For burst sources, without any knowledge of the waveform, 50% of the sources could be localized within 50 sq-degs (worst case) at an SNR of 10, but this can be reduced to 8 sq-degs if predicted waveforms are available [133]. These estimates are similar for the initial or advanced detectors [133], at a fixed SNR. The inclusion of an additional detector in the Southern Hemisphere, such as AIGO, can further improve these values as it contributes a longer baseline, additional energy flux, extended signal space, and breaks the plane–degeneracy formed by the three detector network of LIGO Livingston, LIGO Hanford and Virgo [133].

Another recent independent study [55] presented results for the accuracy with which sources could be localized with a network of GW detectors, using only timing information in the various detectors. Fairhurst [55] found that increasing the number of detectors at different sites increases both the absolute number of observable sources, and greatly increases the fraction of sources that can be well localized. For instance, at a fixed SNR of 8, and using the advanced detector network comprising the two LIGO detectors at Hanford (HH) and LIGO Livingston (L), no sources can be localized within 20 sq-degs. Adding another detector at a different site, e.g., a LIGO detector in Australia (A), or Advanced Virgo (V), or the Japanese LCGT detector (J), the networks HLA, HHLV, HHJL, can localize up to 50% of the signals within 20 sq-degs, and the loudest signals within 5 sq-degs. In all these results, it was found that for the networks involving an Australian detector, the peak of the localization distributions occurs between 5 and 10 sq-degs. The results I have obtained, suggest that it will be possible to determine the location of the source in the sky to an accuracy of ~ 12 sq-degs at

a network SNR of 8. This estimate is the statistical median value obtained from the Monte Carlo simulations. Hence, my results are in good accord with existing estimates of the angular resolution that may be achieved by the advanced detector network.

Furthermore, Table 6.1 shows that for non-spinning systems, a 3 ET network will resolve the plunge time t_0 to within ~ 30 ms when normalised to an SNR of 10. This estimate is also in good accord with the results obtained independently by Ajith et al. [2] and Luna et al. [88].

The Monte Carlo simulations also show that ET observations may determine the total mass of non-spinning binaries with component masses $m = 10M_\odot, M = 100M_\odot$ to an accuracy of $\sim 0.1\%$, at fixed SNR of 8. This estimate is in good accord with previous estimates for related systems. For instance, in [65], it was estimated that using the same 3ET detector network that has been considered in the previous analysis, it should be possible to determine the total mass of a non-spinning $m = 23M_\odot, M = 100M_\odot$ binary (mass ratio $\eta = 0.16$) to an accuracy of $\sim 0.1\%$ at a network SNR of 8. This estimate was obtained using the phenomenological waveform model described in [1], which includes the inspiral, merger and ringdown for non-spinning, comparable-mass binaries in a consistent way.

Figure 6.2 shows the accuracy with which one expects to determine the masses of the small CO and the IMBH for the spinning systems, as well as the IMBH spin parameter q . This Figure also shows that for binaries that stay the longest in band, namely the $m = 1.4M_\odot, M = 100M_\odot, q = 0.3$ system (~ 291 seconds in band), one can determine the masses of the CO and the IMBH to an accuracy of 0.01%, 0.005%, respectively, at the reference SNR of 30. The accuracy gradually decreases for the shorter-lived events. For instance, for binaries with $m = 10M_\odot, M = 500M_\odot, q = 0.3$, which stay in band about ~ 8.3 seconds, one expects to measure the CO's and IMBH's masses to an accuracy of only $\sim 0.15\%$, $\sim 0.05\%$ respectively, at the same SNR of 30.

These results also suggest that ET observations will determine the spin parameter more accurately for rapidly rotating binaries. For instance, the estimated accuracy with which one can measure the IMBH spin parameter for binaries with masses $m = 10M_\odot, M = 100M_\odot$, and IMBH spin $q = 0.9$, is $\sim 0.05\%$. This is about a factor of 2 better than for binaries with the same component masses but with spin $q = 0.3$. This is a trend to be expected since, for more rapidly spinning systems, the small CO comes much closer to the outer horizon of the Kerr IMBH before merging, and this is the regime where the CO can more strongly feel the effects of the IMBH spin. It is also interesting to point out that the *percentage* error in the spin is quite similar in the two cases. This is consistent with this understanding — the spin is measured

6. Parameter estimation using IMRIs

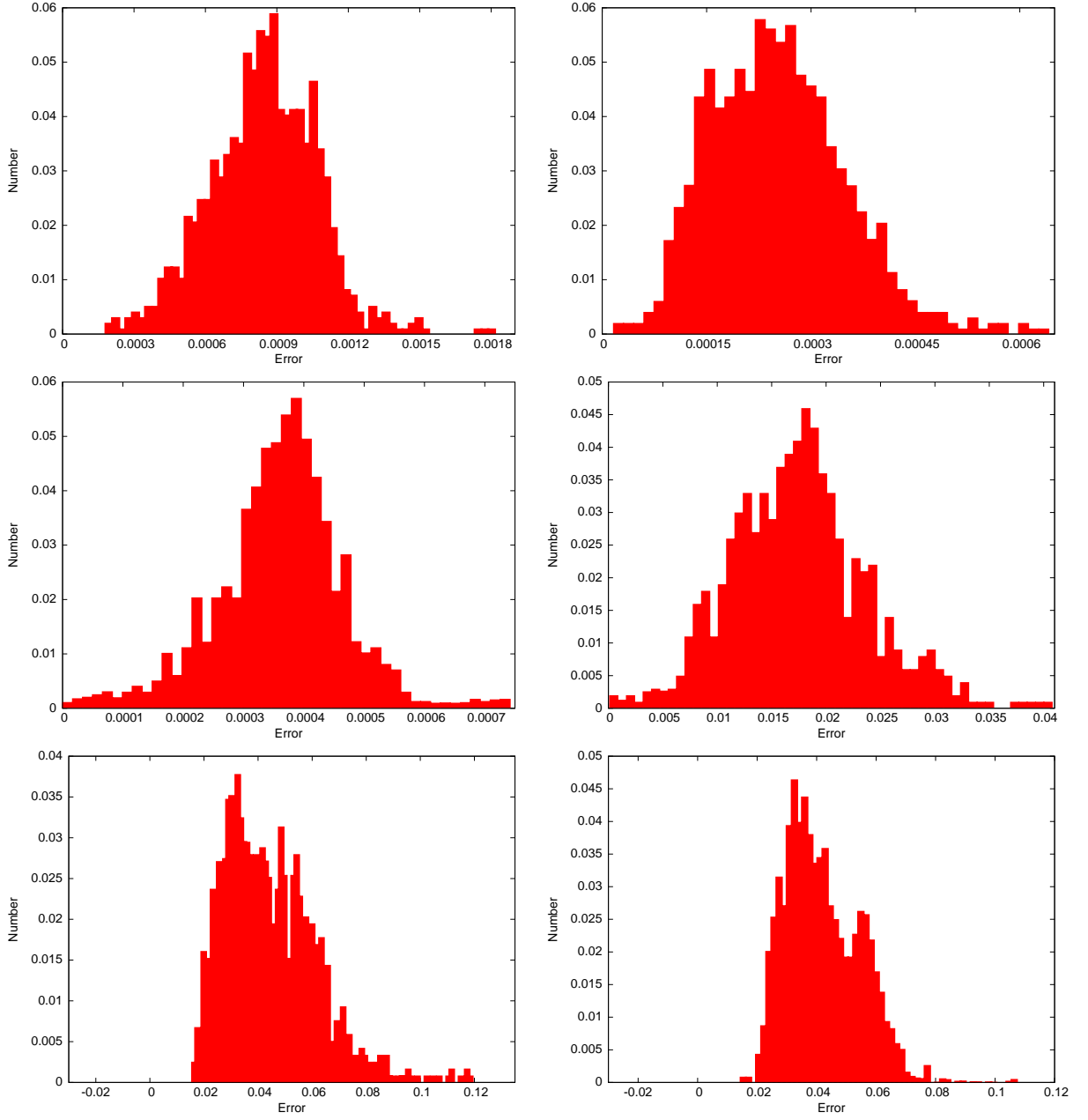


Figure 6.1: Distribution of parameter error estimates for the system with masses $m = 10M_\odot$, $M = 100M_\odot$, and IMBH spin parameter $q = 0.9$. The panels show the error distributions in the following order, top row, from left to right, $\Delta(\ln m)$, $\Delta(\ln M)$; middle row, Δq , Δt_0 ; bottom row, $\Delta\theta_S$, $\Delta\phi_S$.

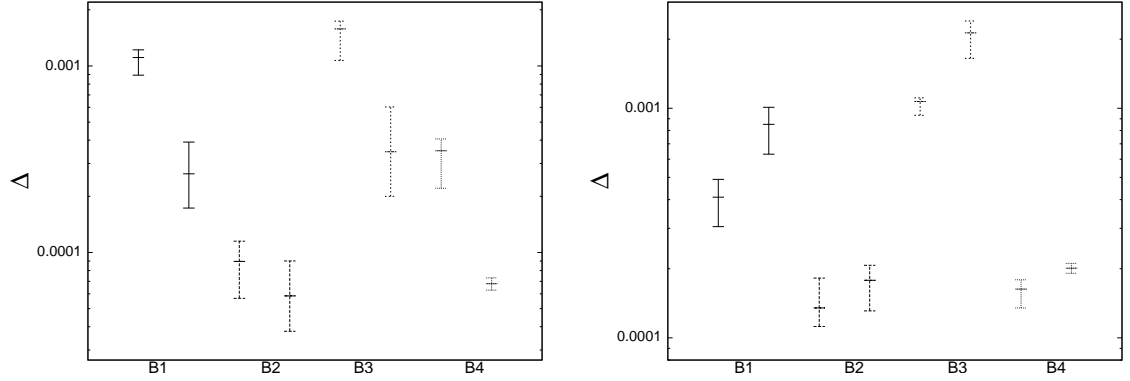


Figure 6.2: Left panel: expected fractional measurement errors, Δ , in the mass of the CO and the mass of the IMBH for a fixed value of the IMBH spin parameter $q = 0.3$. There is a pair of candlesticks for each of the four binary systems. For each binary, the candlestick representing the CO’s mass error estimate is to the left of that for the IMBH’s mass error estimate. The error bars indicate the lower and upper quartiles found in the Monte Carlo simulation. Right panel: expected measurement errors in the IMBH spin parameter for two different values of the spin parameter q . For each system, the candlestick corresponding to a central IMBH with $q = 0.3$ is to the right of that associated with the error estimate for a system with $q = 0.9$. The continuous, long-dashed, dashed and dotted lines represent systems B1: $m = 10M_{\odot}, M = 100M_{\odot}$, B2: $m = 1.4M_{\odot}, M = 100M_{\odot}$, B3: $m = 10M_{\odot}, M = 500M_{\odot}$, and B4: $m = 1.4M_{\odot}, M = 500M_{\odot}$, respectively.

more precisely when it is larger because it has a correspondingly greater effect on the system. For less massive COs, the inspiral proceeds more slowly and the early inspiral has a correspondingly greater importance in the estimation of the system parameters. For such systems, one might expect the precision of spin determination to be less sensitive to the system spin, and this is borne out by these results—the spin precision is comparable for $q = 0.9$ and $q = 0.3$ in the $1.4M_{\odot} + 100M_{\odot}$ and $1.4M_{\odot} + 500M_{\odot}$ systems.

In general, one expects that the precision with which the parameters of a binary can be measured depends on the number of GW cycles that are observed. Therefore, one might expect the precision to depend on the source masses as, from best to worst, $1.4M_{\odot} + 100M_{\odot}$, $1.4M_{\odot} + 500M_{\odot}$, $10M_{\odot} + 100M_{\odot}$, $10M_{\odot} + 500M_{\odot}$. Tables 6.1–6.4, and Figure 6.2 confirm this expectation. These Tables also show that the precision improves for more rapidly spinning IMBHs. This is because, for greater spins, the inspiral phase evolution lasts longer and so there are more cycles of information in the waveform. The SNR of the spinning systems will also be larger at a given distance, as compared with slowly spinning IMBHs, so these systems can be seen further away. This does not affect the results quoted here, which are normalised to fixed SNR=30.

Tables 6.1–6.4 also confirm that the two independent waveform models developed in Chapter 5 make predictions for the parameter estimation errors, for non-spinning systems, that are consistent to better than ten per cent.

An additional point that must be highlighted is the consistency of the distributions of Figure 6.1, in the sense that they are smooth with few outliers. This is a clear indication that the results are convergent. I particularly want to draw attention to this point because it is well known that Fisher Matrices encountered in parameter estimation calculations for GW sources can have very large condition numbers. However, the results I have presented here were obtained from Fisher Matrices that exhibited convergence over at least two orders of magnitude in the offsets used to compute the numerical waveform derivatives. The inverse matrices were computed using an LU decomposition, and I verified that the inverse Fisher matrices were also convergent to $\lesssim 10\%$ over an order of magnitude in the numerical offsets. I also found that the offsets required for the various network configurations were consistent, as one would expect, since the convergence of the FM should depend on the intrinsic waveform, rather than the choice of network.

6.4.2 Dependence of parameter estimation errors on network configuration

In this Section I explore the science that could be done with more modest network configurations, namely the networks C1–C4 described earlier. These consist of combinations of ET’s and right–angle detectors at 2 or 3 sites chosen from Virgo, LIGO Livingston and Perth (Australia). These results obtained are summarised in Tables 6.5–3¹ for the four different mass combinations considered earlier, but with the central IMBH spin fixed at $q = 0.3$. As expected, one finds that a single ET is sufficient for accurate intrinsic parameter determination. This is because the signature of the intrinsic parameters is encoded in the phase evolution, which can be accurately measured by a single instrument. After normalising the parameter errors to a fixed network SNR of 30, Figure 6.3 shows clearly that the accuracy with which the intrinsic parameters of a binary can be determined is not dramatically improved by changes in the network configuration.

However, it is not possible to constrain the location of the source in the sky nor the luminosity distance using a single detector. This is also expected, as the determination of the extrinsic parameters comes primarily from the time–delays between the arrival

¹Note that only Table 6.5 has been included in the main text. Tables 1–3 may be found in Appendix 1.

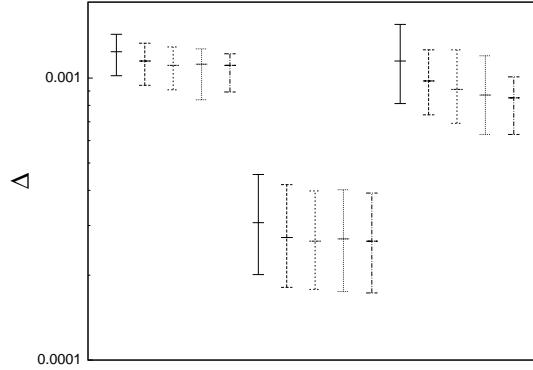


Figure 6.3: Arranged from left to right in the panel, the Figure shows the expected measurement errors in the CO’s mass, IMBH mass and IMBH spin parameter, as a function of the network configuration for binary systems with masses $10M_{\odot} + 100M_{\odot}$ and IMBH spin $q = 0.3$. In each group the candlesticks are arranged in order C1–C5 from left to right. As before, the CO and IMBH mass errors are quoted as fractional errors, i.e., these are the errors in $\ln(m)$, $\ln(M)$.

of the signal in different detectors. It appears that the inclusion of an additional right–angle detector (configuration C2) is enough to constrain the source sky position and luminosity distance to moderate precision ~ 30 sq–degs, $\sim 15\%$, for slowly rotating $10M_{\odot} + 100M_{\odot}$ BH IMRIs at SNR of 30. Replacing this right–angle detector by another ET at the same location (configuration C3) enhances the determination of these parameters to ~ 12 sq–degs, $\sim 10\%$, respectively. Assuming a configuration consisting of 1 ET, plus two right–angle detectors (configuration C4), these estimates are further improved to ~ 11 sq–degs, $\sim 10\%$. These two estimates are rather close to the precision obtained from a 3 ET network, namely, ~ 8 sq–degs, $\sim 10\%$, respectively.

Moreover, these results also show that the distributions become narrower for the more complex configurations, i.e., there is less variation in the precisions with which the extrinsic parameters can be determined as one randomises over the source position and orientation. This is also an expected trend, as a more complex network should provide more complete sky coverage.

In order to put to the test the robustness of the parameter error estimates summarised above, I have cross-checked the predictions of my models with the results for the luminosity distance quoted in Table I of [65]. These latter results are valid in the non–spinning limit and are given at a network SNR of 8. Hence, re-normalising my results for the non–spinning systems to an SNR of 8, I have found that network C2 would be able to measure the luminosity distance to an accuracy of $\sim 40\%$. For configuration C3, GW observations would be able to determine the luminosity distance

to an accuracy of 30% and for C4, this improves marginally to $\sim 28\%$. This estimate is roughly the same for the 3ET detector network (C5). All of these estimates are in good accord with Table I of [65], which were computed for a $\sim 20M_{\odot} + 100M_{\odot}$ binary system using a comparable-mass inspiral-merger-ringdown waveform model. This comparison provides further support that even if the IMRI models used in this studies are not accurate enough to be used for detection of IMRI systems, they do still give reasonable results and can be used for parameter estimation studies to illustrate the potential scientific impact of the ET.

In summary, a single ET will be enough to measure the intrinsic parameters of a system, but will not be sufficient to accurately reconstruct the extrinsic parameters. Extrinsic parameter determination will be possible with the addition of one right-angle detector, but a 2 ET configuration will improve the accuracy with which one can measure the source’s sky position and luminosity distance by roughly a factor of ~ 2 . A more optimistic configuration consisting of a single ET and two right-angle detectors upgraded to ET’s sensitivity will generate results that are competitive with the highly optimistic 3 ET network. This configuration (C3) might be more realistic, since it will have lower overall costs, although it is not simply an upgrade of existing sites as this network assumes the existence of 10km scale right-angle interferometers.

Tables 6.1–3 show that GW observations will produce valuable astrophysical results. A network of 2 ETs operating in coincidence will be able to measure accurately the masses of two merging black holes, and less accurately the sky position and luminosity distance at which the merger is taking place. The results presented in Chapter 5 suggest that a a few tens to a few hundreds of IMRI events could be detected per year by an ET network, provided that IMBHs are relatively abundant in globular clusters, and the various mechanisms leading to CO capture — secular Kozai resonance, binary exchange processes, gravitational radiation and three and four-body interactions — are efficient at starting IMRIs. The ET network would be able to achieve good parameter determinations for all the systems that are detected, which will have important scientific implications.

One important question will be whether the IMBHs detected have been formed in clusters, or are primordial, population III, black holes formed in the early Universe. The precision achievable with network C4, of ~ 11 sq-degs in sky position and $\sim 10\%$ in luminosity distance will not be enough to determine the host galaxy of an IMRI uniquely, let alone if it is occurring in a cluster within that galaxy. If the the ET low-frequency cut-off does extend down to 1Hz, these precisions improve to ~ 1 sq-degs, and $\sim 7\%$, but even that is unlikely to be enough. However, primordial IMBHs are

likely to be hosted in dwarf galaxies today, and the stellar density is sufficiently low that is very unlikely that IMRIs could occur there [64]. Thus, it would be a reasonable assumption that any IMRIs detected would be from cluster IMBHs and not population III black holes. The measured masses and IMBH spins thus provide constraints on the cluster IMBH population, and their evolution.

IMRI systems could be detected up to redshifts as high as $z \sim 6$, if the system has redshifted masses $[10 + 100]M_{\odot}$ and IMBH spin $q = 0.9$, assuming a 3ET network with a frequency cut-off of 1Hz [73]. At such redshifts, the existence of light black holes, no matter how they formed, provides some constraints on the hierarchical assembly of structure. If IMBHs exist at $z \sim 6$, they will inevitably grow and may be progenitors of some fraction of today's supermassive black holes. IMRI detections with ET could therefore be important for cosmology, which relies on the ability to confidently say that an event is at high redshift, which these studies have demonstrated is possible.

A redshift $z \sim 6$ is probably not high enough to provide strong constraints on structure growth, but ET might also detect IMBHs when they merge with comparable mass IMBHs, and these can be seen out to redshifts $z \gtrsim 10$ [64; 65]. Again, the IMBHs involved in such mergers could form either in clusters or in the early Universe. As many as a few tens of mergers involving primordial IMBHs could be detected by ET [65] in the light-seed scenario. The number of comparable mass mergers of IMBHs formed in clusters could be much higher, as many as several thousand [64], but this is very dependent on the efficiency of IMBH formation in the cluster environment. As mentioned above, the IMRIs detected by ET are most likely to be occurring in clusters and thus provide a direct constraint on the existence, number density and properties of IMBHs in clusters. This information can be used to estimate how many of the observed IMBH-IMBH mergers might be coming from the cluster channel and hence what fraction of events might be primordial. IMRI observations will therefore also have indirect applications to our understanding of structure formation.

The Monte Carlo results I have presented in this Chapter are the first results for IMRI sources detectable by ET to appear in the literature. The results must be taken with some caution, because of the approximations in the waveform models that have been made, as discussed earlier. However, these results should be a reasonable guide to the likely order-of-magnitude of the parameter measurement errors that will be achievable. The precise astrophysical implications will depend primarily on the number of events that are seen, which is very difficult to predict given current uncertainties in the astrophysics of IMBHs, and indeed their very existence.

Model		Statistics of distribution for error ΔX in parameter $X =$									
		$\ln(m)$	$\ln(M)$	q	t_0	ϕ_0	θ_S	ϕ_S	θ_K	ϕ_K	$\ln(D)$
q=0.9	Mean	8.31e-4	2.81e-4	3.97e-4	1.66e-2	1.37e-1	4.07e-2	5.09e-2	8.19e-2	1.01e-1	1.01e-1
	St. Dev.	2.27e-4	1.47e-4	1.63e-4	9.17e-3	4.98e-2	1.71e-2	2.74e-2	6.59e-2	6.92e-2	6.64e-2
	L.Qt.	6.86e-4	1.74e-4	3.05e-4	8.69e-3	1.24e-1	2.92e-2	3.46e-2	4.04e-2	4.95e-2	5.15e-2
	Med.	8.45e-4	2.60e-4	4.10e-4	1.50e-2	1.68e-1	4.16e-2	4.62e-2	6.54e-2	7.09e-2	8.01e-2
	U. Qt.	9.59e-4	3.44e-4	4.90e-4	2.23e-2	1.96e-1	5.49e-2	6.06e-2	9.55e-2	1.10e-1	1.28e-1
q=0.3	Mean	1.09e-3	2.96e-4	8.76e-4	1.51e-2	1.13e-1	4.28e-2	5.42e-2	7.80e-2	9.77e-2	1.05e-1
	St. Dev.	3.68e-4	1.22e-4	3.13e-4	8.39e-3	3.55e-2	1.54e-2	2.48e-2	5.17e-2	4.35e-2	7.14e-2
	L.Qt.	8.93e-4	1.73e-4	6.31e-4	1.12e-2	8.95e-2	2.95e-2	3.54e-2	3.93e-2	4.64e-2	5.53e-2
	Med.	1.11e-3	2.64e-4	8.51e-4	1.66e-2	1.29e-1	4.16e-2	5.04e-2	5.73e-2	7.45e-2	8.64e-2
	U. Qt.	1.22e-3	3.91e-4	1.01e-3	2.34e-2	1.59e-1	5.22e-2	6.96e-2	8.64e-2	1.24e-1	1.39e-1
q=0	Mean	4.46e-4	2.29e-4	N/A	1.41e-2	1.21e-1	4.32e-2	5.95e-2	8.53e-2	1.07e-1	1.19e-1
	St. Dev.	2.04e-4	1.39e-4	N/A	5.62e-3	5.17e-2	1.61e-2	3.23e-2	6.51e-2	7.94e-2	7.16e-2
	L.Qt.	3.10e-4	1.70e-4	N/A	9.33e-3	8.49e-2	3.09e-2	3.54e-2	4.00e-2	4.85e-2	5.97e-2
	Med.	4.91e-4	2.51e-4	N/A	1.32e-2	1.06e-1	4.16e-2	5.07e-2	6.48e-2	7.43e-2	8.76e-2
	U. Qt.	6.18e-4	3.89e-4	N/A	1.69e-2	1.48e-1	5.32e-2	7.42e-2	8.79e-2	1.19e-1	1.45e-1
EOB	Mean	3.95e-4	2.11e-4	N/A	1.15e-2	1.23e-1	4.50e-2	5.79e-2	8.48e-2	9.77e-2	1.16e-1
	St. Dev.	1.94e-4	1.29e-4	N/A	6.02e-3	4.87e-2	1.93e-2	2.98e-2	5.89e-2	6.26e-2	6.37e-2
	L.Qt.	2.90e-4	1.55e-4	N/A	7.24e-3	9.17e-2	3.08e-2	3.46e-2	4.19e-2	4.74e-2	5.94e-2
	Med.	4.01e-4	2.25e-4	N/A	1.07e-2	1.17e-1	4.13e-2	4.91e-2	6.56e-2	7.76e-2	8.45e-2
	U. Qt.	5.32e-4	2.99e-4	N/A	1.29e-2	1.48e-1	5.49e-2	7.21e-2	8.73e-2	1.01e-1	1.50e-1

Table 6.1: Summary of Monte Carlo results for parameter estimation errors. The Table shows the mean, standard deviation, median and quartiles of the distribution of the error in each parameter. Results are given for a $m = 10M_\odot$ CO inspiralling into a $M = 100M_\odot$ IMBH for various choices of the IMBH spin, q , computed using the transition model waveform. I also show results for $q = 0$ computed using the EOB waveform model.

Model		Statistics of distribution for error ΔX in parameter $X =$									
		$\ln(m)$	$\ln(M)$	q	t_0	ϕ_0	θ_S	ϕ_S	θ_K	ϕ_K	$\ln(D)$
q=0.9	Mean	9.53e-6	4.30e-6	1.32e-4	1.94e-2	1.44e-1	4.18e-2	4.67e-2	8.32e-2	8.90e-2	9.39e-2
	St. Dev.	4.35e-6	2.17e-6	4.10e-5	7.26e-3	6.21e-2	1.41e-2	1.57e-2	6.51e-2	6.62e-2	6.02e-2
	L.Qt.	6.47e-6	3.12e-6	1.12e-4	1.31e-2	9.18e-2	2.95e-2	3.16e-2	4.27e-2	5.28e-2	5.08e-2
	Med.	9.22e-6	4.51e-6	1.35e-4	1.86e-2	1.51e-1	4.06e-2	4.39e-2	6.79e-2	7.26e-2	6.90e-2
	U. Qt.	1.17e-5	5.94e-6	1.82e-4	2.51e-2	2.09e-1	5.24e-2	5.94e-2	9.44e-2	9.98e-2	1.12e-1
q=0.3	Mean	9.41e-5	5.99e-5	1.80e-4	1.65e-2	1.36e-1	3.97e-2	4.63e-2	7.91e-2	9.15e-2	9.96e-2
	St. Dev.	4.24e-5	3.13e-5	6.86e-5	8.11e-3	6.83e-2	1.25e-2	1.84e-2	5.48e-2	6.27e-2	5.84e-2
	L.Qt.	5.68e-5	3.78e-5	1.31e-4	1.28e-2	1.05e-1	3.05e-2	3.18e-2	3.86e-2	4.91e-2	5.11e-2
	Med.	8.96e-5	5.85e-5	1.78e-4	1.69e-2	1.37e-1	3.96e-2	4.59e-2	5.74e-2	7.81e-2	7.24e-2
	U. Qt.	1.15e-4	9.01e-5	2.07e-4	2.08e-2	1.67e-1	5.17e-2	5.98e-2	1.04e-1	9.95e-2	1.20e-1
q=0	Mean	8.43e-5	6.03e-5	N/A	1.34e-2	1.15e-1	4.19e-2	5.16e-2	8.72e-2	9.41e-2	1.00e-1
	St. Dev.	3.98e-5	3.02e-5	N/A	7.52e-3	4.55e-2	1.51e-2	2.50e-2	6.50e-2	7.49e-2	6.40e-2
	L.Qt.	7.21e-5	3.82e-5	N/A	9.33e-3	8.58e-2	2.91e-2	3.38e-2	4.08e-2	4.41e-2	5.67e-2
	Med.	8.71e-5	5.85e-5	N/A	1.28e-2	1.09e-1	4.07e-2	4.57e-2	6.09e-2	7.38e-2	6.92e-2
	U. Qt.	1.05e-4	7.75e-5	N/A	1.77e-2	1.67e-1	5.28e-2	6.47e-2	9.46e-2	1.09e-1	1.11e-1
EOB	Mean	8.61e-5	5.65e-5	N/A	1.20e-2	1.24e-1	4.30e-2	5.64e-2	8.93e-2	9.65e-2	1.04e-1
	St. Dev.	3.16e-5	2.15e-5	N/A	5.72e-3	4.34e-2	1.86e-2	2.71e-2	6.97e-2	7.48e-2	6.87e-2
	L.Qt.	7.08e-5	3.69e-5	N/A	1.09e-2	8.95e-2	3.01e-2	3.28e-2	4.13e-2	4.98e-2	5.36e-2
	Med.	8.51e-5	5.21e-5	N/A	1.25e-2	9.59e-2	4.16e-2	4.68e-2	5.93e-2	7.66e-2	7.56e-2
	U. Qt.	1.02e-4	7.18e-5	N/A	1.38e-2	1.71e-1	5.39e-2	7.14e-2	9.72e-2	1.13e-1	1.31e-1

Table 6.2: As Table 6.1, but now for binary systems with a CO of mass $m = 1.4M_\odot$.

Model		Statistics of distribution for error ΔX in parameter $X =$									
		$\ln(m)$	$\ln(M)$	q	t_0	ϕ_0	θ_S	ϕ_S	θ_K	ϕ_K	$\ln(D)$
q=0.9	Mean	1.33e-3	5.10e-4	1.01e-3	1.41e-2	1.21e-1	4.47e-2	5.59e-2	9.86e-2	1.07e-1	1.15e-1
	St. Dev.	6.04e-4	1.66e-4	2.79e-4	4.77e-3	4.87e-2	1.64e-2	2.42e-2	6.80e-2	7.47e-2	4.66e-2
	L. Qt.	9.53e-4	4.39e-4	9.32e-4	1.15e-2	8.21e-2	3.02e-2	3.41e-2	4.86e-2	5.68e-2	6.80e-2
	U. Qt.	1.26e-3	5.08e-4	1.07e-3	1.57e-2	1.11e-1	4.16e-2	4.89e-2	6.86e-2	6.83e-2	8.91e-2
q=0.3	Mean	1.41e-3	3.63e-4	2.09e-3	1.19e-2	1.05e-1	3.95e-2	5.12e-2	9.57e-2	1.08e-1	1.12e-1
	St. Dev.	6.39e-4	1.87e-4	5.72e-4	5.07e-3	5.20e-2	1.19e-2	2.03e-2	6.74e-2	8.75e-2	7.67e-2
	L. Qt.	1.07e-3	2.00e-4	1.65e-3	7.41e-3	7.83e-2	2.96e-2	3.43e-2	5.74e-2	5.75e-2	5.93e-2
	U. Qt.	1.58e-3	3.47e-4	2.13e-3	1.24e-2	9.38e-2	3.86e-2	4.79e-2	6.91e-2	8.79e-2	8.82e-2
q=0	Mean	4.06e-3	1.54e-3	N/A	1.01e-2	9.86e-2	4.36e-2	5.54e-2	1.00e-1	1.14e-1	1.25e-1
	St. Dev.	2.47e-3	6.58e-4	N/A	5.69e-3	5.05e-2	1.63e-2	2.65e-2	6.31e-2	7.58e-2	8.10e-2
	L. Qt.	2.95e-3	1.20e-3	N/A	8.14e-3	7.71e-2	2.96e-2	3.53e-2	4.50e-2	5.25e-2	5.82e-2
	U. Qt.	4.09e-3	1.51e-3	N/A	1.17e-2	1.04e-1	4.06e-2	4.99e-2	6.84e-2	8.31e-2	9.11e-2
EOB	Mean	6.21e-3	1.99e-3	N/A	1.35e-2	1.24e-1	5.55e-2	7.01e-2	1.13e-1	1.21e-1	1.71e-1
	St. Dev.	3.59e-3	1.53e-3	N/A	1.02e-2	1.00e-1	4.63e-2	5.72e-2	9.69e-2	1.07e-1	1.31e-1
	L. Qt.	1.07e-3	5.89e-4	N/A	5.46e-3	3.46e-2	2.01e-2	2.91e-2	7.56e-2	8.94e-2	8.29e-2
	U. Qt.	2.88e-3	1.04e-3	N/A	7.94e-3	8.77e-2	3.02e-2	3.44e-2	4.22e-2	5.62e-2	6.31e-2
EOB	Mean	3.62e-3	1.39e-3	N/A	1.10e-2	9.92e-2	4.16e-2	5.24e-2	6.56e-2	8.12e-2	9.92e-2
	St. Dev.	4.09e-3	1.75e-3	N/A	1.38e-2	1.26e-1	5.71e-2	7.42e-2	1.01e-1	1.19e-1	1.79e-1
	L. Qt.	2.88e-3	1.04e-3	N/A	7.94e-3	8.77e-2	3.02e-2	3.44e-2	4.22e-2	5.62e-2	6.31e-2
	U. Qt.	4.09e-3	1.75e-3	N/A	1.38e-2	1.26e-1	5.71e-2	7.42e-2	1.01e-1	1.19e-1	1.79e-1

Table 6.3: As Table 6.1, but now for binary systems with a central IMBH of mass $M = 500M_\odot$.

Model		Statistics of distribution for error ΔX in parameter $X =$									
		$\ln(m)$	$\ln(M)$	q	t_0	ϕ_0	θ_S	ϕ_S	θ_K	ϕ_K	$\ln(D)$
q=0.9	Mean	2.69e-4	8.71e-5	1.38e-4	1.41e-2	1.14e-1	4.34e-2	5.77e-2	9.61e-2	1.18e-1	9.44e-2
	St. Dev.	1.14e-4	3.21e-5	5.90e-5	4.57e-3	4.41e-2	1.68e-2	2.85e-2	7.54e-2	7.70e-2	5.45e-2
	L.Qt.	1.95e-4	7.41e-5	1.35e-4	1.23e-2	9.79e-2	2.92e-2	3.56e-2	4.79e-2	5.08e-2	4.94e-2
	Med.	2.78e-4	8.91e-5	1.63e-4	1.47e-2	1.21e-1	4.26e-2	5.02e-2	6.51e-2	8.18e-2	6.81e-2
	U. Qt.	3.49e-4	1.01e-4	1.79e-4	1.73e-2	1.44e-1	5.49e-2	7.18e-2	1.16e-1	1.50e-1	1.21e-1
q=0.3	Mean	3.17e-4	6.82e-5	2.03e-4	1.14e-2	9.02e-2	4.02e-2	5.75e-2	8.59e-2	1.10e-1	9.68e-2
	St. Dev.	1.03e-4	8.51e-6	4.31e-5	5.22e-3	5.32e-2	1.28e-2	2.84e-2	6.22e-2	9.12e-2	6.10e-2
	L.Qt.	2.21e-4	6.28e-5	1.91e-4	1.02e-2	7.02e-2	3.02e-2	3.23e-2	4.48e-2	5.25e-2	4.91e-2
	Med.	3.51e-4	6.80e-5	2.01e-4	1.17e-2	9.34e-2	4.16e-2	5.17e-2	6.14e-2	8.22e-2	7.39e-2
	U. Qt.	4.06e-4	7.31e-5	2.11e-4	1.65e-2	1.24e-1	5.09e-2	6.97e-2	1.06e-1	1.50e-1	1.21e-1
q=0	Mean	2.71e-4	1.07e-4	N/A	1.03e-2	9.18e-2	4.33e-2	5.69e-2	8.35e-2	1.10e-1	1.11e-1
	St. Dev.	5.44e-5	2.10e-5	N/A	3.09e-3	5.43e-2	1.58e-2	2.81e-2	6.35e-2	8.71e-2	7.23e-2
	L.Qt.	2.51e-4	1.00e-4	N/A	6.31e-3	6.32e-2	3.09e-2	3.46e-2	4.17e-2	4.75e-2	5.09e-2
	Med.	2.63e-4	1.17e-4	N/A	1.09e-2	9.41e-2	4.27e-2	5.12e-2	5.84e-2	7.81e-2	8.70e-2
	U. Qt.	2.95e-4	1.23e-4	N/A	1.25e-2	1.17e-1	5.49e-2	7.21e-2	1.03e-1	1.50e-1	1.30e-1
EOB	Mean	2.87e-4	1.25e-4	N/A	1.07e-2	9.46e-2	4.75e-2	5.70e-2	8.53e-2	1.07e-1	1.23e-1
	St. Dev.	8.23e-5	3.33e-5	N/A	4.37e-3	3.22e-2	1.66e-2	2.94e-2	6.72e-2	7.61e-2	8.49e-2
	L.Qt.	2.29e-4	1.02e-4	N/A	7.94e-3	7.06e-2	3.02e-2	3.54e-2	4.36e-2	4.79e-2	6.02e-2
	Med.	2.75e-4	1.20e-4	N/A	1.04e-2	9.18e-2	4.16e-2	4.82e-2	5.91e-2	7.53e-2	8.75e-2
	U. Qt.	3.09e-4	1.35e-4	N/A	1.23e-2	1.16e-1	5.85e-2	7.41e-2	9.98e-2	1.36e-1	1.34e-1

Table 6.4: As Table 6.2, but now for binary systems with a central IMBH of mass $M = 500M_\odot$.

Model		Statistics of distribution for error ΔX in parameter $X =$									
		$\ln(m)$	$\ln(M)$	q	t_0	ϕ_0	θ_S	ϕ_S	θ_K	ϕ_K	$\ln(D)$
C1	Mean	1.23e-3	3.45e-4	1.15e-3	2.04e-2	1.62e-1	2.2995	2.7421	3.7537	4.0738	4.2386
	St. Dev.	4.19e-4	1.99e-4	4.23e-4	9.71e-3	5.90e-2	3.4104	4.0524	3.9352	4.0112	4.1351
	L.Qt.	1.02e-3	2.01e-4	8.12e-4	1.41e-2	1.23e-1	0.0866	0.1018	1.0189	1.1825	1.2491
	Med.	1.24e-3	3.07e-4	1.15e-3	1.99e-2	1.62e-1	0.6820	0.8174	2.2722	2.6118	2.6707
	U. Qt.	1.43e-3	4.55e-4	1.55e-3	2.81e-2	1.84e-1	2.9151	3.3087	4.9711	5.3026	5.7026
C2	Mean	1.11e-3	3.13e-4	9.12e-4	1.69e-2	1.34e-1	6.19e-2	7.61e-2	1.50e-1	1.88e-1	1.76e-1
	St. Dev.	4.84e-4	1.84e-4	3.57e-4	8.43e-3	4.35e-2	3.77e-2	4.62e-2	1.28e-1	1.76e-1	1.54e-1
	L.Qt.	9.43e-4	1.81e-4	7.41e-4	1.23e-2	1.08e-1	3.31e-2	3.76e-2	6.60e-2	6.34e-2	9.05e-2
	Med.	1.15e-3	2.72e-4	9.77e-4	1.82e-2	1.45e-1	5.18e-2	6.22e-2	1.01e-1	1.28e-1	1.47e-1
	U. Qt.	1.33e-3	4.19e-4	1.26e-3	2.63e-2	1.75e-1	7.79e-2	1.07e-1	2.03e-1	2.48e-1	2.74e-1
C3	Mean	1.07e-3	3.04e-4	8.87e-4	1.66e-2	1.29e-1	4.56e-2	5.81e-2	8.47e-2	1.14e-1	1.11e-1
	St. Dev.	3.73e-4	1.75e-4	3.59e-4	8.01e-3	4.12e-2	2.15e-2	3.27e-2	6.78e-2	9.85e-2	8.35e-2
	L.Qt.	9.09e-4	1.78e-4	6.91e-4	1.12e-2	1.08e-1	2.89e-2	3.24e-2	4.07e-2	4.92e-2	5.81e-2
	Med.	1.11e-3	2.64e-4	9.12e-4	1.77e-2	1.45e-1	4.29e-2	4.92e-2	6.07e-2	7.83e-2	8.73e-2
	U. Qt.	1.29e-3	3.98e-4	1.26e-3	2.63e-2	1.75e-1	5.95e-2	7.20e-2	9.78e-2	1.49e-1	1.45e-1
C4	Mean	1.05e-3	3.01e-4	8.79e-4	1.58e-2	1.18e-1	4.47e-2	5.61e-2	8.24e-2	1.14e-1	1.12e-1
	St. Dev.	4.27e-4	1.78e-4	3.56e-4	8.14e-3	4.38e-2	2.09e-2	2.87e-2	6.38e-2	9.81e-2	8.07e-2
	L.Qt.	8.38e-4	1.75e-4	6.31e-4	1.12e-2	1.04e-1	3.21e-2	3.54e-2	4.46e-2	4.82e-2	5.38e-2
	Med.	1.12e-3	2.69e-4	8.71e-4	1.77e-2	1.45e-1	4.06e-2	5.02e-2	6.91e-2	7.71e-2	8.52e-2
	U. Qt.	1.27e-3	4.02e-4	1.20e-3	2.39e-2	1.69e-1	5.45e-2	6.91e-2	9.54e-2	1.33e-1	1.40e-1
C5	Mean	1.09e-3	2.96e-4	8.76e-4	1.51e-2	1.13e-1	4.28e-2	5.42e-2	7.80e-2	9.77e-2	1.05e-1
	St. Dev.	3.68e-4	1.22e-4	3.13e-4	8.39e-3	3.55e-2	1.54e-2	2.48e-2	5.17e-2	4.35e-2	7.14e-2
	L.Qt.	8.93e-4	1.73e-4	6.31e-4	1.12e-2	8.39e-2	2.95e-2	3.54e-2	3.93e-2	4.64e-2	5.53e-2
	Med.	1.11e-3	2.64e-4	8.51e-4	1.66e-2	1.29e-1	4.16e-2	5.04e-2	5.73e-2	7.45e-2	8.64e-2
	U. Qt.	1.22e-3	3.91e-4	1.01e-3	2.34e-2	1.59e-1	5.22e-2	6.96e-2	8.64e-2	1.24e-1	1.39e-1

Table 6.5: As Table 6.1, but for binary systems with a central IMBH of spin parameter $q = 0.3$ and assuming four alternative configurations for the detector network, C1-C4, as described in Section 6.2. Configuration C5 is the network of three ETs which has been used for all results elsewhere in this Chapter.

6.5 Conclusions

Making use of the waveform models introduced in Chapter 5, I have estimated the precision with which the ET will be able to determine the parameters of circular–equatorial IMRIs. I have presented results for a set of twelve “typical” systems, comprising four different combinations of component masses — $1.4M_{\odot} + 100M_{\odot}$, $1.4M_{\odot} + 500M_{\odot}$, $10M_{\odot} + 100M_{\odot}$, and $10M_{\odot} + 500M_{\odot}$ — and three different IMBH spins — $q = 0, 0.3, 0.9$. For the non–spinning systems, I have compared the results between the transition and the EOB–based waveform models, and have found that these models make predictions that are consistent to better than ten percent. This final check provides confidence in these results.

I have also explored how the accuracy of parameter determination depends on the configuration of the detector network using the “ET–B” noise curve, and assuming a cut–off frequency of 5Hz. I have shown that a single ET is sufficient to accurately determine the intrinsic parameters of these systems. However, a network of detectors is required to obtain accurate estimates of the extrinsic parameters. A network of 2 ETs should be sufficient to measure the source’s sky position and luminosity distance to accuracies of ~ 12 sq–degs and $\sim 10\%$, respectively, for a BH IMRI into a $100M_{\odot}$ IMBH with spin parameter $q = 0.3$. A more sophisticated network comprising 1 ET and two right–angle detectors would have comparable precisions. The results for the latter networks are comparable to the precisions that could be achieved with a 3 ET network, which are ~ 8 sq–degs, 10% , respectively (at a source SNR of 30). Any one of these ET networks would simultaneously be able to constrain the BH and IMBH masses and the IMBH spin magnitude to fractional accuracies of $\sim 10^{-3}$, $10^{-3.5}$ and 10^{-3} , respectively. The amount of variation in the parameter precision over random choices of the source location and orientation also decreases for more complex network configurations. A 3 ET network is a highly optimistic assumption about a future third–generation GW detector network, but these results indicate that a more modest network comprising one ET and right–angle interferometers in LIGO Livingston and Perth can recover parameters to almost the same precision. This network would have lower associated costs and might therefore be more feasible. These results should be regarded as conservative in the sense that using a lower low–frequency cut–off, or assuming a different ET design, e.g., the xylophone configuration [69], may improve the accuracy with which a detector network can determine the systems’ parameters. For these studies I made use of the “ET–B” noise curve [77], but a study of the potential applications of ET using both lower cut–off frequencies and more optimistic designs should be carried out in the

future.

The scientific payoffs that will be obtained through the detection of IMRIs are numerous. The detection of an IMBH as a GW source would provide the first robust confirmation of the existence of IMBHs. As discussed in the previous section, IMRIs are most likely to occur in globular clusters, thus IMRI observations will provide information about whether IMBHs form at all in these stellar environments, and whether they remain in the clusters or are ejected. The masses, spins and abundance of IMBHs detected via IMRIs will provide constraints on the formation efficiency and evolution of globular cluster systems. In conjunction with ET observations of comparable mass IMBH-IMBH mergers, IMRI observations could shed light on the hierarchical growth of structure, in particular to distinguish between light and heavy seed models, as described in more detail at the end of Section 6.4.

A further potentially exciting payoff of ET IMRI observations will be that of testing whether the central object in an IMRI is described by the Kerr metric of general relativity. During the inspiral, the CO traces out the geometry of the spacetime of the central object. Hence, the GWs emitted during the inspiral encode a map of the spacetime. In [66; 67], it was shown that any stationary, axisymmetric, vacuum spacetime in relativity can be decomposed into mass, M_ℓ , and current, S_ℓ , multipole moments. Ryan [115] went on to show that, for nearly equatorial, nearly circular inspirals, these multipole moments are redundantly encoded in gravitational wave observables, namely the periapsis precession frequency, the orbital plane precession frequency and the gravitational wave energy spectrum. The multipole moments of a Kerr black hole are completely determined by its mass, M , and spin, S_1 , through the relation [67]

$$M_\ell + iS_\ell = M (ia)^\ell, \quad (6.3)$$

where $a = S_1/M$ is the reduced spin of the black hole. Extracting three moments of the spacetime from GW emission, and finding them inconsistent with 6.3, would suffice to demonstrate that the central object is not a Kerr black hole. Tests of this nature have been carried out for observations of EMRI systems with LISA. Using a kludge model that included a non-Kerr value for the quadrupole moment of the central black hole, Barack and Cutler [7] showed that LISA could measure the quadrupole moment, $Q = -S^2/M$, of the central black hole to an accuracy $\Delta Q/M^3 \sim 10^{-3}$, while simultaneously measuring the mass and spin to an accuracy $\sim 10^{-4}$. In the context of IMRIs detected by Advanced LIGO, it has been shown that it is possible to measure an $\mathcal{O}(1)$ fractional deviation in the mass quadrupole moment for typical systems [22]. ET

could improve this precision by more than an order of magnitude, since ET's enhanced sensitivity will allow a significantly larger number of GW cycles to be observed. For instance, for a $1M_{\odot} + 100M_{\odot}$ system, Advanced LIGO could measure ~ 500 cycles until plunge. In contrast, ET, with a low-frequency cut-off at 1Hz, will observe up to ~ 25000 cycles [57]. Hence, ET has, in principle, the potential to improve previous strong-field regime tests in the intermediate-mass regime, but further work is required to properly quantify its ability to carry out tests of this nature.

These results are a first attempt to explore the precision of IMRI parameter estimation that will be achievable with the ET. My results have been derived using a particular waveform model, which reflects the best information currently available, and combines results from both comparable mass binaries and extreme-mass-ratio inspirals. These waveforms are unlikely to be accurate enough to be used in a search to recover source parameters, but they should capture most of the main features of true IMRI waveforms and, therefore, provide a fair estimate of the level of precision that could be achieved by GW measurements. The waveform models could be improved in various ways, by including conservative corrections, by generalizing the waveform models to consider both eccentric orbits and orbits inclined to the equatorial plane, and by including the leading order effects of the spin of the smaller object, as I have already done for EMRIs in Chapter 3. The EOB model can also now be extended to spinning systems, for circular-equatorial inspirals at least [136], which will provide further important consistency checks for the transition model. These will be important improvements to consider in the future in order to confirm the present results, and to extend the calculations to generic IMRI systems.

Chapter 7

Conclusions

In his book *“Black Holes and time warps: Einstein’s outrageous legacy”* [128] Kip Thorne describes a hypothetical situation in which gravitational wave (GW) observations, in conjunction with information obtained through complementary high-energy astrophysics techniques, are used to unravel “the details of how gigantic black holes (BHs) are born”. In his digression, penned back in 1993, he guessed that by 2007, eight interferometers located in various parts on the Earth would be gathering information from incoming bursts of GWs. His vision was even bolder for 2017, when he imagined that an interferometric detector would be in operation on the Moon. Although we are not at this stage, the description by Thorne of the methodology, involving the use of waveform templates to analyse GW data to reconstruct the parameters of GW sources, is in close accord with the methodology employed today.

Over the last few decades, a number of stellar mass and supermassive black holes (SMBHs) have been discovered by means of the study of dynamics of stars around them [3], and through X-ray observations. Since many of these objects, and a vast number of yet unseen objects, may be GW sources, a major program that aims to develop powerful mathematical and numerical tools to study the gravitational radiation emitted by these sources has been under way for the last few years. In parallel to this theoretical effort, the construction of ground-based detector networks, and the ongoing upgrade in sensitivity of these detectors will increase the possibility of directly detecting GWs for the first time within the coming decade.

The realisation of a low-frequency GW detector in space will also play a crucial role in the detection of GW sources whose existence has been inferred by other means, such as merging SMBHs, compact object binaries in the Milky Way with periods less than a few hours, and extreme-mass-ratio inspirals (EMRIs). It is very likely that a space-based GW detector will provide the means, and possibly the best chance, to

detect GW sources that radiate in the low-frequency band.

In this thesis I have considered two types of low-frequency GW sources, namely EMRIs and intermediate-mass-ratio inspirals (IMRIs). The detection of the GWs emitted by these systems will provide information about the astrophysical properties of SMBHs and intermediate-mass black holes (IMBHs) that would be difficult, if not impossible, to obtain by other means.

With regard to EMRIs, it is hoped that a future low-frequency GW detector will shed light on the mass and spin distributions of SMBHs in a mass range that is extremely difficult to observe through electromagnetic observations. To do this science, it is essential to develop accurate waveform templates for use in data analysis. In Chapter 2 I explored the importance of including conservative self-force corrections in EMRI models for detection and for parameter estimation, using a numerical kludge waveform model for circular, equatorial EMRIs. From a Monte Carlo simulation of the parameter estimation errors, I found that for a $10M_{\odot}$ BH captured by a $10^6 M_{\odot}$ SMBH at signal-to-noise-ratio (SNR) of 30, GW observations should be able to determine the component masses of the system to within a fractional error of $\sim 10^{-4}$, measure the SMBH spin parameter to $\sim 10^{-4.5}$, and determine both the location of the source in the sky, and the SMBH spin orientation to within $\sim 10^{-3}$ steradians. Additionally, I found that for this model, the ratio \mathcal{R} of the systematic error—which arises from omitting the conservative corrections on the template—to the noise-induced error is $\mathcal{R} \lesssim 1$ for all parameters in the model over much of the parameter space. So, conservative corrections may be marginally ignored for parameter estimation. Using accurate self-force corrections for Schwarzschild BHs, I found that the second order radiative piece of the self-force contributes to the phase at a comparable level to the first order conservative piece of the self-force, and systematic errors are a few times the noise-induced errors. This then implies that for accurate parameter estimation, it may be necessary to include conservative corrections in approximate models to constrain the source to a sufficiently small area of parameter space. One then could follow up the sources using more accurate templates to get more precise estimates.

The results described in Chapter 2 are valid for circular, equatorial EMRIs. In order to verify that these conclusions are representative of the more general case, i.e., eccentric inclined EMRIs, one needs to perform a more realistic treatment of the capture problem. Capture orbits are expected to be generally non-equatorial; and Monte Carlo simulations [6] suggest that about half of the captures of $\sim 10M_{\odot}$ BHs should have eccentricity $e \gtrsim 0.2$ at the last stable orbit. The initial eccentricity of these captures a year before plunge will be significantly larger. One possible approach to find

out whether conservative self-force corrections have a more significant impact on parameter estimation and detection in the generic case, would consist of extending the analysis carried out in Chapter 2 to such orbits. This would require amending the azimuthal frequency, the perihelion precession frequency and the rate of precession of the orbital plane with conservative corrections. By identifying the rate of change of these frequencies between the kludge model and post-Newtonian (PN) results, one can derive the conservative corrections in a manner similar to that used in Chapter 2. This will require identifying the radius, eccentricity and orbital inclination between the kludge and PN waveform models. The second part of this project would involve developing a code to compute convergent Fisher matrices, and reliable numerical routines to provide an inverse Fisher Matrix that is both convergent and stable.

In Chapter 3 I showed that including small body spin corrections would be important for parameter estimation in the context of IMRIs for systems whose mass ratio $\eta \gtrsim 10^{-3}$. At a fixed SNR of 1000, GW observations from rapidly spinning systems with masses $5 \times 10^3 M_\odot + 10^6 M_\odot$, will be able to determine the mass of the inspiralling body, the mass of the central SMBH, the SMBH spin magnitude, and the inspiralling body spin magnitude, to within fractional errors of $\sim 10^{-3}, 10^{-4}, 10^{-3}, 10\%$, respectively. This analysis also showed that small body spin effects will have a significant impact on parameter estimation when both components of the binary are rapidly rotating, but not if the central SMBH is slowly rotating.

In addition, I showed that including conservative corrections up to 2PN order in IMRI waveform templates will be important to reduce systematic errors to an acceptable level. For rapidly rotating sources with masses $5 \times 10^3 M_\odot + 10^6 M_\odot$, the error ratio $\mathcal{R} \lesssim 4$ when comparing a 2PN waveform to one truncated at 1.5PN order. In contrast, for the comparison to a waveform truncated at 0PN, this error ratio \mathcal{R} is a factor of 20/30 larger for intrinsic/extrinsic parameters. This is an important result, since previous studies had found that systematic errors were a limiting factor for determining the system parameters accurately [35].

A natural extension of this work would consist of including conservative corrections up to 3.5PN order to find out whether systematic errors are further reduced. The methodology for such an analysis would be the same as that used in Chapter 3. Another extension of this work, related to the importance of conservative corrections for parameter estimation in IMRIs, would consist of using the generic model described above to explore the extent to which conservative corrections affect systematic errors for eccentric inclined IMRIs.

In Chapter 4 I presented a few results relevant to a current study organised by ESA

which is trying to assess the science that could be done with alternative configurations of the original LISA mission. The results presented in that Chapter indicate that more modest LISA configurations will be able to do high precision science with EMRIs, since the parameter estimation errors using the descope designs are very similar, at fixed SNR, to the results quoted in Chapter 2 for the baseline LISA mission.

The second half of this thesis dealt with IMRIs in the context of ground-based detector networks. In contrast with EMRIs, which have been the subject of exhaustive study, and whose existence has some support from observations, IMRI sources lie on comparatively weaker grounds. No IMBHs are known in binaries in the Local Group, and no mapping of stellar motion around IMBHs has ever been obtained due to their small radii of influence.

However, as discussed in Chapter 5, there is indirect evidence for their existence, and it is expected that GW observations could play a decisive role in confirming the existence of IMBHs. The templates to model GW radiation from these systems are in a very early stage of development, and numerical relativity has only recently been used to study these systems. In the work recently published in [87], Lousto et al., presented a fully non-linear numerical simulation of non-spinning BH binaries with mass-ratio 100:1 that complete two orbits before plunge. However, using numerical relativity simulations to model IMRIs that complete hundreds of cycles before plunge would be very computationally expensive, and lie beyond current capabilities.

For these reasons, and in order to make progress in this area, in Chapter 5 I introduced models for IMRI waveforms for circular equatorial inspirals. These models combine the best information currently available from two regimes that have been extensively studied in the past, namely, BH perturbation theory (for EMRIs), and PN theory (for comparable mass binaries). I used the kludge waveform model, introduced in Chapter 2, to model the inspiral phase for the two alternative models I developed in Chapter 5. In one of the models, valid for spinning IMBHs, I have used the transition regime, developed by Ori and Thorne [104], to describe the merger phase. The second model, valid for non-spinning BHs, used the effective-one-body approach to model the merger phase. I then showed how to smoothly match the merger phase of both models onto a ringdown waveform. I showed that these two models make SNR predictions for non-spinning inspirals that are consistent to about ten percent. Using these models in the context of the Einstein Telescope (ET), assuming a frequency cut-off of 5Hz, and at redshift $z = 1$, I found that typical SNRs for IMRI systems with redshifted masses $1.4M_{\odot} + 100M_{\odot}$, $10M_{\odot} + 100M_{\odot}$, $1.4M_{\odot} + 500M_{\odot}$, $10M_{\odot} + 500M_{\odot}$ will be in the range $\sim 10 - 25, \sim 40 - 80, \sim 3 - 15, \sim 10 - 60$. Using this information I found that, de-

pending on the intrinsic distribution of masses and spins of IMRIs, ET could detect as many as several hundred of these events up to redshift $z \lesssim 5$. If ET achieves sensitivity down to 1Hz, these systems could be detected up to $z \lesssim 6$. I also explored the IMRI science that could be done with a variety of networks, including 1ET only, 1ET plus 1 right-angle detector (RAD), 2ETs, 1ET plus 2RADs, and 3 ETs. This study showed that a 1ET plus 2RADs configuration will have almost as great a sensitivity to IMRIs as a network of 3ETs.

In Chapter 6 I used the Fisher Matrix formalism, introduced in Chapter 2, to explore the precision with which the ET will be able to determine the parameters of IMRIs. I showed that for systems with masses $10M_{\odot} + 100M_{\odot}$, at fixed SNR of 30, and at redshift $z = 1$, a 3ET network will be able to constrain the BH and IMBH masses, and the IMBH spin magnitude to within fractional errors of $\sim 10^{-3}$, $10^{-3.5}$, and 10^{-3} , respectively. This network would also be able to determine the position of the source in the sky, and the luminosity distance to accuracies of ~ 8 square degrees, and $\sim 10\%$, respectively. I showed that a network comprising 1ET in Italy, and 2RADs in LIGO Livingston and Perth would recover parameters with similar precision. This exercise may prove useful if the ET is realised, since this network would have a better science-cost relationship.

It is important to press forward in the development of accurate waveform templates for generic IMRIs since advanced detectors, such as advanced LIGO, will be searching for these events, and could therefore shed light on the astrophysical properties of IMBHs, and in turn provide new information on the physics of core-collapsed globular clusters.

A natural extension of these circular-equatorial IMRI models to eccentric inclined models would involve using the generic kludge model developed in [5], the generic transition model for the merger phase described in [122], and the ringdown model developed in [14]. These three ingredients can be combined, using the methodology described in Chapter 5, to build a generic IMRI model. Another ingredient that could be used to improve these models is the inclusion of small body spin effects, using the inspiral model introduced in Chapter 3.

The waveform models developed in this thesis, and the results I have obtained using them, will contribute to the development of GW astronomy. This thesis has shed light on the astrophysical payoffs that will be obtained through GW observations. I have explored the regime at which conservative self-force corrections and small body spin effects should be included in waveform templates to enhance their accuracy, and enable the measurement of the physical parameters of inspiralling objects. These two issues

were addressed for the first time in the literature. The final contribution of this thesis is the development of complete IMRI models, and their use to explore IMRI science using a third generation GW interferometer. This study rendered two interesting results. Firstly, the prospects of detection of IMBHs through IMRI observations, and secondly, valuable input for the design of the ET.

In addition to these astrophysical payoffs, GW observations may also be used to test predictions of general relativity in the strong field. Data gathered from these observations may be used to rule out rival theories, and/or to confirm their consistency with the data. These observations will supersede any previous attempts to study the properties of astrophysical compact objects, and will provide a wealth of information on the astrophysical processes taking place in the local and early Universe.

Appendix A

.1 Dependence of parameter estimation errors on network configuration

This Appendix contains Tables 1–3. These Tables show how the expected parameter measurement errors depend on the network configuration. I explore how parameter estimation accuracies are modified for five network configurations, C1–C5. These configurations are, C1: one ET at the geographic location of Virgo; C2: as configuration C1 plus a right-angle detector at the location of LIGO Livingston; C3: as configuration C1 plus another ET at the location of LIGO Livingston; and C4: as configuration C2 plus another right-angle detector in Perth. Note that the reference 3-ET network is referred to as configuration C5.

Model		Statistics of distribution for error ΔX in parameter $X =$									
		$\ln(m)$	$\ln(M)$	q	t_0	ϕ_0	θ_S	ϕ_S	θ_K	ϕ_K	$\ln(D)$
C1	Mean	1.26e-4	7.76e-5	1.96e-4	2.63e-2	2.01e-1	3.7418	4.1009	6.6255	7.4131	9.2443
	St. Dev.	6.54e-5	4.57e-5	9.27e-5	1.30e-2	1.09e-1	4.0925	4.7919	4.5011	5.2979	6.6406
	L.Qt.	6.73e-5	4.47e-5	1.84e-4	1.73e-2	1.29e-1	0.5762	0.4917	2.8422	3.5419	5.2586
	Med.	9.93e-5	7.08e-5	2.19e-4	2.51e-2	1.85e-1	2.0259	2.0586	5.8983	6.9206	8.5296
	U. Qt.	1.66e-4	1.17e-4	2.36e-4	3.54e-2	2.56e-1	6.1471	6.1689	8.9838	11.4924	12.6824
C2	Mean	1.09e-4	6.61e-5	1.84e-4	1.77e-2	1.64e-1	5.85e-2	7.58e-2	1.70e-1	2.34e-1	1.98e-1
	St. Dev.	5.84e-5	3.73e-5	9.13e-5	1.02e-2	8.48e-2	3.08e-2	4.71e-2	1.40e-1	2.78e-1	1.53e-1
	L.Qt.	6.17e-5	4.07e-5	1.44e-4	1.34e-2	1.14e-1	3.30e-2	3.56e-2	6.64e-2	7.24e-2	8.31e-2
	Med.	8.81e-5	6.17e-5	1.90e-4	1.65e-2	1.50e-1	5.22e-2	6.02e-2	1.28e-1	1.81e-1	1.45e-1
	U. Qt.	1.46e-4	1.02e-4	2.19e-4	2.33e-2	2.17e-1	7.73e-2	1.04e-1	2.36e-1	5.01e-1	2.50e-1
C3	Mean	9.82e-5	6.31e-5	1.81e-4	1.65e-2	1.50e-1	4.36e-2	4.95e-2	8.71e-2	1.44e-1	1.05e-1
	St. Dev.	5.28e-5	3.48e-5	9.09e-5	9.11e-3	7.71e-2	1.55e-2	2.15e-2	6.34e-2	1.39e-1	7.11e-2
	L.Qt.	5.62e-5	3.80e-5	1.29e-4	1.28e-2	1.17e-1	2.95e-2	3.06e-2	4.36e-2	5.37e-2	5.46e-2
	Med.	8.11e-5	5.62e-5	1.86e-4	1.54e-2	1.47e-1	4.57e-2	4.49e-2	6.30e-2	1.28e-1	7.94e-2
	U. Qt.	1.31e-4	9.77e-5	2.14e-4	2.13e-2	1.95e-1	5.72e-2	6.54 e-2	1.14e-1	2.69e-1	1.31e-1
C4	Mean	9.79e-5	6.03e-5	1.81e-4	1.65e-2	1.50e-1	3.97e-2	4.67e-2	8.74e-2	1.41e-1	1.02e-1
	St. Dev.	4.78e-5	3.37e-5	8.81e-5	8.81e-3	5.84e-2	1.18e-2	1.72e-2	6.33e-2	1.20e-1	6.84e-2
	L.Qt.	5.66e-5	3.74e-5	1.29e-4	1.31e-2	1.17e-1	3.03e-2	3.17e-2	4.45e-2	4.89e-2	5.24e-2
	Med.	7.61e-5	5.83e-5	1.82e-4	1.69e-2	1.50e-1	3.96e-2	4.41e-2	6.44e-2	1.00e-1	8.12e-2
	U. Qt.	1.20e-4	9.35e-5	2.08e-4	2.13e-2	1.95e-1	4.97e-2	5.89e-2	1.17e-1	1.96e-1	1.34e-1
C5	Mean	9.41e-5	5.99e-5	1.80e-4	1.65e-2	1.36e-1	3.97e-2	4.63e-2	7.91e-2	9.15e-2	9.96e-2
	St. Dev.	4.24e-5	3.13e-5	6.86e-5	8.11e-3	6.83e-2	1.25e-2	1.84e-2	5.48e-2	6.27e-2	5.84e-2
	L.Qt.	5.68e-5	3.78e-5	1.31e-4	1.28e-2	1.05e-1	3.05e-2	3.18e-2	3.86e-2	4.91e-2	5.11e-2
	Med.	8.96e-5	5.85e-5	1.78e-4	1.69e-2	1.37e-1	3.96e-2	4.59e-2	5.74e-2	7.81e-2	7.24e-2
	U. Qt.	1.15e-4	9.01e-5	2.07e-4	2.08e-2	1.67e-1	5.17e-2	5.98e-2	1.04e-1	9.95e-2	1.20e-1

Table 1: Summary of Monte Carlo results for parameter estimation errors. The Table shows the mean, standard deviation, median and quartiles of the distribution of the error in each parameter. Results are given for a $m = 1.4M_\odot$ CO inspiralling into a $M = 100M_\odot$ IMBH with spin parameter $q = 0.3$, and assuming four alternative configurations for the detector network, C1–C4, as described in Section 6.2. Configuration C5 is the network of three ETs.

Model		Statistics of distribution for error ΔX in parameter $X =$									
		$\ln(m)$	$\ln(M)$	q	t_0	ϕ_0	θ_S	ϕ_S	θ_K	ϕ_K	$\ln(D)$
C1	Mean	2.14e-3	5.01e-4	2.34e-3	2.08e-2	2.34e-1	1.5332	2.3089	2.3442	2.7840	2.5105
	St. Dev.	1.07e-3	3.51e-4	1.03e-3	7.33e-3	1.30e-1	2.0017	3.1318	1.9584	2.2266	1.8864
	L.Qt.	1.78e-3	2.63e-4	1.95e-3	1.02e-2	1.62e-1	0.1341	0.2344	0.8615	1.1489	1.1982
	Med.	2.51e-3	5.01e-4	2.34e-3	1.62e-2	2.45e-1	0.6232	0.8482	1.9277	2.0915	1.8508
	U. Qt.	3.16e-3	8.51e-4	2.63e-3	2.69e-2	3.38e-1	2.1273	3.1569	3.4303	3.8956	3.2680
C2	Mean	1.70e-3	4.17e-4	2.19e-3	1.31e-2	1.51e-1	6.08e-2	9.23e-2	1.99e-1	2.28e-1	2.39e-1
	St. Dev.	1.15e-3	3.13e-4	7.79e-4	6.46e-3	7.06e-2	3.02e-2	5.75e-2	1.73e-1	1.90e-1	1.86e-1
	L.Qt.	1.26e-3	2.09e-4	1.82e-3	8.71e-3	1.12e-1	3.50e-2	4.27e-2	8.03e-2	8.81e-2	9.77e-2
	Med.	2.29e-3	3.72e-4	2.19e-3	1.28e-2	1.47e-1	5.95e-2	7.01e-2	1.29e-1	1.63e-1	1.63e-1
	U. Qt.	2.88e-3	7.24e-4	2.51e-3	2.04e-2	2.08e-1	7.81e-2	1.37e-1	2.51e-1	2.87e-1	3.16e-1
C3	Mean	1.48e-3	3.80e-4	2.09e-3	1.23e-2	1.34e-1	4.38e-2	5.56e-2	1.11e-1	1.31e-1	1.32e-1
	St. Dev.	9.07e-4	2.43e-4	7.01e-4	5.76e-3	4.70e-2	1.56e-2	2.52e-2	9.34e-2	1.08e-1	1.02e-1
	L.Qt.	1.05e-3	2.14e-4	1.78e-3	8.13e-3	1.04e-1	2.99e-2	3.41e-2	5.37e-2	5.60e-2	6.74e-2
	Med.	2.14e-3	3.55e-4	2.14e-3	1.25e-2	1.28e-1	4.18e-2	4.95e-2	7.82e-2	9.88e-2	9.70e-2
	U. Qt.	2.69e-3	6.76e-4	2.45e-3	1.90e-2	1.73e-1	5.71e-2	7.43e-2	1.35e-1	1.70e-1	1.76e-1
C4	Mean	1.51e-3	3.72e-4	2.09e-3	1.20e-2	1.28e-1	3.97e-2	5.31e-2	1.05e-1	1.21e-1	1.20e-1
	St. Dev.	8.06e-4	2.51e-4	6.08e-4	5.09e-3	4.75e-2	1.13e-2	1.96e-2	8.40e-2	9.73e-2	9.51e-2
	L.Qt.	1.15e-3	1.95e-4	1.70e-3	7.59e-3	1.04e-1	3.16e-2	3.49e-2	5.24e-2	5.71e-2	6.66e-2
	Med.	2.09e-3	3.39e-4	2.14e-3	1.23e-2	1.31e-1	4.06e-2	4.85e-2	8.21e-2	9.40e-2	9.82e-2
	U. Qt.	2.63e-3	6.56e-4	2.45e-3	1.86e-2	1.62e-1	4.99e-2	7.01e-2	1.39e-1	1.59e-1	1.72e-1
C5	Mean	1.41e-3	3.63e-4	2.09e-3	1.19e-2	1.05e-1	3.95e-2	5.12e-2	9.57e-2	1.08e-1	1.12e-1
	St. Dev.	6.39e-4	1.87e-4	5.72e-4	5.07e-3	5.20e-2	1.19e-2	2.03e-2	6.74e-2	8.75e-2	7.67e-2
	L.Qt.	1.07e-3	2.00e-4	1.65e-3	7.41e-3	7.83e-2	2.96e-2	3.43e-2	5.74e-2	5.75e-2	5.93e-2
	Med.	1.58e-3	3.47e-4	2.13e-3	1.24e-2	9.38e-2	3.86e-2	4.79e-2	6.91e-2	8.79e-2	8.82e-2
	U. Qt.	1.74e-3	6.03e-4	2.40e-3	1.41e-2	1.22e-1	4.92e-2	6.51e-2	1.14e-1	1.24e-1	1.56e-1

Table 2: As Table 1, but for binary systems with a CO of mass $m = 10M_\odot$, and a central IMBH of mass $M = 500M_\odot$.

Model		Statistics of distribution for error ΔX in parameter $X =$									
		$\ln(m)$	$\ln(M)$	q	t_0	ϕ_0	θ_S	ϕ_S	θ_K	ϕ_K	$\ln(D)$
C1	Mean	3.90e-4	6.97e-5	2.14e-4	2.75e-2	3.37e-1	1.0248	1.4132	1.73984	1.98796	1.96526
	St. Dev.	9.60e-5	1.30e-5	5.03e-5	1.12e-2	2.11e-1	1.0433	1.5308	0.98158	1.25075	1.21136
	L. Qt.	3.56e-4	6.24e-5	1.87e-4	2.23e-2	1.33e-1	0.1554	0.2162	0.94480	0.93815	0.97202
	Med.	4.04e-4	7.02e-5	2.12e-4	2.69e-2	2.76e-1	0.6771	0.8102	1.60984	1.78872	1.76174
	U. Qt.	4.43e-4	7.79e-5	2.32e-4	3.80e-2	6.02e-1	1.5840	2.2538	2.42813	2.82516	2.74045
C2	Mean	3.37e-4	6.92e-5	2.10e-4	1.81e-2	1.38e-1	5.69e-2	8.02e-2	1.93e-1	2.37e-1	1.88e-1
	St. Dev.	1.31e-4	1.29e-5	5.00e-5	9.60e-3	1.07e-1	2.85e-2	5.13e-2	1.61e-1	2.05e-1	1.31e-1
	L. Qt.	2.41e-4	6.23e-5	1.91e-4	1.62e-2	6.26e-2	3.24e-2	3.67e-2	7.81e-2	9.54e-2	8.84e-2
	Med.	3.89e-4	7.02e-5	2.11e-4	1.99e-2	8.27e-2	5.02e-2	6.51e-2	1.39e-1	1.54e-1	1.43e-1
	U. Qt.	4.23e-4	7.46e-5	2.25e-4	2.57e-2	1.81e-1	7.23e-2	1.15e-1	2.56e-1	3.16e-1	2.56e-1
C3	Mean	3.23e-4	6.90e-5	2.05e-4	1.62e-2	1.25e-1	4.36e-2	5.96e-2	1.00e-1	1.38e-1	9.97e-2
	St. Dev.	1.30e-4	1.18e-5	4.57e-5	6.12e-3	1.06e-1	1.77e-2	3.07e-2	8.18e-2	1.11e-1	6.14e-2
	L. Qt.	2.10e-4	6.23e-5	1.95e-4	1.47e-2	6.30e-2	2.75e-2	3.31e-2	4.84e-2	6.45e-2	5.62e-2
	Med.	3.75e-4	6.97e-5	2.06e-4	1.77e-2	8.12e-2	3.96e-2	5.75e-2	6.82e-2	9.11e-2	7.89e-2
	U. Qt.	4.13e-4	7.58e-5	2.19e-4	2.23e-2	2.45e-1	5.82e-2	7.43e-2	1.29e-1	1.73e-1	1.39e-1
C4	Mean	3.21e-4	6.85e-5	2.03e-4	1.20e-2	1.23e-1	4.06e-2	5.88e-2	9.12e-2	1.24e-1	9.74e-2
	St. Dev.	1.19e-4	1.01e-5	4.43e-5	5.33e-3	7.95e-2	1.47e-2	2.81e-2	6.56e-2	1.03e-1	6.36e-2
	L. Qt.	2.30e-4	6.25e-5	1.93e-4	1.07e-2	5.88e-2	2.99e-2	3.46e-2	4.64e-2	6.38e-2	5.09e-2
	Med.	3.73e-4	6.86e-5	2.04e-4	1.23e-2	8.12e-2	3.96e-2	5.62e-2	6.81e-2	8.71e-2	7.63e-2
	U. Qt.	4.13e-4	7.45e-5	2.15e-4	1.73e-2	2.51e-1	5.17e-2	6.61e-2	1.19e-1	1.66e-1	1.29e-1
C5	Mean	3.17e-4	6.82e-5	2.03e-4	1.14e-2	9.02e-2	4.02e-2	5.75e-2	8.59e-2	1.10e-1	9.68e-2
	St. Dev.	1.03e-4	8.51e-6	4.31e-5	5.22e-3	5.32e-2	1.28e-2	2.84e-2	6.22e-2	9.12e-2	6.10e-2
	L. Qt.	2.21e-4	6.28e-5	1.91e-4	1.02e-2	7.02e-2	3.02e-2	3.23e-2	4.48e-2	5.25e-2	4.91e-2
	Med.	3.51e-4	6.80e-5	2.01e-4	1.17e-2	9.34e-2	4.16e-2	5.17e-2	6.14e-2	8.22e-2	7.39e-2
	U. Qt.	4.06e-4	7.31e-5	2.11e-4	1.65e-2	1.24e-1	5.09e-2	6.97e-2	1.06e-1	1.50e-1	1.21e-1

Table 3: As Table 1, but for binary systems with a central IMBH of mass $M = 500M_\odot$.

References

- [1] P. AJITH, S. BABAK, Y. CHEN, M. HEWITSON, B. KRISHNAN, A. M. SINTES, J. T. WHELAN, B. BRÜGMANN, P. DIENER, N. DORBAND, J. GONZALEZ, M. HANNAM, S. HUSA, D. POLLNEY, L. REZZOLLA, L. SANTAMARÍA, U. SPERHAKE, AND J. THORNBURG. Template bank for gravitational waveforms from coalescing binary black holes: Nonspinning binaries. *Phys. Rev. D* , **77**[10]:104017–+, May 2008. [104](#), [144](#)
- [2] P. AJITH AND S. BOSE. Estimating the parameters of nonspinning binary black holes using ground-based gravitational-wave detectors: Statistical errors. *Phys. Rev. D* , **79**[8]:084032–+, April 2009. [144](#)
- [3] P. AMARO-SEOANE, J. R. GAIR, M. FREITAG, M. C. MILLER, I. MANDEL, C. J. CUTLER, AND S. BABAK. *TOPICAL REVIEW: Intermediate and extreme mass-ratio inspirals—astrophysics, science applications and detection using LISA*. *Class. Quantum Grav.*, **24**:113–+, September 2007. [14](#), [30](#), [59](#), [64](#), [159](#)
- [4] T. A. APOSTOLATOS, C. CUTLER, G. J. SUSSMAN, AND K. S. THORNE. Spin-induced orbital precession and its modulation of the gravitational waveforms from merging binaries. *Phys. Rev. D* , **49**:6274–6297, June 1994. [125](#)
- [5] S. BABAK, H. FANG, J. R. GAIR, K. GLAMPEDAKIS, AND S. A. HUGHES. “Kludge” gravitational waveforms for a test-body orbiting a Kerr black hole. *Phys. Rev. D* , **75**[2]:024005–+, January 2007. [11](#), [15](#), [21](#), [23](#), [24](#), [25](#), [28](#), [66](#), [70](#), [105](#), [163](#)
- [6] L. BARACK AND C. CUTLER. *LISA capture sources: Approximate waveforms, signal-to-noise ratios, and parameter estimation accuracy*. *Phys. Rev. D* , **69**[8]:082005–+, April 2004. [13](#), [14](#), [15](#), [16](#), [42](#), [43](#), [45](#), [48](#), [50](#), [62](#), [63](#), [82](#), [92](#), [126](#), [160](#)

-
- [7] L. BARACK AND C. CUTLER. Using LISA extreme-mass-ratio inspiral sources to test off-Kerr deviations in the geometry of massive black holes. *Phys. Rev. D* , **75**[4]:042003–+, February 2007. [157](#)
- [8] L. BARACK AND N. SAGO. *Gravitational self-force on a particle in circular orbit around a Schwarzschild black hole*. *Phys. Rev. D* , **75**[6]:064021–+, March 2007. [10](#), [15](#), [28](#), [35](#), [36](#), [70](#)
- [9] L. BARACK AND N. SAGO. Gravitational Self-Force Correction to the Innermost Stable Circular Orbit of a Schwarzschild Black Hole. *Phys.Rev. Lett* , **102**[19]:191101–+, May 2009. [110](#)
- [10] L. BARACK AND N. SAGO. Gravitational self-force on a particle in eccentric orbit around a Schwarzschild black hole. *Phys. Rev. D* , **81**[8]:084021–+, April 2010. [10](#), [28](#), [70](#)
- [11] E. BARAUSSE AND A. BUONANNO. Improved effective-one-body Hamiltonian for spinning black-hole binaries. *Phys. Rev. D* , **81**[8]:084024–+, April 2010. [116](#)
- [12] E. BARAUSSE, E. RACINE, AND A. BUONANNO. Hamiltonian of a spinning test particle in curved spacetime. *Phys. Rev. D* , **80**[10]:104025–+, November 2009. [116](#)
- [13] E. BERTI, V. CARDOSO, J. A. GONZALEZ, U. SPERHAKE, M. HANNAM, S. HUSA, AND B. BRÜGMANN. Inspiral, merger, and ringdown of unequal mass black hole binaries: A multipolar analysis. *Phys. Rev. D* , **76**[6]:064034–+, September 2007. [112](#)
- [14] E. BERTI, V. CARDOSO, AND C. M. WILL. Gravitational-wave spectroscopy of massive black holes with the space interferometer LISA. *Phys. Rev. D* , **73**[6]:064030–+, March 2006. [113](#), [126](#), [163](#)
- [15] L. BLANCHET AND T. DAMOUR. The post-Minkowskian iteration method and the structure of radiative gravitational fields. *Academie des Science Paris Comptes Rendus Serie B Sciences Physiques*, **298**:431–434, March 1984. [11](#)
- [16] L. BLANCHET AND T. DAMOUR. Post-Newtonian generation of gravitational waves. *Annales de L’Institut Henri Poincare Section Physique Theorique*, **50**:377–408, 1989. [11](#)

-
- [17] L. BLANCHET, T. DAMOUR, G. ESPOSITO-FARÈSE, AND B. R. IYER. Dimensional regularization of the third post-Newtonian gravitational wave generation from two point masses. *Phys. Rev. D* , **71**[12]:124004–+, June 2005. [116](#)
- [18] L. BLANCHET, T. DAMOUR, B. R. IYER, C. M. WILL, AND A. G. WISEMAN. *Gravitational-Radiation Damping of Compact Binary Systems to Second Post-Newtonian Order*. *Phys.Rev. Lett* , **74**:3515–3518, May 1995. [28](#), [30](#), [62](#), [70](#)
- [19] L. BLANCHET AND G. FAYE. General relativistic dynamics of compact binaries at the third post-Newtonian order. *Phys. Rev. D* , **63**[6]:062005–+, March 2001. [117](#)
- [20] H. BONDI, F. A. E. PIRANI, AND I. ROBINSON. Gravitational Waves in General Relativity. III. Exact Plane Waves. *Royal Society of London Proceedings Series A*, **251**:519–533, June 1959. [6](#)
- [21] H. BONDI, M. G. J. VAN DER BURG, AND A. W. K. METZNER. Gravitational Waves in General Relativity. VII. Waves from Axi-Symmetric Isolated Systems. *Royal Society of London Proceedings Series A*, **269**:21–52, August 1962. [7](#)
- [22] D. A. BROWN, J. BRINK, H. FANG, J. R. GAIR, C. LI, G. LOVELACE, I. MANDDEL, AND K. S. THORNE. Prospects for Detection of Gravitational Waves from Intermediate-Mass-Ratio Inspirals. *Physical Review Letters*, **99**[20]:201102–+, November 2007. [157](#)
- [23] A. BUONANNO, Y. CHEN, AND M. VALLISNERI. Detection template families for gravitational waves from the final stages of binary black-hole inspirals: Nonspinning case. *Phys. Rev. D* , **67**[2]:024016–+, January 2003. [119](#)
- [24] A. BUONANNO, G. B. COOK, AND F. PRETORIUS. Inspiral, merger, and ring-down of equal-mass black-hole binaries. *Phys. Rev. D* , **75**[12]:124018–+, June 2007. [112](#), [113](#)
- [25] A. BUONANNO AND T. DAMOUR. Effective one-body approach to general relativistic two-body dynamics. *Phys. Rev. D* , **59**[8]:084006–+, April 1999. [11](#), [117](#)
- [26] A. BUONANNO AND T. DAMOUR. Transition from inspiral to plunge in binary black hole coalescences. *Phys. Rev. D* , **62**[6]:064015–+, September 2000. [120](#)

-
- [27] A. BUONANNO, Y. PAN, J. G. BAKER, J. CENTRELLA, B. J. KELLY, S. T. MCWILLIAMS, AND J. R. VAN METER. Approaching faithful templates for non-spinning binary black holes using the effective-one-body approach. *Phys. Rev. D* , **76**[10]:104049–+, November 2007. [112](#), [119](#), [120](#), [124](#)
- [28] A. BUONANNO, Y. PAN, H. P. PFEIFFER, M. A. SCHEEL, L. T. BUCHMAN, AND L. E. KIDDER. Effective-one-body waveforms calibrated to numerical relativity simulations: Coalescence of nonspinning, equal-mass black holes. *Phys. Rev. D* , **79**[12]:124028–+, June 2009. [11](#), [116](#)
- [29] L. M. BURKO. Orbital evolution of a test particle around a black hole. II. Comparison of contributions of spin-orbit coupling and the self-force. *Phys. Rev. D* , **69**[4]:044011–+, February 2004. [16](#)
- [30] B. CARTER. Axisymmetric Black Hole Has Only Two Degrees of Freedom. *Physical Review Letters*, **26**:331–333, February 1971. [7](#)
- [31] S. CHANDRASEKHAR. *The mathematical theory of black holes*. Research supported by NSF. Oxford/New York, Clarendon Press/Oxford University Press (International Series of Monographs on Physics. Volume 69), 1983, 663 p., 1983. [3](#), [25](#)
- [32] S. CHANDRASEKHAR AND F. P. ESPOSITO. The 2-1/2 POST-NEWTONIAN Equations of Hydrodynamics and Radiation Reaction in General Relativity. *Astrophys. J.*, **160**:153–+, April 1970. [8](#)
- [33] LISA COLLABORATION. http://list.caltech.edu/doku.php?id=mission_documents. [19](#)
- [34] C. CUTLER. *Angular resolution of the LISA gravitational wave detector*. *Phys. Rev. D* , **57**:7089–7102, June 1998. [41](#)
- [35] C. CUTLER AND M. VALLISNERI. *LISA detections of massive black hole inspirals: Parameter extraction errors due to inaccurate template waveforms*. *Phys. Rev. D* , **76**[10]:104018–+, November 2007. [15](#), [17](#), [24](#), [53](#), [54](#), [55](#), [63](#), [84](#), [90](#), [92](#), [93](#), [161](#)
- [36] T. DAMOUR. Coalescence of two spinning black holes: An effective one-body approach. *Phys. Rev. D* , **64**[12]:124013–+, December 2001. [116](#)

-
- [37] T. DAMOUR AND N. DERUELLE. Radiation reaction and angular momentum loss in small angle gravitational scattering. *Physics Letters A*, **87**:81–84, December 1981. [116](#)
- [38] T. DAMOUR, B. R. IYER, AND A. NAGAR. Improved resummation of post-Newtonian multipolar waveforms from circularized compact binaries. *Phys. Rev. D*, **79**[6]:064004–+, March 2009. [11](#), [122](#)
- [39] T. DAMOUR, P. JARANOWSKI, AND G. SCHÄFER. Effective one body approach to the dynamics of two spinning black holes with next-to-leading order spin-orbit coupling. *Phys. Rev. D*, **78**[2]:024009–+, July 2008. [116](#)
- [40] T. DAMOUR AND A. NAGAR. Final spin of a coalescing black-hole binary: An effective-one-body approach. *Phys. Rev. D*, **76**[4]:044003–+, August 2007. [112](#), [116](#)
- [41] T. DAMOUR AND A. NAGAR. Comparing effective-one-body gravitational waveforms to accurate numerical data. *Phys. Rev. D*, **77**[2]:024043–+, January 2008. [122](#)
- [42] T. DAMOUR AND A. NAGAR. Improved analytical description of inspiralling and coalescing black-hole binaries. *Phys. Rev. D*, **79**[8]:081503–+, April 2009. [116](#)
- [43] T. DAMOUR AND A. NAGAR. The Effective One Body description of the Two-Body problem. *ArXiv e-prints*, June 2009. [104](#), [117](#), [118](#), [122](#)
- [44] THIBAUT DAMOUR, PIOTR JARANOWSKI, AND GERHARD SCHÄFER. Determination of the last stable orbit for circular general relativistic binaries at the third post-newtonian approximation. *Phys. Rev. D*, **62**[8]:084011, Sep 2000. [118](#), [119](#)
- [45] B. S. DEWITT AND R. W. BREHME. Radiation damping in a gravitational field. *Annals of Physics*, **9**:220–259, February 1960. [10](#)
- [46] P. A. M. DIRAC. Classical Theory of Radiating Electrons. *Royal Society of London Proceedings Series A*, **167**:148–169, August 1938. [10](#)
- [47] A. EDDINGTON. *The propagation of Gravitational Waves*. *Proceedings of the Royal Society of London, series A* **102**:268–282, 1922. [4](#)
- [48] A. EDDINGTON. *The Spontaneous Loss of Energy of a Spinning Rod according to the Relativity Theory*. *Philosophical Magazine*, **46**:1112–1117, 1923. [4](#)

-
- [49] A. EINSTEIN. *Zur Elektrodynamik bewegter Körper*. *Annalen der Physik*, **322**:891–921, 1905. [2](#)
- [50] A. EINSTEIN. *Die Feldgleichungen der Gravitation*. *Königlich Preussische Akademie der Wissenschaften Zu Berlin, Sitzungberichte*, **1915**:844–847, 1915. [2](#)
- [51] A. EINSTEIN. *Näherungsweise Integration der Feldgleichungen der Gravitation*. *Königlich Preussische Akademie der Wissenschaften Zu Berlin, Sitzungberichte*, **1916**:688–696, 1916. [3](#)
- [52] A. EINSTEIN. *Über Gravitationswellen*. *Königlich Preussische Akademie der Wissenschaften Zu Berlin, Sitzungberichte*, **1918**:154–157, 1918. [4](#)
- [53] A. EINSTEIN, L. INFELD, AND B. HOFFMANN. The Gravitational Equations and the Problem of Motion. *The Annals of Mathematics*, **39**:65–100, 1938. [3](#)
- [54] A. EINSTEIN AND N. ROSEN. On Gravitational Waves. *Journal of The Franklin Institute*, **223**:43–54, January 1937. [5](#)
- [55] S. FAIRHURST. Source localization with an advanced gravitational wave detector network. *ArXiv e-prints*, October 2010. [104](#), [143](#)
- [56] M. FAVATA. Conservative self-force correction to the innermost stable circular orbit: Comparison with multiple post-Newtonian-based methods. *Phys. Rev. D*, **83**[2]:024027–+, January 2011. [68](#)
- [57] L. S. FINN AND K. S. THORNE. Gravitational waves from a compact star in a circular, inspiral orbit, in the equatorial plane of a massive, spinning black hole, as observed by LISA. *Phys. Rev. D*, **62**[12]:124021–+, December 2000. [158](#)
- [58] A. FREISE, S. CHELKOWSKI, S. HILD, W. DEL POZZO, A. PERRECA, AND A. VECCHIO. Triple Michelson interferometer for a third-generation gravitational wave detector. *Classical and Quantum Gravity*, **26**[8]:085012–+, April 2009. [18](#), [93](#), [102](#)
- [59] M. FREITAG, M. A. GÜRKAN, AND F. A. RASIO. Runaway collisions in young star clusters - II. Numerical results. *MNRAS*, **368**:141–161, May 2006. [20](#)
- [60] J. R. GAIR. Probing black holes at low redshift using LISA EMRI observations. *ArXiv e-prints*, November 2008. [14](#), [49](#)

-
- [61] J. R. GAIR. The black hole symphony: probing new physics using gravitational waves. *Royal Society of London Philosophical Transactions Series A*, **366**:4365–4379, December 2008. [13](#)
- [62] J. R. GAIR, L. BARACK, T. CREIGHTON, C. CUTLER, S. L. LARSON, E. S. PHINNEY, AND M. VALLISNERI. Event rate estimates for LISA extreme mass ratio capture sources. *Class. Quantum Grav.*, **21**:1595–+, October 2004. [59](#)
- [63] J. R. GAIR AND K. GLAMPEDAKIS. Improved approximate inspirals of test bodies into Kerr black holes. *Phys. Rev. D*, **73**[6]:064037–+, March 2006. [15](#), [24](#), [26](#), [27](#), [29](#), [68](#), [69](#), [92](#)
- [64] J. R. GAIR, I. MANDEL, M. C. MILLER, AND M. VOLONTERI. Exploring intermediate and massive black-hole binaries with the Einstein Telescope. *ArXiv e-prints*, July 2009. [19](#), [20](#), [102](#), [131](#), [132](#), [133](#), [138](#), [139](#), [150](#)
- [65] J. R. GAIR, I. MANDEL, A. SESANA, AND A. VECCHIO. Probing seed black holes using future gravitational-wave detectors. *Classical and Quantum Gravity*, **26**[20]:204009–+, October 2009. [19](#), [144](#), [148](#), [149](#), [150](#)
- [66] R. GEROCH. Multipole Moments. II. Curved Space. *Journal of Mathematical Physics*, **11**:2580–2588, August 1970. [157](#)
- [67] R. O. HANSEN. Multipole moments of stationary space-times. *Journal of Mathematical Physics*, **15**:46–52, January 1974. [157](#)
- [68] A. HEWISH, S. J. BELL, J. D. H. PILKINGTON, P. F. SCOTT, AND R. A. COLLINS. Observation of a Rapidly Pulsating Radio Source. *Nature*, **217**:709–713, February 1968. [8](#)
- [69] S. HILD, S. CHELKOWSKI, A. FREISE, J. FRANC, N. MORGADO, R. FLAMINIO, AND R. DESALVO. A Xylophone Configuration for a third Generation Gravitational Wave Detector. *ArXiv e-prints*, June 2009. 0906.2655. [18](#), [102](#), [156](#)
- [70] J. M. HOBBS. A vierbein formalism of radiation damping. *Annals of Physics*, **47**:141–165, March 1968. [10](#)
- [71] D. W. HOGG. Distance measures in cosmology. *ArXiv Astrophysics e-prints*, May 1999. [132](#)

-
- [72] E. A. HUERTA AND J. R. GAIR. Influence of conservative corrections on parameter estimation for extreme-mass-ratio inspirals. *Phys. Rev. D* , **79**[8]:084021–+, April 2009. [23](#), [24](#), [66](#), [70](#), [73](#), [105](#)
- [73] E. A. HUERTA AND J. R. GAIR. Intermediate-mass-ratio inspirals in the Einstein Telescope. I. Signal-to-noise ratio calculations. *Phys. Rev. D* , **83**[4]:044020–+, February 2011. [102](#), [150](#)
- [74] E. A. HUERTA AND J. R. GAIR. Intermediate-mass-ratio inspirals in the Einstein Telescope. II. Parameter estimation errors. *Phys. Rev. D* , **83**[4]:044021–+, February 2011. [140](#)
- [75] S. A. HUGHES AND R. D. BLANDFORD. Black Hole Mass and Spin Coevolution by Mergers. *Astrophys. J. Lett* , **585**:L101–L104, March 2003. [113](#)
- [76] R. A. HULSE AND J. H. TAYLOR. *Discovery of a pulsar in a binary system.* *ApJL*, **195**:L51–L53, January 1975. [9](#)
- [77] C. KANT MISHRA, K. G. ARUN, B. R. IYER, AND B. S. SATHYAPRAKASH. Parametrized tests of post-Newtonian theory using Advanced LIGO and Einstein Telescope. *ArXiv e-prints*, May 2010. [102](#), [156](#)
- [78] S. KAWAMURA AND ET AL. The Japanese space gravitational wave antenna—DECIGO. *Classical and Quantum Gravity*, **23**:125–+, April 2006. [19](#)
- [79] D. KENNEFICK. *Traveling at the Speed of Thought: Einstein and the Quest for Gravitational Waves.* Princeton University Press, 2007. [1](#), [7](#)
- [80] D. KENNEFICK AND A. ORI. *Radiation-reaction-induced evolution of circular orbits of particles around Kerr black holes.* *Phys. Rev. D* , **53**:4319–4326, April 1996. [26](#), [69](#), [105](#)
- [81] I. R. KENYON. *General Relativity.* OXFORD SCIENCE PUBLICATIONS, 1990. [9](#)
- [82] R. P. KERR. Gravitational Field of a Spinning Mass as an Example of Algebraically Special Metrics. *Physical Review Letters*, **11**:237–238, September 1963. [7](#)
- [83] C. KÖNIGSDÖRFFER, G. FAYE, AND G. SCHÄFER. Binary black-hole dynamics at the third-and-a-half post-Newtonian order in the ADM formalism. *Phys. Rev. D* , **68**[4]:044004–+, August 2003. [116](#)

-
- [84] S. J. KOVACS AND K. S. THORNE. The generation of gravitational waves. III - Derivation of bremsstrahlung formulae. *Astrophys. J.*, **217**:252–280, October 1977. [9](#)
- [85] S. J. KOVACS, JR. AND K. S. THORNE. The generation of gravitational waves. IV - Bremsstrahlung. *Astrophys. J.*, **224**:62–85, August 1978. [9](#)
- [86] C. LI AND G. LOVELACE. [12](#)
- [87] C. O. LOUSTO AND Y. ZLOCHOWER. Extreme-Mass-Ratio-Black-Hole-Binary Evolutions with Numerical Relativity. *ArXiv e-prints*, September 2010. [162](#)
- [88] M. LUNA AND A. M. SINTES. Parameter estimation of compact binaries using the inspiral and ringdown waveforms. *Classical and Quantum Gravity*, **23**:3763–3782, June 2006. [144](#)
- [89] D. LYNDEN-BELL. Galactic Nuclei as Collapsed Old Quasars. *Nature*, **223**:690–694, August 1969. [7](#)
- [90] MICHELE MAGGIORE. *Gravitational Waves*. OXFORD, 2008. [11](#)
- [91] I. MANDEL. Spin distribution following minor mergers and the effect of spin on the detection range for low-mass-ratio inspirals. *ArXiv e-prints*, July 2007. [113](#)
- [92] I. MANDEL, D. A. BROWN, J. R. GAIR, AND M. C. MILLER. Rates and Characteristics of Intermediate Mass Ratio Inspirals Detectable by Advanced LIGO. *Astrophys. J.*, **681**:1431–1447, July 2008. [132](#)
- [93] T. A. MATTHEWS AND A. R. SANDAGE. Optical Identification of 3c 48, 3c 196, and 3c 286 with Stellar Objects. *Astrophys. J.*, **138**:30–+, July 1963. [7](#)
- [94] MICHEL JANSSEN, ROBERT SCHULMANN, JÓZSEF ILLY, CHRISTOPH LEHNER, AND DIANA KORMOS BUCHWALD. *The collected papers of Albert Einstein*. Princeton University Press, 2002. [3](#)
- [95] M. C. MILLER. Gravitational Radiation from Intermediate-Mass Black Holes. *Astrophys. J.*, **581**:438–450, December 2002. [113](#)
- [96] M. C. MILLER AND E. J. M. COLBERT. Intermediate-Mass Black Holes. *International Journal of Modern Physics D*, **13**:1–64, January 2004. [19](#), [20](#)

-
- [97] Y. MINO, M. SASAKI, M. SHIBATA, H. TAGOSHI, AND T. TANAKA. Chapter 1. Black Hole Perturbation. *Progress of Theoretical Physics Supplement*, **128**:1–121, 1997. [26](#), [69](#), [114](#)
- [98] Y. MINO, M. SASAKI, AND T. TANAKA. Chapter 7. Gravitational Radiation Reaction. *Progress of Theoretical Physics Supplement*, **128**:373–406, 1997. [10](#)
- [99] C. W. MISNER, K. S. THORNE, AND J. A. WHEELER. *Gravitation*. San Francisco: W.H. Freeman and Co., 1973, 1973. [2](#), [25](#), [41](#), [111](#)
- [100] S. D. MURRAY AND D. N. C. LIN. Coalescence, Star Formation, and the Cluster Initial Mass Function. *Astrophys. J.*, **467**:728–+, August 1996. [20](#)
- [101] S. NISSANKE AND L. BLANCHET. Gravitational radiation reaction in the equations of motion of compact binaries to 3.5 post-Newtonian order. *Classical and Quantum Gravity*, **22**:1007–1031, March 2005. [11](#), [116](#)
- [102] R. M. O’LEARY, F. A. RASIO, J. M. FREGEAU, N. IVANOVA, AND R. O’SHAUGHNESSY. Binary Mergers and Growth of Black Holes in Dense Star Clusters. *Astrophys. J.*, **637**:937–951, February 2006. [20](#)
- [103] J. R. OPPENHEIMER AND H. SNYDER. On continued gravitational contraction. *Phys. Rev.*, **56**[5]:455–459, Sep 1939. [6](#)
- [104] A. ORI AND K. S. THORNE. Transition from inspiral to plunge for a compact body in a circular equatorial orbit around a massive, spinning black hole. *Phys. Rev. D* , **62**[12]:124022–+, December 2000. [21](#), [101](#), [107](#), [109](#), [110](#), [138](#), [162](#)
- [105] Y. PAN, A. BUONANNO, L. T. BUCHMAN, T. CHU, L. E. KIDDER, H. P. PFEIFFER, AND M. A. SCHEEL. Effective-one-body waveforms calibrated to numerical relativity simulations: Coalescence of nonprecessing, spinning, equal-mass black holes. *Phys. Rev. D* , **81**[8]:084041–+, April 2010. [11](#), [116](#)
- [106] M. E. PATI AND C. M. WILL. Post-Newtonian gravitational radiation and equations of motion via direct integration of the relaxed Einstein equations. II. Two-body equations of motion to second post-Newtonian order, and radiation reaction to 3.5 post-Newtonian order. *Phys. Rev. D* , **65**[10]:104008–+, May 2002. [116](#)
- [107] R. PENROSE. Gravitational Collapse: the Role of General Relativity. *Nuovo Cimento Rivista Serie*, **1**:252–+, 1969. [7](#)

-
- [108] P. C. PETERS AND J. MATHEWS. *Gravitational Radiation from Point Masses in a Keplerian Orbit*. *Phys. Rev. D* , **131**:435–440, July 1963. [8](#), [14](#)
- [109] E. POISSON, A. POUND, AND I. VEGA. The motion of point particles in curved spacetime. *ArXiv e-prints*, February 2011. [10](#)
- [110] F. PRETORIUS. Evolution of Binary Black-Hole Spacetimes. *Physical Review Letters*, **95**[12]:121101–+, September 2005. [11](#)
- [111] M. PUNTURO AND ET AL. The third generation of gravitational wave observatories and their science reach. *Classical and Quantum Gravity*, **27**[8]:084007–+, April 2010. [18](#)
- [112] T. C. QUINN AND R. M. WALD. Axiomatic approach to electromagnetic and gravitational radiation reaction of particles in curved spacetime. *Phys. Rev. D* , **56**:3381–3394, September 1997. [10](#)
- [113] T. REGIMBAU AND SCOTT A. HUGHES. Gravitational-wave confusion background from cosmological compact binaries: Implications for future terrestrial detectors. *Phys. Rev. D* , **79**[6]:062002, Mar 2009. [18](#), [19](#)
- [114] L. REZZOLLA, P. DIENER, E. N. DORBAND, D. POLLNEY, C. REISSWIG, E. SCHNETTER, AND J. SEILER. The Final Spin from the Coalescence of Aligned-Spin Black Hole Binaries. *Astrophys. J. Lett* , **674**:L29–L32, February 2008. [112](#)
- [115] FINTAN D. RYAN. *Gravitational waves from the inspiral of a compact object into a massive, axisymmetric body with arbitrary multipole moments*. *Phys. Rev. D* , **52**[10]:5707–5718, Nov 1995. [12](#), [157](#)
- [116] N. SAGO, L. BARACK, AND S. DETWEILER. Two approaches for the gravitational self-force in black hole spacetime: Comparison of numerical results. *Phys. Rev. D* , **78**[12]:124024–+, December 2008.
- [117] M. SAIJO, K.-I. MAEDA, M. SHIBATA, AND Y. MINO. Gravitational waves from a spinning particle plunging into a Kerr black hole. *Phys. Rev. D* , **58**[6]:064005–+, September 1998. [16](#), [65](#), [66](#), [67](#), [68](#), [90](#), [92](#)
- [118] M. SASAKI AND T. NAKAMURA. Gravitational Radiation from a Kerr Black Hole. I—Formulation and a Method for Numerical Analysis—. *Progress of Theoretical Physics*, **67**:1788–1809, June 1982. [10](#)

-
- [119] G. SCHALLER, D. SCHAERER, G. MEYNET, AND A. MAEDER. New grids of stellar models from 0.8 to 120 solar masses at $Z = 0.020$ and $Z = 0.001$. *A&AS* , **96**:269–331, December 1992. [20](#)
- [120] S. SIGURDSSON AND L. HERNQUIST. Primordial black holes in globular clusters. *Nature* , **364**:423–425, July 1993. [20](#)
- [121] L. SMARR. Numerical Construction of Space-Time. *Royal Society of London Proceedings Series A*, **368**:15–16, September 1979. [10](#)
- [122] P. A. SUNDARARAJAN. Transition from adiabatic inspiral to geodesic plunge for a compact object around a massive Kerr black hole: Generic orbits. *Phys. Rev. D* , **77**[12]:124050–+, June 2008. [163](#)
- [123] H. TAGOSHI. *Post-Newtonian Expansion of Gravitational Waves from a Particle in Slightly Eccentric Orbit around a Rotating Black Hole*. *PTP*, **93**:307–333, February 1995. [26](#)
- [124] T. TANAKA, Y. MINO, M. SASAKI, AND M. SHIBATA. *Gravitational waves from a spinning particle in circular orbits around a rotating black hole*. *Phys. Rev. D* , **54**:3762–3777, September 1996. [28](#), [62](#), [69](#), [70](#), [92](#)
- [125] Y. TANIGUCHI, Y. SHIOYA, T. G. TSURU, AND S. IKEUCHI. Formation of Intermediate-Mass Black Holes in Circumnuclear Regions of Galaxies. *PASJ* , **52**:533–537, June 2000. [20](#)
- [126] S. A. TEUKOLSKY. Perturbations of a Rotating Black Hole. I. Fundamental Equations for Gravitational, Electromagnetic, and Neutrino-Field Perturbations. *Astrophys. J.*, **185**:635–648, October 1973. [9](#)
- [127] K. S. THORNE. Multipole expansions of gravitational radiation. *Reviews of Modern Physics*, **52**:299–340, April 1980. [10](#)
- [128] K. S. THORNE. *Black holes and time warps: Einstein’s outrageous legacy*. 1994. [159](#)
- [129] K. S. THORNE AND S. J. KOVACS. The generation of gravitational waves. I - Weak-field sources. *Astrophys. J.*, **200**:245–262, September 1975. [9](#)
- [130] M. VALLISNERI. Use and abuse of the Fisher information matrix in the assessment of gravitational-wave parameter-estimation prospects. *Phys. Rev. D* , **77**[4]:042001–+, February 2008. [141](#)

-
- [131] N. WARBURTON AND L. BARACK. Self-force on a scalar charge in Kerr spacetime: Circular equatorial orbits. *Phys. Rev. D* , **81**[8]:084039–+, April 2010. [10](#), [70](#)
- [132] N. WARBURTON AND L. BARACK. Self force on a scalar charge in Kerr spacetime: eccentric equatorial orbits. *ArXiv e-prints*, March 2011. [10](#), [70](#)
- [133] L. WEN AND Y. CHEN. Geometrical expression for the angular resolution of a network of gravitational-wave detectors. *Phys. Rev. D* , **81**[8]:082001–+, April 2010. [104](#), [143](#)
- [134] HERMANN WEYL. *Raum, Zeit, Materie*. Translation by Henry L. Brose as *Space, Time, Matter* (Metheun, London, 1922). 4th ed. Springer, Berlin, 1921. [4](#)
- [135] N. E. WHITE AND J. VAN PARADIJS. The Galactic Distribution of Black Hole Candidates in Low Mass X-ray Binary Systems. *Astrophys. J. Lett* , **473**:L25+, December 1996. [20](#)
- [136] N. YUNES, A. BUONANNO, S. A. HUGHES, Y. PAN, E. BARAUSSE, M. C. MILLER, AND W. THROWE. Extreme Mass-Ratio Inspirals in the Effective-One-Body Approach: Quasi-Circular, Equatorial Orbits around a Spinning Black Hole. *ArXiv e-prints*, September 2010. [11](#), [116](#), [158](#)